Proceedings of the 3rd Conference

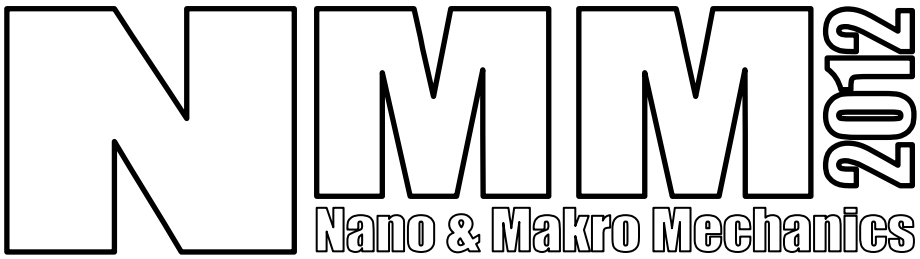

20th September 2012

All contributions in this book have been reviewed. However, the authors take responsibility for the content and for the correctness of their texts, the quality of the tables, graphs and figures. The editors therefore cannot accept responsibility for the final appearance of the manuscripts.

Edited by:

Tomáš Plachý, Pavel Padevět, Pavel Tesárek, Jan Stránský, Ondřej Zobal

Published by:

Department of Mechanics, Faculty of Civil Engineering, Czech Technical University in Prague, Thákurova 7, 166 29 Praha 6

Printed by:

Česká technika - nakladatelství ČVUT, Thákurova 1, 160 41 Praha 6, pages 276, 1st Edition

Acknowledgement:

SVK 06/12/F1

ISBN 978-80-01-05205-1

Table of Contents

IMPLEMENTATION OF NUMERICAL SIMULATION OF VISCOUS INCOMPRESSIBLE FLOW

Matej BEŇO[1], **Bořek PATZÁK**[2]

Abstract:*The method for solving viscous incompressible flows, based on [1], is presented for the numerical simulation of viscous incompressible flow. It uses a finite element discretization in space and an operator-splitting technique for discretization in time.The linearly constrained quadratic minimization problems which arise from this splitting are solved using Uzawa conjugate-gradient algorithms. The goal is to developefficient and accurate numerical tool for computing viscous flows, which will be later extended to non-Newtonian flows. The accuracy of the presented method has been confirmed on two common cases: the Poiseuille flow test and on driven cavity flow test.*

Keywords:*finite element method, operator splitting, Navier-Stokes equations, Uzawa Conjugate-gradient*

1. INTRODUCTION

The aim of this article is to present a method for solving viscous incompressible flows. The Eulerian based finite element implementation is based on the incompressible Navier-Stokes equations on two dimensional triangular meshes using operator splitting for time discretization [2]. The linearly constrained quadratic minimization problems which arise from this splitting are solved using conjugate gradient algorithms. The fractional-time-step scheme described by Marchuk [3] has been employed. Liquid is supposed to be incompressible and Newtonian. The advantage of this method is that no repeated remeshing is required. Also the assembled mass matrix remains constant thus it does not have to be assembled at every time step. By splitting one time step into three successive substeps the discretization enables better approximation of results. Velocity together with pressure are computed in this case in the first sub-step by using Uzawaconjugate-gradient algorithm while velocity is computed at each substep. To discretize the domain the Taylor-Hood triangular elements have been used with quadratic approximation of velocity and linear approximation of pressure. The implementation is validated using the Poiseuille flow test and driven cavity flow test.

[1]Ing. Matej Beňo, Department of Mechanics, Faculty of Civil Engineering, CTU in Prague; matej.beno@fsv.cvut.cz

[2]prof. Dr. Ing. BořekPatzák, Department of Mechanics, Faculty of Civil Engineering, CTU in Prague; borek.patzak@fsv.cvut.cz

2. PROBLEM FORMULATION

2.1. THE GOVERNING EQUATIONS

Assume incompressible viscous Newtonian fluid occupying at the given time $\boldsymbol{t} \in (\mathbf{0}, \boldsymbol{T})$, delimited domain $\boldsymbol{\Omega} \subset \mathbf{R^2}$ with boundary $\boldsymbol{\Gamma}$. Let denote by $\boldsymbol{x} = \{\boldsymbol{x_i}\}_{\boldsymbol{i=1}}^{\boldsymbol{2}}$ a generic point in $\boldsymbol{\Omega}$.Let further denote by $\boldsymbol{u}(\boldsymbol{x}, \boldsymbol{t})$ velocity and by $\boldsymbol{p}(\boldsymbol{x}, \boldsymbol{t})$ pressure, both governed by Navier-Stokes equations:

$$\boldsymbol{\rho}\frac{\mathbf{du}}{\mathbf{dt}} = \boldsymbol{\rho}\mathbf{g} + \boldsymbol{\nabla}.\boldsymbol{\sigma} \text{on} \boldsymbol{\Omega} \text{ - momentum equation,} \quad (1)$$

$$\boldsymbol{\nabla}.\boldsymbol{u} = \mathbf{0} \text{on } \boldsymbol{\Omega}. \text{ – incompressibility condition,} \quad (2)$$

where$\boldsymbol{\rho}$ is density of the fluid, $\mathbf{u}$ is velocity of the fluid, and $\boldsymbol{\sigma}$ is fluid stress. For an incompressible Newtonian viscous fluid, the stress is decomposed into its hydrostatic and shear components,

$$\boldsymbol{\sigma} = -\boldsymbol{p}\mathbf{I} + \mathbf{2}\boldsymbol{\eta}\mathbf{D}[\mathbf{u}], \quad (3)$$

where$\boldsymbol{p}$ is hydrostatic pressure in the fluid, $\boldsymbol{\eta}$ is the viscosity (assumed constant), and $\mathbf{D}[\mathbf{u}]$ is rate-of-strain tensor.

Relations (1)-(3) are to be supplemented by the appropriate initial conditions

$$\mathbf{u}(\mathbf{0}) = \mathbf{u_0} \text{on } \boldsymbol{\Omega}, \quad \boldsymbol{\nabla}.\mathbf{u_0} = \mathbf{0}, \quad (5)$$

and the boundary conditions

$$\mathbf{u} = \mathbf{u_\Gamma}(\boldsymbol{t}) \text{on } \boldsymbol{\Gamma}, \int_{\boldsymbol{\Gamma}} \mathbf{u_\Gamma}(\boldsymbol{t})\,\hat{\mathbf{n}} = \mathbf{0}, \quad (6)$$

where$\hat{\mathbf{n}}$ is unit normal vector pointing out of the $\boldsymbol{\Gamma}$.

2.2. FINITE ELEMENT FORMULATION

For the discrete velocity-pressure space the triangular Taylor-Hood elements have been used, with the quadratic velocity and linear pressure interpolation (see Figure 1).

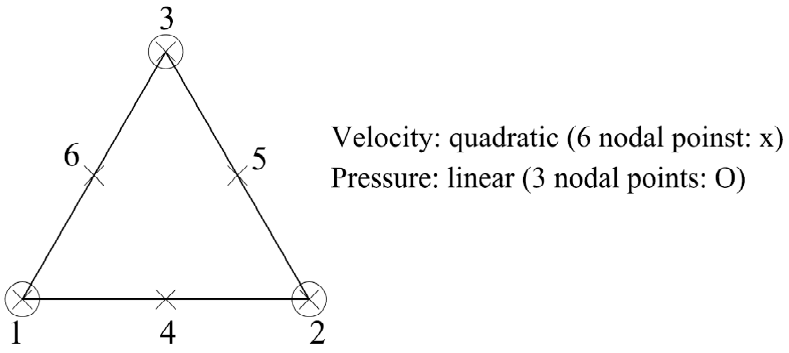

Fig. 1 The Taylor-Hood element.

Let introduce spaces of approximation and test functions of velocities and pressure:

$$\mathbb{W}_h = \{v_h \in C^0(\Omega)^2, \forall T \in \mathcal{T}_h\},$$
$$\mathbb{W}_{oh} = \{v_h \in \mathbb{W}_h, v_h = 0 \; on \Gamma\},$$
$$L_h = \{q_h \in C^0(\Omega), \forall T \in \mathcal{T}_h\},$$
$$L_{0h} = \left\{q_h \in L_h \middle| \int_\Omega q_h dx = 0\right\}.$$

By using these finite-dimensional spaces we arrive at the following finite-element approximation of the problem (1)-(7):

Find $\mathbf{u}_h \in \mathbb{W}_{0h}$, $p \in L_{0h}$ satisfying:

$$\int_\Omega \left(\rho\left(\frac{\mathrm{d}\mathbf{u}_\mathrm{h}}{\mathrm{dt}}\right) + (\mathbf{u}_\mathrm{h}.\nabla)\mathbf{u}_\mathrm{h}\right).\mathbf{v}_\mathrm{h}\mathrm{dx} - \int_\Omega \mathrm{p_h}\,\nabla.\mathbf{v}_\mathrm{h}\mathrm{dx} + \int_\Omega 2\eta\mathbf{D}[\mathbf{u}] : \mathbf{D}[\mathbf{v}]\mathrm{dx} = 0 \qquad (7)$$

for all $\mathbf{v}_h \in \mathbb{W}_{0h}$,

$$\int_\Omega q_h\nabla.\mathbf{u}_h = 0 \text{ for all } q_h \in L_h, \qquad (8)$$

$$\mathbf{u}_\mathrm{h}(0) = \mathbf{u}_{0h} \text{ on } \Omega, \qquad (9)$$

where $\mathbf{u}_{0h}$ is an approximation of $\mathbf{u}_0$ satisfying the compatibility conditions

$$\int_\Omega q_h\nabla.\mathbf{u}_{0h} = 0 \text{ for all } q_h \in L_h. \qquad (10)$$

Since, in (7), $\mathbf{u}$ is divergence-free and satisfies a Dirichlet boundary condition on all of Γ, we can write:

$$\int_\Omega 2\eta\mathbf{D}[\mathbf{u_h}] : \mathbf{D}[\mathbf{v_h}]dx = \int_\Omega \eta\nabla\mathbf{u_h} : \nabla\mathbf{v_h}dx \text{ for all } \mathbf{v}_h \in \mathbb{W}_{0h}.$$

3. TIME DISCRETIZATION BY OPERATOR SPLITTING

3.1. PRINCIPLE OPERATOR SPLITTING

As stated by Glowinski [2] numerical solutions of the relations (1)-(6) are not trivial due to the following reasons:

- The above equations are nonlinear
- Handling of the incompressibility condition (2)
- The above equations are system of partial differential equations, coupled through the nonlinear term $(\mathbf{u}\,.\nabla)\mathbf{u}$, the incompressibility condition $\nabla.\mathbf{u} = 0$, and sometimes through the boundary conditions.

The time discretization by operator splitting will partly overcome the above difficulties; in particular, decoupling of difficulties associated with the nonlinearity from those associated with the incompressibility condition. To introduce operator splitting, the approach by Glowinski&Pironneau [4] will be used. Let assume the following initial value problem:

$$\frac{\mathrm{d}\varphi}{\mathrm{d}t} + A(\varphi) = 0,$$

$$\varphi(0) = \varphi_0,$$

where A is an operator (possibly nonlinear, and even multivalued) from a Hilbert space H into itself and where $\varphi_0 \in$ H. There are numerous splitting operators to solve this problem [2].

3.2. FRACTIONAL-STEP SCHEME

In this work, the fractional-step scheme described by Marchuk [3] is employed. Let assume decomposition of the operator A into the following nontrivial decomposition:

$$A = A_1 + A_2 + A3,$$

(by nontrivial, we mean A1, A2 and A3 are individually simpler than A). In the following, Δt is a time step.

Set $\varphi^0 = \varphi_0$, for n>= 0, φ^n being known we compute $\varphi^{n+1/3}$, $\varphi^{n+2/3}$ and φ^{n+1} as follows

$$\frac{\varphi^{n+\frac{1}{3}}-\varphi^n}{\Delta t} + A_1\left(\varphi^{n+\frac{1}{3}}\right) = f_1^{n+1},$$
$$\frac{\varphi^{n+\frac{2}{3}}-\varphi^{n+\frac{1}{3}}}{\Delta t} + A_2\left(\varphi^{n+\frac{2}{3}}\right) = f_2^{n+1},$$
$$\frac{\varphi^{n+1}-\varphi^{n+\frac{2}{3}}}{\Delta t} + A_3(\varphi^{n+1}) = f_3^{n+1}.$$

By applying operator splitting to the problem (7-10) we obtain (with $0 \le \alpha, \beta \le 1$and $\alpha + \beta = 1$):

Find: $\mathbf{u}^{n+1/3} \in \mathbb{W}_h$ and $p^{n+1/3} \in L_h$

$$\rho \int_\Omega \frac{\mathbf{u}^{n+1/3}-\mathbf{u}^n}{\Delta t}.\mathbf{v}dx - \int_\Omega p^{n+1/3}\nabla.\mathbf{v}dx = 0 \text{ for all } \mathbf{v}_h \in \mathbb{W}_{0h} \qquad (11)$$

$$\int_\Omega q\nabla.\mathbf{u}^{n+1/3}dx = 0 \text{ for all } q_h \in L_h. \qquad (12)$$

Find: $\mathbf{u}^{n+2/3} \in \mathbb{W}_h$

$$\rho \int_\Omega \frac{\mathbf{u}^{n+2/3}-\mathbf{u}^{n+1/3}}{\Delta t}.\mathbf{v}dx - \rho \int_\Omega \left(\mathbf{u}^{n+1/3}.\nabla\right)\mathbf{u}^{n+2/3}.\mathbf{v}dx + 2\alpha\eta \int_\Omega \mathbf{D}\left[\mathbf{u}^{n+2/3}\right] : \mathbf{D}[\mathbf{v}]dx = 0 \qquad (13)$$

for all $\mathbf{v}_h \in \mathbb{W}_{0h}$.

Finally find $\mathbf{u}^{n+1} \in \mathbb{W}_h$

$$\rho \int_\Omega \frac{\mathbf{u}^{n+1}-\mathbf{u}^{n+2/3}}{\Delta t}.\mathbf{v}dx + 2\beta\eta \int_\Omega \mathbf{D}[\mathbf{u}^{n+1}] : \mathbf{D}[\mathbf{v}]dx = 0 \text{ for all } \mathbf{v}_h \in \mathbb{W}_{0h}. \qquad (14)$$

4. THE UZAWA ALGORITHM

To compute $\mathbf{u}^{n+1/3}$ and $p^{n+1/3}$the Uzawa conjugate-gradient algorithm operating is used [5, 6]. Discretized equations (11-12) have following form

$$\begin{pmatrix} A & & B_1^t \\ & A & B_2^t \\ B_1 & B_2 & 0 \end{pmatrix}\begin{pmatrix} u_1 \\ u_2 \\ p \end{pmatrix} = \begin{pmatrix} f_1 \\ f_2 \\ 0 \end{pmatrix}, \qquad (15)$$

whereAis a symmetric positive definite matrix and (B_1, B_2), (B_1^t, B_2^t) are discrete divergence operator and discrete gradient operator respectively.

This algorithm is based on constructing a positive semidefinite problem for the pressure

$$(B_1A^{-1}B_1^t + B_2A^{-1}B_2^t)p = B_1A^{-1}f_1 + B_2A^{-1}f_2 \qquad (16)$$

by substituting the velocity vector in the velocity divergence equation. Because the matrix

$\hat{A} = (B_1 A^{-1} B_1^t + B_2 A^{-1} B_2^t)$issymmetric and positive-definite, the pressure field can be solved using a preconditioned conjugate gradient algorithm. The final Uzawa algorithm is summarized as follow:

Initialization: $k = 0; p^0 = 0$

Solve $Au_1^0 = f_1, Au_2^0 = f_2$

$r_0 = B_1 u_1^0 + B_2 u_2^0$

Iteration:while $|r_k|$ >a given tolerance, ε

$k = k + 1$

if$k = 1$

$s_1 = r_0$

else

$\beta_k = r_{k-1}^t r_{k-1} / r_{k-2}^t r_{k-2}$

$s_k = r_{k-1} + \beta_k s_{k-1}$

end

Solve $Aw_1^k = B_1^t s_k, Aw_2^k = B_2^t s_k$ *(17)*

$\delta = (B_1^t s_k)^t w_1^k + (B_2^t s_k)^t w_2^k$

$\alpha_k = r_{k-1}^t r_{k-1} / \delta$

$p^k = p^{k-1} + \alpha_k s_k$

$u_1^k = u_1^{k-1} - \alpha_k w_1^k$

$u_2^k = u_2^{k-1} - \alpha_k w_2^k$

$r_k = r_{k-1} - \alpha_k B_1 w_1^k - \alpha_k B_2 w_2^k$

end

This iterative solution method requires significantly less memory and computation than direct solution approaches based on solving the full problem. The efficiency of this algorithm depends on how efficiently equation (17) is solved.

5. NUMERICAL VALIDATIONS:

The accuracy of prototype Matlab implementation has been verified using two benchmark problems: the Poiseuille flow between parallel plates and driven cavity flow.

5.1. POISEUILLE FLOW

In this classic test, the steady state velocity and pressure distributions is simulated for a fluid moving laterally between two plates whose length and width is much greater than a distance separating them. The geometry, boundary and initial conditions are illustrated on Fig 2. The domain is divided into 400 elements, the height is 1 and the length is 4. The stationary profile of velocity profile at outflow is quadratic. The mass density is $\rho = 1.0\, kg/m^3$, and the viscosity is $\eta = 10^{-2} Pas$. The results correspond with analytic solution.

When time step $\Delta t = 0.005$ s is chosen the implemented simulations renders results in time $t = 1{,}5\ s$.

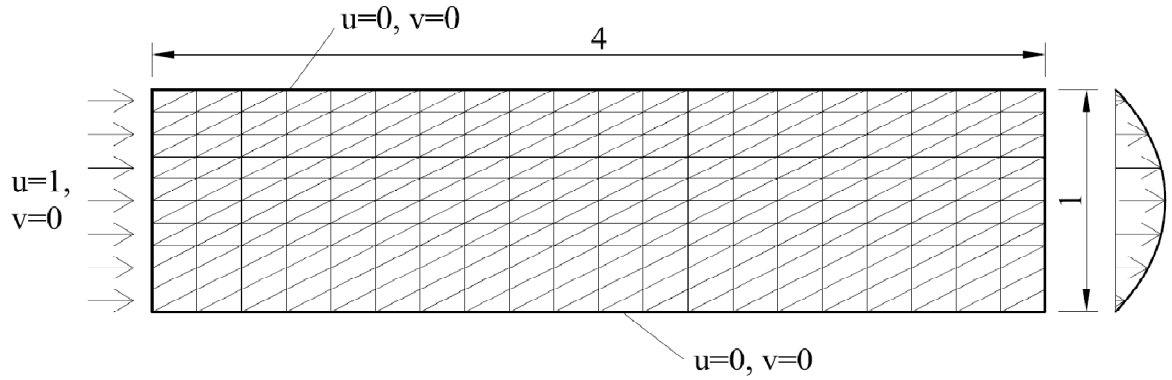

Fig. 2 The geometry and the boundary conditions of flow in tube test. The used mesh consists of 861 nodes and 400 elements.

5.2. DRIVEN CAVITY FLOW

The driven cavity flow is a typical problem applied to verify numerical model in fluid dynamics. We simulate the flow inside closed cavity and compare the results with the model developed by the other researches [7, 8]. Figure 3 shows geometry of the problem, computational mesh and applied boundary conditions. The viscosity is set to $\eta = 10^{-2} Pas$, and the Reynold's number is computed as $1/\eta$ (based on geometry of size 1 and maximum velocity 1). The mass density is $\rho = 1.0\ kg/m^3$, and the time step is $\Delta t = 0.01$ s. The results are in good agreement, even though the present values are restricted to the 30x30 grid points (see table No. 1).

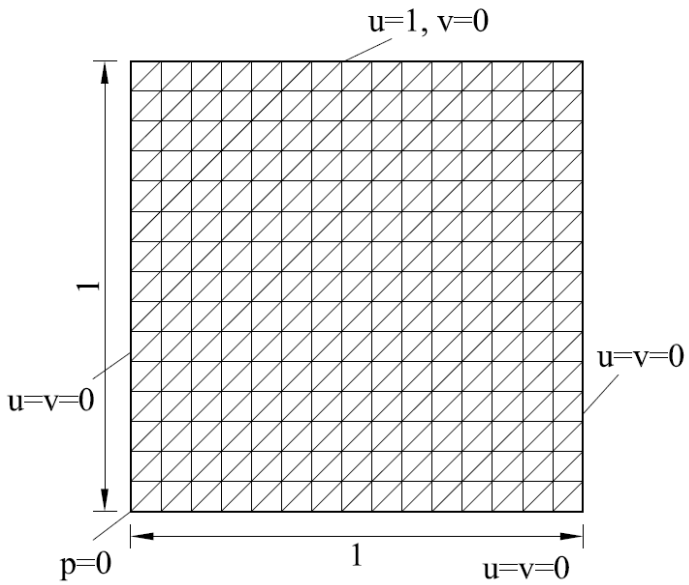

Fig. 3 The geometry and the boundary conditions of driven cavity flow test. The used mesh consists of 961 nodes and 450 elements.

Tab. 1: Velocity extreme through cavity centerlines at $Re = 100$

method	u_{min}	v_{min}	v_{max}
Present UCG	-0.2165	-0.2493	0.1771
Present with UCG*	-0.2165	-0.2493	0.1771
Botella and Peyret	-0.21279	-0.25266	0.17854
Rabenold	-0.2140424	-0.2538030	0.1795728

*number of iteration: 74

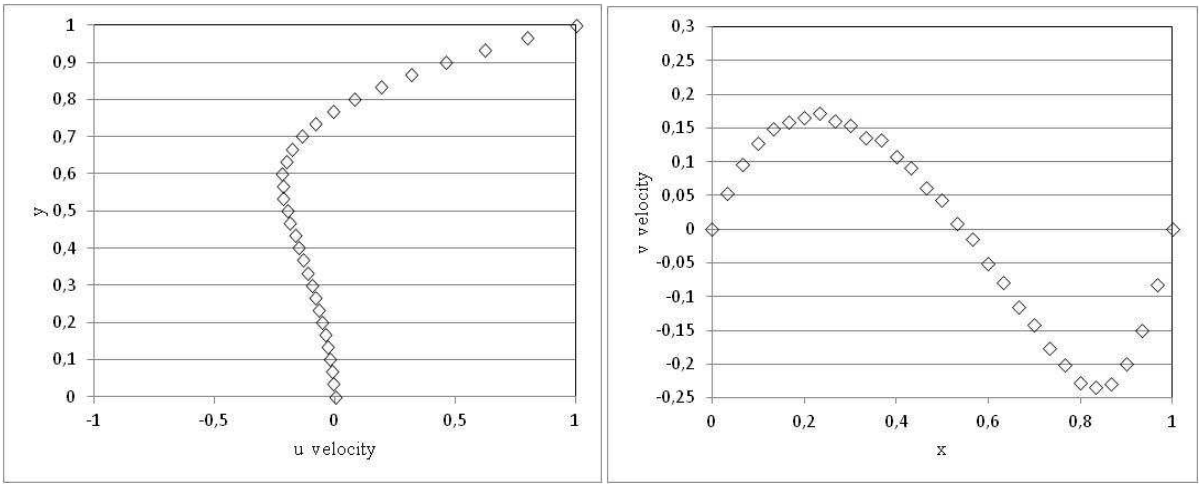

Fig. 4 Velocity profiles through cavity centerlines at $\eta = 10^{-2} Pas$ and 30 x 30 grid size.

6. CONCLUSION

Presented work describes formulation and implementation of non-stationary, incompressible flow finite element solver. The Taylor-Hood elements (P2-P1) have been implemented. For time discretization the operator splitting method is used. Discretized equations are solved using Uzawa conjugate gradient algorithm.The model is verified using standard benchmark tests from the literature.

ACKNOWLEDGEMENT

The support of this work by the Czech Technical University in Prague SGS project No. SGS12/027/OHK1/1T/11 is gratefully acknowledged.

REFERENCES

[1] Glowinski, R., Pan, T.W., Hesla, T.I., Joseph, D.D., A distributed Lagrange multiplier-fictitious domain method for particulate flows,In: Int. J. Multiphase Flows, 25, 1998, pp. 755–794.

[2] Glowinski, R., Finite Element Methods for Incompressible Viscous Flow, In: Handbook of Numerical Analysis, 9 (P.G. Ciarlet, J.L. Lions eds), North-Holland, Amsterdam, 2003,pp. 3-76.

[3] Marchuk, G.I, Splitting and Alternating Direction Methods, In: Handbook of Numerical Analysis, 1 (P.G. Ciarlet, J.L. Lions eds), North-Holland, Amsterdam, 1990,pp.197-462.

[4] Glowinski, R., Pironneau, O., Finite element methods for navier-stokes equations, In: Annual Reviews Fluid Mech. 24, 1992,pp.167-204

[5] Zhong, S., Yuen, D.A., Moresi, L.N., Numerical Methods For Mantle Convection, In: Schubert, Gerald (Ed.) Treatise on Geophysics, 7, 2007, pp. 227-252.

[6] Glowinski, R., Pan, T.W., Périaux, J., Fictitious domain methods for incompressible viscous flow around moving rigid bodies, In: J.R Whiteman (Ed.) The Mathematics of Finite Elements and Applications, Wiley, Chichester, 1997,pp. 155-174.

[7] Botella, O., Peyret, R.,Benchmark spectral results on lid-driven cavity flow, Computers&Fluids, 27 (4), 1998,pp.421-433.

[8] Rabenold, P.T, Lid-driven flow in a rectangular cavity with corner obstacles, [online], [2010], available from <http://www-users.math.umd.edu/~rabenold/enme646_project.pdf>.

CREEP OF A CEMENT PASTE WITH ADDITION OF THE FLY ASH - COMPARISON

Petr BITTNAR[1], **Pavel PADEVĚT**[2]

Abstract: *Different quantities of fly ash contained in the cement paste causes change properties of the final product. One of the properties is creep. The size of creep may influence the size ratio of fly ash and cement in the cement paste. Furthermore, measurement results and their comparison are presented. Creep was observed in the specimen's age of 1, 5 and 12 months.*

Keywords: *cement paste, shrinkage, creep, fly ash, lever mechanism*

1. INTRODUCTION

Processing waste materials allows observing the properties of materials, where such waste material is occurring. One example is the fly ash, which is produced as a waste during combustion of the brown and black coal. According to the method, and in particular combustion reached temperature, the fly ash can be divided into two basic groups, free flowing and classical. Particulate the fluidized fly ash is produced by burning coal at high temperatures and ash capture using limestone. Conversely the classic ash is a result from burning the coal in conventional furnaces at temperatures of 1200-1700 °C. Its annual production in countries where electricity is produced from coal combustion is negligible.

One of the sectors where the waste finds application is the construction industry. The fly ash has a number of suitable properties, which fit in the manufacture of building materials and in construction. The classical ash is chemically the inert material with a very fine granulometry 0.001 to 1 mm. The ash has a low content of SO_3 and relatively low volume density.

Listed properties predispose to use the fly ash as filler in the concrete. Fly ash in concrete is characterized by the so-called secondary hydration. This means that the fly ash reacts with gels which are formed after the hydration of cement and formation of CSH [1] gels. By reaction of the fly ash and gels are generated new types of gels in the cement matrix.

Due to the reaction between the cement gel and the fly ash, attention is focused on properties of the cement paste mixed with the fly ash. Between the primary properties such as compression and

[1] Ing. Petr Bittnar, Department of Mechanics, Faculty of Civil Engineering, CTU in Prague; petr.bittnar@fsv.cvut.cz

[2] Ing. Pavel Padevět, Ph.D., Department of Mechanics, Faculty of Civil Engineering, CTU in Prague; pavel.padevet@fsv.cvut.cz

tensile strength, flexural strength and modulus of elasticity, the creep is one of the essential characteristics for the design of structures [2].

2. SPECIMENS AND THEIR PREPARATION

The length 70 mm was chosen for the tests of the specimens. It is the limit for the use of measuring sensors. The diameter of the test specimens is 10 mm, the size is sufficient to ensure the homogeneity of the material. The cement paste was prepared with a water coefficient (w/c) 0.4 [3]. The coefficient in this case is the ratio of water to the weight of cement and fly ash.

The ratio between the weight of cement and fly ash was 1:1. Water was added to a mixture of cement and fly ash and cement slurry created. The cylindrical moulds were filed by cement slurry. The hardened cement paste was removed and inserted into the water, where it was stored until use after hardening. The specimens were cut to the required length of bodies for creep tests (Fig. 1) before their first testing.

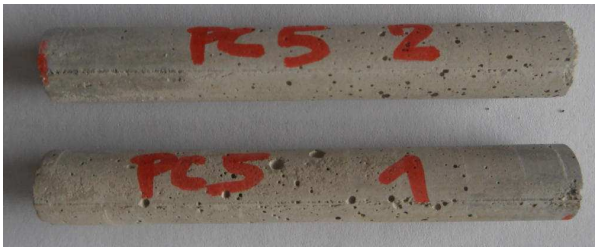

Fig. 1 Specimens for the creep test.

Specimens were tested at the age of one month, then in 5 months and 1 year [4]. At the age of 5 and 12 months, the same specimens were used. Material properties - compressive strength, modulus of elasticity - were measured on the same type of specimens produced simultaneously with the test samples for creep. Before testing, some specimens were dried and some were left in water.

3. PRICIPLES OF MEASURMENT AND TESTING OF THE SPECIMENS

The measurement principle was to monitor the creep increase of dry and water-saturated specimens. Shrinkage of the cement paste with the fly ash was measured together with the measurement of creep. Two dried specimens were used for measuring of the dried solid creep. The creep was measured on the two saturated specimens and on the other two specimens the shrinkage was measured. Shrinkage was measured on dried specimens.

Testing was carried out in every specimen leverage mechanism. The creep was measured by three sensors with a resolution of 0.1 microns. The specimens were loaded on size of the load 0.69 kN. Stress near to 8.82 MPa was originated in the cement paste. The average compressive strength is 40 MPa in the one month old cement paste. The load level corresponds to 22% of the strength of the cement paste.

The time interval of testing was one month. The measurement procedure consisted in the establishment specimens to the test equipment. Furthermore, the lever mechanisms were loaded with weights in order to achieve a defined level of load. Then, the test of specimens ran for 25 to 30 days. After the testing time, the specimens were unloaded and then test of finished. To ensure moisture conditions during the test, the specimens were wrapped in foil to prevent the admission and removal of moisture from solids.

4. MEASURING OF THE CREEP

The results of the creep cement pastes with addition of fly ash are presented in Fig. 2-4. In all cases there is the basic creep, which expresses the creep of the material without the influence of shrinkage. The dried specimens were deducted influence waning and the same principle was applied also for water-saturated body.

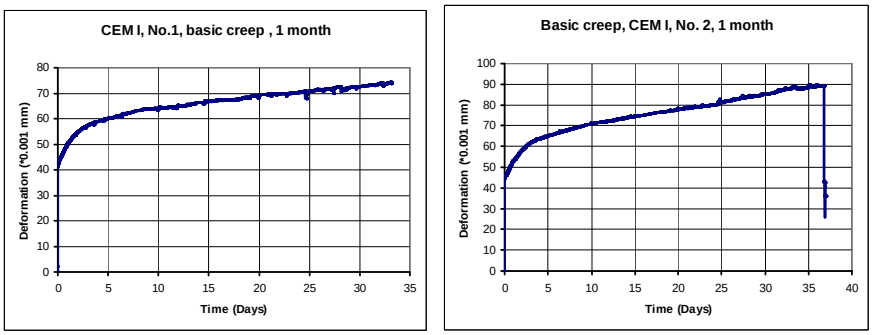

Fig. 2 Basic creep of the cement paste in 1 month age.

During the measurements, the size of the basic creep of the specimens with the length 70 mm reached 25 or 35 microns in 25 days. In these specimens, the beginning of the creep measurements started at 1 month of age. Size of the creep saturated water specimens without the influence of shrinkage after 25 days achieved values of 237 and 185 microns.

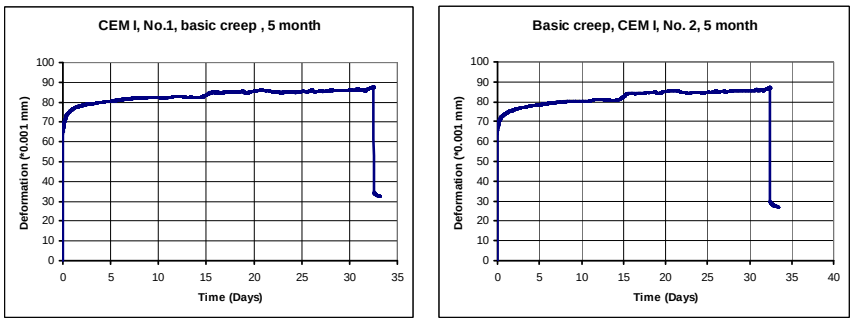

Fig. 3 Basic creep of the cement paste in 5 month age.

The basic creep of the cement paste tested at the age of 5 months reached 15.6 and 15.3 microns after 25 days. Water-saturated specimens showed the size of creep 263 and 253 microns after 25 days. In comparison with the younger specimens, the increase of deformation of dried specimens and

increasing of the deformation in a given time at the water-saturated specimens were reduced. All carried tests were held at a constant temperature of 20 ° C.

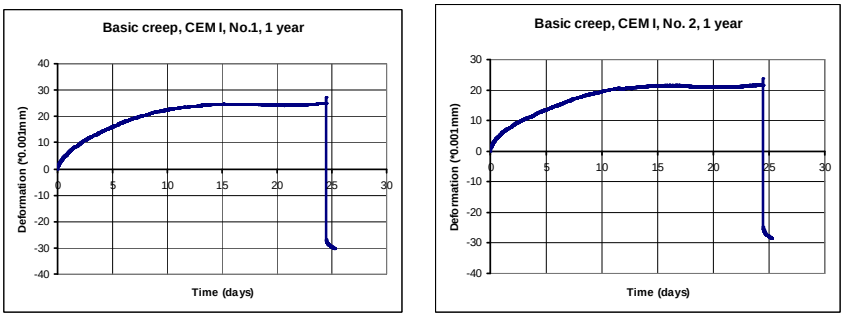

Fig. 4 Basic creep of the cement paste in 1 year age.

Both one year old specimens achieved the creep size 22 microns after 25 days of measurement. Water-saturated specimens had the deformation size 126 and 135 microns after 25 days of measurement. In all cases of measurements were deducted Influences of cement paste shrinkage cement paste with fly ash was deducted from all measurement of creep.

5. SUMMARY

From the creep measurement in chronological observation of maturation cement paste it can be seen that the decisive factor for the deformation is the water content in the specimen. The dried specimens did not show changes in the creep development during the year. On contrary, specimens that have been saturated with water showed a trend of reducing the size distortion. Although after 5 months, the creep size was higher than at the beginning and end of the measurement. It is possible to notice that the increase of deformation for the same period is almost 0.1 mm lower after one year from the specimen maturation than after the first measurement.

ACKNOWLEDGEMENT

The financial support of this experiment by the Faculty of Civil Engineering, Czech Technical University in Prague (SGS project No. 12/117/OHK1/2T/11) is gratefully acknowledged.

REFERENCES

[1] Bentz, D.P., Hansen, A.S., Guynn, J.M., Optimization of cement and fly ash particle sizes to produce sustainable concretes, Cement & Concrete Composites, 33, 2011, pp. 824–831.

[2] Van Mier, J.G.M., Fracture Processes of Concrete, CRC Press, 1997, ISBN 0-8493-9123-7.

[3] Neville, A.M., Properties of Concrete, John Wiley & Sons, 1997, ISBN 0-470-23527-6 .

[4] Padevět, P., Bittnar, P., Zobal, O., Changing the Properties of Cement Paste with Addition of Fly Ash in Time, In: Experimental Stress Analysis 2012, Tabor, 2012, ISBN 978-80-01-05060-6.

INFLUENCE OF CONTROLLED BIOMECHANICAL PROCESSES ON BONE TISSUE FORMATION IN INTERFRAGMENTAL GAP OF INTERRUPTED DIAPHYSIS

František DENK[1], Miroslav PETRTÝL[2]

Abstract:*Gradual distraction combined with controlled phases of harmonic oscillations in the process of long bone lengthening by distraction osseogenesis have due to deformations during patient's natural physiological movement a significant effect on bone tissue formation in the interfragmental space of diaphysis. Size of the deformation amplitudes, rate and frequency of oscillation cycles in individual stages of elongation process comprehensively affect formation of extracellular matrix and development of structure of new bone tissue.Suitable optimization of loading program in different stages of initial callus formation, proliferation and active distraction, relaxation and neutral fixation in the process of consolidation and final ossification can significantly contribute to increase the formation velocity and improve the qualitative properties of new bone tissue.*

Keywords:*distraction osseogenesis, external fixation, biomechanical stimulations, interfragmental callus*

1. INTRODUCTION

Acceleration of bone tissue formation and healing of the callus between the opposite vital fragments of interrupted diaphysis within the distraction osteogenesis method application can be achieved by their gradual and controlled procrastination, i.e. distraction, which is combined with micro-oscillations in the direction of extension of the treated long bone, usually along its longitudinal axis. Oriented and time-limited micro-oscillations with amplitudes range from 10^1 to 10^3 μm, frequencies of 10^{-1}to10^1 Hz and withindividualconfigurations(the parameters are dependent mainly on the phases of distraction process) in bone tissue stimulate fibrogenesis, chondrogenesis and osteogenesis. They contribute to accelerating the process of extracellular matrix organization and bone tissue healing process. Distraction process combined with micro-oscillations favorably affects the phase of proliferation and early consolidation, micro-oscillations have a positive impact in the late phase of consolidation. Controlled prolongation leads to the simultaneous complex acceleration of

[1]Ing.arch. et Ing. František Denk; Laboratory of Biomechanics and Biomaterial Engineering, Department of Mechanics, Faculty of Civil Engineering, CTU in Prague; frantisek.denk@fsv.cvut.cz

[2]prof. Ing. Miroslav Petrtýl, DrSc.; Laboratory of Biomechanics and Biomaterial Engineering, Department of Mechanics, Faculty of Civil Engineering, CTU in Prague; petrtyl@fsv.cvut.cz

metabolic processes, amplification of fibrogenic, chondrogenic and osteogenic signals and acceleration of intercellular communications, which generally improve the quality of tissue regeneration(Fig. 1.).

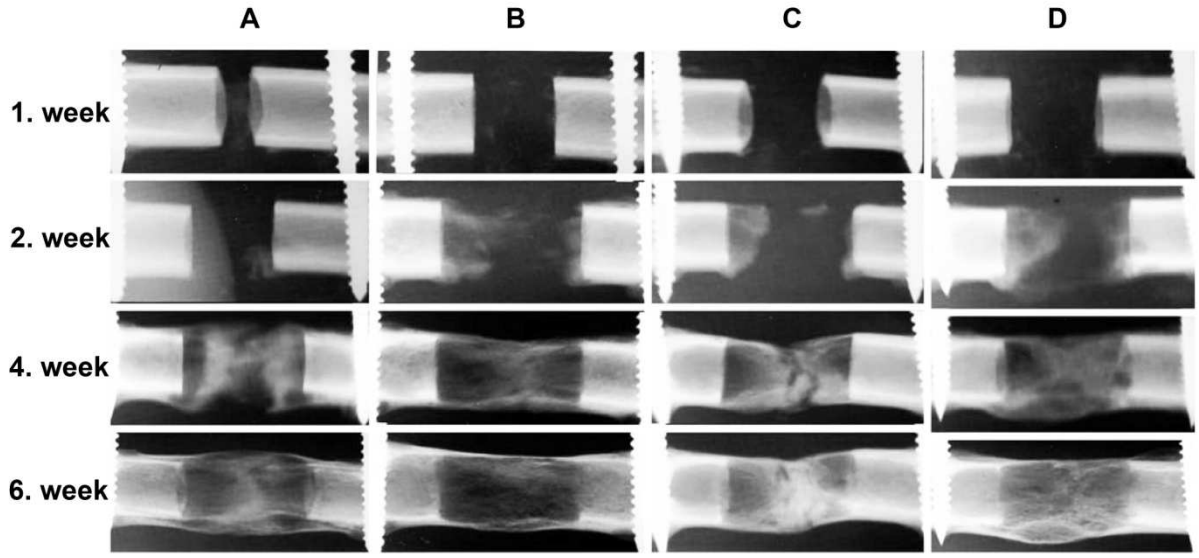

Fig. 1 X-ray analysis of the consolidation processof interfragmental tissue in Japanese white rabbits A, B, C, D

2. BIOMECHANICS OF BONE TISSUE REGENERATION

Regeneration of bone tissue is a natural, very complex process ensuring restoration of form and original function of damaged parts of the human skeleton, and involving coordinated participation of colonization, differentiation and proliferation of inflammatory cells, angioblasts, fibroblasts, chondroblasts and osteoblasts, which synthesize and release bioactive substances of extracellular matrix components (e.g. different types of collagen and growth factors)[1]. The first phase of healing occurs immediately after tissue damage, when the hematoma from discontinued blood vessels promptly fills the interfragmental space. Macrophages remove the dead tissue and generate granular structure of stabilizing callus for colonization of undifferentiated mesenchymal cells which are migrating and multiplying from the surrounding soft tissues[2]. In the next stage these cells differentiate into fibroblasts, chondrocytes or osteoblasts, depending on the biological and mechanical conditions, which play a very important role[3, 4]. Differentiated cells synthesize extracellular matrix structure to the corresponding tissue type(Fig. 2.), and after callus completing by cartilage structure continues endochondral ossification involving intricate complex of processes of maturation, osteogenesis, resorption and final remodeling of newly formed bone tissue. Pauwels[5]was one of the first authors who already in the 60s years described on the basis of experimental and clinical results the theory of tissue differentiation depending on the effects of mechanical stress(Fig. 3A). Perren andCordey[6]have established that tissue differentiation is stimulated, depending on their stiffness (“Interfragmentary strain theory” [7]) (Fig. 3B). Carter et al. [8]developed a new

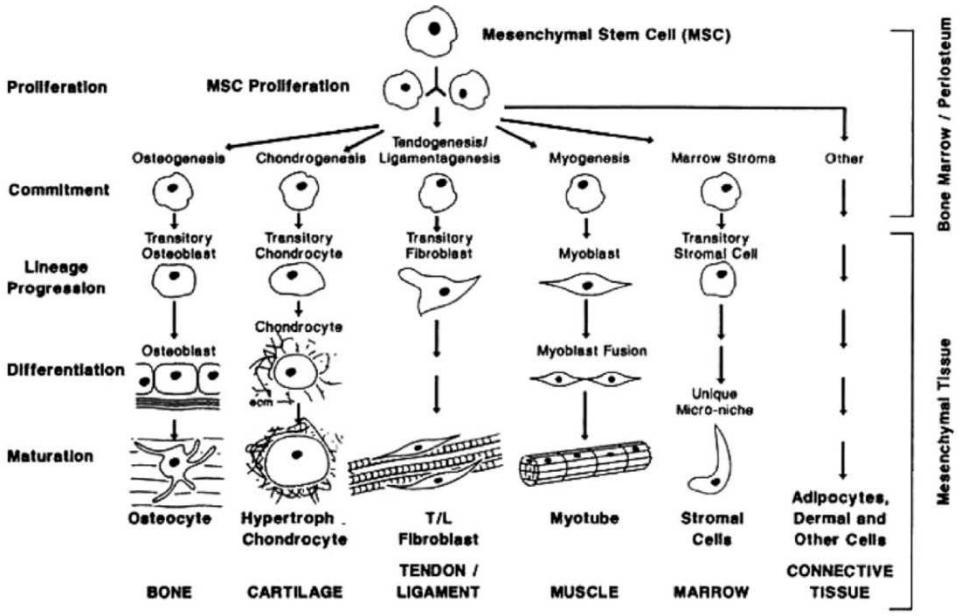

Fig. 2 The hierarchy of mesengenic processes [6]

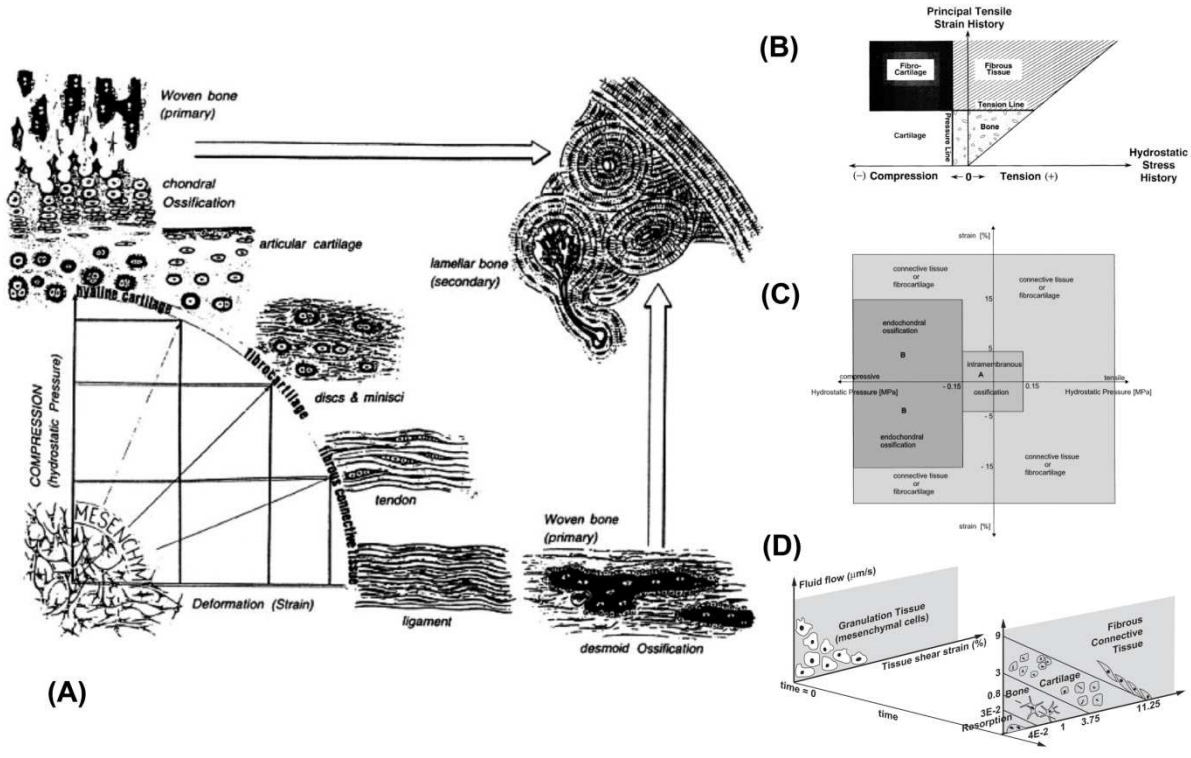

Fig. 3 (A) Pauwel's concept of tissue differentiation [7], (B) relationship between mechanical stimulation and tissue differentiation [9], (C) tissue differentiation rules [10], (D) tissue differentiation based on mechanical stimulation and fluid flow [11]

theory of tissue differentiation based on the correlation of new tissue formation with history of mechanical stress, provided that the callus tissue is formed by a single solid phase. Since theconfirmation of these theories many authors now use computational models based on FEM to quantify the local stress at different stages of healing processes. In 1999 Claes et al. [9] set by a similar path quantitative tissue differentiation theory, which reviews fields of deformation and hydrostatic pressure with tissue generated within the healing process(Fig. 3C). Kuiper et al. [10] developed using a bi-phase axial-symmetric FEM model the theory based on the mechanical stimulation by analysis of shear stress fields and fluid flow regulating differentiation processes, and strain energy regulating resorptive processes. Lacroix et al. [11]applied the rules of tissue differentiation derived by Prendergast et al. [12]and predicted by FEM analysis various options of the bone tissue healing, depending on the origin of stem cells(Fig. 3D). In 2002, García et al. [13]developed a continuum mathematical model that simulates the process of tissue regulation and callus growth with respect to different cellular events (migration of mesenchymal cells, proliferation, differentiation and extinction of different cell types), matrix synthesis, resorption, damage, mineralization and remodeling processes.

3. EXPERIMENTAL NUMERICAL STUDY OF INTERFRAGMENTAL REGENERATE DEVELOPMENT

The development of interfragmental solid in the extension process is dependent on many, especially unknown, parameters, which prevents find the appropriate exact (mathematical) formulation. The task of presented experimental numerical study is to estimate the majority of unknown functional parameters (function of development of material properties, volume expansion, geometric changes, the impact of force effects, etc.) at intervals defined by the sub-stages of distraction and healing process through verified theories in combination with results from clinical practice. Expected conditions of “functional continuity” on the boundary of intervals are always secured. Computational process performed on a simplified 3D FEM model in ANSYS APDL environment evaluates the development of geometry changes, the internal state of stress fields, and external and internal deformation changes, tracks and approximates the functional dependences on the course of input parameters in important points of interfragmental regenerate volume. Balance analysis was done separately for process of extension and neutral fixation.

3.1. METHODOLOGY OF SOLUTION AND USED MATERIAL PROPERTIES

Submitted work presents the initial iterative study of process of interfragmental regenerate formation during lengthening by distraction osteogenesis method. Configured model situation simulates the distraction process of femoral diaphyses elongation to 80 mm. The implemented standard prolongation program consists of primary osteotomy including initial mutual bone fragments delaying to value of 10 mm and distraction process after 5 days of calm with a frequency of 1 mm per 24 hours. Particular diaphysis extension lasts 70 days, then neutral fixation phase comes and consists

Tab. 1 Recapitulation of analysis and healing process according to the degree of interfragmentalcallus development in time

Time	0 days	5 days	30 days	75 days	105 days	135days	195 days	225 days	255 days	285 days	315 days
Healing phase	Osteotomy, begining of treat.	Beginning of active distraction		Beginning of neutral fixation							Removing of fix., end of treatment
Phase of regenerate development	Blood hematoma formation between fragments of diaphysis	Formation of stable interfragmental callus	Creating of blood supply system	Formation of high-quality oriented fibrous tissue	The inflection point of stress, the onset of early consolidation	Beginning of hardening from the contact faces of fragments		Early volume consolidation process		Late consolidation, homogeneous ossification	
Type of mainly formed tissue		Blood fluid	Formation of granulation tissue	Fibrous tissue			Immature bone tissue		Mature bone tissue		Cortical bone

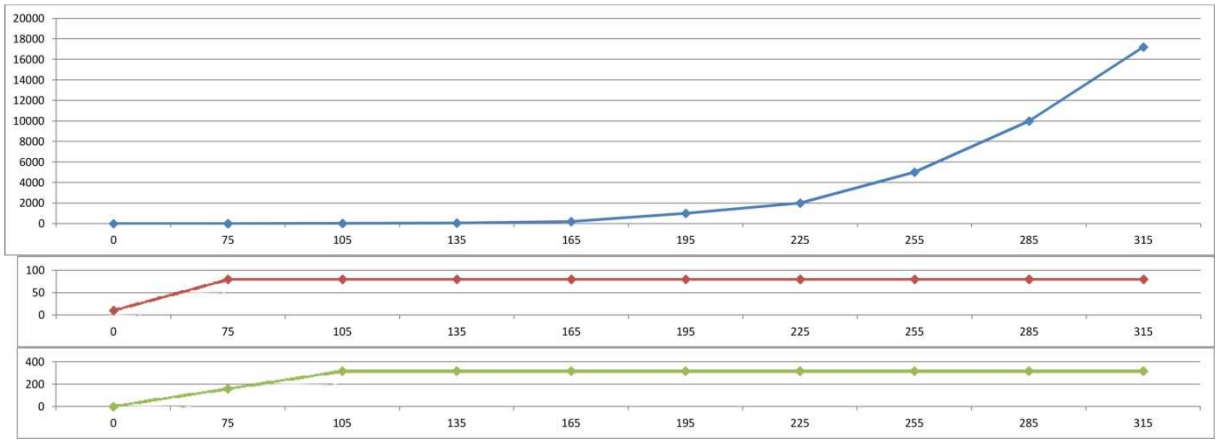

Fig. 4 Graphic dependences of input parameters, x-axis – time (days), y-axis – elasticity modulus development E (MPa) (blue line), distraction process (mm) (red line), volume expansion (%) (green line)

Tab. 2 Considered homogenized material properties of different tissue types

Tissue type	Granulation	Fibrous	Cartilage	Trabecular	Immature b.	Mature bone	Corticalis
E (MPa)	0.2	2.0	10.0	2.0	1000	6000	17200
ν (-)	0.167	0.167	0.167	0.167	0.325	0.325	0.325

ofan early stage of consolidation, the consolidation process and late consolidation, part of which is homogeneous ossification. The final phase of the remodeling process occurs only after removal of the

fixation apparatus. Total recovery time is expected 315 days. Comprehensive simulation of treatment course involves the introduction of the functional dependence of input parameters driving the regenerate solid evolution and homogenized material properties depending on the degree of consolidation, solidification and ossification process. Recapitulation of all parameters, including interdependences are given in presented tables and graphs(Tab. 1, 2, Fig. 4).

3.2. NUMERICAL ANALYSIS

Numerical analysis of stress fields was performed in sagittal section of the interfragmentalcallus

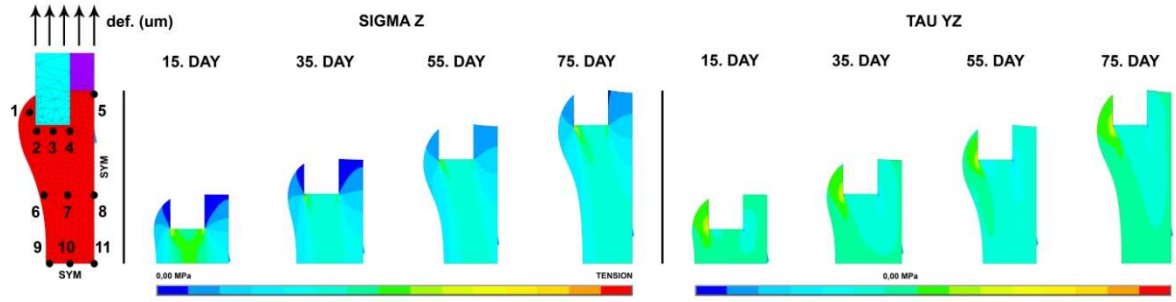

Fig. 5 Diagram of stress distribution in the sagittal section of callus, active distraction – formation during distraction steps 1 mm/24 hours

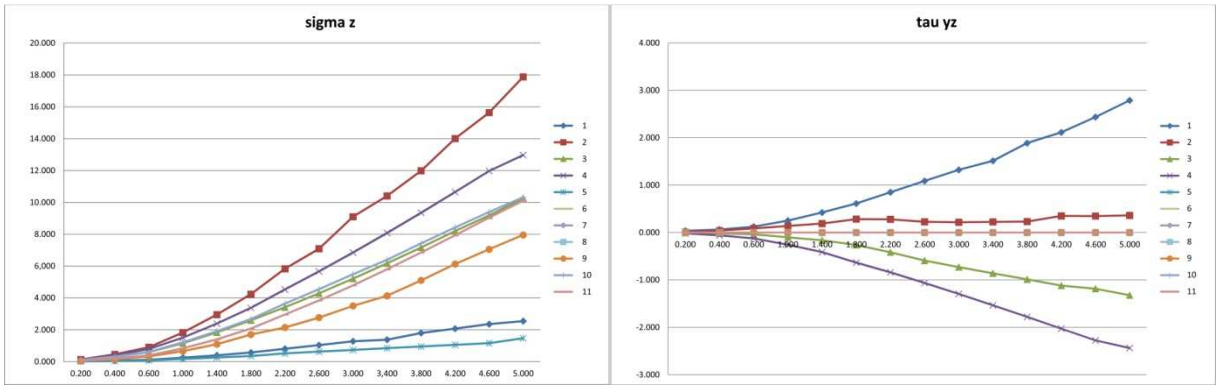

Fig. 6 Stress history in the observed points, x – E (MPa), y – σ, τ (MPa)

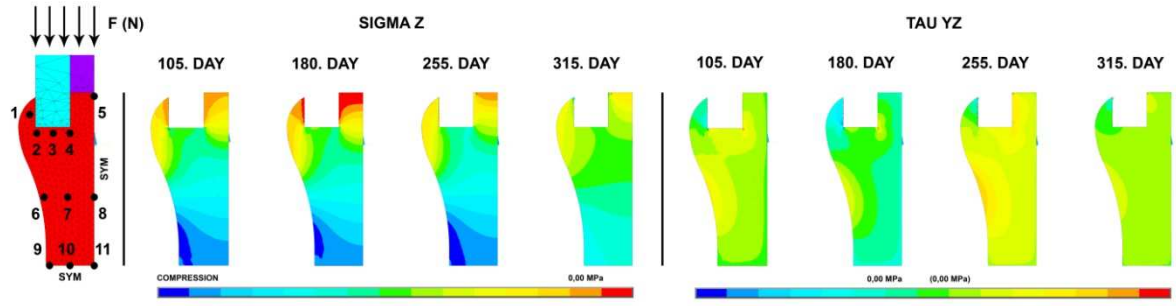

Fig. 7 Diagram of stress distribution in the sagittal section of callus, neutral fixation – consolidation at a constant load F = 800 N

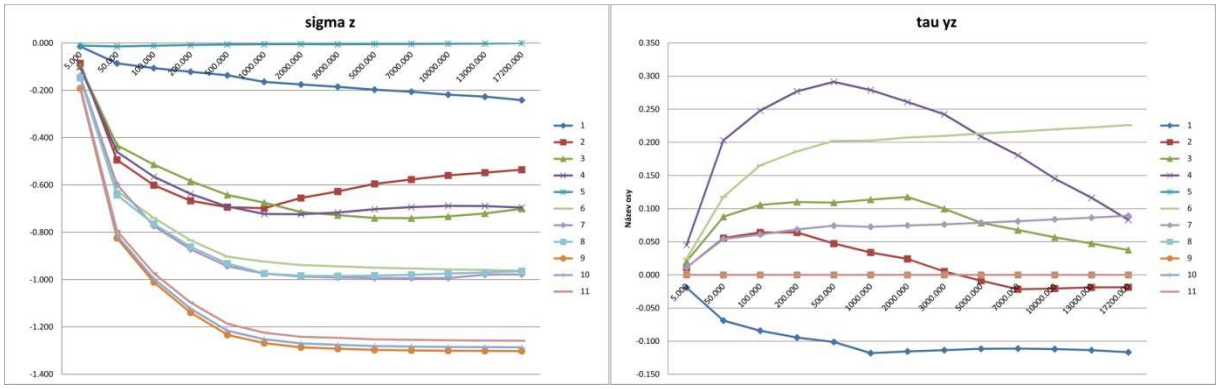

Fig. 8 Stress history in the observed points, x – E (MPa), y – σ, τ (MPa)

in various stages of the iteration process on the basis of compiled reference treatment program. Computational processes include detailed monitoring of specific important points with regard to the concentration field sites, distribution of normal component $\boldsymbol{\sigma_z}$ and shear component $\boldsymbol{\tau_{yz}}$ of stress, whose history and mutual dependence are graphically recorded, analyzed and evaluated (Fig. 5.,6.,7.,8.).

4. SUMMARY, CONLUSIONS

The following key conclusions, which constitute basic results for next phases of detail interfragmental space verification, can be mentioned on the basis of presented analysis:

(1) The analysis can be completed with other important derived mechanical properties of callus in its various stages of distraction process, which provide a comprehensive picture of its behavior, such as the history of the overall stiffness in compression, development of deformation parameters including the impact of fixation apparatus, development of power needed to perform a distraction step, etc. Harmonized results can be subsequently smoothed in equalizing curves and then balanced with regression dependencies of used electronic fixation system. This experimental way may allow to determine the secondary biomechanical properties of interfragmental callus during parallel or subsequent clinical testing.

(2) Experimental numerical verifications demonstrate the different evolution of tissue mechanical properties, with the dependence on theparticular stages oflengthening process and on the localization in callus volume. While the phase of active prolongation is important for the formation of quality highly oriented tissue structure and its density expansion, the phase of neutral fixation can be divided into several sub-parts with respect to the percentage effect of biomechanical stimulations to the qualitative development of callus. While the controlled harmonic stimulations with large amplitudes between $+10^2$ and $+10^3$ µm with low frequencies are important for the active phase of distraction process, stimulations of small amplitudes from -10^{-1} to -10^2 µm with higher frequency ranges have positive effect for the stages of neutral fixation. Proportion of biomechanical stimulations on increasing the quality parameters and the interfragmental tissue evolution velocity is from the complex

point of view critical in the case of presented configuration from the 5th to the 180th day of treatment (total 315 days of treatment).

ACKNOWLEDGEMENT

The financial support of this experiment by the Faculty of Civil Engineering, Czech Technical University in Prague (SGS project No. SGS12/117/OHK1/2T/11) is gratefully acknowledged.

REFERENCES

[1] Doblaré, M., García, J.M., Gómez, M.J., Modelling bone tissue fracture and healing: Review, Engineer Fracture Mechanics, 71, 2004, pp. 1809-1840, ISSN 0013-7944

[2] Einhorn, T.A., The cell and molecular biology of fracture healing,ClinOrthopRel Res, 355, 1998, pp. S7–S21, ISSN 1528-1132 (electronic version)

[3] Stokes, I.A.F., Aronsson, D.D., Dimock, A.N., et al.,Endochondral growth in growth plates of three species at two anatomical locations modulated by mechanical compression and tension,Journal of Orthopaedics Research,24(6), 2006, pp.1327-1334, ISSN 1554-527X

[4] Caplan, A.I., Boyan, B.D.,Endochondral bone formation: the lineage cascade, In: Mechanism of bone development and growth, Boca Raton, FL: CRC Press; 1994, ISBN: 0849389038

[5] Pauwels, F.,Eineneuetheorieüber den einflubmechanischerreize auf die differenzierung der stützgewebe, Z anatEntwicklungsgeschichte, 121, 1960, pp. 478–515, ISSN 1432-0568

[6] Perren, S.M., Cordey, J., The concept of interfragmentary strain, In: Current concepts of internal fixation of fractures, Berlin: Springer-Verlarg, 1980, pp. 63–77, ISBN 9783540098461

[7] Lacroix, D., Simulation of tissue differentiation during fracture healing, PhD thesis, University of Dublin, 2000.

[8] Carter, D.R., Beaupré, G.S., Giori, N.J., Helms, J.A.,Mechanobiology of skeletal regeneration,ClinOrthopRel Res,355, 1998, pp. S41–S55, ISSN 1528-1132 (electronic version)

[9] Claes, L.E., Heigele, C.A., Magnitudes of local stress and strain along bony surfaces predict the course and type of fracture healing, J Biomech, 32, 1999, pp. 255-266, ISSN 0021-9290

[10] Kuiper, J.H., Ashton, B.A., Richardson, J.B., Computer simulation of fracture callus formation and stiffness restoration, In: Prendergast, P.J., Lee, T.C., Carr, A.J., (editors),Proc 12th EuropSocBiomech, 2000, 61 p., ISBN 0953880907

[11] Lacroix, D., Prendergast, P.J., A mechano-regulation model for tissue differentiation during fracture healing: analysis of gap size and loading, J Biomech, 35, pp. 1163–71, ISSN 0021-9290

[12] Prendergast, P.J., Huiskes, R., Soballe, K., Biophysical stimuli on cells during tissue differentiation at implant interfaces, J Biomech, 6, 1997, pp. 539–548, ISSN 0021-9290

[13] García, J.M., Kuiper, J.H., Doblaré, M., Richardson, J.B., A numerical model to study the mechanical influences on bone fracture healing,Acta of Bioengineering and Biomechanics, 4 (S1), 2002, pp. 394–395, ISSN 1509-409X

INFLUENCE OF WATER/GYPSUM RATIO TO DYNAMIC MODULUS OF ELASTICITY OF GREY GYPSUM

Tereza DOVRTĚLOVÁ[1], **Pavel TESÁREK**[2], **Tomáš PLACHÝ**[3]

Abstract: *The paper describes the influence of water/gypsum ratio to the dynamic modulus of elasticity of grey gypsum. For the experiment, five sets of specimens with different water/gypsum ratio were prepared. These specimens were tested by nondestructive method – impulse excitation method, which determines modulus of elasticity based on the fundamental resonant frequencies. During these experiments fundamental resonant frequencies of longitudinal vibration were measured. Using the nondestructive method we can observe the evolution of the dynamic Young's modulus of elasticity in timeline.*

Keywords: *impulse excitation method, dynamic modulus of elasticity, gypsum, water/gypsum ratio*

1. INTRODUCTION

The main aim of this research is to determine influence of water/gypsum ratio on mechanical properties of grey gypsum and also their development in time. Grey gypsum is very cheap and easily reachable building material, which is obtained as a waste product from thermal power desulphurization. The gypsum is currently used for non-bearing structures, but there is a potential of using gypsum also for load bearing structures.

To achieve the aim of the research, non-destructive method was used. The Impulse Excitation Method (IEM) was used for determination of the dynamic Young's modulus. The measuring of the fundamental resonant frequency is its base. IEM is already used and described in some experimental studies [1], [2].

2. DESCRIPTION OF MATERIAL AND SPECIMENS

Tested specimens were prepared according to the Czech standard ČSN 72 2301 [3]. The specimens of dimensions 40×40×160 mm were made from the grey gypsum. For the experiment, five different sets

[1] Bc. Tereza Dovrtělová, Department of Mechanics, Faculty of Civil Engineering, CTU in Prague; tereza.dovrtelova@fsv.cvut.cz

[2] Ing. Pavel Tesárek, Ph.D., Department of Mechanics, Faculty of Civil Engineering, CTU in Prague; tesarek@fsv.cvut.cz

[3] Ing. Tomáš Plachý, Ph.D., Department of Mechanics, Faculty of Civil Engineering, CTU in Prague; plachy@fsv.cvut.cz

of specimens with various water/gypsum ratios were made. Optimal water/gypsum ratio for this type of gypsum is 0.71. Also specimens with water/gypsum ratio 0.60, 0.65, 0.85 and 1.00 were prepared for the experiment. Three specimens were prepared for every w/g ratio, altogether 15 specimens were prepared and tested.

2.1. PREPARATION OF SPECIMENS AND MEASURING PROCESS

Each set of specimens was prepared separately. First, the required amount of water and gypsum according to w/g gypsum ratio were measured. The gypsum was slowly poured into the water and the mixture was properly mixed approximately for 3 minutes. Then the mixture was poured in the mould. Each specimen was designated with a unique code, which describes w/g ratio, number of set and specimen, date and time of preparation. Preparation time was determined as a time, when all gypsum was poured in water.

The specimens were tested in certain intervals. The first measuring was executed in 20 – 30 minutes after the preparation. The weight and dimensions of each specimen were measured. At the beginning the intervals were short, measurements were taken approximately in 1 hour, 3 hours, 24 hours and 48 hours. When the weight stopped changing or the weight was changing very slowly, the measurements were taken in 3, 7, 14, 21, 60 days.

3. IMPULSE EXCITATION METHOD

The Impulse Excitation Method (IEM) was used for determination of the dynamic Young's modulus. The measuring of the fundamental resonant frequency is its base. The test can be set for flexural, torsional or longitudinal vibration. This part of our research deals with the longitudinal vibration. Performance of the method was similar to that in previous studies [1], [2]. The specimen was supported in the middle of its span, the fundamental longitudinal nodal position. Vibration has been actuated by striking the impact hammer Brüel&Kjær type 8206 on one side of the sample. The response was measured using acceleration transducer Brüel&Kjær type 4519-003. This transducer was located to the centre of the opposite end face of the gypsum specimen. The measured excitation force and acceleration were recorded and transformed from the time domain to the frequency domain using Fast Fourier Transform. The Frequency Response Functions were evaluated from these signals using the vibration control station Brüel&Kjær Frong-end 3560-B-120 and program PULSE 14.0. This procedure was repeated five times for each gypsum specimen. Outcomes were averaged for each gypsum specimen and the fundamental longitudinal resonant frequency was determined. The dynamic modulus of elasticity E_d can be determined using the relation:

$$E = \frac{4lmf_l^{\,2}}{bt} \qquad (1)$$

where l [m] is the length of the specimen, m [kg] is the mass of the specimen, f_l [Hz] is the fundamental resonant frequency of the longitudinal vibration of the specimen, b [m] is the width of the specimen and t [m] is the thickness of the specimen.

4. RESULTS

4.1. HOMOGENEITY OF SPECIMENS

All specimens were prepared using the same technology and had same conditions for drying. Despite this, it can be seen the diversity of measured values between particular samples in one set. Measured values of all three specimens in some sets are almost the same. On the other hand, in some cases significant variance of measured values was registered. It can be clearly seen in Fig. 1. For example, set number IV (w/g ratio 0.71) showed the most homogeneous results of all sets. For all three specimens of this set, the basic longitudinal resonant frequencies were almost identical. In contrast, sets I and III (w/g ratio 0.60 and 0.65), it means sets with the lowest water/gypsum ratio showed the greatest heterogeneity in measured basic longitudinal resonant frequencies, density and also in the calculated modulus of elasticity. This is probably caused by the low w/g ratio, which causes difficult workability. The mixture had tough consistency and probably not the proper mixing, which probably resulted in a large variance of measured values between the three tested specimens.

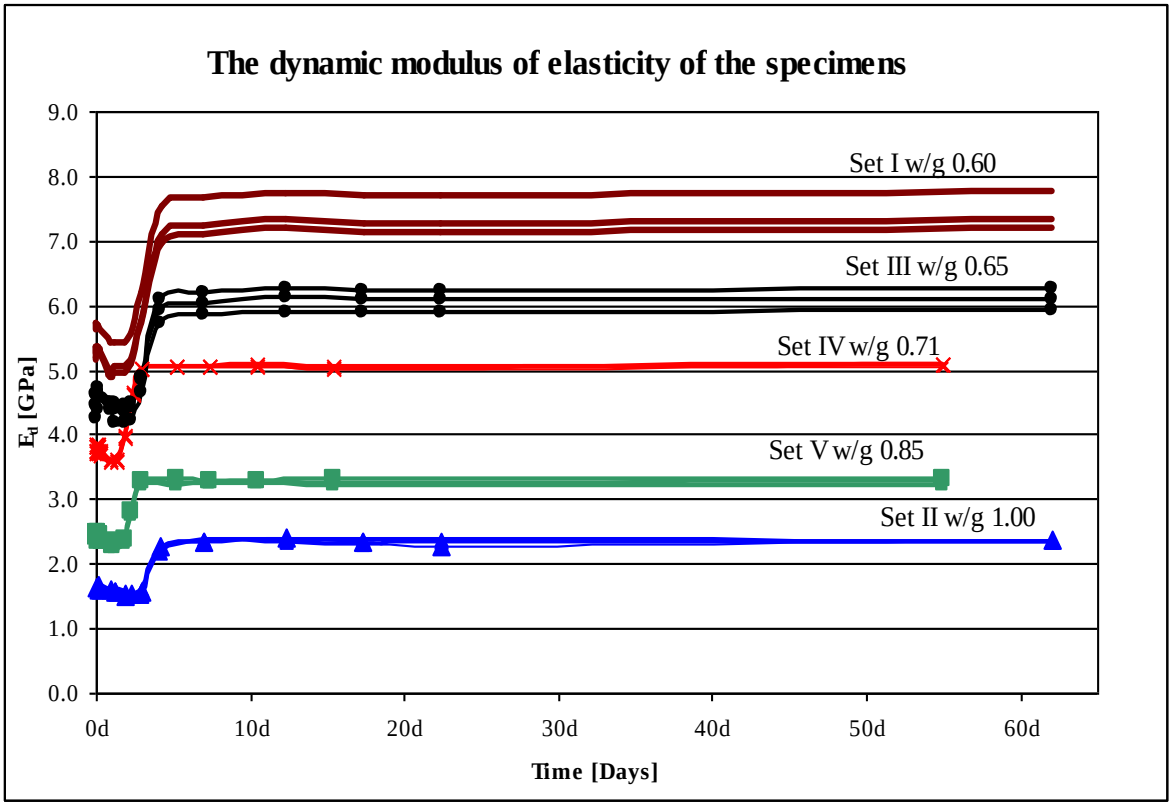

Fig. 1 Dynamic modulus of elasticity of particular specimens in timeline

For example, in the Set I the biggest difference between two specimens is 0.59 GPa. On the other side, in the Set IV maximal difference between two samples is only 0.05 GPa.

4.2. INFLUENCE OF W/G RATIO ON DYNAMIC MODULUS OF ELASTICITY

In the experiment, the influence of water/gypsum ratio on the modulus of elasticity was monitored.

Young's modulus of elasticity was calculated from the measured longitudinal resonant frequencies. In the Fig. 2, there are shown the measured longitudinal resonant frequencies, from which the modulus of elasticity was calculated (Fig. 3), according to the theoretical basis of this research.

Similarly like in [4], the highest values of the basic resonant frequencies and also dynamic moduli were measured on the set with the lowest water/gypsum ratio (w/g 0.60). The lowest values were measured on the set with the highest w/g ratio (w/g 1.00). Dynamic modulus of elasticity decreases in dependence on increase of the used water/gypsum ratio of the grey gypsum. The dynamic modulus of elasticity is shown in Fig. 3, it is an average value of three tested specimens. There can be also seen its development in time.

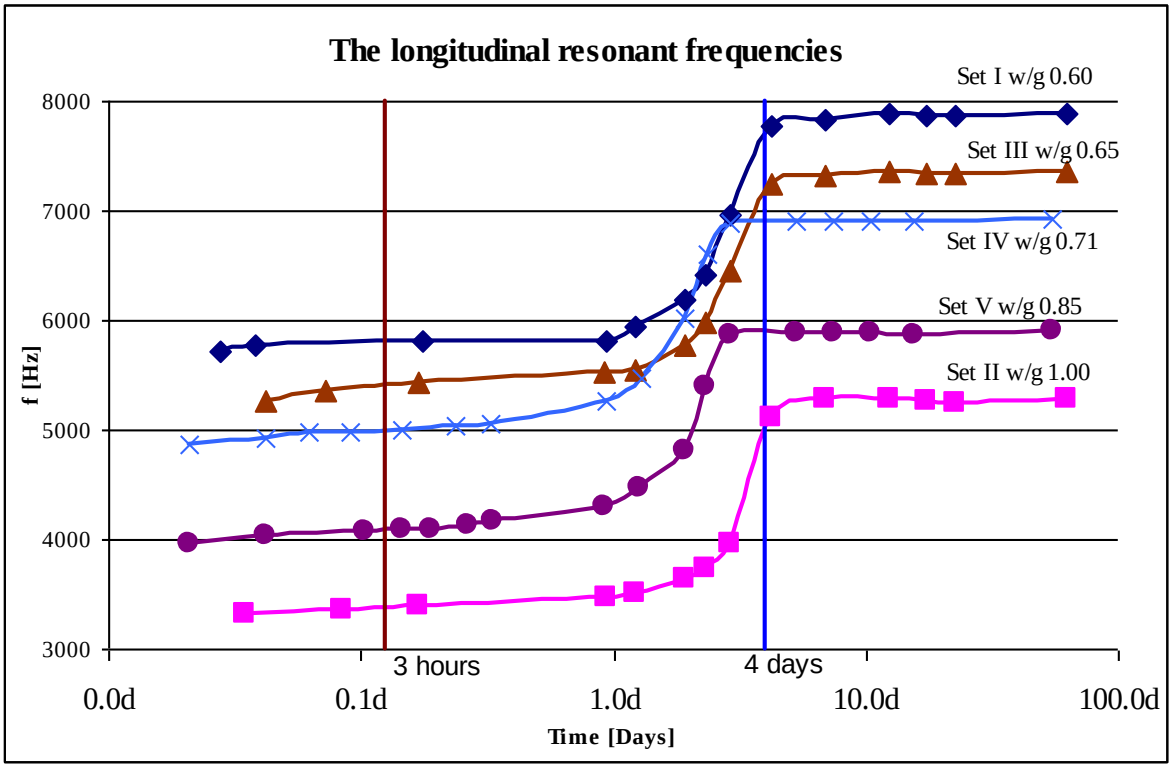

Fig. 2 The longitudinal resonant frequencies – time in the logarithmic scale

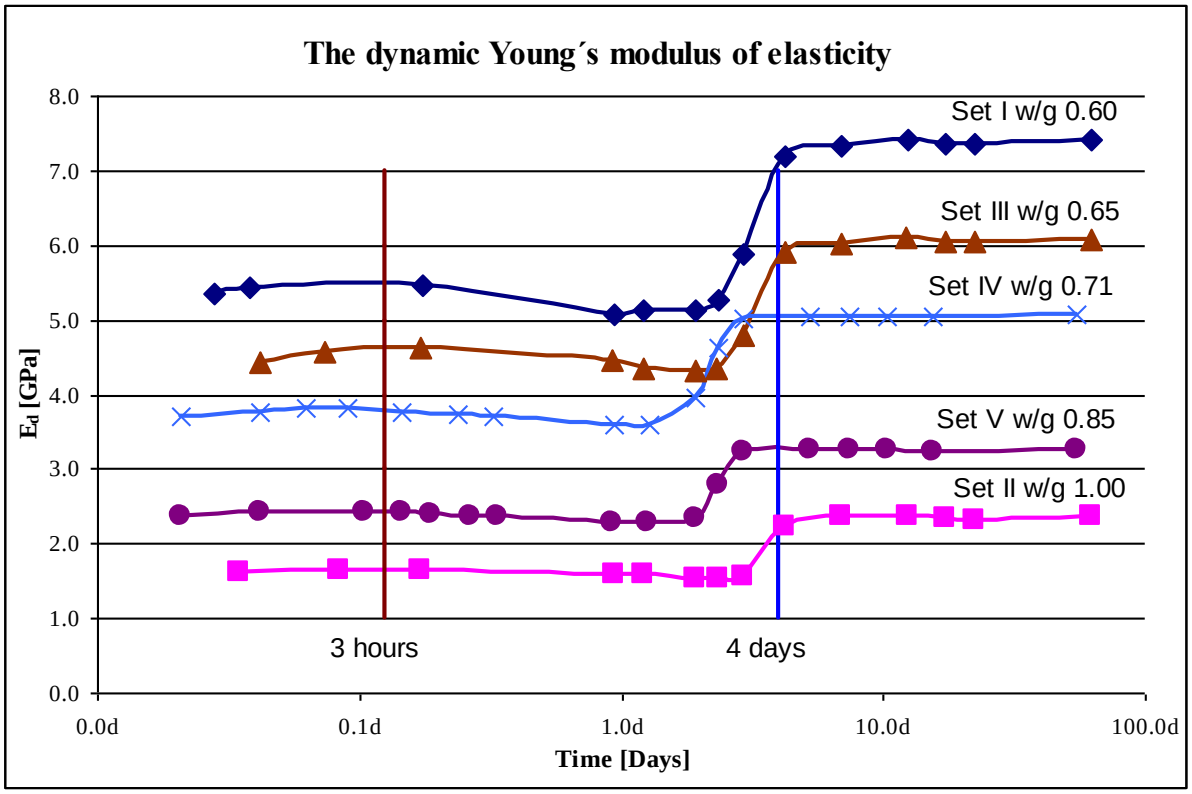

Fig. 3 The dynamic Young's modulus of elasticity – time in the logarithmic scale

4.3. THE DEVELOPMENT OF DYNAMIC MODULUS OF ELASTICITY IN TIME

The development of modulus of elasticity in time was also monitored. In general, progress of all tested sets was similar (Fig. 3). In the first hours, the dynamic modulus increased, approximately after three hours the modulus began to decline. Repeated increase of the dynamic modulus started after 1-2 days, after 3-4 days stopped and since then was almost constant. After detailed analysis, differences between particular sets can be seen. Because all the specimens had the same conditions during preparation, hardening and drying, this difference is probably caused by different w/g ratio of particular sets.

Sets with the water/gypsum ratio 0.71 and 0.85 have steep increase in resonant frequencies and also moduli of elasticity. Simultaneously, these two sets reached the constant values of frequencies and of moduli of elasticity first of all. On the contrary, very slow increase was registered on the sets with w/g 0.60, w/g 0.65 and w/g 1.00. Also the achievement of constant values last longer. For example, the second increase of modulus of the Set IV w/g 0.71 started in 24 hours, Set II w/g 1.00 started to increase in 69 hours.

Achievement of constant values of resonant frequencies and moduli of elasticity is for the most of the sets equal to finishing drying of the specimens, i.e. achievement of constant weight. An exception is set IV with optimal water/gypsum ratio 0.71, despite a constant weight continue increasing values of natural frequencies and moduli. For this set, drying stopped in 2.3 days, constant frequency was achieved in 2.9 days. The Set IV w/g 0.71 was the fastest in drying. Drying of Sets I w/g 0.60 and II

w/g 1.00 was slower. The time of drying of sets with the highest and the lowest water/gypsum ratio were identical - 4 days.

5. CONCLUSION

In the experiment there was shown, that water/gypsum ratio has probably influence on resonant frequencies and dynamic moduli of elasticity. The dynamic modulus of elasticity decreases in dependence on increase of the used water/gypsum ratio of the grey gypsum.

Water/gypsum ratio has also influence on time of drying of specimens. This time is not in direct correlation with w/g ratio. The Set IV with optimal w/g ratio (0.71) was the fastest in drying, Sets I (w/g 0.60) and II (w/g 1.00), i.e. sets with the lowest and highest w/g ratio, were the slowest.

The influence of water/gypsum ratio on workability of mixture and on homogeneity of results is also presented. Sets with the lowest water/gypsum ratio showed the greatest heterogeneity in basic longitudinal resonant frequencies, and also in the modulus of elasticity. Set IV with optimal w/g ratio 0.71 showed the most homogeneous results of all sets.

ACKNOWLEDGEMENT

The financial support of this experiment by the Faculty of Civil Engineering, Czech Technical University in Prague (SGS project No. 12/117/OHK1/2T/11) is gratefully acknowledged.

REFERENCES

[1] Němcová, H., Plachý, T., Ťoupek, R., Tesárek, P., Polák, M., Influence of moisture to mechanical properties of materials, In: Proceedings of the 17th International Conference Engineering Mechanics 2011, Prague, Institute of Thermomechanics Academy of Sciences of the Czech Republic, 2011, pp. 411-414, ISBN 978-80-87012-33-8

[2] Plachý, T., Němcová, H., Tesárek, P., Hájková, A., Polák, M., Determination of Poisson's Ratio of Gypsum Materials, In: Proceedings of the 49th International Scientific Conference Experimental Stress Analysis 2011, Brno University of Technology, Brno, 2011, pp. 315-320, ISBN 978-80-214-4275-7

[3] ČSN 72 2301, Gypsum binders (in Czech), Prague, Czech Standards Institute, 2009, 17 p.

[4] Plachý, T., Němcová, H., Tesárek, P., Polák, M., Dynamic modulus of elasticity of dental gypsum, In: Proceedings of the 17th International Conference Engineering Mechanics 2011, Prague, Institute of Thermomechanics Academy of Sciences of the Czech Republic, 2011, pp. 463-466, ISBN 978-80-87012-33-8

[5] Papán, D., Experimental measurements of paraseismic effects due to traffic. Proceedings of the 20th European Regional Earthquake Engineering Seminar: Seismic assessment and upgrading of existing structures, Institute Universitaire Kurtz Bosch, Sion, Switzerland, p. 144-145, 2001

VERIFICATION OF FE MODEL OF CRASH BARRIER POST USING EXPERIMENTAL MODAL ANALYSIS

Jiří DROZDA[1], **JanMAREK**[2], **TomášPLACHÝ**[3]

Abstract:*Basic aim of this project is to determine a procedure of finite element (FE) models verification. This is proved on a real scenario. The first part was creation of FE models of the newly-designed crash barrier. Afterwards, the crash barrier post was tested using methods of an experimental modal analysis (EMA). FE models are verified with observed modal characteristics. Such verified models can be subjected to detailed structure analysis with certain reliability.Project should lead to improve professional public knowledge about FE models verification using EMA. This should lead to safer, more accurate and profitable design of such structures.*

Keywords:*crash barrier post, modal analysis, verification, FE modeling*

1. INTRODUCTION

Main purpose of crash barriers is to restrain a vehicle and protect it from veering off the road. Bridge crash barriers protect from falling from the bridge. The second purpose is to reduce the injuries of vehicle occupants and other road traffic participants and to minimize damages of objects. Bridge crash barriers can be divided into two groups: steel barriers and concrete barriers. Concrete crash barriers due to their weight are notcommonly used on bridges. Therefore only steel crash barriers are discussed below. The steel bridge crash barrier consists of several major parts, which are guardrail, distance spacer, post (column), base plate and anchoring bolts. After all these parts are joined together, the bridge crash barrier acts upon its purpose.

2. CRASH BARRIERS

Main problem in designing is fact that bridge crash barriers, which are installed on public road bridges in Europe, have to fulfill requirements of the European standard EN 1317 [1]. This standard prescribes full scale test to certify barrier design. To reduce the development and testing costs of new crash barrier design, there can be used numericalanalysis for early evaluation of crash barrier

[1]Ing. Jiří Drozda, Department of Steel and Timber Structures, Faculty of Civil Engineering, CTU in Prague;jiri.drozda@fsv.cvut.cz

[2]Ing. Jan Marek, Department of Steel and Timber Structures, Faculty of Civil Engineering, CTU in Prague;jan.marek.2@fsv.cvut.cz

[3]Ing.TomášPlachý, Ph.D., Department of Mechanics, Faculty of Civil Engineering, CTU in Prague;plachy@fsv.cvut.cz

behaviourunder vehicle impact. Therefore, the main aim of this project is the creation of verified numericalmodel of the newly designed bridge crash barrier.

This text deals with a new design of the bridge crash barrier post. Commonly used posts are made from hot rolled or cold-formed profiles. These have disadvantages such as a formation of many parts, which leads to corrosion sensitivity; other disadvantage is small variability and small aesthetic potential.

3. THE TESTED POST

The newly designed post consists of two parallel steel plates, which are fillet welded into base plates. The biggest advantage of this post is that there are no parts, where the dirt cumulates and whole construction of crash barrier can be cleaned by sweeper-flusher. Service life of a bridge crash barrier increases. This steel plates post has better shape variability and can be modified according to aesthetic requirements. Another designer´s effort was to make post lighter and easy to weld, which means more economical.

The newly designed crash barrier post was assembled and attached into the massive concrete block by steel bonded anchors. The grout layer was made under the base plates. See Fig.1 left.

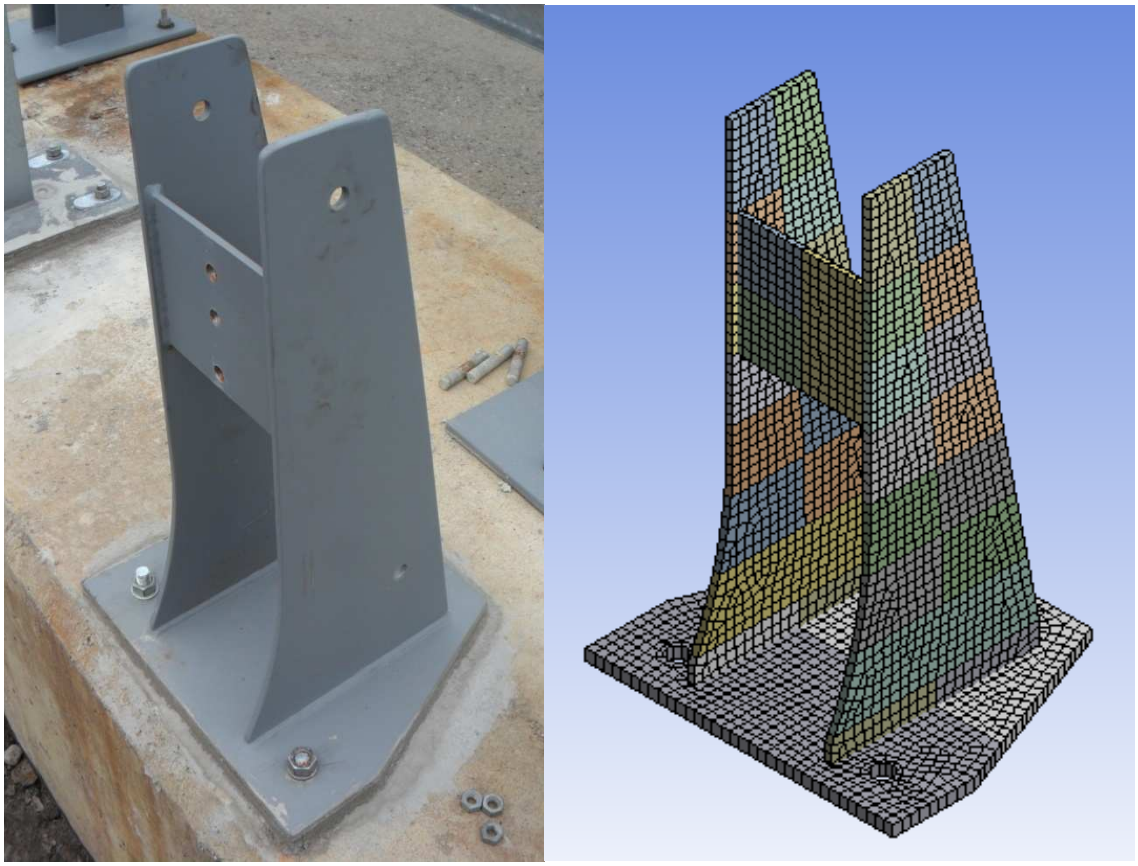

Fig. 1 left: mounted prototype post, right: mesh of FE model

4. FE MODEL

In this part of the project it was important to perform modal analysis of FE model, which can be compared with the experimental modal analysis. A numerical modal analysis is usually the first step before solving more complicated dynamic problems.

5. NUMERICAL MODAL ANALYSIS

Modal analysis, or a free vibration analysis, is performed to obtain the natural frequencies and mode shapes of a structure. Modal analysis is a subset of the general equation of motion. In our analysis the behaviour of a structure is assumed to be linear and the response to be harmonic. For solving FE model we assumed linear elastic material behaviour, small deflection theory and damping not included.

Currently, many software products can be used for modeling these posts e.g. ABAQUS, ANSYS, NASTRAN, etc. ANSYS 13.0-Workbench was chosen mainly because the project purpose is to make a verified FE model which can be in future used for simulation of a crash test. ANSYS supports multifyzical simulations from static structural to dynamic crash. Procedure of verification is based on comparing modal characteristics of computed model and measured prototype post.

Computation was provided on desktop PC with Intel Core 2 Duo CPU 2.1GHz and 3.00 GB RAM.

The first step was creation of 3D model of prototype post, see Fig. 1 right. Whole body of the post is made of steel plates; therefore it had been chosen surface elements in order to reduce computation time. This surface 3D model was created by using DesignModeler, which is included in ANSYS 13.0WB. Parts of the post were divided into subparts, to correspond distribution of solved points and places, where excitation forces were in the real test. This step is necessary for future evaluation and verification FE model. After dividing plates into subsections it was essential to ensure continuity of mesh across subparts of the same plate to preserve real behaviour. It was used tool called Joint in DesignModeler. Joint contacts allow topology sharing between subparts including mesh definition. Same contact was used for modeling of welds. Thickness of each surface corresponded to the thicknesses of steel plates.

The next step was defining material properties. Before solving a modal analysis it is required to define Young's Modulus, Poisson's Ratio, and Mass Density, because stiffness matrix and mass matrix was determined from these material properties. In this project,material properties were used from a steel profile table for the steel S355, so Young's Modulus is 210GPa, Poisson's Ratio is 0.3 and Mass Density is 7850 kg/m^3.

Thereafter mesh was created and boundary condition were determined. It was used default settings for mechanical mesh, i.e. elements with hex dominate shape with mid side nodes and size of elements was adapted to geometry. Quality of mesh was adjusted by definition of Relevance at Relevance

center, which allows changing fineness of mesh. Only one boundary condition was defined at the place, where the post is bolted to the concrete ledge. A fixed support was used.

The solver called Block Lanczos was used for FE model. The Block Lanczos Method uses an assembled stiffness and mass matrix in addition to factoring matrices that are a combination of the mass and stiffness matrices computed at various shift points. Therefore it is the most robust solver, as it handles small & large models and beam, shell or solid meshes.

6. NUMERICAL SOLUTION

The first 10 computed natural frequencies with characters of adequate natural modes are bellow. Visualization of the first four computed modes is in Fig. 3 (Compared with measured modes).

Tab. 1 Computed natural frequencies and modes

Mode	f [Hz]	Character of the natural mode
1	50.76	1st bending - weak axis(plates in phase)
2	154.00	1st torsion(plates in antiphase)
3	237.91	1st torsion(plates in phase)
4	251.07	1st bending (plates in phase)- rigid axis + 2nd torsion(plates in antiphase)
5	258.73	2ndbending - weak axis (plates in phase)
6	274.96	1st bending (plates in antiphase)
7	338.30	2ndtorsion (plates in phase)
8	413.41	2nd bending (plates in antiphase)
9	431.17	3rdbending - weak axis (plates in phase)
10	556.67	3rd torsion (plates in antiphase)

7. MEASUREMENT

The measurement was conducted on July 18th 2012, in an open area of the bridge building shop of the company OK-BE.

8. TESTING METHOD

The single point testing was chosen for the experimental modal analysis. It is the most straightforward category of the phase separation techniques. Phase-separation techniques rely upon a mathematical assumption that the actual responses are formed from a linear combination of the modes. The forced responses to a known excitation are measured and then the dynamic properties are extracted by means of mathematical curve fitting techniques.

An impact hammer was used to strike the structure at the desired excitation points. A very short sharp excitation pulse was produced – approximating a Dirac delta function – which has a flat spectrum over a wide frequency range. The amount of energy contained in the impact pulse is small.

9. EXPERIMENT

In Fig. 2 there is visible the mesh of excitation points and the place where the transducer was located. Miniature DeltaTron TEDS Accelerometer Brüel&Kjær 4507B005was used, mounted by B&K

mounting clip and using beeswax. The mesh of excitation points contains 51 points, 8 levels, in each level 3 points on both main plates, plus 3 extra points on the rung plate.

It is important to note, that the reference transducer location must not be in a nodal point of measured natural modes. If the ordinate of a natural mode in a referencepoint is too small, that natural mode and corresponding natural frequency cannot be measured. This is one of the reasons for a preliminary numerical modal analysis, in order to determine optimal referent transducer placement.

Each excited point was struck five times by the impact hammer Brüel&Kjær of Type 8206. Resultant readings were averaged for each point, which eliminates deficiencies of measurement. Both signals, the excitation force and the acceleration, were recorded in the time domain and transformed using Fast Fourier Transform (FFT) to the frequency domain, and the Frequency Response Function (FRF) was evaluated from these signals using the vibration control station Brüel&Kjær Front-end 3560-B-120 and program PULSE 14.0.

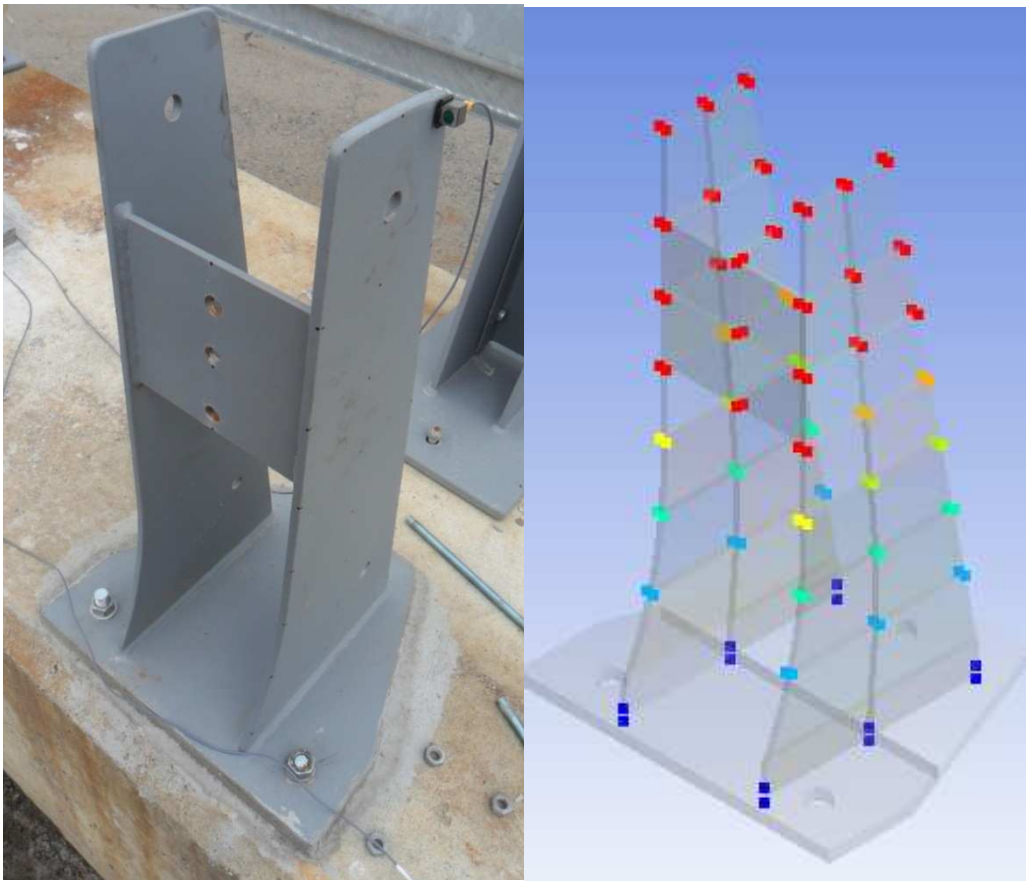

Fig. 2 left: mounted transducer, right: mesh of excitation points

Natural mode shapes were obtained from FRFs using polynomial curve fitting method. The software ME´ scope VES 4.0 was used for this method. The same software tool was used to visualize mode shapes, comparison of the first four measured and computed mode shapes are visible in Fig. 3.

10. COMPARISON

Matching of measured and computed natural mode shapes was made according to MAC values, which were obtained using formula(1) from [2] and [3]:

$$MAC\left(\{\Phi_X\}_i, \{\Phi_A\}_j\right) = \frac{\left|\{\Phi_X\}_{COMP}{}^T, \{\Phi_A{}^*\}_{MEAS}\right|^2}{\left(\{\Phi_X\}_{COMP}{}^T, \{\Phi_X{}^*\}_{COMP}\right)\left(\{\Phi_A\}_{MEAS}{}^T, \{\Phi_A{}^*\}_{MEAS}\right)} \qquad (1)$$

Following comparison of computed and measured natural frequencies was made using formula (2) for frequency difference from [3]:

$$\Delta_{(j)} = \frac{f_{(j)comp} - f_{(j)meas}}{f_{(j)comp}} \qquad (2)$$

In tables bellow there are visible compared natural frequencies, MAC, according to Czech technical standards - [3]. MAC values near 1.0 refer to perfect correspondence of compared natural modes, while values near 0.0 refer to perfect orthogonality. Frequency difference values should be in <-15%; +10%> for $f_{(1)}$ and <-(14+$f_{(j)comp}/f_{(1)comp}$); 14+$f_{(j)comp}/f_{(1)comp}$> for $f_{(>1)}$.

Tab. 2Modal assurance criterion (MAC)

Meas	Comp $f_{(j)}$[Hz]	1	2	3	4	5	6	7	8	9	10
		50.8	154.0	237.9	251.1	258.7	275.0	338.3	413.4	431.2	556.7
1	52.963	0.975	0.002	0.045	0.001	0.007	0.001	0.072	0.001	0.036	0.001
2	168.320	0.037	0.896	0.029	0.066	0.012	0.014	0.035	0.000	0.002	0.018
3	279.583	0.007	0.006	0.007	0.008	0.913	0.035	0.001	0.017	0.09	0.000
4	299.926	0.010	0.06	0.014	0.336	0.017	0.893	0.025	0.069	0.007	0.008
5	331.327	0.037	0.153	0.527	0.081	0.003	0.079	0.511	0.013	0.008	0.032
6	447.346	0.006	0.001	0.005	0.07	0.035	0.251	0.002	0.834	0.078	0.053
7	465.166	0.046	0.001	0.004	0.005	0.208	0.008	0.054	0.021	0.959	0.004
8	596.518	0.002	0.018	0.004	0.008	0.006	0.014	0.032	0.05	0.045	0.733

Tab. 3Comparison of natural frequencies, pairs matched according MAC

Computed $f_{(j)}$[Hz]	1	2	3	4	5	6	7	8	9	10
	50.8	154.0	237.9	251.1	258.7	275.0	338.3	413.4	431.2	556.7
Measured $f_{(j)}$[Hz]	1	2			3	4	5	6	7	8
	52.96	168.32			279.58	299.93	331.33	447.35	465.17	596.52
Δ(j) [%]	-4.3	-9.3	NA	NA	-8.1	-9.1	2.1	-8.2	-7.9	-7.2
Min [%]	-15	-17.0	-18.7	-18.9	-19.1	-19.4	-20.7	-22.1	-22.5	-25.0
Max [%]	10	17.0	18.7	18.9	19.1	19.4	20.7	22.1	22.5	25.0

In Fig. 3belowthere are visible the first four natural mode shapes, comparison of measured and computed.

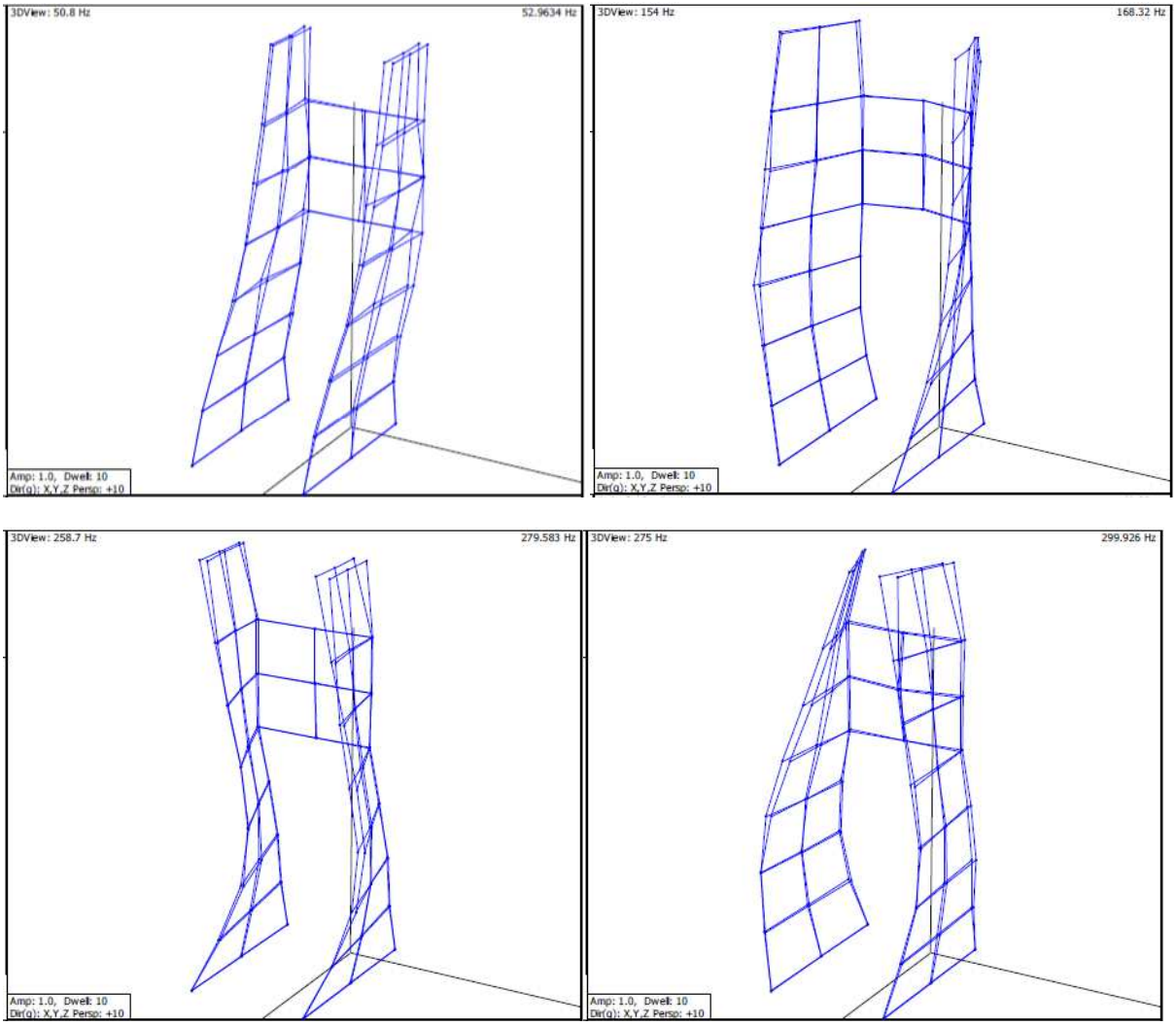

Fig. 3 Top left: 1st mode, top right: 2nd mode, bottom left: 3rd mode, bottom right: 4th mode

11. CONCLUSION

The verified FE model of the crash barrier post was obtained using methods of the experimental and numerical modal analysis. It follows from the comparison that computed and measured natural frequencies and modes correspond very well.However, a little discrepancy is visible, particularly in vibration to a rigid axis, where the real construction behaves with more rigidity than FE model. This behaviour is probably caused by insufficient closeness of modelling of contact between the steel base plate and the concrete ledge.

SGS project will continue next year. First of all, FE model will be updated in order to improve correspondence of natural frequencies and mode shapes. By parametric study of FE model behaviour and results sensitivity to changes of edge conditions, the model should be made more appropriate. The base plate connection to the concrete ledge must be described more aptly.

Another experiment will be conducted to verify FE model of whole crash barrier system, i.e. two or three posts connected together with guardrail, distance spacers, anchored with bolts into concrete ledge. Differences between behaviour of single post and whole system will be the main subject of a following research.

ACKNOWLEDGEMENT

The financial support of this experiment by the Faculty of Civil Engineering, Czech Technical University in Prague (SGS project No. SGS12/119/OHK1/2T/11) is gratefully acknowledged.

REFERENCES

[1] ČSN EN 1317-1:2010,Road restraint systems– Part1: Terminology and general criteria for test methods, (in Czech),Praha: Úřad pro technickounormalizaci, metrologii a státnízkušebnictví, 2011.

[2] Maia, Silva et al., Theoretical and Experimental Modal Analysis. Taunton, Somerset, England, Research Studies Press Ltd., 1997. ISBN 0 86380 208 7

[3] ČSN 73 2044,Dynamic tests of building structures, (in Czech), Czech Standards Institute, 1984.

[4] ČSN 73 6209, Load tests of bridges, (in Czech), Czech Standards Institute, 1996.

[5] ČSN 73 6209 Change Z1, Load tests of bridges, (in Czech), Czech Standards Institute, 2005.

MODELING OF DETERIORATION PROCESSES OF CONCRETE STRUCTRURES DUE TO CYCLIC LOADING AND AGGRESSIVE ENVIRONMENT

Jakub GÖRINGER[1], **Marek FOGLAR**[2]

Abstract: Concrete *is used for various kinds of structures which are exposed to different types of loading and aggressive environment. Fatigue is a process of permanent progressive changes in the structure of a material subjected to cyclic loading. Cracks propagation caused by cyclic loading leads to stiffness reduction, increase of deflections and can cause fatigue failure of the structural element. Aggressive agents which penetrate into the concrete (acids etc.) cause decomposition of the microstructure of hydrated cement paste, reducing its cohesion with the aggregate and steel reinforcement and contribute to corrosion. This paper describes current ways of modeling of deterioration of concrete structures caused by cyclic loading and aggressive environment.*

Keywords: *cyclic loading, aggressive environment, deterioration of concrete, fatigue of concrete*

1. INTRODUCTION

Fatigue is a process of permanent progressive changes in the structure of a material subjected to cyclic loading. Study of the effect of fatigue on the durability of concrete structures is a matter of past decades, as well as for the effect of the aggressive environment. Agents contained in the aggressive environment penetrate into the structure of concrete and initiate chemical reactions. These reactions lead to the reduction of material matrix stiffness and the structure lifetime reduction due to localized stress increases and cracks development. Various analysis and material models are used to describe the mentioned phenomena. Appropriate steps for reduction of deterioration effects are dependent on results of these models.

2. DETERIORATION MODELS OF CONCRETE

The deterioration models of concrete may be divided into the groups according these criteria – mathematical nature of model, scale of the model, model focus, input/output model parameters etc.

[1] Ing. Jakub Göringer, Departement of Concrete and Masonry Structures, Faculty of Civil Engineering, CTU in Prague; jakub.goringer@fsv.cvut.cz

[2] Ing. Marek Foglar, Ph.D., Departement of Concrete and Masonry Structures, Faculty of Civil Engineering, CTU in Prague; marek.foglar@fsv.cvut.cz

2.1. MATHEMATICAL APPROACH

Models can be divided by their mathematical nature as empirical, semi-empirical, analytical, numerical and probabilistic. Combinations of these approaches can occur in the advanced models.

Empirical or semi-empirical models are based on large data sets obtained by long-term testing or monitoring of existing structures. Usually these are multi-criteria models limited to a specific cases. They are used especially in standards and recommendations that can be used in routine design practice.

Analytical models are formed by the system of equations resulting from given research. The mathematical solution is sought for in a closed form. This presumption restricts these models to solve simple or simplified phenomena. It is extremely difficult or in some cases even impossible to find closed-form solution for complex equations.

Numerical modeling is applied in complex tasks if the problem is solved by differential equations. The solution doesn't need to be sought for in closed form as in analytic models. The most widely used is Finite Element Method (FEM), but nowadays due to their many advantages the usage of the meshless methods is expanding.

Probabilistic models are mostly composed of groups of functions describing one or more deterioration processes. The functions are used for evaluation of stochastic data sets, which affect these processes. The solution of mentioned models is e.g. failure probability, remaining lifetime etc.

2.2. SCALE OF THE DETERIORATION MODEL

The models could be divided by their dimension within the structure or in the experiments into macro-scale, meso-scale and micro-scale models. Accordingly, the used scales are in the order of meters, millimeters and even micrometers.

Macro-scale models are applied mainly for analysis of the whole structure with a presumption of homogeneous material. Their utilization can be found in the common design praxis.

Meso-scale models considering heterogeneous material in the calculation; therefore they are used for analysis of details as well as entire structures. On contrary to the macro-scale models the meso-scale models can describe interaction of cement paste, aggregate and pores.

Micro-scales models deal with issues on C-S-H gel base. They describe behavior of the matrix under specific loading and exposure conditions, which can be further utilized in meso-scale and macro-scale models.

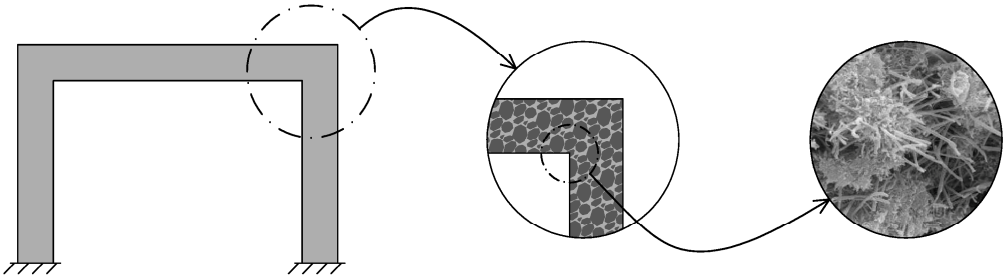

Fig. 1 Models divided by the scale - (a) macro-scale, (b) meso-scale, (c) micro-scale

2.3. MODEL FOCUS AND OTHER PARAMETERS

Other possible way to divide models is by the type of solved problems. Deterioration models of concrete deal with the effects of aggressive environment, failures caused by cyclic loading, i.e. fatigue. Last but not least, there are models which describe the residual durability of the structure and its life cycle.

The models can be divided by the number of used parameters (single or multi-parametric) and also by amount of solved phenomena. The optimal choice of the model is crucial for achieving realistic results and effective calculation times.

3. MODELS FOR FATIGUE BEHAVIOUR

Fatigue is a process of permanent progressive changes in the structure of a material subjected to cyclic loading. Macro-cracks can cause collapse of the structural element or even collapse of the entire structure. The development of cracks is caused by the increased local stresses on the tips of cracks. The micro-cracks are present in the material structure of concrete from the time of its fabrication (pores) or they develop during curing of concrete (shrinkage).

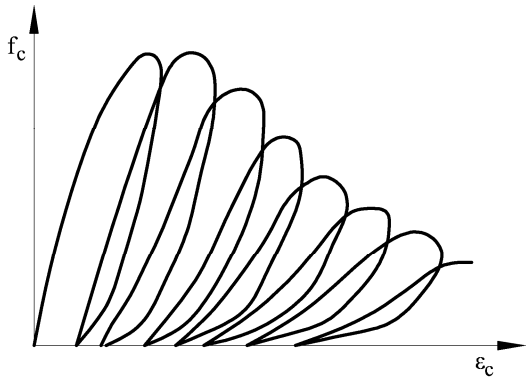

Fig. 2 Typical stress-strain curve for concrete under cyclic loading [3]

Depending on the mentioned facts, material models can be created based on thermodynamic laws which are able to describe energy development in the elements. Other models can be established based on damage theory with use of damage parameter in tensorial form in conjunction with fatigue

damage development [1], [2]. Team of Rueda [3] chose an easier way to model fatigue. They proposed material model with strain-stress dependence regarding to cyclic loading. Such a model can be used in non-linear analysis softwares. Apparently most sophisticated model was proposed by Maekawa and colleagues [4]. Their model is based on inclusion of constitutive model of cracked concrete with use of direct pat-integral method of fatigue damage simulation into the 3D orthogonal space.

An experimental model based on Young's modulus modification was proposed by Foglar [5]. The fatigue damage function was developed to give a value of modulus of elasticity in every particular moment of cyclic loading.

4. MODELS FOR AGGRESSIVE ENVIRONMENT EFFECTS

Deterioration models for aggressive environment are mainly developed for carbonation, chloride-ion penetration and ASR reaction. Models describe deterioration of concrete caused by the rise of micro-cracks due to increase of local tensile stresses.

4.1. CARBONATION

The carbonation decreases alkalinity of concrete. With the decreasing pH, the concrete loses its ability to protect the reinforcements from corrosion. The computational models focus only on the speed of the reaction itself. From the Fick's 2nd law of diffusion we can deduce a simple formula for carbonation depth check.

$$\frac{\partial \phi}{\partial t} = D\frac{\partial^2 \phi}{\partial x^2} \qquad \Rightarrow \qquad x = k \cdot \sqrt{t} \tag{1}$$

where ϕ = concentration of aggressive agents in environment in g/m^3,

t = time in - s (div version), years (simplified version),

D = diffusion coefficient in m^2/s,

x = position,

k = carbonation coefficient in mm/year^{0,5}.

The advanced models can be created on the basis of Fick's diffusion laws together with transmission of heat and moisture. Several authors ([6] and [7]) propose coupled model of heat transfer, moisture transfer and carbonation process numerically solved by FEM analysis. Also probability models are used for the modeling of carbonation. These models are based on searching of the safety factor of steel rebar corrosion or more précised models on Monte Carlo simulations for service life determining [8]. Duprat and Sellier [9] proposed FEM model of carbonation depth further improved with the probability model solving reliability index. The solution was found in a form of quadratic response surface.

4.2. CHLORIDE-ION PENETRATION

On contrary to the carbonation models, the deterioration models caused by chlorides include both processes of the transmission of aggressive agents into the material structure and the failure of material caused by reinforcement corrosion which causes its expansion. Due to a nature of process Fick's laws of diffusion can be used again.

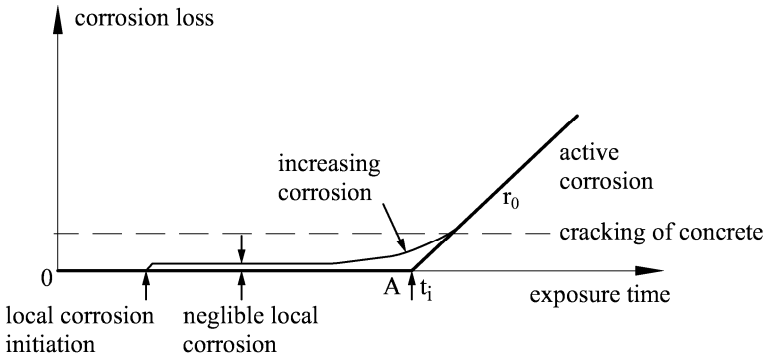

Fig. 3 Corrosion loss–time behavior and simplified bi-linear model (bold line) [10]

Melchers et al. [10] included the influence of concrete heterogeneity caused by cracks via stress dependent diffusion coefficient into the deterioration model of concrete by creating probability model for bearing capacity calculation and for deflections caused by rigidity reduction due to reinforcement loss simulated by probability method Monte Carlo. A model dependent on Cl^- and O_2 diffusion was proposed by Takewaka et al. [12]. Cracks influence on aggressive agents' penetration rate was included by their random generation on surface and thus shortening the distance between exposed surface and the reinforcement. A failure of the element occurs when amount of corrosion products reach the limit value. Shodja and colleagues [13] proposed analytical model based on smeared crack calculations. For solution was used modern meshless – gradient reproducing kernel particle method.

4.3. ALKALI-SILICA REACTION (ASR)

Numerical models are used to describe the ASR reaction in concrete structures. Micro-scale models include transportation processes and are created mainly for better understanding of ASR reaction itself. The most frequently used are macro-scale models based on two independent procedures (1) modeling of kinetics of chemical processes and (2) modeling of mechanical concrete failures [11]. Due to applicable standards which try to limit the ASR reaction inception in structures, models are used foremost for current structures and especially water dams.

Larive [14] deduced the ASR reaction kinetics in dependence on temperature and relative humidity. With various modifications it can be found in all available chemo-thermo-damage based models. The biggest differences are found in approach to model concrete failure process. Dunant uses damage law [15], Comi [16] uses isotropic concrete model, Farage [17] works with anisotropic model

with smeared crack. The approach of Capra [18] is unique. It uses dependence of crack creation on probability.

5. MODELS FOR REALIBILITY AND LIFE-CYCLE COST

Accordingly to their usage reliability deterioration models can be divided into two types. First type includes deterioration models which analyze structure condition, its failure probability or residual durability. The second type includes decision models for establishing maintenance plan and structure repairs. It is also possible to incorporated life-cycle cost to determine decision efficiency for established maintenance plan and repairs.

There are many possibilities to choose specific model for calculation. Reliability index models are defined by the difference of resistance of element and applied load. Models are commonly solved by First-order reliability method (FORM), Monte Carlo method etc. To incorporate maintenance and repairs we can use Time-dependent reliability index [19]. Failure rate (hazard rate) models indicate failure probability between time intervals, e.g. the interval between the construction inspections [20]. Markov chains present another potential approach to modeling. It is discrete-time stochastic model composed of particular states. The change probability of current state to any other state is dependent only on current state. In case of N conditions, change probability results in $N \times N$ transition matrix [21].

6. CONCLUSION

This paper provides a review of the state-of-the-art of deterioration modeling of concrete. The mechanism of deterioration is first outlined and then model approaches for fatigue and aggressive environment effects are summarized. Models have been divided by their mathematical approach, scale and focus depending on solved phenomena. The paper should provide an overview of the possibilities and advantages of usage of mentioned models.

ACKNOWLEDGEMENT

The financial support of the Czech Technical University grant project No. 12/029/OHK1/1T/11 and the Czech Ministry of Industry and Trade project FR-TI3/531 is gratefully acknowledged.

REFERENCES

[1] Alliche, A., Damage model for fatigue loading of concrete, International Journal of Fatigue, 26, 2004, pp. 915-921, ISSN 0142-1123

[2] Papa, E., Taliercio, A., Anisotropic damage model for the multiaxial static and fatigue behavior of plain concrete, Engineering Fracture Mechanics, 55, 1996, pp. 163-179, ISSN 0013-7944

[3] Martínez-Rueda, J.E., Elnashai, A.S., Confined concrete model under cyclic load, Materials and Structures, 30, 1997, pp. 139-147, ISSN 0025-5432

[4] Maekawa, K., Gebreyouhannes, E., Mishima, T., An, X., Three-Dimensional Fatigue Simulation of RC Slabs under Traveling Wheel-Type Loads, Journal of Advanced Concrete Technology, 4, 2006, pp. 445-457, ISSN 1347-3913

[5] Foglar, M., Vývoj přetvoření betonu při cyklickém zatížení a jeho matematický popis funkcí únavového poškození, Beton TKS, 1, 2008, pp. 60-65, ISSN 1213-3116

[6] Song, H.-W., Kwon, S.-J., Byun, K.-J., Park, C.-K., Predicting carbonation in early-aged cracked concrete, Cement and Concrete Research, 36, 2006, pp. 979-989, ISSN 0008-8846

[7] Steffens, A., Dinkler, D., Ahrens, H., Modeling carbonation for corrosion risk prediction of concrete structures, Cement and Concrete Research, 32, 2002, pp. 935-941. ISSN 0008-8846

[8] Ann, K.Y., Pack, S.-W., Hwang, J.-P., Song, H.-W., Kim, S.-H., Service life prediction of a concrete bridge structure subjected to carbonation, In: Construction and Building Materials, 24, 2010, pp. 1494-1501, ISSN 0950-0618

[9] Duprat, F., Sellier, A., Probabilistic approach to corrosion risk due to carbonation via an adaptive response surface method, Probabilistic Engineering Mechanics, 21, 2006, pp. 207-216, ISSN 0266-8920

[10] Melchers, R.E., Li, C.Q., Lawanwisut, W., Probabilistic modeling of structural deterioration of reinforced concrete beams under saline environment corrosion, Structural Safety, 30, 2008, pp. 447-460, ISSN 0167-4730

[11] Bažant, Z. P., Steffens A., Mathematical model for kinetics of alkali-silica reaction in concrete, Cement and Concrete Research, 30, 2000, pp. 419-428, ISSN 0008-8846

[12] Takewaka, K., Yamaguchi, T., Maeda, S., Simulation Model for Deterioration of Concrete Structures due to Chloride Attack, Journal of Advanced Concrete Technology, 1, 2003, pp. 139-146, ISSN 1347-3913

[13] Shodja, H. M., Kiani, K., Heshemian, A., A model for the evolution of concrete deterioration due to reinforcement corrosion, Mathematical and Computer Modelling, 52, 2010, pp. 1403-1422, ISSN 0895-7177

[14] Larive, C., Apport combinés de l'expérimentation et de la modélisation à la compréhension de l'alcali-réaction et des ses effets mécaniques, PhD. Thesis, Laboratoire Central des Ponts et Chaussées, Paris, 1998

[15] Dunant, C.F., Scrivener, K.L., Micro-mechanical modelling of alkali–silica-reaction-induced degradation using the AMIE framework, Cement and Concrete Research, 40, 2010, pp. 517-525, ISSN 0008-8846

[16] Comi, C., Fedele, R., Perego, U., A chemo-thermo-damage model for the analysis of concrete dams affected by alkali-silica reaction, Mechanics of Materials, 41, 2009, pp. 210-230, ISSN 0167-6636

[17] Farage, M.C.R., Alves, J.L.D., Fairbairn, E.M.R., Macroscopic model of concrete subjected to alkali–aggregate reaction, Cement and Concrete Research, 34, 2004, pp. 495-505, ISSN 0008-8846

[18] Capra, B., Sellier, A., Orthotropic modelling of alkali-aggregate reaction in concrete structures: numerical simulations, Mechanics of Materials, 35, 2003, pp. 817-830, ISSN 0167-6636

[19] Frangopol, D.M., Lin, K.-Y., Estes, A.C., Reliability of reinforced concrete girders under corrosion attack, Journal of Structural Engineering, 123, 1997, pp. 286-297, ISSN 0733-9445

[20] Kaito, K., Sugisaki, K., Kobayashi, K., Modeling of Combined Deterioration of Concrete Structures by Competing Hazard Model, In: IABSE Symposium Report, Helsink: IABSE, 2008, pp. 25-32, ISSN 2221-3783

[21] Setunge, S., Hasan, S., Concrete Bridge Deterioration Prediction using Markov Chain Approach, In: Proceedings of the International Conference on Structural Engineering, Construction and Management, Peradeniya: ICSECM, 2011.

USE OF ULTRASOUND FOR A HISTORICAL TIMBER STRUCTURES INVESTIGATION

Hana HASNÍKOVÁ[1], Petr KUKLÍK[2],

Abstract:*Performance of building materials is investigated within construction and technical research. It is appropriate to use non-destructive testing methods to determine mechanical properties of material, because they leave almost no remains or damages after testing as the other methods do.Velocity measurement of ultrasound wave propagation is one of simply used non-destructive methods. The dynamic modulus of elasticity, as a mechanical property determining material quality of timber, is an indirect output of the method. Preliminary investigation of structural members from the Masaryk Railway Station in Prague is described in the paper for illustration.*

Keywords:*non-destructive testing, ultrasound velocity, modulus of elasticity, timber*

1. INTRODUCTION

Many reconstructions of historical buildings and structures have been made recently, so nondestructive testing became popular for primary investigations. It doesn't leave any damages and its outputs bring results with adequate accuracy.

Ultrasound testing operates with stress wave with frequency higher than 20 kHz passaging through the material and itssignificantly lowervelocity could detect potential problematic places, such as cracks or decayed areas. Knowing the bulk density even the modulus of elasticity, i.e. the basic mechanical property, could be calculated. It is suggested that the wave spreads directly between transducers; the material is modeled as viscoelastic in general [1].

2. MEASURED QUANTITIES

The measured quantity is the time *t* that wave needs to passage through the sample from transmitter to receiver. The final speed propagation*c* [$\times 10^3$km.s^{-1}] iscalculated very simply as

$$c = \frac{L}{t} \qquad (1)$$

[1]Ing. Hana Hasníková, Department of Steel and Timber Structures, Faculty of Civil Engineering, CTU in Prague; hana.hasnikova@fsv.cvut.cz

[2]doc. Ing. PetrKuklík, CSc., Department of Steel and Timber Structures, Faculty of Civil Engineering, CTU in Prague; kuklik@fsv.cvut.cz

where*L*[m] is the distance between transducers and *t*[μs]is the measured time.

The important mechanical property that characterizes the material is dynamic modulus of elasticity *E* [$\times 10^{-3}$GPa]. Dynamic modulus of elasticity could be calculated from ultrasound speed propagation *c* and bulk density ρ [kg.m^{-3}] of the material, see equation *(2)* below. [2]

$$E = c^2 \rho \qquad (2)$$

For quick determination of bulk density ρ on site according to the *(3*) have been used dimensions of an individual structural member to calculate its volume *V* [m^3] and removable balance to measure its weight *m* [kg]. Also, the temperature*T* [°C] and humidity of the timber*w* [%] have been measured for further detailed investigation.

$$\rho = \frac{m}{V} \qquad (3)$$

3. EXPERIMENTAL WORK

The experiments took place on site in June 2011 while reconstruction of the hall of the Masaryk Railway Station. The task was to assess the quality of the original material, so that it could be used again in a new structure.

4. MATERIAL SPECIFICATION OF TIMBER

Timber is an organic material whose properties are influenced by a tree growth. Material is heterogenic, e.g. there are places with higher local density in the wood, and anisotropic; kind of orthotropic behavior is caused by annul rings. Timber used for the hall structure of Masaryk Railway Station was spruces and firs; eachbeam has been made from appropriately chosen tree, especially the bigger ones with atypical dimensions. The age of timber was about 70 years and higher.

5. THE BUILDING OF THE MASARYK RAILWAY STATION IN PRAGUE

The railway station has been planned as a terminal station of line Prague – Olomouc at the beginning; the building of the Masaryk Railway Station was designed by architect Antonín Jüngling and was built in 1844-1845. It has enlarged few times during its life; the most considerable change comes from 1940's and also from 1980's, when Prague underground was constructed. At the end of 20th century there was a reconstruction that tried to bring back the original look.

The last reconstruction of the central part of the building was made in 2011. Controllers from National Heritage Institute would like to preserve the original structural members of the roof, so that the investigation with non-destructive devices has been made. It took place in a hall between an arrival part and a departure part; the cast iron columns carried timber beams with glass covering. Beams chosen by controllers and contractor have been investigated in-situ.

6. USED DEVICE AND TEST SET UP

The ultrasound wave velocity was measured in longitudinal direction along the axis of the beam. French device Sylvatest was used for testing. It composes of a control box, two conical transducers (transmitting one and receiving one) especially designed for timber and a probe for humidity measurement. Frequency used for testing was 22 kHz. Test composition is demonstrated on Fig.1. Contact between transducers and the material is ensured by special shape, so that they go directly into the mass of timber fibres.

The specimen dimensions were generally 100 mm × 230 mm × 4000 mm; distance between transducers was 3000 mm. The angle, which is contained by transducer and surface of the sample, should be about 45°. The balance was used as a support at the end of the beam; therefore the registered valuewas the half of the total weight of the beam.

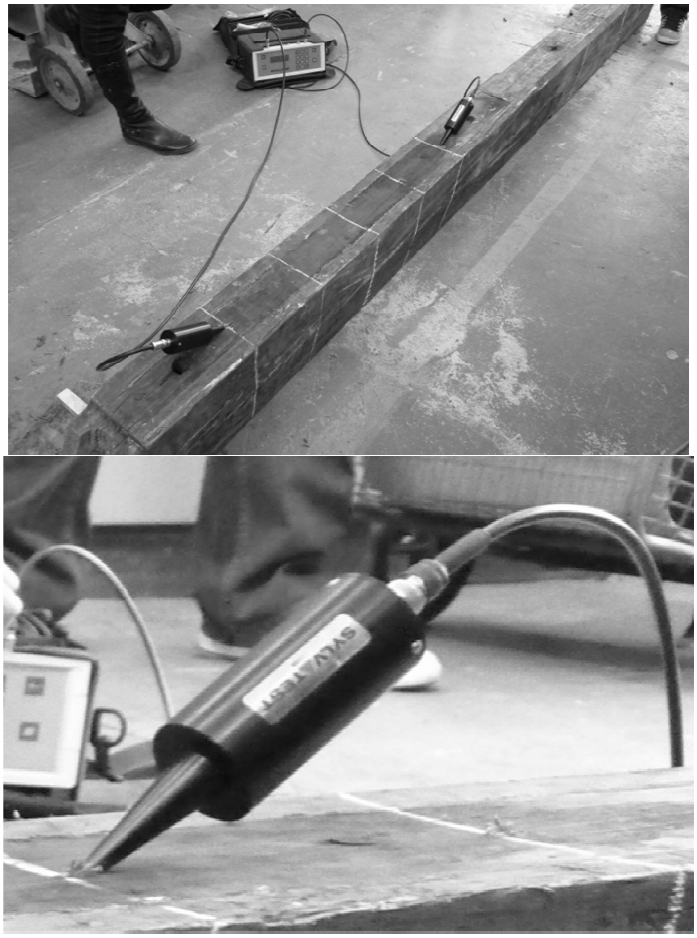

Fig. 1 Illustration picture of typical set up of Sylvatest measurement with a detail of a conical transducer

7. CONCLUSION

Preliminary assessment of timber structural members was based on modulus of elasticity calculated according to *(3)*. All in-situ measured quantities and following steps are shown in Tab. 1 below.

Staticmodulus of elasticity is about 90 % of dynamic modulus [3], evidently final values correspond to timber of low quality that could not fulfill strict requirements for today's structures.

Tab. 1 Measured and calculated quantities for timber investigation

Structural member	Dimensions			SYLVATEST							**E [GPa]**
	b [mm]	h [mm]	l [mm]	L [m]	T [°C]	w [%]	t [μs]	0.5*m [kg]	ρ [kg/m^3]	c [km/s]	
VK-1-3-P	98.3	232.0	3820	3.00	26.0	13.4	533	16.540	379.6	5.63	**12.0**
VK-4-6	147.3	240.0	3820	3.00	27.0	14.1	531	19.620	290.5	5.65	**9.3**
VK-9-6	100.0	229.7	3820	3.00	27.0	18.0	542	17.880	407.6	5.54	**12.5**
VK-12-6	103.7	233.3	3820	3.00	30.0	17.0	562	16.630	360.0	5.34	**10.3**
VK-15-5	103.0	235.3	4310	4.00	27.0	13.5	713	16.800	321.7	5.61	**10.1**
VK-19-6	97.7	233.3	3820	3.00	28.0	18.0	548	16.270	373.8	5.47	**11.2**

ACKNOWLEDGEMENT

The financial support of this experiment by the Faculty of Civil Engineering, Czech Technical University in Prague (SGS project No. 12/120/OHK1/2T/11) is gratefully acknowledged.

REFERENCES

[1] Kuklík, P.,Kuklíková, A.,Methods for evaluation of structural timber, Wood research, 46 (1), pp. 1-10, 2001, ISSN 0012-6136

[2] Kasal, B.,Tannert, T.,In Situ Assessment of Structural Timber,State of the Art Report of the RILEM, 2010,ISBN 978-94-007-0559-3

[3] Kloiber, M.,Kotlínová, M. Porovnání dynamického a statického modulu pružnosti poškozeného dřeva, In:Proceedings of the 8th International Scientific Conference Applied Mechanics, 2006.

ACCELERATED ALGORITHM FOR RECONSTRUCTION OF RANDOM HETEROGENEOUS MATERIALS

Jan HAVELKA[1], **Jan SÝKORA**[2],
Anna KUČEROVÁ[3]

Abstract: *The suitable statistical descriptor suitable for the description of phase continuity in the microstructure is lineal path function. Due to its computational cost, it is necessary to accelerate evaluation procedure using graphics processing units (GPU). Our goal is to present accelerated algorithm of the lineal path evaluation and its utilization in the reconstruction procedure of random heterogeneous materials.*

Keywords: *Lineal path function, homogenization, statistically equivalent periodic unit cell, graphics processing unit.*

1. INTRODUCTION

This contribution is focused on the reconstruction of random heterogeneous two-phase microstructure, namely spongeous bone (Fig. 1). When dealing complex random microstructures, the unit cell representing exactly periodic morphology needs to be replaced by a statistically equivalent periodic unit cell (SEPUC) preserving the important material properties in the statistical manner, for more details see [1]. One of the statistical descriptors suitable for SEPUC definition is the lineal path function.

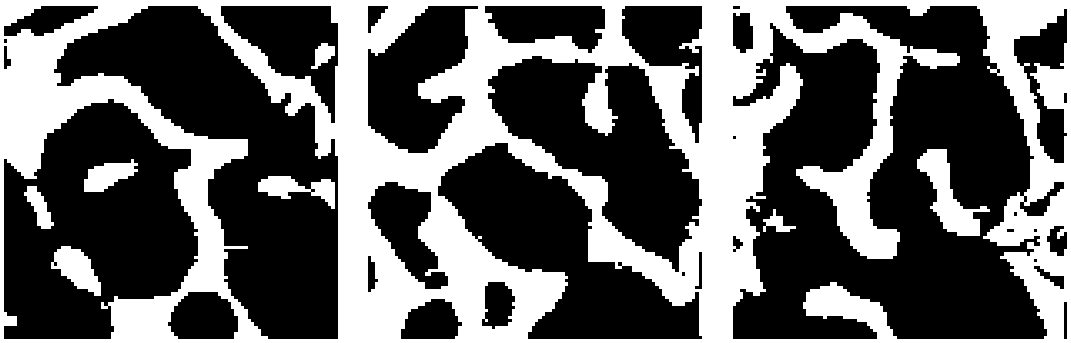

Fig. 1 Trabecular bone microstructure obtained by micro computed tomography [2]

[1]Bc. Jan Havelka , Faculty of Civil Engineering, CTU in Prague, jan.havelka.1@fsv.cvut.cz

[2]Ing. Jan Sýkora, Ph.D., Faculty of Civil Engineering, CTU in Prague, jan.sykora.1@fsv.cvut.cz

[3]Ing. Anna Kučerová, Ph.D., Faculty of Civil Engineering, CTU in Prague, anicka@cml.fsv.cvut.cz

2. METHODOLOGY

The reconstruction framework basically consists of following steps. :

- The first step is the mathematical description of the original microstructure using statistical descriptor. There are plenty of them, like n-point probability, surface correlation, chord-length density, lineal-path or percolation and cluster functions. Since there is certain connection between the studied microstructure and physical properties, one should take considerable attention to the choice of statistical descriptor. Because of significant phase connectedness of trabecular bone (see Fig. 2a), lineal path function was chosen as proper statistical descriptor. It is a low-order descriptor based on a more complex fundamental function able to capture certain information about the phase structure. Its main disadvantage is the computational cost. The evaluation of the lineal path function is based on construction of segments, which are defined as a set of pixels within the digital image. The sets of pixels for segments are obtained by algorithm given in [3]. The group of segments is complemented by covering all possible lengths and orientations. Once having the defined segments, the computation of lineal path function involve simple translations of each segment throughout the image and the comparison whether all pixels of the segment at a given position correspond to image pixels with the value representing the investigated phase.

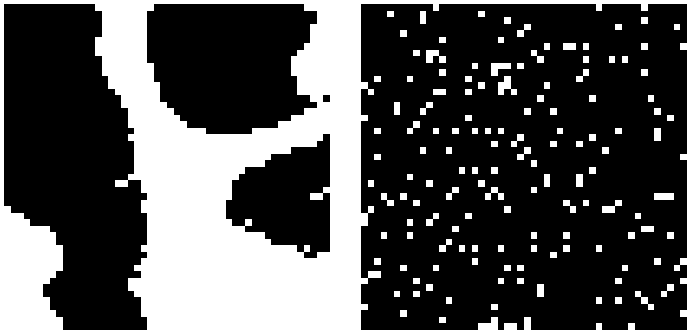

(a) (b)

Fig. 2 a) Initial microstructure, b) Fragmented microstructure [4]

- The next step is a reconstruction of random heterogeneous media utilizing optimization algorithm. We focused our attention on the simulated re-annealing algorithm, which can overcome the local extremes by acceptance a worse solution with certain probability. The crucial point in the optimization procedure is evaluation of lineal path function in each step of algorithm and thus the using of accelerated computation of statistical descriptor is inevitable. (Fig. 3) shows the basic behavior of the simulated re-annealing algorithm, the blue line corresponds to the admitted error, the green line is the lowest error and the red line is a temperature, which in some sense represents a probability of accepted solution with higher error.

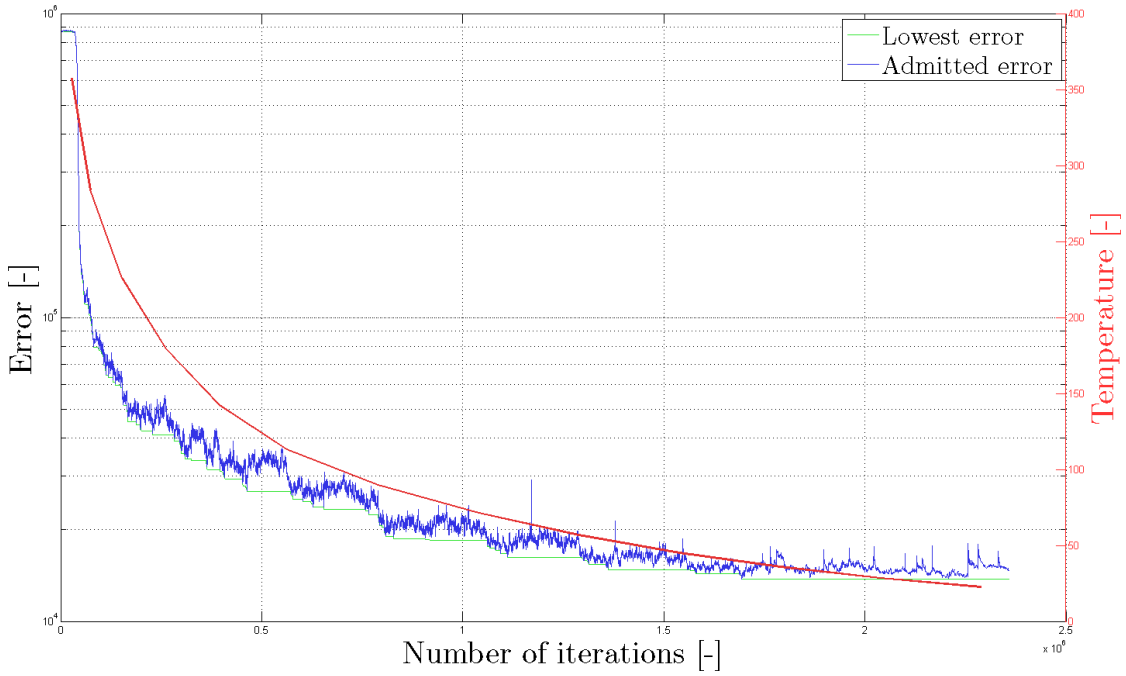

Fig. 3 Numerical result of simulated re-annealing function [4]

2.1. IMPLEMENTATION AND OPTIMIZATION

The algorithmic structure of sequential code for evaluation of lineal path function is shown in (Fig. 4). This version of lineal path function was firstly optimized in C language and used as a benchmark function for parallel version.

```
1  Generate_Segments();
2  for( i=0; i < nseg; i++ ){
3     for( j=0; j < npix; j++ ){
4        Is_Inside();
5     }
6  }
```

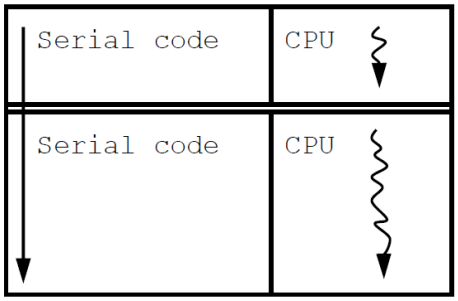

Fig. 4 Serial code structure [5]

As was mentioned before, the computation of statistical description in optimization algorithm is very time consuming procedure. Therefore, we present the reformulation of the sequential C code for evaluation of the lineal path function into the parallel C code with Compute Unified Device Architecture (CUDA) extensions enabling the usage of computational potential of the NVIDIA graphics processing unit (GPU), see Fig. 5.

```
1  Generate_Segments();
2
3  for( i=0; i < nseg; i++ ){
4       // Parallel kernel
5       Is_Inside<<<>>>(nseg,npix);
6  }
```

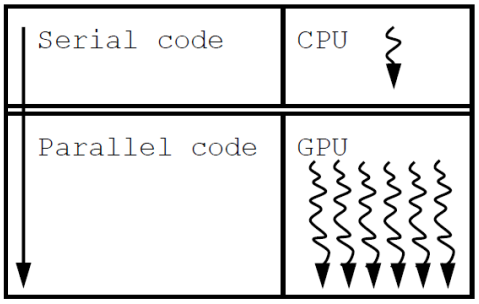

Fig. 5 Paralel code structure [5]

Another step in acceleration of overall computational time was done by the overclocking of the hardware units. The linear dependency between the clock of graphics processing units core and computational time was observed.

2.2. RESULTS

The most effort was devoted to acceleration of the target function. Fig. 6 shows the time consumption of sequential and parallel version of lineal path function.

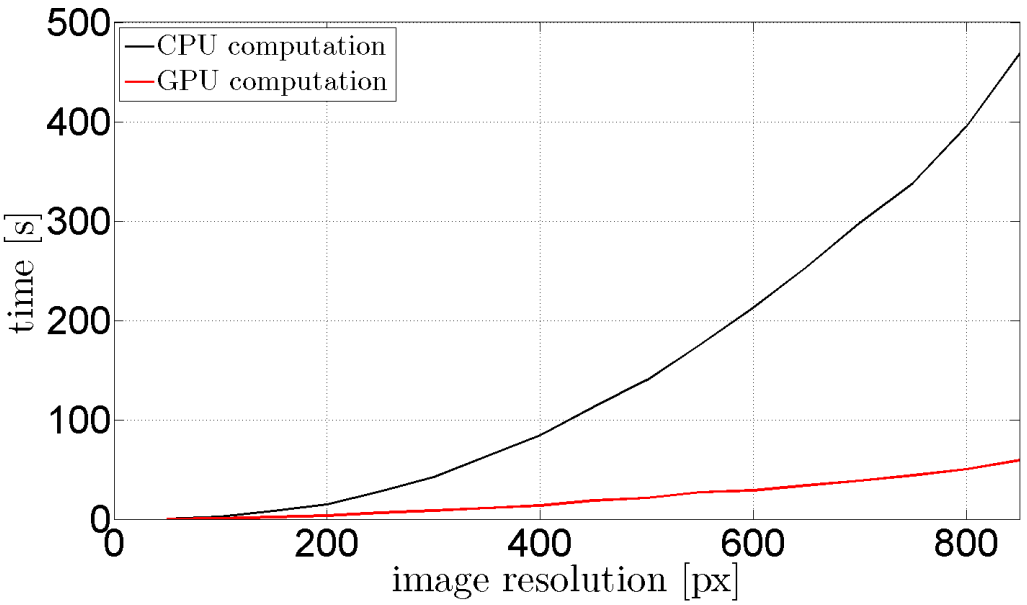

Fig. 6 Numerical results for given sizes of images [4]

Standard				*Enhanced*				
D/ML [px]/[px]	GPU [s]	CPU [s]	**ratio**	D/ML [px]/[px]	GPU [s]	CPU [s]	**ratio**	**Overall speedup**
50/50	0.179	0.328	**1.83**x	50/50	0.156	0.265	**1.69**x	**2.10**x
100/100	1.075	4.617	**4.29**x	100/100	0.722	2.371	**3.28**x	**6.39**x
150/150	3.957	21.653	**5.47**x	150/150	1.954	8.018	**4.10**x	**11.08**x
200/200	10.209	66.425	**6.51**x	200/200	3.621	14.742	**4.07**x	**18.34**x
250/250	22.276	169.245	**7.59**x	250/250	6.427	27.612	**4.29**x	**26.33**x
300/300	43.429	357.022	**8.22**x	300/250	8.413	42.338	**5.03**x	**42.44**x
350/350	76.644	649.195	**8.47**x	350/250	10.909	63.304	**5.80**x	**59.51**x
400/400	127.841	1127.897	**8.82**x	400/250	13.481	84.287	**6.25**x	**83.67**x
450/450	209.693	1821.911	**8.69**x	450/250	18.608	122.569	**6.59**x	**97.91**x
500/500	315.951	2846.712	**9.01**x	500/250	21.145	139.698	**6.61**x	**134.64**x

Tab. 1 Numerical results (D=Dimension, ML=maximum segment length) [4]

Hardware:

Processor: Intel Core i7 950 @ 3,07GHz

GPU 1: NVIDIA GeForce 210

GPU 2: computation: NVIDIA Quadro 4000 @ 650Mhz

Operating memory: 12GB DDR3 1600MHz CL9

Hard drive: OCZ RevoDrive 80GB

Motherboard: Asus Sabertooth x58

Operating system: Microsoft Windows 7, 64bit

CUDA version: 4.0

ParalelNsight version: 1.2

The final image is displayed in the following figure. The obtained difference between original and reconstructed lineal path function was about 0,62%. the reconstruction of random heterogeneous material lasted 3 days and consisted of 2,5 million steps.

(a) (b)

Fig. 7 Trabecular bone reconstruction: (a) Reference medium; (b) Final reconstruction [4]

3. CONCLUSION

The whole problem was firstly solved on the level of microstructure description and its sequential version was written in C++ language. After several optimization steps, the code was rewritten to parallel version using CUDA C language. After achievement of desired speed-up, the accelerated algorithm was implemented into a simulated re-annealing framework. The final version works flawlessly for images up to 100x100 pixels with our hardware configuration. A single computations of the lineal path function can be done for images up to 500x500 pixels, without any hardware limitations of GPU QUADRO 4000.

ACKNOWLEDGEMENT

The financial support of this work by the Czech Science Foundation (projects No. P105/12/1146 and 105/11/P370) is gratefully acknowledged.

REFERENCES

[1] Šejnoha, M. and Zeman, J. *Overall viscoelastic response of ran-dom fibrous composites with statistically quasi uniform distribution of reinforcements*, Comp. Methods in Appl. Mech. and Eng., vol. 191(44), pages 5027-5044, 2002, ISSN 0045-7825.

[2] Jiroušek, O. and Vavřík, D. and Jakůbek, J. and Dammer, J., *Correlation of trabecular bone mechanical properties to its microstructure, using mCT-based FE modeling*, Institute of Thermomechanics AS CR, Prague, Svratka, 2008, proc. Engineering Mechanics, ISBN 978-80-87012-11-6.

[3] Bresenham, J.E. *Algorithm for computer control of a digital plotter*, IBM System journal, vol. 4(1), pages 25-30, 1965, ISBN:1-58113-052-X.

[4] Havelka, J. *Computationally efficient algorithms for evaluation of statistical descriptors*, Bachelor's thesis, Czech Technical University in Prague, Faculty of Civil Engineering, in czech, 2012.

[5] Havelka, J. and Sýkora, J. and Kučerová, A. *Fast evaluation of lineal path fiction using graphics processing unit*, In Proceedings of the 17th International Conference Engineering Mechanics, pages 179-182, 2011.

[6] Torquato, S. *Random heterogeneous materials*, Springer-Verlag, New York, 2002, ISBN-13: 978-0387951676.

MODELING OF NONLINEAR MOISTURE TRANSPORT IN CONCRETE

Petr HAVLÁSEK[1], Milan JIRÁSEK[2]

Abstract: *Modeling of moisture transport in cementitious materials has many applications, ranging from predictions of shrinkage and creep of concrete to durability of materials and structures or health issues. A material model based on the approach of Bažant and Najjar [1] has been implemented and it has been found that the numerical results presented in [1] cannot be obtained with the values of parameters given in that paper. In this contribution, optimal values of the material parameters are recommended and the model is applied to other experiments reported in the literature. Attention is also paid to the influence of the boundary condition.*

Keywords: *concrete, moisture, diffusion, transport, modeling*

1. INTRODUCTION

Modeling of moisture transport in cementitious materials has many applications, ranging from predictions of shrinkage and creep of concrete to durability of materials and structures or health issues.

In the last five decades, many models for simulation of nonlinear moisture diffusion have been developed, see e.g. [2]. One of the most frequently used models was proposed by Bažant and Najjar [1] forty years ago. This model provides quite accurate predictions of time development of moisture in concrete structures while its formulation remains simple enough for engineering practice. For these reasons the model has been recommended in a prestandard document [3] (see section 5.1.12.2.1 - Diffusion of water).

The material model based on the approach of Bažant and Najjar has been implemented by the present authors into the MATLAB environment for 1D diffusion and into the finite element package OOFEM [4] for more general problems. It has been found that the numerical results presented not only by Bažant and Najjar [1], but also by Kim and Lee [5] (who used the same model) cannot be obtained with the published values of parameters. Section 4 presents numerical results obtained with the 1) recommended parameters, 2) parameters according to fib 2010 Model Code [3], and 3) optimized parameters.

[1]Ing. Petr Havlásek , Department of Mechanics, Faculty of Civil Engineering, Czech Technical University in Prague, petr.havlasek@fsv.cvut.cz

[2]Prof. Ing. Milan Jirásek, DrSc., Department of Mechanics, Faculty of Civil Engineering, Czech Technical University in Prague, milan.jirasek@fsv.cvut.cz

2. MODEL FOR NONLINEAR MOISTURE DIFFUSION IN CONCRETE

2.1. DIFFERENTIAL EQUATION

The presented material model results from the combination of two equations. The first one is the mass conservation equation

$$\frac{\partial w}{\partial t} = -\nabla \cdot \vec{J} \tag{1}$$

where w is the moisture content [kg/m^3], t stands for time [s], $\nabla\cdot$ is the divergence operator and $\vec{J}$ is the mass flux [kg/m^2·s] (mass of water passing through a unit area in unit time). The second equation

$$\vec{J} = -c(\varphi, T)\nabla\varphi \tag{2}$$

relates the flux $\vec{J}$ to the gradient of a potential, which is in this case the pore relative humidity φ [-]. In this equation ∇ is the gradient operator and c is a temperature- and humidity-dependent coefficient called permeability [kg/m·s]. Combining these two equations one gets

$$\frac{\partial w}{\partial t} = \nabla \cdot (c(\varphi, T)\nabla\varphi) \tag{3}$$

Assuming that the desorption isotherm has a constant slope, $k = \mathrm{d}w/\mathrm{d}\varphi$ [kg/m^3] (often called "moisture capacity"), equation (3) can be modified to

$$\frac{\partial \varphi}{\partial t} = \nabla \cdot (C(\varphi, T)\nabla\varphi) \tag{4}$$

where $C = c/k$ is the diffusivity [m^2/s]. For concrete and other cementitious materials the dependence of diffusivity on relative humidity is highly nonlinear. According to [1] it can be approximated by

$$C(\varphi) = C_1 \left(\alpha_0 + \frac{1-\alpha_0}{1 + \left(\frac{1-\varphi}{1-\varphi_c}\right)^n} \right) \tag{5}$$

where C_1 is the diffusivity at full saturation [m^2/s], φ_c is the relative pore humidity at which $C(\varphi_c) = 0.5C_1$. Parameter α_0 expresses the ratio of the minimum and maximum diffusivity $C(0)/C_1$ and n is a constant exponent.

The fib Model Code 2010 provides default values of parameters: $\alpha_0 = 0.05$, $\varphi_c = 0.8$, $n = 15$. The maximum diffusivity can be estimated from

$$C_1 = \frac{10^{-8}}{f_{cm} - 8} \tag{6}$$

where f_{cm} is the mean compressive stress [MPa] and C_1 is in [m^2/s].

2.2. BOUNDARY CONDITIONS

The Dirichlet boundary condition, prescribing the value of environmental relative humidity h_{env} on the surface, is not very realistic. Reference [1] recommends to add to all exposed (drying) surfaces the so-called "equivalent surface thickness" of 0.75 mm. This should correctly capture the effect of additional diffusion resistance of the surface.

Another approach used e.g. in [6] postulates a mixed boundary condition relating the moisture flux on the boundary to the difference between the relative humidity on the boundary and in the environment,

$$\vec{J}/k = f \cdot (h_{env} - \varphi_{boundary}) \tag{7}$$

where f is the surface factor [m/s] (0.75 - 7.5 mm/day according to [6]).

3. EXPERIMENTAL DATA AND RESULTS FROM LITERATURE

3.1. BAŽANT AND NAJJAR

Two sets of experimental data (originally published in [7] and [8]) related to 1-D diffusion were taken from [1]. In Fig. 1 dots denote experimentally measured data, dashed lines correspond to the best fit with the linear theory (constant diffusivity) and the results obtained with the proposed model are drawn using solid lines.

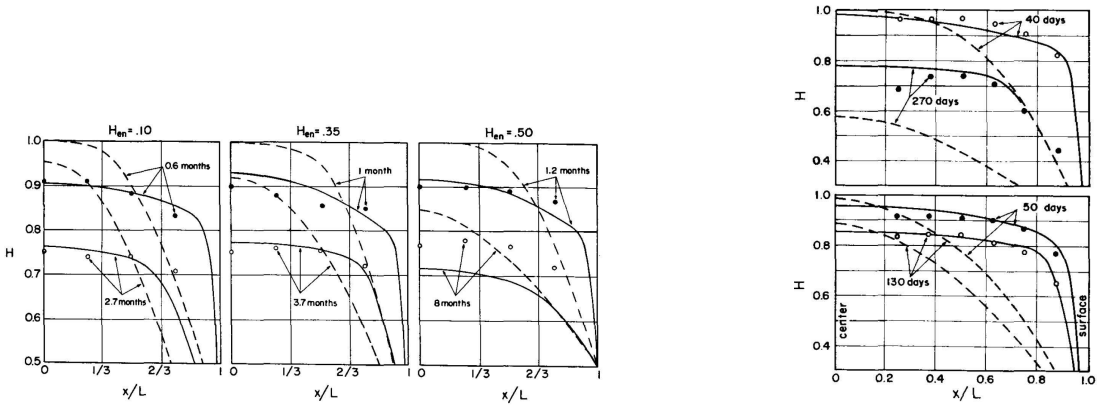

(a) (b)

Fig. 1 Distribution of the relative humidity in (a) three different drying specimens 6 in. (125.4 mm) thick exposed to $h_{env} = 0.1$, 0.35 and 0.5; (original Fig. 7 from [1], experimental data from [8]); (b) in one drying specimen 12 in. (304.8 mm) thick, $h_{env} = 0.1$ (original Fig. 8 from [1], experimental data from [7])

3.2. NILSSON

Reference [9] contains four data sets of measured relative humidity in drying specimens. In the experiment, prismatic specimens with four sealed sides (aluminum sealing) were used. The effective thickness of the specimens (i.e. the distance between the opposite drying surfaces) was 160 mm. Before drying at $h_{env} = 40\%$ all specimens were cured under sealed conditions. The third set of experimental data exhibits a non-monotonous behavior (see Fig. 2c) and the fourth one used concrete with a very high water-to-cement ratio, hence only the first two sets are used in the present simulations (Fig. 2a, b). Unfortunately no information of the concrete strength is available, therefore it is not possible to determine the maximum diffusivity according to (6).

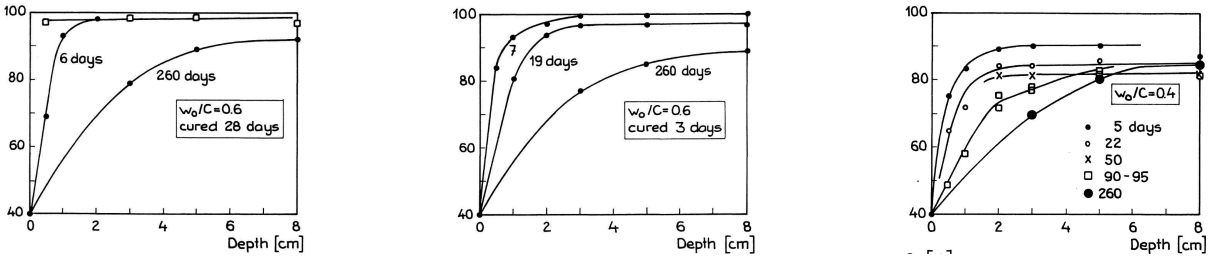

(a) (b) (c)

Fig. 2 Measured relative humidity in concrete specimens with w/c ratio 0.6, cement content 325 kg/m^3 cured (a) 28 days, (b) 3 days, and (c) w/c 0.4, cement content 490 kg/m^3, cured 3 days; original Fig. 9.5 in [9]

3.3. KIM AND LEE

In [5], drying was studied on prismatic specimens with all sides sealed except one; the effective thickness was 400 mm. Concretes of three compositions were used in the study. The first composition (L) had w/c = 0.68 and 28-day compressive strength $f_c = 22$ MPa, the second one (M) w/c = 0.4 and $f_c = 53$ MPa, and the last one (H) w/c = 0.28 and $f_c = 76$ MPa. The specimens were demolded after the first day and were water-cured until the beginning of the experiment, i.e. until the age of 3 or 28 days. During drying the relative humidity of the environment was approx. 50%. Only the concrete of the first composition (L) (Fig. 3) is used in the study. Modeling of drying of the other two would be too inaccurate due to a high drop of relative humidity caused by self-desiccation. In order to compensate for the (measured) drop in relative humidity due to self-desiccation the authors of [5] used a somewhat incorrect procedure to recover the measured data of drying specimens. This was done simply by adding the difference between drying and self-desiccation to the actually measured data. This procedure leads to a considerable change (increase) of the gradient of relative humidity near the drying surface.

4. NUMERICAL SIMULATIONS

The problem has been solved in the MATLAB environment using the bvp4c solver. In order to find the best combination of parameters of formula (5) to match the experimentally measured data, the problem has been solved for all reasonable combinations of parameters and the error (sum of squares) of the solution has been assessed.

4.1. BAŽANT AND NAJJAR

First, the recommended values of parameters from [1] have been used to check the difference between the original solution (Figures 7 and 8 in [1], see Fig. 1) and the new solution (solid red lines in Figs. 4 and 5a). These values of parameters are listed in Tab. 1 in columns labeled Bažant. For the first case (Fig. 1a and Fig. 4), these solutions differ, but not as dramatically as for the second case (Fig. 1b and Fig. 5a).

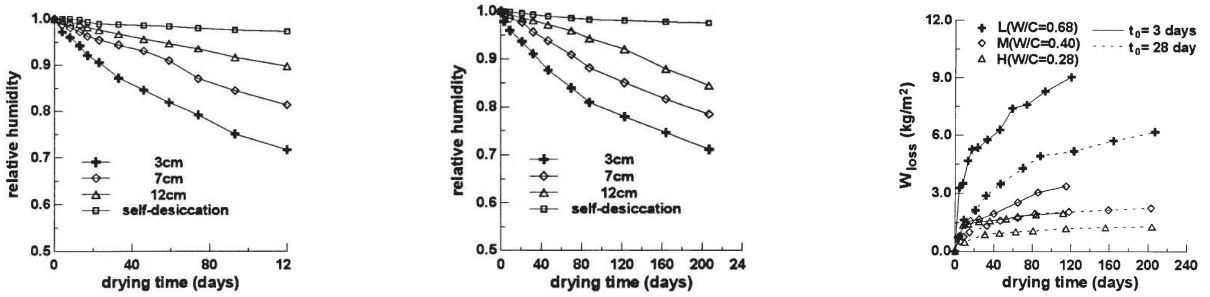

(a) (b) (c)

Fig. 3 Measured relative humidity in specified depths from surface of drying specimens and relative humidity drop due to self-desiccation for (a) L cured 3 days, (b) L cured 28 days and (c) measured water mass loss per unit drying surface; pictures taken from [5]

For the first case the overall error seems to be even smaller than in the original paper. The recommended set of parameters for the second case does not give a good agreement with the experimental data—the diffusivity is too low. The optimal solutions are drawn in Fig. 4 and 5a in green (Dirichlet b.c.) and blue (mixed b.c.) lines. The corresponding sets of parameters are listed in Tab. 1. Comparing the newly found parameters with the old ones, the biggest difference is in the value of the maximum diffusivity C_1, which almost doubled in the first case and increased five times in the second case.

Tab. 1 Recommended [1] and optimized parameters related to Fig. 4 (columns 2-4) and to Fig. 5 (columns 5-7)

parameter / variant	Bažant	Dirichlet b.c.	mixed b.c.	Bažant	Dirichlet b.c.	mixed b.c.
α_0 [-]	0.05	0.05	0.05	0.05	0.05	0.1
φ_c [-]	0.75	0.8	0.75	0.75	0.8	0.8
n [-]	16	16	16	16	10	10
C_1 [mm^2/day]	38.2	60	70	18.7	90	100
f [mm/day]	-	-	1	-	-	0.5

Figure 5b shows the time evolution of the relative water loss for the best (red) and 49 next best combinations (black). For these combinations the difference between the experimental data and the solution is almost the same, however, the sets of parameters differ considerably, see Fig. 5c. The optimized range of parameters (50 best combinations of approx. 1500) remains quite wide (original: $\alpha_0 = 0.05 - 0.5$, $\varphi_c = 0.6 - 0.9$, $n = 10 - 16$, $C_1 = 15 - 90$ mm^2/day; optimized: $\alpha_0 = 0.05 - 0.1$, $\varphi_c = 0.7 - 0.8$, $n = 10 - 16$, $C_1 = 40 - 90$ mm^2/day).

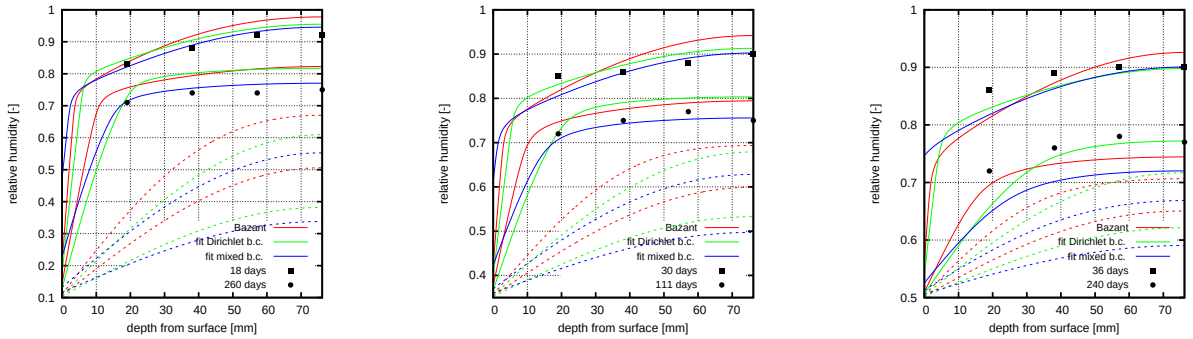

(a) (b) (c)

Fig. 4 Fit of data from Bažant's Fig. 7: distribution of relative humidity over the cross section at specified times (and after 500 and 1000 days of drying) for (a) $h_{env} = 0.1$, (b) $h_{env} = 0.35$ and (c) $h_{env} = 0.5$

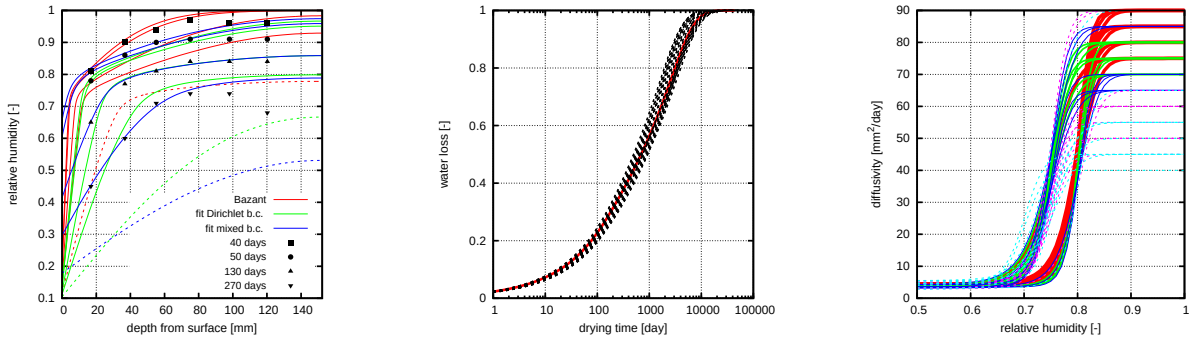

(a) (b) (c)

Fig. 5 (a) Fit of data from Bažant's Fig. 8: distribution of relative humidity over the cross section at specified times (and at 1000 days of drying), (b) computed moisture loss expressed as a fraction of the total loss, and (c) diffusivity functions for the best 50 combinations (the thicker the line, the smaller the error)

4.2. NILSSON

The best fits of Nilsson's data are shown in Fig. 6. The relative humidity is captured correctly even in the core of the specimen at early ages. This has been made possible by the initial condition reflecting the drop of relative humidity due to self-desiccation. To fit the first experimental data set the following parameters have been used: $\alpha_0 = 0.4$, $\varphi_c = 0.9$, $n = 20$, $C_1 = 6$ mm^2/day (Dirichlet b.c.) and $\alpha_0 = 0.3$, $\varphi_c = 0.6$, $n = 16$, $C_1 = 3$ mm^2/day, $f = 5$ mm/day (mixed b.c.). The second set of experimental data has been best fit with $\alpha_0 = 0.3$, $\varphi_c = 0.7$, $n = 6$, $C_1 = 5$ mm^2/day (Drichlet b.c.) and $\alpha_0 = 0.3$, $\varphi_c = 0.7$, $n = 10$, $C_1 = 6$ mm^2/day, $f = 1$ mm/day (mixed b.c.). It is clear that these values differ considerably from those in Tab. 1; the values of maximum diffusivity are about $10\times$ to $30\times$ smaller. Also, the diffusivity functions do not exhibit a pronounced difference between

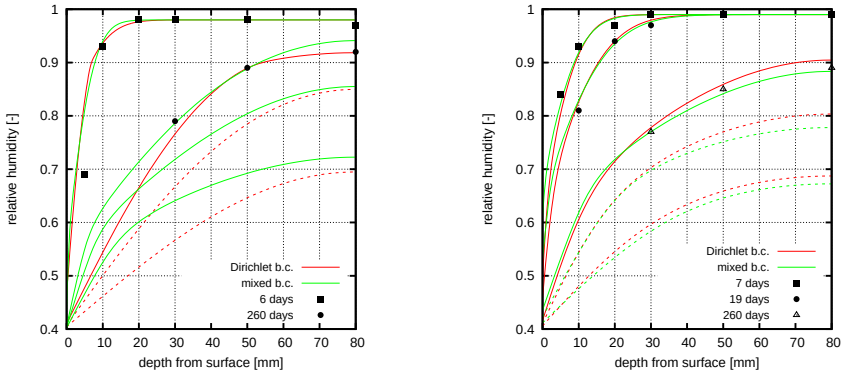

(a) (b)

Fig. 6 Fit of Nilsson's data at specified times and at 500 and 1000 days of drying

low and high humidity (the minimum diffusivity is 30% or 40% of the maximum value, instead of the recommended value of 5% or 10%).

4.3. KIM AND LEE

Neither the parameters recommended by fib MC 2010 nor the parameters from [5] give a satisfactory agreement with the experimental data; see Fig. 7a and Fig. 8a. In these figures the difference between the calculated profiles of relative humidity is almost inobservable, because these two sets of parameters share all values except maximum diffusivity C_1, which differs very slightly (see Tabs. 2 and 3). Keeping all parameters except C_1 fixed to their values recommended by fib, it has been found that values of $C_1 = 64$ mm^2/day (see solid lines Fig. 7b) and 83 mm^2/day (see solid lines Fig. 8b) give the smallest error. However, the agreement with the experimental data is not deemed to be good, especially for the data points near surface. Dashed lines in Fig. 7b show the solution which has been obtained by optimizing all the parameters.

Definitely the best fit has been obtained with mixed boundary conditions (and not with Dirichlet b.c. as in previous cases), see Figs. 7c and 8c. The self-desiccation has been treated in two different ways: it has been reflected either by the initial condition at the beginning of the simulation, or by a slightly more complicated procedure applied during whole computation. This procedure consists of the following steps: 1) fitting the time evolution of self-desiccation with a power function (in both cases: $0.035(1 - \exp(-0.05t^{0.65}))$); 2) evaluating the increment of this function in every time step and then subtracting it from the computed solution. Such a procedure is not perfect (the same value is subtracted from all points of the cross section, independently of the actual relative humidity), but it should be more realistic than the method used in [5].

The development of shrinkage and its final magnitude is closely related to the time evolution of water loss and to the total content of evaporable water. Therefore, to guarantee a realistic prediction of

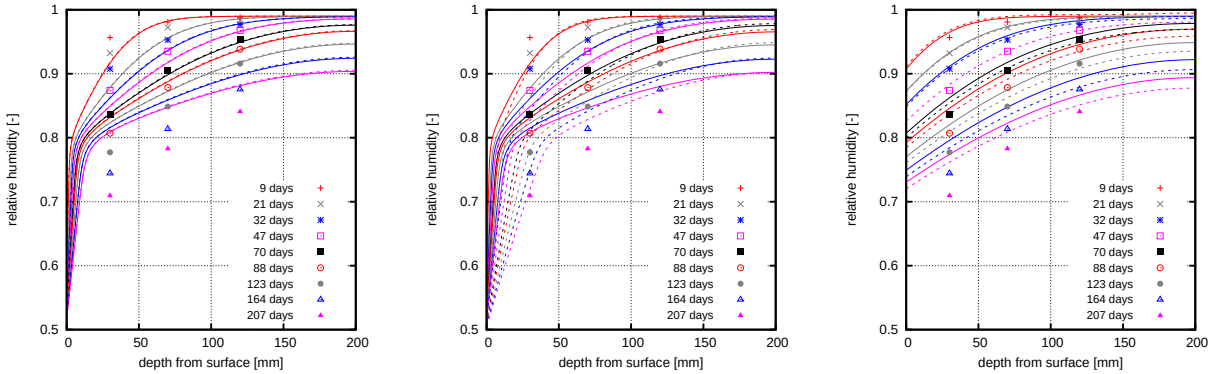

(a) (b) (c)

Fig. 7 Evolution of relative humidity in time (Kim-Lee, "L", curing time 28 days) (a) Dirichlet b.c.; solid lines: parameters from [5]; dashed lines: parameters according to fib; (b) Dirichlet b.c.; solid lines: optimized value of C_1, other parameters according to fib; dashed lines: best fit; (c) mixed b.c.; desiccation reflected by initial condition (solid lines) or by a function (dashed lines)

Tab. 2 Kim-Lee, "L", curing time 28 days, variants related to Fig. 7

parameter / variant	(a) solid	(a) dashed	(b) solid	(b) dashed	(c) solid	(c) dashed
α_0 [-]	0.05	0.05	0.05	0.2	0.05	0.1
φ_c [-]	0.8	0.8	0.8	0.8	0.6	0.6
n [-]	15	15	15	20	16	16
C_1 [mm^2/day]	62.88	61.71	64	55	75	75
f [mm/day]	-	-	-	-	0.5	0.5

Tab. 3 Kim-Lee, "L", curing time 3 days, variants related to Fig. 8

parameter / variant	(a) solid	(a) dashed	(b)	(c)
α_0 [-]	0.05	0.05	0.05	0.05
φ_c [-]	0.8	0.8	0.8	0.5
n [-]	15	15	15	14
C_1 [mm^2/day]	63.6	61.71	83	55
f [mm/day]	-	-	-	1

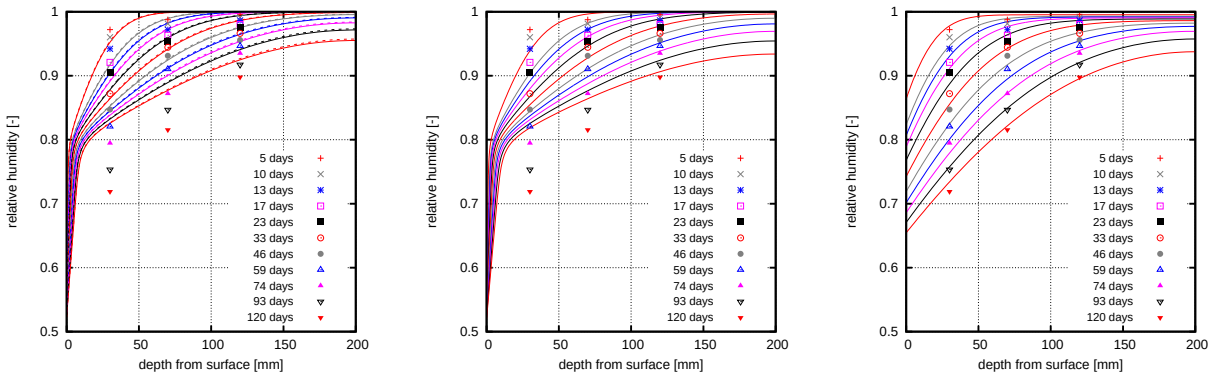

(a) (b) (c)

Fig. 8 Evolution of relative humidity in time (Kim-Lee, "L", curing time 3 days) (a) Dirichlet b.c.; solid lines: values from [5], dashed lines: values according to fib; (b) Dirichlet b.c.; optimized value of C_1 with other parameters according to fib; (c) mixed b.c.; desiccation described by a function

shrinkage, it is vital to be able to accurately simulate the development of moisture loss. The moisture loss can be computed either by time integration of the moisture flux at the boundary or by subtracting total moisture content at given time from its initial value at the onset of drying. Fig. 9 shows the experimentally measured data and the computed water loss for some previously mentioned cases. Note that the slope of the desorption isotherm is assumed to be constant, equal to 100 kg/m^3. This value works only as a scalar multiplier, while the computed shapes remain the same. Fig. 9a shows that a more accurate development of water loss has been obtained with Dirichlet boundary conditions and that the shape of the moisture loss curve computed using the mixed boundary conditions is initially too flat and in the main phase of drying too steep. For the shorter curing period the experimental data are far from any computed solution (see Fig. 9b).

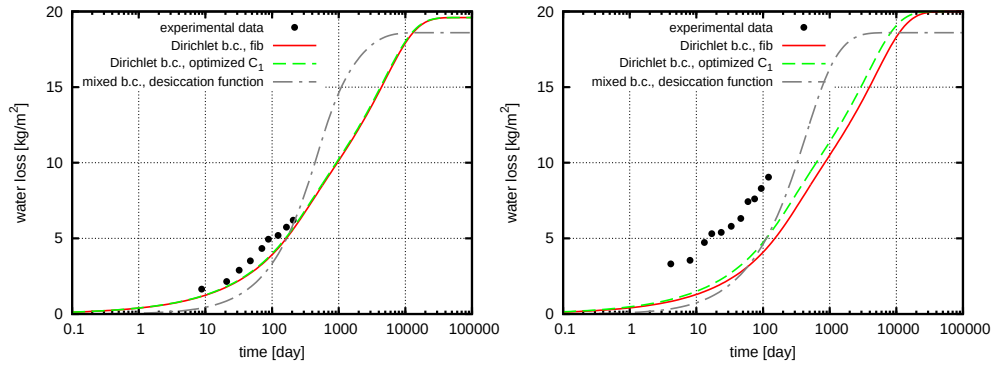

(a) (b)

Fig. 9 Time evolution of water loss per square meter of drying surface, assumed slope of desorption isotherm is the same for all data series: 100 kg/m^3, Kim-Lee, "L", curing time (a) 28 days, (b) 3 days

5. CONCLUSIONS

The material model based on [1] has been successfully implemented in the MATLAB environment and into the FE package OOFEM. It has been found that values of parameters published in the original papers [1] and [5] give different results from those published. The recommendation of parameters in [3] is too simplistic and gives a poor agreement with experimental measurements. The model proposed in [1] is almost insensitive to the specific choice of some parameters, namely to the exponent n. The best agreement with experimental data has been obtained when using the mixed boundary conditions instead of the Dirichlet b.c.. The assumption of a linear isotherm might be sufficient when modeling the time development of relative humidity in the specimen, but it seems that it is necessary to use a more general model when the moisture loss is of interest, too.

ACKNOWLEDGMENT

Financial support received from the Czech Technical University under project No. SGS12/027/OHK1/1T/11 is gratefully acknowledged.

REFERENCES

[1] Bažant, Z.P. and Najjar, L.J., *Nonlinear water diffusion in nonsaturated concrete*, Materials and Structures, Vol. 5, Issue 1, pp. 3 –20, 1972.

[2] Kuenzel, H., *Simultaneous Heat and Moisture Transport in Building Components*, IRB, Stuttgart, 1995.

[3] Fédération Internationale du Béton, *Model Code 2010*, Vol. 1, International Federation for Structural Concrete (fib), 2010.

[4] Patzák, B., *OOFEM home page*, http://www.oofem.org, 2000.

[5] Kim, J.K. and Lee, C.S., *Moisture diffusion of concrete considering self-desiccation at early ages*, Cement and Concrete Research, Vol. 29, Issue 12, pp. 1921–1927, 1999.

[6] Sakata, K., *A study on moisture diffusion in drying and drying shrinkage of concrete*, Cement and Concrete Research, Vol. 13, Issue 2, pp. 216–224, 1983.

[7] Abrams, M.S. and Monfore, G.E., *Application of a small probe-type relative humidity gage to research on fire resistance of concrete*, Journal of the Portland Cement Association Research and Development Laboratories, Vol. 7, Issue 3, pp. 2–12, 1965.

[8] Abrams, M.S. and Orals, D.L., *Concrete drying methods and their effect on fire resistance*, Moisture of materials in relation to fire tests, Issue 385, pp. 52–73, Am.Society for Testing Mat., 1965.

[9] Nilsson, L.O., *Hygroscopic Moisture in Concrete - Drying, Measurements Related Material Properties*, Lund University, 1980.

AUTOGENOUS SHRINKAGE OF ALKALI ACTIVATED MATERIALS

Petr HLAVÁČEK[1], Vít ŠMILAUER[2], Jiří LITOŠ[3]

Abstract: *Autogenous shrinkage of alkali activated fly ashes was measured on various compositions on the level of paste. Mixing fly ash with alkalies and/or ordinary Portland cement (OPC) creates a new binder with improved durability and strength compared to the traditional OPC. The shrinkage of this new material is not well known and was not sufficiently measured before. Two different mixes with high application potential for the civil engineering were investigated. The results were compared with the autogenous shrinkage of the OPC paste.*

Keywords: *autogenous shrinkage, alkali-activation, fly-ash, cement*

1. INTRODUCTION

The main objective of this work is to determine the unknown autogenous shrinkage of the paste prepared from alkali activated fly ash (AAFA). Two different methods of alkali activation were testified and the results were compared with the autogenous shrinkage of ordinary Portland cement paste.

The world annual production of fly ashes (FA) is estimated to be 600 million tons [1]. The current production of FA in the Czech Republic is about 6 million tons per year [2] (the thermal power plants release about 80 g of FA per production of 1 MWh of electric power). It is estimated that only 20-30% of FA is secondarily used, the rest is stored on landfills/lagoons which present due to the risk of air and ground water pollution the biggest ecological problem in the Czech Republic nowadays. Due to those facts a suitable utilization of FA is searched. Previous research testified that fly ash can enter the process of alkali-activation. Alkali activated materials show excellent performance in acid resistance, fire resistance, low drying shrinkage, low calcium content, improved durability, no alkali-silica reaction, freeze/thaw performance or lower creep induced by mechanical load, when compared to ordinary concrete [3]. On the other hand the autogenous shrinkage presenting a crucial factor for practical usability of AAFA is not sufficiently described yet.

[1]Ing. Petr Hlaváček , Department of Mechanics, Faculty of Civil Engineering, Czech Technical University in Prague, petr.hlavacek@fsv.cvut.cz

[2]Doc. Ing. Vít Šmilauer, PhD., Department of Mechanics, Faculty of Civil Engineering, Czech Technical University in Prague, vit.smilauer@fsv.cvut.cz

[3]Doc. Ing. Jiří Litoš, PhD., Experimental Centre, Faculty of Civil Engineering, Czech Technical University in Prague, litos@fsv.cvut.cz

Fig. 1 Left computer controlled climatic chamber, right bellow equipped with laser sensor for autogenous shrinkage determination.

2. MATERIALS AND METHODS

The fly ash class F from Opatovice brown coal power station (FA) (Blaine 210 m^2/kg) and ordinary Portland cement CEM I 42.5 R from Mokrá cement works (OPC) (Blaine 357 m^2/kg), both the Czech Republic, were used as the source material for alkali activation. The chemical compositions are given in the Table 1. Two different methods of fly ash activation were utilized in the experiments:

Tab. 1 Chemical composition of fly ash and cement (wt %).

	SiO_2	Al_2O_3	Fe_2O_3	CaO	K_2O	TiO_2
Fly ash	51.9	32.8	6.3	2.7	2.12	1.89
OPC 42.5 R	18.98	5.04	3.46	65.63	1.11	0.27

- Mix 1: Pure fly ash activation using NaOH and sodium water glass, the NaOH is dissolved in water, intermixed with sodium water glass and the solution is mixed with fly ash.
- Mix 2: Alkali activation of mix of 80% of FA and 20% of OPC using Na_2CO_3, the dry substances are intermixed together firstly (FA + OPC + Na_2CO_3) and water is added subsequently.

The composition of both mixes is given in the Table 2. The machine stirring took 4 minutes, the subsequent casting to the bellows (Figure 1 right) and vibrating took additional 4 minutes. The bellows were covered by foil to avoid water evaporation, equipped with dilatometers and given to the climatic chamber (Figure 1 left) at ambient 25 °C. Three specimens of each mix were produced and testified.

Tab. 2 Composition of paste mixes used in the experiments, mass needed to fill up three bellows (approximately 0.5 liter each).

	OPC	FA	water/binder	NaOH	Na_2CO_3	water glass	glenium ACE 40
Mix 1	-	1200 g	0.35	84 g	-	463 g	12 g
Mix 2	224 g	896 g	0.35	-	56 g	-	9 g

The autogenous shrinkage of a cement paste is defined as the macroscopic volume change with avoided moisture transfer from/to the specimen [4]. The autogenous shrinkage was calculated from the measured length changes of the bellows filled up with the fly ash paste. The length of bellows was measured each 5 minutes during hardening of the paste. The autogenous shrinkage R in the time step t_n was determined as

$$R(t_n) = \frac{l(t_0) - l(t_n)}{l(t_0)}, \tag{1}$$

where $l(t_0)$ is the initial length of the specimen and $l(t_n)$ is the length at given time step.

3. RESULTS AND DISCUSSION

The shrinkage evolution of AAFA paste during hardening with assumed final setting time is depicted in Figure 2 left. The shrinkage in the first hours before final set occurs is related to a plastic shrinkage. The material is still fresh (plastic) and the skeleton is under formation thus no stress is caused by early age shrinkage. The measured shrinkage after 32 days reads 8.1 mm/m for the Mix 1 (FA + NaOH + sodium water glass) and 2.7 mm/m for the Mix 2 (80% FA + 20% OPC + Na_2CO_3). According to Neville and Brooks, 1987 [5], the autogenous shrinkage of OPC paste after 10 hours of hydration reads about 6.2 mm/m.

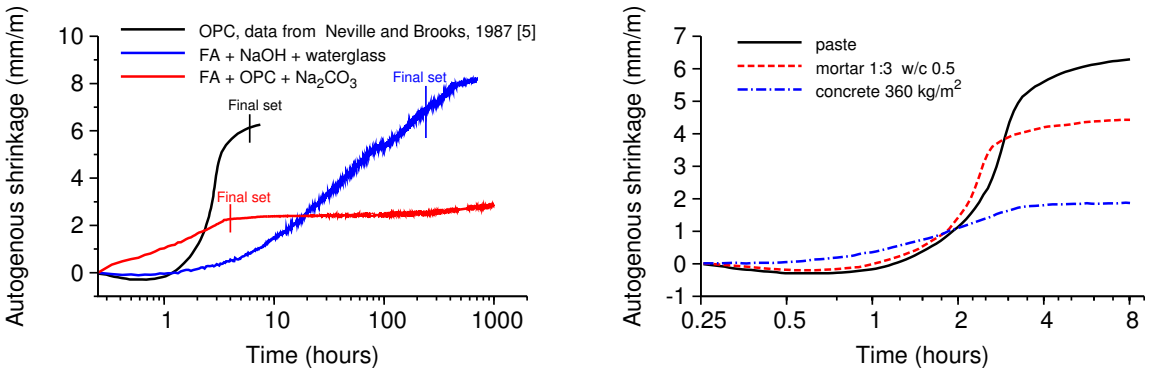

Fig. 2 Left: Measured autogenous shrinkage of two different mixes of AAFA compared with autogenous shrinkage of OPC - data from Neville and Brooks, 1987 [5]. Right: Autogenous shrinkage of OPC based paste, mortar and concrete, data from Neville and Brooks, 1987 [5].

Comparing the AAFA paste with OPC paste the AAFA Mix 2 exhibits even smaller autogenous shrinkage than a half value of the OPC, see Figure 2 left. The Figure 2 right shows the reduction of autogenous shrinkage with addition of sand and aggregates [5]. All those results confirm the potential of AAFA to be used as construction material in civil engineering.

4. CONCLUSION

The measured values of autogenous shrinkage of AAFA confirmed the high application potential of this new material in the civil engineering. Two different mixes were investigated. The mix of FA + NaOH + sodium water glass exhibits little bigger autogenous shrinkage compared to the OPC but the mix of 80% FA + 20% OPC + Na_2CO_3 showed even smaller autogenous shrinkage than OPC. The biggest advantage of the second composition is the presence of dry activator, similar to OPC. The FA and dry activator could be intermixed previously and only water need to be added subsequently, as in the case of OPC. The another big benefit is significant reduction of price of the AAFA in case of water glass exclusion.

All the results confirmed the AAFA, especially the mix with Na_2CO_3, as a practically usable material. A similar composition to this mix is already standardized in the Ukraine as an "Alkaline cement" [6].

The long-term mechanical properties, chemical- and fire-resistance and workability in a large volume will be testified in the future work.

ACKNOWLEDGEMENT

Authors gratefully acknowledge the financial support from the Czech Technical University Foundation under grant No. SGS12/116/OHK1/2T/11.

REFERENCES

[1] Ahmaruzzaman, M. *A review on the utilization of fly ash*, Progress in Energy and Combustion Science 36, 2010.

[2] CEZ web page. *CEZ web page* [online, 2012]. Available from WWW: <http://www.cez.cz>.

[3] Wallah, S.E., Rangan, B.V. *Low-calcium Fly Ash-based Geopolymer Concrete: Long Term Properties*, Research Report GC 2, Perth, Australia, 2006.

[4] Holt, E.E. *Early age autogenous shrinkage of concrete*, Technical Research Centre of Finland, VTT Publications 446, Espoo, Finnland, 2001.

[5] Neville, A.M. - Brooks, J.J. *Concrete technology* Longman, UK, 1987.

[6] DSTU B.V. 2.7-181, 2009 *Alkaline cements specifications*, Kiev: National Standard of Ukraine.

NUMERICAL ANALYSIS OF THE MICROSTRUCTURE OF CEMENT PASTES

Michal HLOBIL[1], **Vít ŠMILAUER**[2]

Abstract: *This paper presents the results of numerical modelling of mechanical properties of cement pastes based on images of their microstructure. 3D images of paste specimens for different w/c ratios were generated using x-ray microtomography and these images were then sliced to obtain 2D images of suitable resolution. Each 2D image was cropped to a RVE size and thresholded to identify main phases (unhydrated clinker grains, hydration products and pores). A finite element mesh was created on each cropped image, each phase was assigned a material model and computed using OOFEM. The overall mechanical behaviour was observed and stress-strain diagrams for different w/c ratios were generated and compared.*

Keywords: *cement paste, image analysis, microstructure, numerical modelling*

1. INTRODUCTION

Clinker production and composition (crystal size, phase distribution and surface area) have an impact on the properties of cement paste and concrete [1]. The study of cement paste microstructure can provide valuable information about the material and its behaviour on macroscale. It can reveal potential threads (such as carbonation, sulfate attack, delayed ettringite formation and alkali-silika reactions) that cannot be observed on macroscale. For example porosity and its spacial distribution can reveal technological problems or even point to a reduced durability of the structure.

Nowadays, there are several techniques used to investigate the microstructure of materials, each with its own strengths and weaknesses: scanning electron microscope using backscattered electrons (BSE) and x-ray microtomography (μCT), among others. The first technique, BSE, produces two dimensional monochrome images with a wide range of magnification (resolution down to $100\ nm$). This makes possible to observe the arrangement of aggregate in concrete at low magnifications and the morphology of hydrate phases using highest magnifications [2]. When coupled with X-ray spectroscopy a chemical composition of the observed phases can be identified. But there are certain limitations, as pointed out by K. Scrivener [3], that have to be taken into account when analysing 2D images: the thickness of layers (presumably hydration products around clinker grains) tends be overestimated, particle

[1]Ing. Michal Hlobil, Department of Mechanics, Faculty of Civil Engineering, Czech Technical University in Prague, michal.hlobil@fsv.cvut.cz

[2]doc. Ing. Vít Šmilauer, Ph.D., Department of Mechanics, Faculty of Civil Engineering, Czech Technical University in Prague, vit.smilauer@fsv.cvut.cz

size distribution is skewed towards smaller particles and spatial pore connectivity cannot be deduced from 2D images.

The second technique, μCT, creates a three dimensional image of the sample using sequential scans from different angles along all axes of rotation of the specimen. The connectivity and tortuosity of capillary pore network in space of cement based materials can be studied using this technique [4]. Another advantage of this nondestructive method is that specimens do not need specific preparation before analysis. Gallucci et. al. [4] states that from a qualitative point of view, the resolution of images (obtained from μCT) is comparable to that usually observed using scanning electron microscopy at an equivalent magnification, leading even to a similar phase contrast (between individual phases). The resolution at a scale of micrometers is sufficient for studying hydration products [5].

Because both techniques provide almost identical monochrome images (regarding resolution of the image), a qualitative analysis of the image can be conducted regardless of technique used. Each image is composed of pixels containing information on the intensity of greyscale level. On the images, porosity appears as the darkest phase. Unhydrated clinker grains appear as the brightest phase (due to their highest density [4]). Everything in between can be considered as hydration products. It is even possible to distinguish between individual hydration products and identify inner and outer C-S-H gels, portlandite, ettringite and monosulphate based on their shape but in our case they were all considered as one phase. A detailed description of greyscale level and corresponding hydrates can be found in [1], [3].

2. IMAGES OF PASTE MICROSTRUCTURE

A broad image database of Portland cement paste microstructures had to be created. Because such images were not available, an already existing database was used. NIST (stands for National Institute of Standards and Technology) offered a database of three dimensional images of cement pastes (with various water/cement ratios at different hydration times), plaster of Paris and clinker bricks. The database was a part of a project called The Visible Cement Data Set created by Dale Bentz et. al. [5]. All images were obtained using three dimensional microtomography at the European Synchrotron Radiation Facility in Grenoble, France.

Cement paste specimens were produced in Cement and Concrete Reference Laboratory (CCRL) using a single reference cement (N^0133) of a well documented clinker composition. For a prescribed water/cement ratio, both materials were mixed in a plastic beaker and small pats of the paste were "extruded" into sample tube molds (inner diameter $1\ mm$) and cured under prescribed conditions [5]. Improper compaction (resulting in entrapped air bubbles) could not be avoided due to some processing difficulties associated with low w/c ratios.

3. IMAGE PROCESSING

Three cement pastes (with a different water/cement ratio) were selected from the NIST database for image analysis. For each w/c ratio, two hydration times were also selected – the first representing early hydration time (up to 24 hours) and the second time showing a paste as old as could be found in the database (see Table 1). Next, a three dimensional image of the microstructure for a given w/c ratio and a specified hydration time was extracted form the database. The size of each image was $1024 \times 1024 \times 512$ $pixels$ having a resolution of 1 $pixel = 0.95$ μm. This provided an image of $973 \times 973 \times 486$ μm. The specimen itself was cylinder-shaped so the completely black edges around the circle were discarded from further analysis, see Figure 1.

Tab. 1 Specimens selected from the NIST database

Water/cement ratio	Early-age paste [hours]	Old paste [hours]
0.30	24	162
0.35	23	136
0.45	11	124

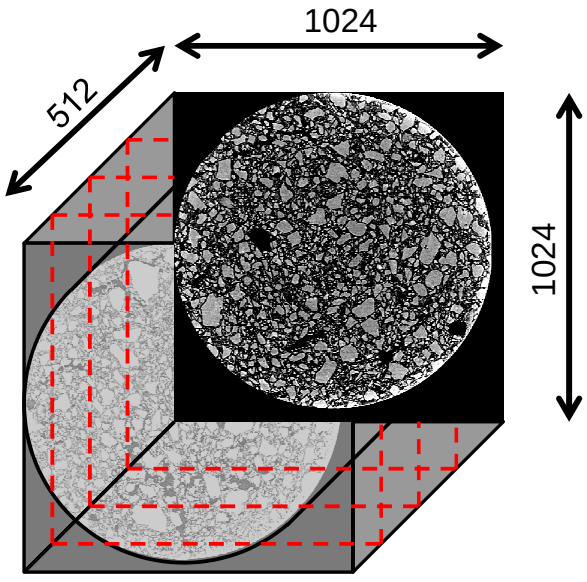

Fig. 1 Scheme of a 3D image obtained from μCT

Once the 3D image was created, it was then sliced at different heights (100 $pixels$ apart). The height of each image was 512 $pixels$ so five separate images were created. Dale Bentz [5] described problems during the production of samples so voids of entrapped air can be observed on some of the

images, see Figure 2. These images were discarded from future image processing because they were not representative.

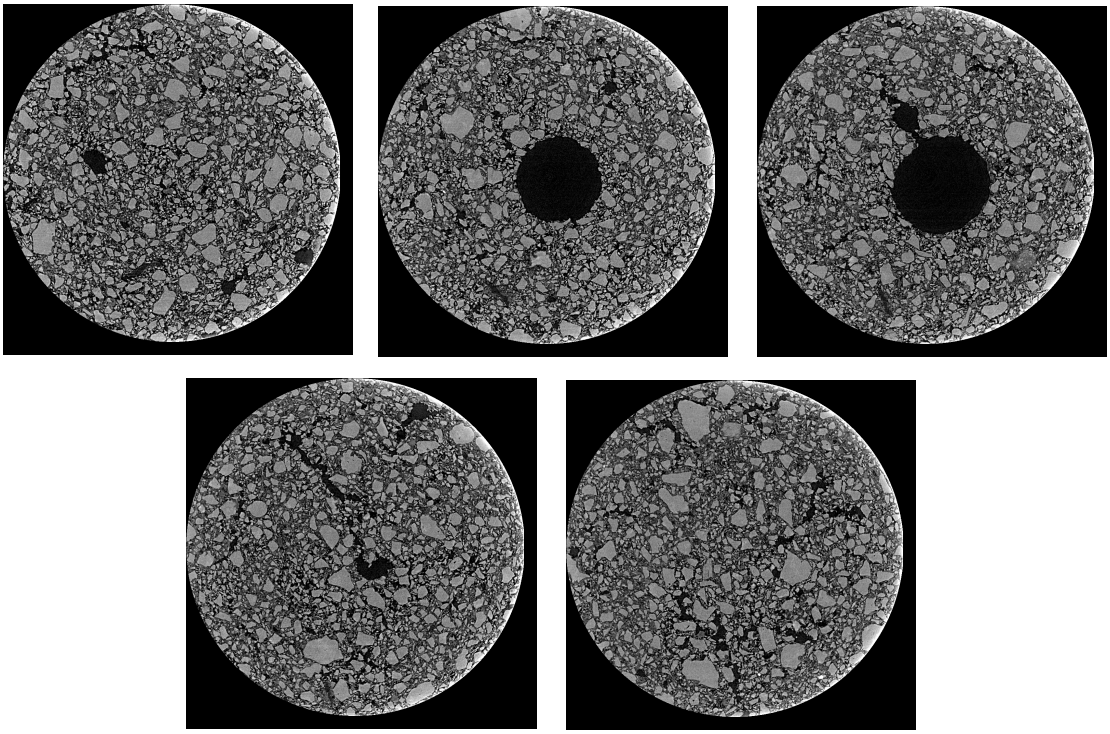

Fig. 2 Slices created from a single 3D image; paste shown: w/c = 0.30; t = 162 hrs

One representative image (out of five generated) was selected for each w/c ratio and hydration time. The image size (as mentioned above) was $1024 \times 1024\ pixels$ $(= 973 \times 973\ \mu m)$. For further image analysis a representative volume (or rather "area" in this case) element was chosen on each image. The size of RVE was selected considering the size and scale of observed microstructure. The cement fineness was $350\ kg/m^2$ and the mean grain radius of unhydrated cement approximately $15\ \mu m$. The RVE image size chosen was $100 \times 100\ pixels$ $(= 95 \times 95\ \mu m)$ and the original 2D image was then cropped to this size, see Figure 3. It was then displayed and checked visually whether it is representative enough. Images out of range of the circular region (without containing the microstructure itself) or containing large pores of entrapped air (a problem during production that has nothing to do with the paste itself) were discarded from further analysis.

3.1. HISTOGRAM

A histogram was created for each cropped image. Each pixel on the image contained a single value of 256 levels of greyscale colour from clear black to pure white. These values were projected on the X-axis and the number of pixels containing the given greyscale level on the Y-axis. In the next step a cumulative histogram for the same image was generated. The X-axis stayed unchanged meanwhile the Y-axis was normed and showed not only the given number of pixels for the given greyscale but also a sum of the

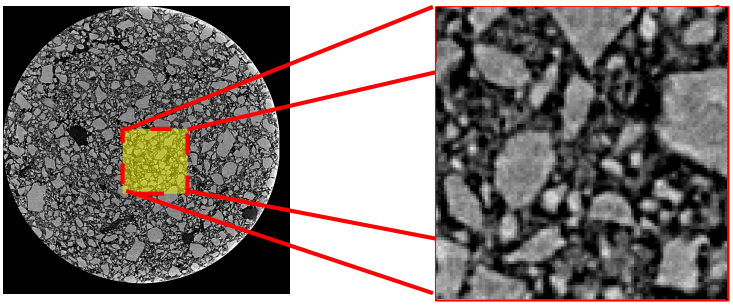

Fig. 3 Cropped image showing a RVE area

previous values, see Figure 4.

The appropriate volume fractions for porosity and unhydrated clinker grains were calculated in CEMHYD3D for each specimen studied. The cumulative histogram was then used to determine threshold values and the corresponding greyscale levels for each phase. Any greyscale pixel value that was lower than porosity threshold was considered as porosity. Any greyscale pixel value that was higher than unhydrated clinker threshold was then considered as clinker phase. Pixel values that lied in between these thresholds were considered as hydration products.

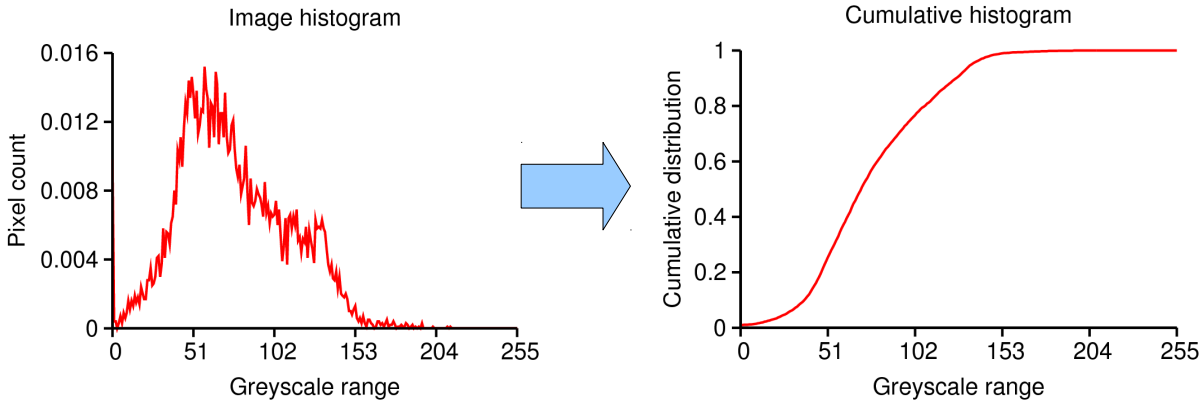

Fig. 4 A standard histogram for the cropped image (left) and a cumulative histogram (right)

3.2. THRESHOLDING

After determining specific threshold values for porosity and unhydrated clinker, the cropped image (still containing 256 greyscale levels) was coloured using filter masks in the following way: if a given greyscale pixel value was below a threshold value for porosity, it was considered as porosity and coloured in black. If a given greyscale pixel value was over a threshold value for unhydrated clinker, it was considered as clinker and coloured in light gray. Any pixels whose greyscale value that lied in-between both thresholds was considered as hydration product without further specifying its type (C-S-H gel, portlandite, ettingite or monosulphate) and coloured in blue, see Figure 5.

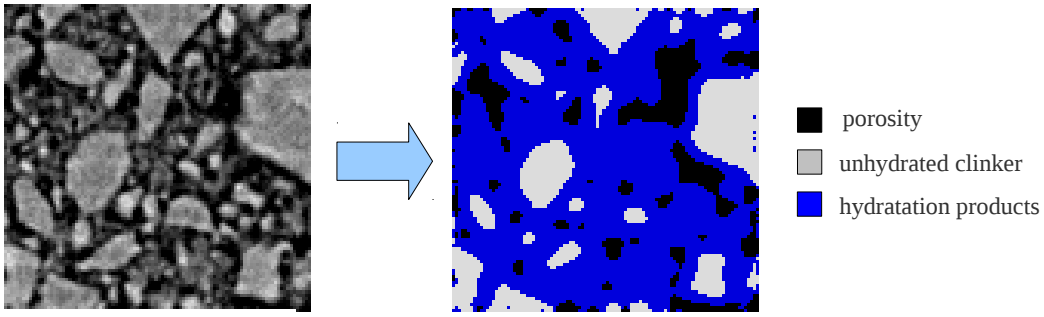

Fig. 5 Thresholding a cropped image

A series of smoothing filters were applied on each image in order to reduce the noise and obtain a clearer image. The borders of clinker grains were sharpened as well as hydration products precipitating on them, leaving sharply edged empty spaces for porosity. Some data was lost due to the application of these filters but an increase in stability of the calculation was expected.

4. NUMERICAL ANALYSIS

Based on threshold values (as described in section 3.2) the image now contained three separate phases (porosity, hydration products and unhydrated clinker), each described by its "colour". Each thresholded image was then meshed for a numerical analysis in OOFEM. The finite element mesh was created using isoparametric four-node quadrilateral elements, each pixel from the image was one element with four integration points. Linear approximations of displacements were considered.

A Mises plasticity model with isotropic hardening and isotropic damage (based on cumulative plastic strain) was assigned to each element (with modified parameters for each of the three phases, see Table 2). Full explanation of parameters can be found in Material Model Library Manual in [7]. Even though this material model may not be the most precise to simulate mechanical behaviour of cement pastes, it was still used and the obtained results followed expected outcomes. A new material model for cement pastes is in development.

Tab. 2 Main parameters used in the Mises plasticity model for each phase, for full explanation see [7]

Phase	E [GPa]	σ_0 [GPa]	H [GPa]	σ_c [-]	A [-]
porosity	0.001	10	1	0	10
unhydrated clinker	130	0.3	-1	0.9	100
hydration products	30	0.2	0	0.95	31

The problem was considered as plane-strain and Newton-Rhapson method was used to solve it.

Two metallic loading plates were created during meshing on the top and bottom surfaces. The top plate served as a "loading plate" where predescribed displacement was applied. The bottom plate served as a "support" having constrained diplacements. Loading was performed incrementaly, in each step a prescribed displacement was applied in order to get post-peak behaviour on the stress-strain diagram after reaching the ultimate stress.

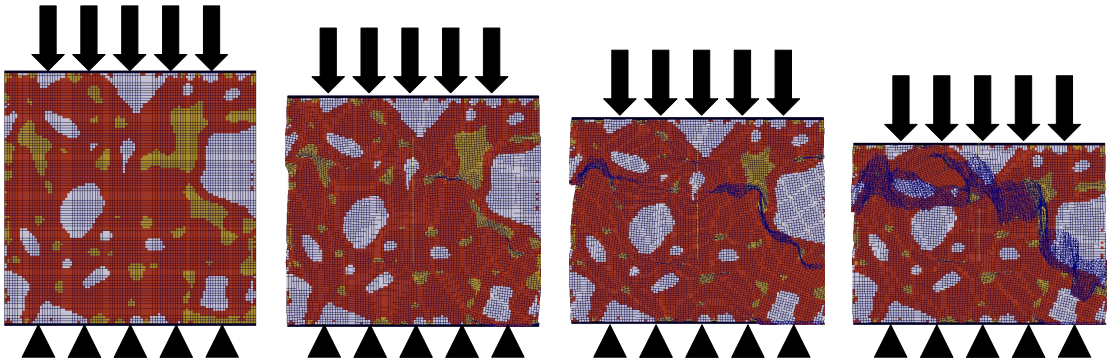

Fig. 6 Loading with prescribed displacement

5. RESULTS

A numerical simulation was performed on cement pastes of different water/cement ratio and hydration time. The results for pastes $w/c = 0.30, 0.35$ and 0.45 are presented below, both early age and old pastes. Results indicate expected behaviour – for a given w/c ratio, the strength of the "mature" paste is much higher. And regardless of hydration time, pastes with lower w/c ratio were stronger in terms of the ultimate compressive strength reached on the stress-strain diagrams, see Figure 7.

6. CONCLUSION

This paper presents the results of numerical modelling of mechanical properties of cement pastes based on images of their microstructure. Three dimensional images from a microtomograph were processed to create 2D images, these were cropped, thresholded and filtered to highlight three separate phases – porosity, hydration products and unhydrated clinker grains. Next a finite element mesh was created over the image, Mises plasticity model with isotropic hardening and isotropic damage (based on cumulative plastic strain) was applied on each phase (using modified parameters for individual phases) and the overall mechanical behaviour of the cement paste was observed. Results indicate expected behaviour – for a given water/cement ratio the older the paste is, the higher the ultimate strength. And regardless of hydration time, the lower the w/c ratio is, the higher the strength of the paste.

These simulations were performed in order to create and test Python scripts for image processing of cement paste microstructure. The material model chosen (Mises plasticity model with isotropic hardening) may not be the best to predict mechanical behaviour of cement pastes but it was still used, as a better model was not available. The predicted results are plausible and follow expected trends based

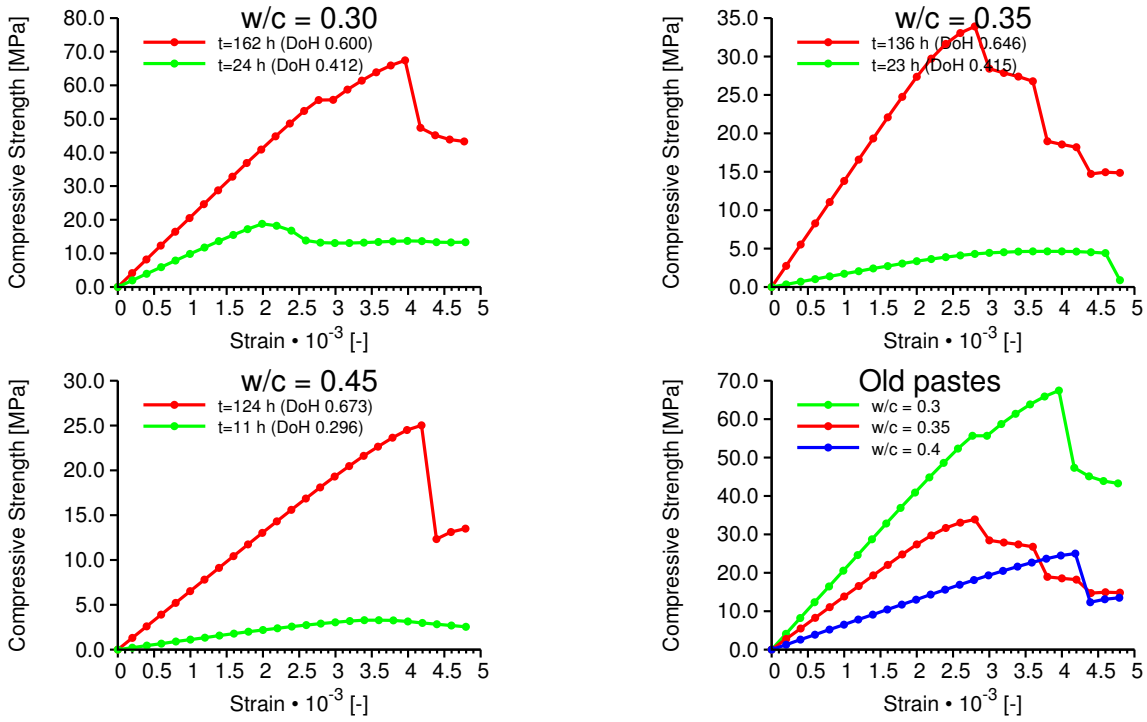

Fig. 7 Stress-strain diagrams for cement pastes with various w/c ratios

on the known impact of porosity on the overall strength of the cement paste. A better material model for cement pastes is in development. It will be based on the Drucker-Prager plasticity model with a Rankine-based cut-off for tensile stress.

REFERENCES

[1] Stutzman, P. *Scanning electron microscopy imaging of hydraulic cement microstructure*, In: Cement and Concrete Composites, Volume 26, Number 8, 2004, p. 957-966.

[2] Diamond, S. *The microstructure of cement paste and concrete – a visual primer*, In: Cement and Concrete Composites, Volume 26, Number 8, 2004, p. 919-933.

[3] Scrivener, K. *Backscattered electron imaging of cementitious microstructures: understanding and quantification*, In: Cement and Concrete Composites, Volume 26, Number 8, 2004, p. 935-945.

[4] Gallucci, E. - Scrivener, K. - Groso, A. - Stampanoni, M. - Margaritondo, G. *3D experimental investigation of the microstructure of cement pastes using synchrotron X-ray microtomography (μCT)*, In: Cement and Concrete Research, Volume 37, Number 3, 2007, p. 360-368.

[5] Bentz, D. P., et. al., 2002. *The Visible Cement Data Set*. In: NIST Journal of Research, Volume 107(2), March-April 2002, p. 137-148.

[6] NIST, 2002. *Visible Cement Dataset* [online]. [2002] [cit. April-May 2002]. Available from WWW: <http://visiblecement.nist.gov>.

[7] Patzák, B. *OOFEM home page* [online]. [2000]. Available from WWW: <http://www.oofem.org>.

OBJECT ORIENTED DESIGN OF COUPLED, MULTI-PHYSICS FEM KERNEL

Martin HORÁK[1], **Bořek PATZÁK**[2]

Abstract: *This paper presents the advanced object-oriented design of finite element representations in a complex multi-physics finite element environment OOFEM [1], [2]. The focus is on reuse of existing single-physics capabilities when implementing elements for coupled simulations. This has been achived by decoupling the description of element geometry, element problem specific capabilities, element interpolation, and integration schemes. The individual problem specific capabilities, represented by a hierarchy of classes derived form ElementEvalautor, can be assembled together to define an evaluator for coupled analysis. Presented design leads to extremely flexible implementation, with clean modular design.*

Keywords: *multi-physics simulations, fem software design*

1. INTRODUCTION

Numerical simulations are routinely used in research and industry and are accepted as reliable analysis tools. However, in recent years, it is becoming clear, that further progress in many scientific and engineering disciplines requires understanding of various complex multi-physics phenomena taking place at different scales of resolution. Therefore, one of the actual chalenges in software engineering is to design an efficient and modular modeling tools. The aim of the this contribution is to present advanced object-oriented design of general multi-physics finite element kernel allowing to reuse single physics formulations in development of coupled multi-physics problems.

The conventional designs of object-oriented finite element codes introduce an abstraction for finite element, which keeps description of element geometry, properties and integration scheme and providing services for evaluating characteristic terms, such as stiffness matrix or element load vector. In more elaborated designs, a hierarchy of classes is developed, where base parent element class contains only problem independent description (such as element geometry) and specific functionality is implemented by derived classes, representing problem related base classes. This scheme works well when elements are to be solely used for specific analysis, e.g. elements for structural analysis.

The problem may arise, when one wants to combine capabilities of two or more elements to obtain element for multi-physics analysis. Multiple inheritance provides only a partial solution, allowing

[1]Ing. Martin Horák , Faculty of Civil Engineering, Czech Technical University, Thákurova 7, 126 77, Prague, martin.horak@fsv.cvut.cz

[2]Prof. Dr. Ing. Bořek Patzák , Faculty of Civil Engineering, Czech Technical University, Thákurova 7, 126 77, Prague, borek.patzak@fsv.cvut.cz

to inherit problem specific capabilities from individual (single physics) elements. This could be an issue in some programming languages (C++ for example) where the use of multiple inheritance leads to duplication of parent element class data, as illustrated in Figure. 1. Here, the *StructuralElement* and *Heat&MassTransportElement* classes represent problem-specific base classes. For example, all structural elements are derived from *StructuralElement* class. When an element for coupled analysis has to be developed, one naturally wants to inherit from *StructuralElement* and *Heat&MassTransportElement* classes to reuse existing implementations. However, as both parent classes are derived from *Element*, the attributes defined at *Element* level are duplicated. Moreover, one has to manually fix name resolution problems with services defined on *Element* level.

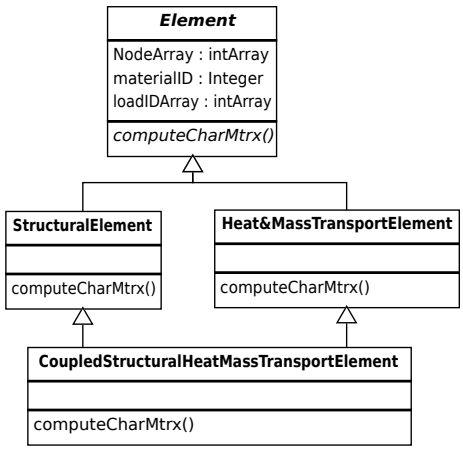

Fig. 1 Traditional approach in element definition.

The proposed solution consists in decoupling element geometry description (represented by *ElementGeometry* class) and problem-specific functionality (represented by classes derived from *Evaluator* class). The particular element is then assembled from base *ElementGeometry* class and suitable *Evaluator* class. The *Evaluator* class evaluates the characteristic terms of governing equation and it is parameterized by geometry, interpolation, and integration defined by element. The essential feature is possibility to assemble individual *Evaluator* classes together to form a high-level evaluator for coupled problem. Such design allows to naturally reuse not only evaluator for different type of problem-specific elements, but also reuse of problem-specific evaluators when implementing complex evaluator for multi-physics problem.

2. OVERALL DESIGN OF OOFEM CODE

The general structure of the OOFEM is shown in Figure 2, using the UML notation. In short, abstract classes are represented by rectangles. The lines with a triangle mark represent the generalization/specialization relation (inheritance), where line from triangle vertex points to the parent class. The lines with a diamond mark represent the whole/part relation, pointing to the “whole” class possessing

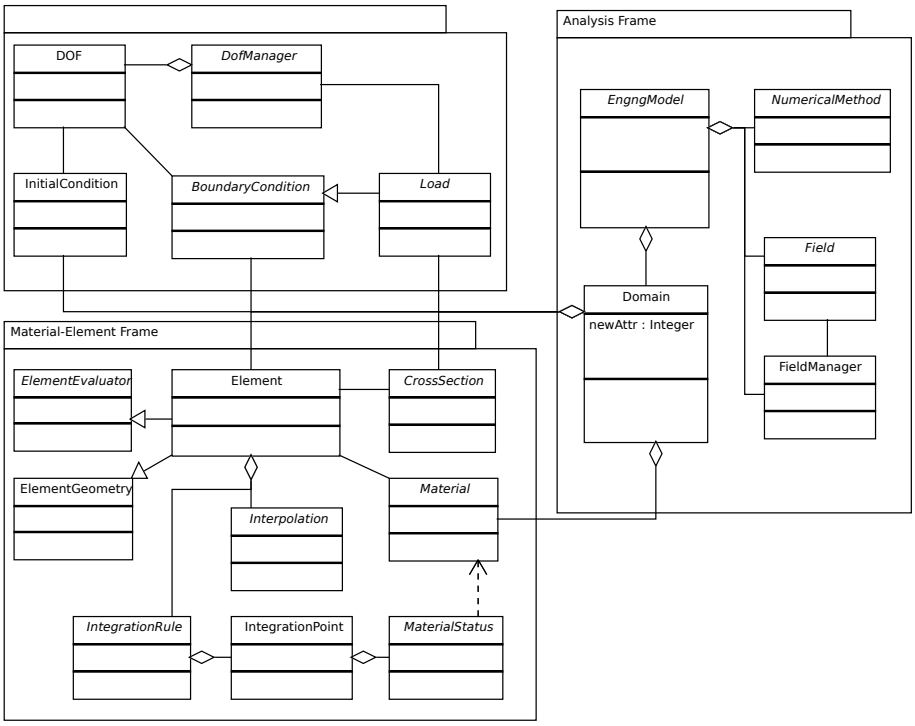

Fig. 2 Overall structure of OOFEM code.

the "part" class. Association is represented by a solid line, drawn between classes. The details can be found in [3].

Class *DOF* represents a single degree of freedom (DOF). It maintains its physical meaning, the associated equation number, and keeps a reference to the applied boundary and initial conditions. The base class *DofManager* represents an abstraction for an entity possessing some DOFs. It manages its DOF collection, list of the applied loadings and optionally its local coordinate system. General services include methods for gathering localization numbers from the maintained DOFs, computing the applied load vector, and computing the transformation to its local coordinate system. Derived classes typically represent a finite element node or an element side, possessing some DOFs. Boundary and initial conditions are represented by the corresponding classes. Classes derived from the base *BoundaryCondition* class, representing particular boundary conditions, can be applied to DOFs (primary BC), DOF managers (typically nodal load), or elements (surface loads, Neumann or Newton boundary conditions, etc.). The problem under consideration is represented by a class derived from the *EngngModel* class. Its role is to assemble the governing equation and use a suitable numerical method (represented by the class derived from the *NumericalMethod* class), to solve the system of equations. The discretization of the problem domain is represented by the *Domain* class, which maintains the lists of objects representing nodes, elements, material models, boundary conditions, etc. The *Domain* class is an attribute of the *EngngModel* and, in general, it provides services for accessing particular components. For each solu-

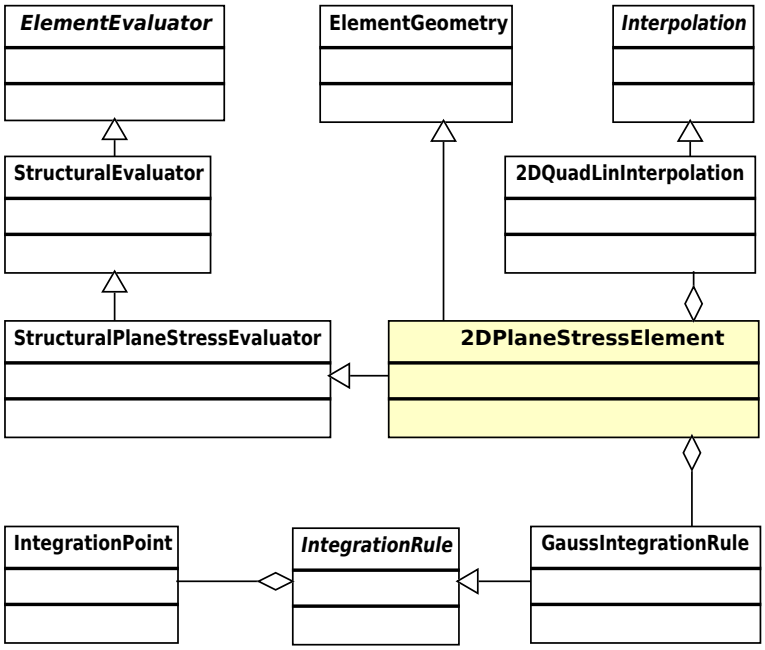

Fig. 3 Collaboration diagram of Element class.

tion step, the *EngngModel* instance assembles the governing equations by summing up the contributions from the domain components. Since the governing equations are typically represented numerically in the matrix form, implementation is based on vector and sparse matrix representations to efficiently store components of these equations. The modular design allows uncoupling the problem formulation, the numerical solution and sparse storage being independent of each other.

3. MULTI-PHYSICS DESIGN OF ELEMENT FRAME

The modular design has been achieved by decoupling of description of element geometry (represented by *ElementGeometry* class), interpolation (represented by *FEIInterpolation* class), integration (represented by *IntegrationRule* class), and evaluation of problem-specific terms (represented by *Evaluator* class). The parent *ElementGeometry* keeps list of element nodes defining its geometry, list of applied loading, list of integration rules (defined by particular element implementation), reference to corresponding cross section and material models. Its abstract interface includes methods for accessing element components, element evaluator, interpolation(s), and integration rule(s). Integration rules, represented by classes derived from base *IntegrationRule* class, define and provide list of integration points. Derived classes represent particular integration schemes. Individual elements can have one or more integration rules; this allows to perform reduced or selected integration, or to have individual integration schemes for different characteristic terms.

Element interpolation is represented by abstract *FEIInterpolation*, which defines general services for evaluation of interpolation (shape) functions, their derivatives, transformation Jacobians, etc. De-

rived classes implement particular interpolation. The evaluation requires access to underling element geometry. In our approach, the element geometry is compulsory parameter of every *FEIInterpolation* method. This allows to share a single instance of *FEIInterpolation* between all elements of the same type (static, class variable in C++). Similar to the integration rule concept, elements can use several interpolations. This is essential for coupled simulation elements, where interpolation of individual fields often varies, but also allows to have different approximation for geometry and unknowns, for example.

As already pointed out, a new abstract base *Evaluator* class has been introduced. Derived classes represent problem specific functionality of an element. Base class declares common abstract services for evaluating characteristic terms (*giveCharacteristicMatrix*, *giveCharacteristicVector*) and corresponding localization arrays. Derived classes provide corresponding implementation. The abstract interface, defined by *Evaluator*, is essential, as it allows to treat all element evaluation and assembly operations using the same general interface. As an example, consider the *StructuralAnalysisEvaluator* class implementing structural analysis functionality, see Figure 3. It provides methods for evaluation of element stiffness and mass matrices and element load vectors, based on element geometry, its interpolation and integration. Particular elements are supposed to be derived from one base *Element* class and one of classes derived from *Evaluator* class.

In coupled multi-physics simulations, one needs to combine functionality from individual subproblems in one element (represented by corresponding classes derived from *Evaluator*) and complemented by definition of coupling terms, which will be also provided by corresponding evaluator. In order to combine individual evaluators into an evaluator for a coupled problem, the *CoupledEvaluator* class has been designed. It is derived from base *Evaluator* class and comes with the capability to group individual low-level evaluators together by performing local assembly from individual contributions. The *CoupledEvaluator* class constructor allows to set up an matrix of slave evaluators whose contributions will be assembled (locally on element level) to obtain characteristic components of coupled problem formulation. This is shown in Figure 4, illustrating mutual class relations for the case of coupled structural and heat&mass analyses.

When problem-specific evaluator is available, the definition of particular elements is straightforward. It consists in (i) defining a new class, derived from *ElementGeometry* and class representing problem-specific evaluator, and (ii) setting up its interpolation and integration rules. No additional coding is necessary.

4. CONCLUSION

The advanced object-oriented design of finite element representations in a complex multi-physics finite element environment has been presented. It allows to reuse of existing single-physics capabilities when implementing elements for coupled simulations. This has been achived by decoupling the description of element geometry, element problem specific capabilities, element interpolation, and integration

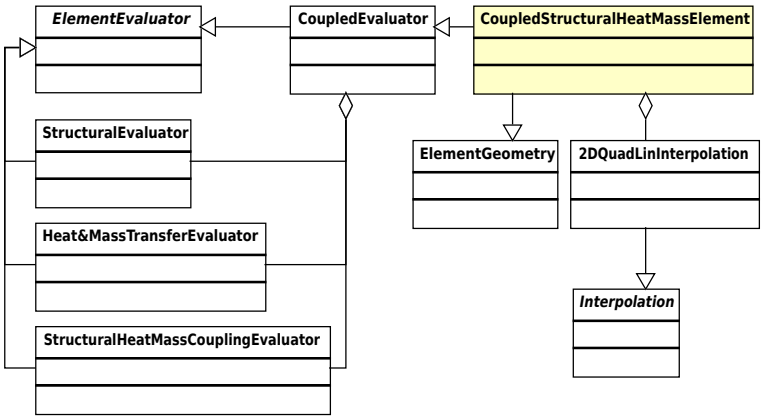

Fig. 4 Collaboration diagram of Element in coupled analysis.

schemes. The individual problem specific capabilities, represented by a hierarchy of classes derived form *ElementEvalautor*, can be assembled together to define an evaluator for coupled analysis. Presented design leads to extremely flexible implementation, with clean modular design.

ACKNOWLEDGEMENT

The financial support of this work by the Faculty of Civil Engineering, Czech Technical University in Prague (SGS project No. SGS12/027/OHK1/1T/11) is gratefully acknowledged.

REFERENCES

[1] Patzák B. and Bittnar Z. , *Design of object oriented finite element code*, Advances in Engineering Software, 2001, 32(10-11): p. 759–767, .

[2] Patzák B. , OOFEM project home page, <http://www.oofem.org>, 2012.

[3] Fowler M. , *UML Distilled: A Brief Guide to the Standard Object Modeling Language*, Addison-Wesley, ISBN 0-321-19368-7, 2003.

CABLE STRUCTURES – NUMERIC ANALYSIS

Miloš HÜTTNER[1], Jiří MÁCA [2]

Abstract: *The aim of this study is to compare the accuracy and time demand of the calculation of approximated cable as one perfectly flexible cable element which is replaced with several bar elements. The comparison is done on sample of cable structures. The used method of calculation is dynamic relaxation.*

Keywords: *dynamic relaxation, cable structures, nonlinear analysis*

1. INTRODUCTION

The cable is an excellent kind of a construction element, which was firstly used exclusively for construction purposes. The cable was primarily used only in the bridge constructions. It was possible to configure more and more complicated cable structures when modern and effective computers came to use. Their utilisation increases in civil engineering.

The cable has before all an excellent flexibility and strength and therefore it can be effectively used for bridging of large areas without internal support. The weight of the roof in contrast with other construction systems is smaller. During the construction of the cable structures one can use all the advantages of prefabrication. The curves of the cable constructions appear very natural and they are much preferred among architects. The disadvantage of the cables is generally their shape instability, especially when they are unequally loaded or when they are loaded with a local force.

1.1. IDEALISATION

For numerical modelling of cable structures in space one uses idealisation of the system structure of elements and joints. Each joint can have space for up to three degrees of freedom (in the plane of the two). The joint in which only one cable element ends or begins is called an outer joint and must be fixed. When one deals with an inner joint (connecting two or more cable elements) it can be a fixed joint or a free joint.

Since the high-strength steels are almost exclusively recycled materials of cables, linear elastic material behaviour of elements (i.e., small deformation) with large displacement is assumed. Further, it is assumed that the deformation of the structure will have no effect on the magnitude and direction of

[1] Ing. Miloš Hüttner, Department of Mechanics, Faculty of Civil Engineering, CTU in Prague; milos.huttner@fsv.cvut.cz

[2] prof. Ing. Jiří Máca, CSc., Department of Mechanics, Faculty of Civil Engineering, CTU in Prague; maca@fsv.cvut.cz

external forces. Effect of temperature on the shape of the structure is not considered. Cable systems represent geometrically nonlinear case, in which we are looking for an equilibrium on a deformed structure.

Several methods exist to solve cable structures, the most common methods are: dynamic relaxation, force density method, finite element method and some other which can be found in [1], [2] or [3]. Dynamic relaxation will be used in this study.

2. SINGLE CABLE

The cable can be approximated as a perfectly flexible element (bending moments are over all its length equal to zero), or it can be composed together from several bar elements interconnected by joints. Homogeneous material with constant cross-section throughout its length is assumed in both cases.

2.1. CABLE ELEMENT

The basic assumption of the analysis of a flexible elastic cable is that the cable is regarded to be perfectly flexible and is devoid of any flexural rigidity. Load on a cable, which must include at least self-weight, is distributed uniformly along the curve of the cable which is assumed to be a parabola. The detailed analysis can be found in [4], [5] and [6].

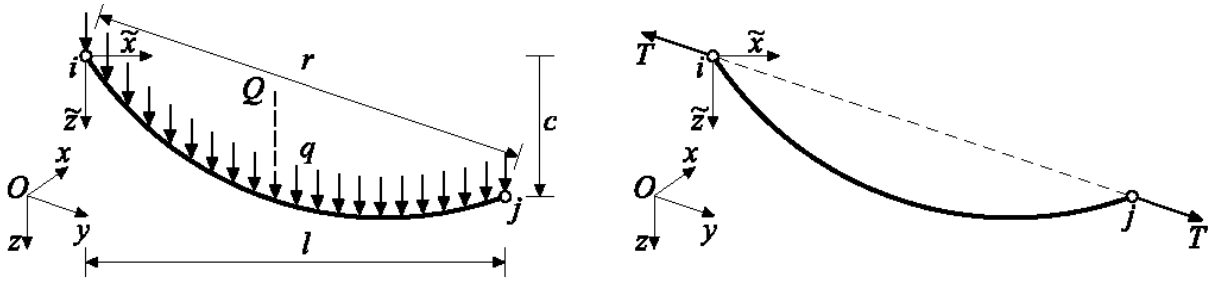

Fig. 1 The cable element

It is necessary for the aim of the study to use an internal force *T*, which is always positive and the importance of which is shown in Fig. 1. Force *T* can be calculated iteratively of equation (1). The function *fsolve* in MATLAB is used to solve this equation; it is a numerical iterative solver.

$$g(T,r,l,c,s_0,Q)=\frac{l^2T}{2rQ}\left[\ln\left(-\frac{2c}{l}+\frac{rQ}{lT}+\frac{\sqrt{b}}{lT}\right)-\ln\left(-\frac{2c}{l}-\frac{rQ}{lT}+\frac{\sqrt{a}}{lT}\right)\right]+$$

$$+\frac{c}{4rQ}\left(\sqrt{a}-\sqrt{b}\right)+\frac{1}{8T}\left(\sqrt{a}-\sqrt{b}\right)-s_0-\frac{T}{EA}\left(\frac{l^2}{r}+\frac{c^2}{r}+\frac{Qr^2}{12t^2}\right)=0 \qquad (1)$$

Slack length s_0 is the un-elongated length of an element, length *r* is the distance between two end joints in the chord direction. Distance *l* is the horizontal distance between the two end joints and *c* is

the vertical separation between the end joint *j* and the end joint *i* (can be negative). Force *Q* is the resultant of the vertical uniform load *q* acting vertically the entire length of parabolic curved cable, while $Q = qs_0$. *E* is the Young's modulus of elasticity and *A* is the cross-sectional area of a cable. For reasons of clarity calculation introduces two more substitutions: $a = Q^2r^2 + 4c^2T^2 + 4l^2T^2 + 4crQT$; $b = Q^2r^2 + 4c^2T^2 + 4l^2T^2 - 4crQT$.

2.2. BAR ELEMENT

The basic assumption of this theory is that the behaviour of a cable can be approximated by a few bars. These bars are interconnected by joints and sustain only positive normal force. The internal force *T* in one bar element can be calculated according to the known equation (2). The force *T* has the meaning so the normal force on the bar.

$$T = \frac{EA}{s_0}\left(r - s_0\right) \qquad (2)$$

3. DYNAMIC RELAXATION

The method uses a fictitious damped dynamic analysis to determinate the solution of a static problem. The method is based on the Newton's second law of motion. Masses and viscous damping factor in the joints are considered fictitious. Damping must be proportional. When calculating the response of the structure we do not prepare the stiffness matrix and therefore the dynamic relaxation is suitable for large scale nonlinear cases.

The theory of this method was first described by Day [7]. This theory was further developed and its detailed overview can be found in [1] or [8].

3.1. PRINCIPLE

The basic equation of motion (3) for joint *i*, direction *x* (and similarly for *y* and *z*) and time *t*:

$$R_{ix}^t = M_{ix} \cdot a_{ix}^t + C_{ix} \cdot v_{ix}^t, \qquad (3)$$

where R_{ix}^t is residual force (i.e. out of balance) at joint *i* in the direction *x* and at time *t*.

M_{ix} is the fictitious mass at joint *i* in the direction *x*.

C_{ix} is the viscous damping factor for joint *i* in the direction *x*.

v_{ix}^t is velocity at joint *i* in the direction *x* and at time *t*.

a_{ix}^t is acceleration at joint *i* in the direction *x* and at time *t*.

The basic unknowns form nodal velocity, which are calculated from nodal displacements. The discretisation from timeline with time step Δt will be performed. During the step Δt a linear change of

velocity is assumed. Acceleration during the step Δt is thus considered to be constant. By substituting the above assumptions and adjusting equation (3) the velocity can be expressed in a new time point $t + \Delta t/2$:

$$v_{ix}^{(t+\Delta t/2)} = v_{ix}^{(t-\Delta t/2)} \frac{M_{ix}/\Delta t - C_{ix}/2}{M_{ix}/\Delta t + C_{ix}/2} + \frac{R_{ix}^{t}}{M_{ix}/\Delta t + C_{ix}/2}. \qquad (4)$$

Current coordinates of the joint i at the time point $t + \Delta t$ can then be expressed as follows:

$$x_i^{(t+\Delta t)} = \Delta t \cdot v_{ix}^{(t+\Delta t/2)}. \qquad (5)$$

From the imbalance (between external and internal forces) in node i one can calculate the residual force for the corresponding node in time $t + \Delta t$.

$$R_{ix}^{t} = P_{ix} - \sum_k T_k^t \frac{x_i^t - x_j^t}{r_k^t},$$

$$R_{iy}^{t} = P_{iy} - \sum_k T_k^t \frac{y_i^t - y_j^t}{r_k^t},$$

$$R_{iz}^{t} = P_{iz} + \sum_k \frac{Q_k}{2} - \sum_k T_k^t \frac{z_i^t - z_j^t}{r_k^t}, \qquad (6)$$

where P_{ix}^{t} is the external load at joint i in the direction x.

k is the index of the element entering into joint i.

j is the second endpoint on the element k.

Internal force T_k is possible for each cable element to be calculated from equation (1) and for each bar element from equation (2). The integration scheme is overlapping because the residual forces are calculated at the end of each time step and the velocities are calculated at a half time step. The factors having an impact on the stability of the method and speed of convergence are: distribution of a fictitious mass of a structure at joints, using of a fictitious damping factor, choice of a time step Δt.

Generally, one of the parameters is fixed, and the others are fine-tuned. The appropriate choice of parameters can be found in the [1] and [8].

3.2. SIMPLE EXAMPLE 1

The comparison of cable and bar elements is first performed on a simple example. The geometric configuration is shown in Fig. 2. The structure is composed of two identical cables and one free joint. The parameters of cables are: $EA = 1 \cdot 10^5$ kN, $s_0 = 3.5$ m, $q = 0.5$ kN/m.

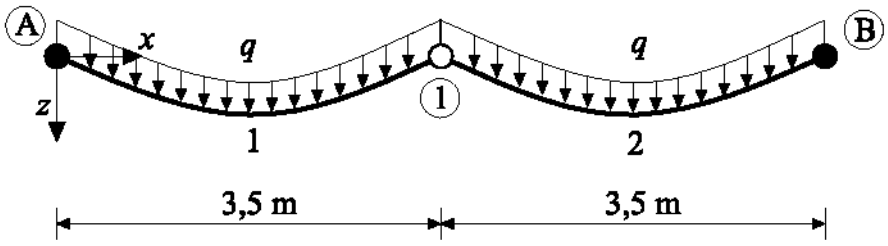

Fig. 2 The geometric schema for the example 1

A total 6 types of calculations carried out. In the first case, each cable was approximated as a perfectly flexible element. In the second case, each cable was approximated as a one bar element. In the third case, each cable was approximated as a two bar elements and the same was done with 3, 5 and 10 bar elements. Accuracy of calculation was determined by values of residual forces and of kinetic energy of the structures. The calculation was terminated when the kinetic energy of the structure was less than 1.10^{-6} kJ and while residual forces of all the degrees of freedom were less than 0.01 kN. The accuracy of the calculation is approximately ± 0.2 mm. Values of fictitious parameters M and C for all calculations were set to the count of iterations to a minimum. Values of fictitious parameters in all directions and all nodes were identical within one calculation. Self-created scripts in MATLAB 7.11.0 (2010b) was used for all calculations. The calculations were carried out on the computer ACER Aspire 3694WLMi, Intel Celeron M processor 440 (1.86 GHz, H33 MHz FSB, 1 MB L2 cache), memory RAM 512MB DDR2. Summary of selected parameters and results are shown in Tab. 1. It can be seen that the cable can be described very well with five bar elements.

Tab. 1 Summary of selected parameters and results for the example 1

Element	Δt	M	C	Count of iteration	Coordinates z of joint 1	Divergence Δz from the cable element
	[s]	[t]	[t.s^{-1}]	-	[mm]	[%]
cable element	0.1	100	85	151	82.6	-
1 bar element	0.1	100	125	126	91.0	10.2
2 bar elements	0.1	500	170	397	84.2	1.9
3 bar elements	0.1	800	220	518	83.6	1.2
5 bar elements	0.1	1400	235	923	83.0	0.5
10 bar elements	0.1	2900	240	1875	82.8	0.2

3.3. EXAMPLE 2

A suspended cable ring shown in Fig. 3, which has been discussed in [3] and [4], is analysed here to show the accuracy and speed of the computations developed in this study.

The structure consists of 16 cables connected to 16 joints (1-8 are free, A-H are fixed) with an inner radius of 35 m and outer radius of 75 m. The structures have 8 radial cables and 8 tangential cables. All cables have the same cross-sectional area $A = 1.96344 \cdot 10^{-3}$ m^2 and the same Young's modulus $E = 170$ GPa. The slack length s_0 of all radial cables is 40 m, and that of all ring cables is 32 m. Any external node loads acts on the structure. An uniform load $q = 1.5105 \cdot 10^{-1}$ kN/m acts on each cable.

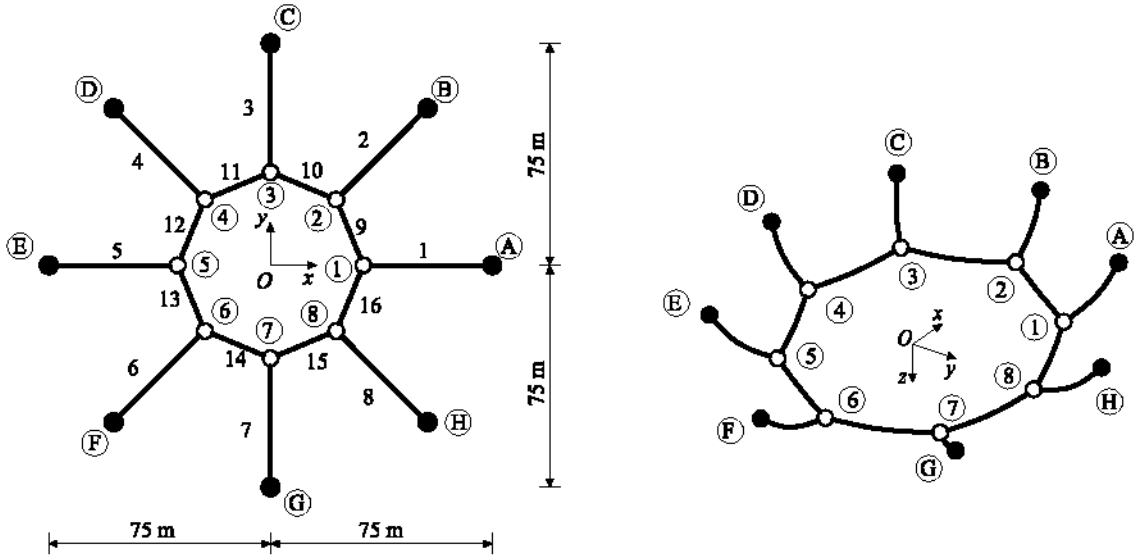

Fig. 3 The geometric schema of the example 2

Terms of calculations are the same as in the example 1. The accuracy of the calculation is approximately ± 1 mm. Coordinates *z* of the unsupported nodes were always set to zero. Joint coordinates, which are obtained by employing the cable elements, at the final equilibrium state are shown in Tab. 2 and correspond to the results in [4].

Tab. 2 Joint coordinates at the final equilibrium state – cable elements

Coor. [m]	Number of joint							
	1	2	3	4	5	6	7	8
x	41.649	29.451	0	-29.451	-41.649	-29.451	0	29.451
y	0	29.451	41.649	29.451	0	-29.540	-41.649	-29.451
z	21.713	21.713	21.713	21.713	21.713	21.713	21.713	21.713

Summary of selected parameters and results are shown in Tab. 3. Again, it is seen that the cable can be described very well with five bar elements. The use of ten or more bar elements is excessively time consuming.

Tab. 3 Summary of selected parameters and results for the example 2

Element	Δt	M	C	Count of iteration	Time of solution	Coordinates of joint 2		Divergence from the cable element	
						x	z	Δx	Δz
	[s]	[t]	[t.s^{-1}]	-	[min]	[m]	[m]	[%]	[%]
cable element	0.1	0,55	1.5	110	0:17	29.451	21.713	-	-
1 bar element	0.1	80	100	250	0:01	29.566	22.331	0.3	2.8
2 bar elements	0.1	200	22	2533	0:01	29.476	21.856	0.1	0.7
3 bar elements	0.1	300	32	5553	0:01	29.460	21.769	0.0	0.3
5 bar elements	0.1	550	28	8861	0:01	29.452	21.725	0.0	0.1
10 bar elements	0.1	1100	32	25575	0:03	29.450	21.708	0.0	0.0
20 bar elements	0.1	2200	30	75974	0:24	29.447	21.701	0.0	0.1

Figures 4 and 5 shows the progress of iteration coordinates of joint 2 in direction z using a cable element (red), and using cutting cable for five bar elements (blue).

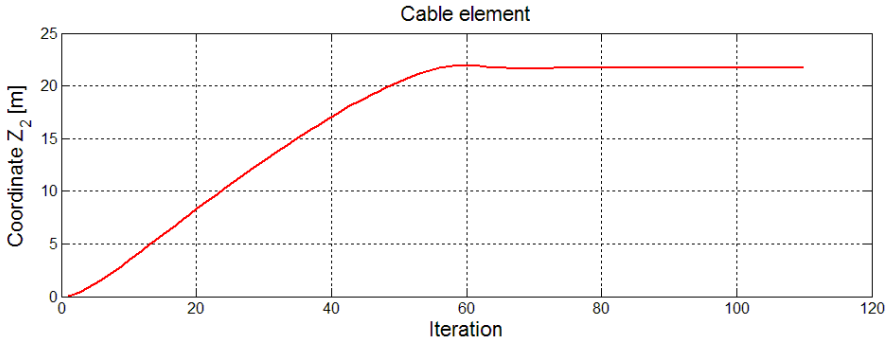

Fig. 4 Cable element – records of the calculation

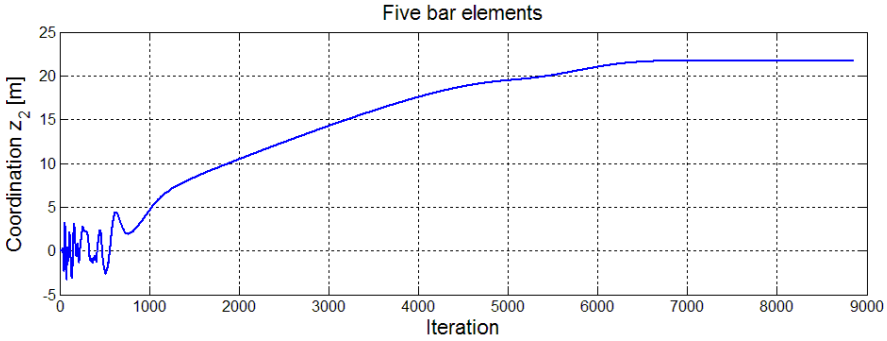

Fig. 5 Five bar elements – records of the calculation

4. CONCLUSION

Conclusions based on these assumptions are tested on the two reference examples. The cables that are loaded with a uniform continuous load without local loads in the joints can be very well approximated by approximately five bar elements. It is guaranteed a very good speed of calculation and sufficient accuracy of the calculation. The use of multiple bar elements has been time consuming.

While the use of a cable element leads to a small number of iterations, the iterative process for solving equations (1) is very time consuming and thus the overall calculation time is much longer than the use of several bar elements. Using of efficient numerical solvers for the solution of equation (1) could reduce the time of solution. Direct numerical solution of cable equation [3], [4], [5] is also possible, because the force *T* would not have to be expressed analytically.

ACKNOWLEDGEMENT

The results presented in this paper are outputs of the research project "P105/11/1529 – Cable - membrane structures analyses" supported by Czech Science Foundation and project "SGS12/027/OHK1/1T/11 – Numerical modelling in mechanics of structures and materials" supported by CTU in Prague.

REFERENCES

[1] Topping, B.H.V., Iványi, P., Computer Aided Design of Cable Membrane Structures, Kippen, Saxe-Coburg Publications, 2008, 233 p., ISBN 978-1-874672-11-1

[2] Kwan, A.S.K., A new approach to geometric nonlinearity of cable structures, In: Computers and Structures, Vol. 67, 1998, iv 4, pp. 243-252, ISSN 0045-7949

[3] Hüttner, M., Analýza lanoplachtové konstrukce, Diplomová práce, Fakulta stavební ČVUT v Praze, 2012, 85 p.

[4] Deng, H., Jiang, Q.F., Kwan, A.S.K., Shape finding of incomplete cable-strut assemblies containing slack and prestressed elements, In: Computers and Structures, Vol. 83 (21-22), 2005, pp. 1767-1779, ISSN 0045-7949

[5] Kadlčák, J., Statika nosných lan visutých stretch, Praha: Academia, 1990, 160 p., ISBN 80-200-0251-0

[6] Fajman, P., Řešení lana s ohledem na jeho deformaci, Stavební obzor, 21 (4), 2012, pp. 105-107, ISSN 1210-4027

[7] Day, A. S., An introduction to dynamic relaxation, In: Engineer, 219, 1965, pp. 218-221, ISSN 0013-8029

[8] Barnes, M. R., Form and stress engineering of tension structures, In: Structural Engineering Review, 6 (3-4), 1994, pp. 175-202, ISSN 0952-5807

EXPERIMENTAL EVALUATION OF THE STRAIN FIELDS IN THE VICINITY OF THE V-NOTCH IN DUCTILE METAL

Ivan JANDEJSEK[1], **Ondřej JIROUŠEK**[2], **Daniel VAVŘÍK**[3]

Abstract: *This work deals with the experimental measurement of full-field displacements and strains evaluation on the surface of flat high-ductile aluminum specimens in the vicinity of the V-notch during loading. Two different specimen geometry configurations, boundary and middle notch, are tested and compared in terms of deformation constraint. The enhanced Digital Image Correlation method in conjunction with strain gage measurement is employed for the precise full-field strain evaluation.*

Keywords: *strain/stress measurement, Digital Image Correlation, fracture mechanics*

1. INTRODUCTION

Precise experimental measurement of strain/stress fields in the vicinity of notches and cracks in high ductile metals such as aluminum alloy is necessary for reliable determination of physical processes accompanying fracture evolution. Amount of plastic deformation can be used for validation of different fracture toughness approaches, verification of FEM models and determination of a suitable material model. Nowadays experimental optical methods provide full-field measurement of displacements and strains of the specimen analyzed. One of these methods is an image processing technique generally known as Digital Image Correlation (DIC), [1]. The technique utilizes a sequence of images that represents a process of a specimen surface deformation. In this sequence DIC observes displacements of individual templates of some pattern employing a correlation technique. The template is a small rectangular part of the pattern that contains a distinguishable distribution of grayscale intensities. Displacement field obtained from this method is utilized for consequent calculation of the strain fields. However, it turns out that the DIC method is error prone when the specimen undergoes even slight rigid body rotations and displacements changing camera-specimen distances during the test. In such cases the consequent changes in magnification cause systematical

[1] Ing. Ivan Jandejsek, Institute of Theoretical and Applied Mechanics AS CR, v. v. i., Prosecká 809/76; 190 00, Prague 9; CZ, e-mail: jandejs@itam.cas.cz

[2] Doc. Ing. Ondřej Jiroušek, PhD.: Institute of Theoretical and Applied Mechanics AS CR, v. v. i., Prosecká 809/76; 190 00, Prague 9; CZ, e-mail: jirousek@itam.cas.cz

[3] Ing. Daniel Vavřík, PhD.: Institute of Theoretical and Applied Mechanics AS CR, v. v. i., Prosecká 809/76; 190 00, Prague 9; CZ, e-mail: vavrik@itam.cas.cz

errors in measured strains. In this study combination of simultaneous optical and strain gage measurement was employed for correction of this error.

One of the DIC method advantage is that one can define an arbitrary grid of vertices at which the particular displacements are measured. Therefore it is beneficial to use the same DIC measurement grid as it is used in the FEM numerical model. This allows direct and easy comparison between experimental and FEM results. Two different specimen geometry configurations, with boundary and middle notches with the same initial notch length, were tested and compared in terms of strain constraint factor and plasticity development.

2. EXPERIMENT

2.1. MATERIAL AND SPECIMENS

Two high-ductile Aluminum alloy (ČSN 424415.21) 2 mm thick flat specimens, one with a symmetric central notch and another with symmetric boundary notches (initial a = 10 mm in both cases), were employed for the fracture experiment. The stress-strain diagram of the material obtained from conventional tension test, chemical composition of the material and its mechanical properties are summarized in Fig. 1.

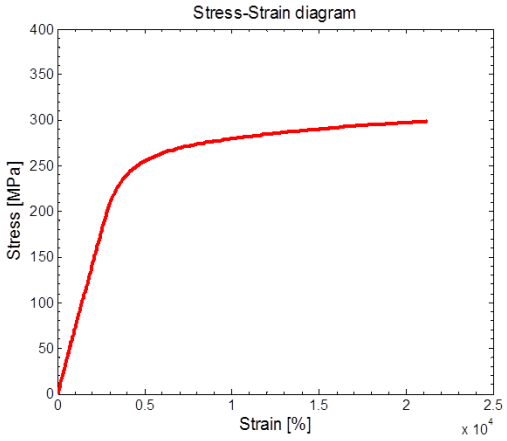

Al-alloy
(ČSN 42 4415.21)

Chemical composition [%]

Al	Cu	Mg	Mn	Si	Fe	Ti	Zn	Cr
94.61	0.03	4.79	0.14	0.12	0.21	0.02	0.01	0.02

Mechanical properties

Modulus of Elasticity E [Mpa]	Poisson ratio ν	Yield point $R_{p0,2}$ [Mpa]
70 600	0.3	252

Fig. 1 Material properties.

The geometry of the specimens tested is depicted in Fig. 2. The V-notches were pre-machined mechanically by the diamond knife and its radius of the tip was under 50 μm. It must be emphasized here that it is very difficult to make an exact sharp pre-crack in such ductile material. Conventional fatigue method here fails because of large plasticity that develops during cycling.

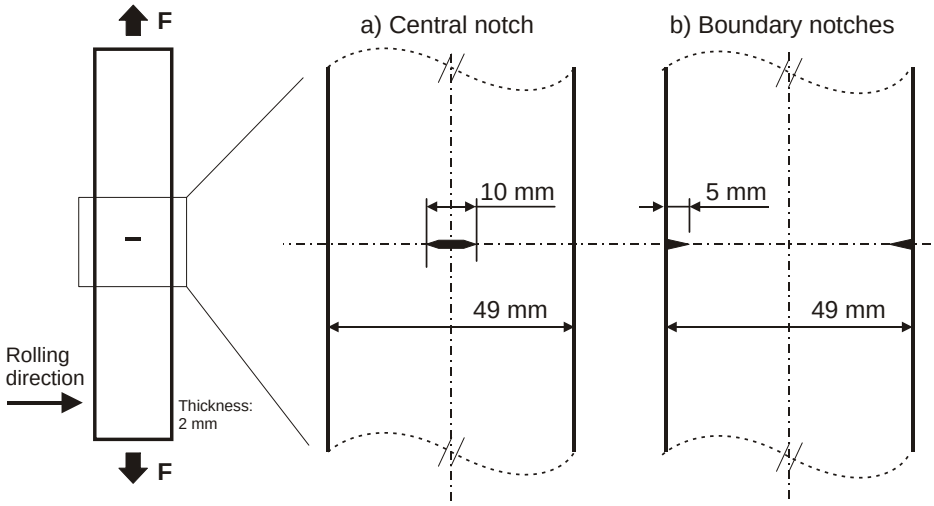

Fig. 2 Specimens geometry and two different notch configurations: Central (a) and Boundary (b) notches (a = 10mm in both cases).

The speckled pattern (black background, white speckles) necessary for DIC measurement was prepared on one side of the specimens using an airbrush gun. Three strain gage rosettes (0°/45°/90°) were installed in the well-defined positions on the opposite side of the specimens; see Fig. 3.

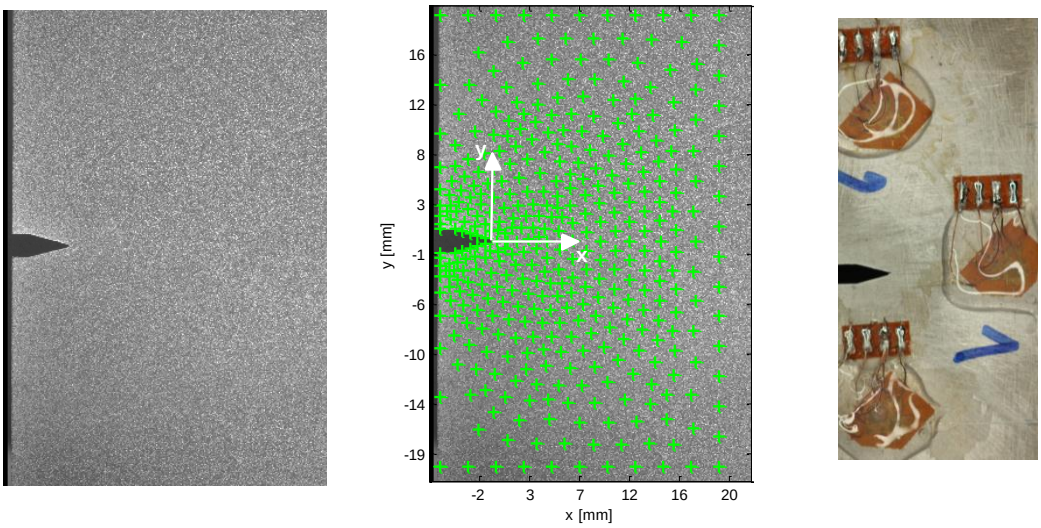

Fig. 3 Speckled pattern necessary for the DIC measurement prepared on the front side of the specimen (boundary notch) that was optically observed (left), triangular mesh (green crosses are the nodes of the mesh) used as the measurement grid for the DIC method (middle), three strain gage rosettes installed on the opposite side of the specimen (right).

These positions were selected for precise measurement of the strains in sufficient distance away from concentrator, where the assumption of relatively small gradients of strains is valid. The strain gages were primary installed to correct influence of slight rigid body motions of the specimen during loading. Such movements which change distance camera-specimen are reflected in the DIC measurement as a systematic error. This systematic error has the form of a linear surface; therefore the

error can be subtracted from results using the knowledge of the correct strains measured at least in three non-collinear positions.

2.2. LOADING TEST

The specimen was subjected to uni-axial tension loading (opening mode I) under the condition of constant grip displacement velocity. Remote force *F* was measured by a load cell with read-out frequency 1 Hz. The resulting load diagrams (Force vs. experiment time) for both specimens are shown in Fig. 4.

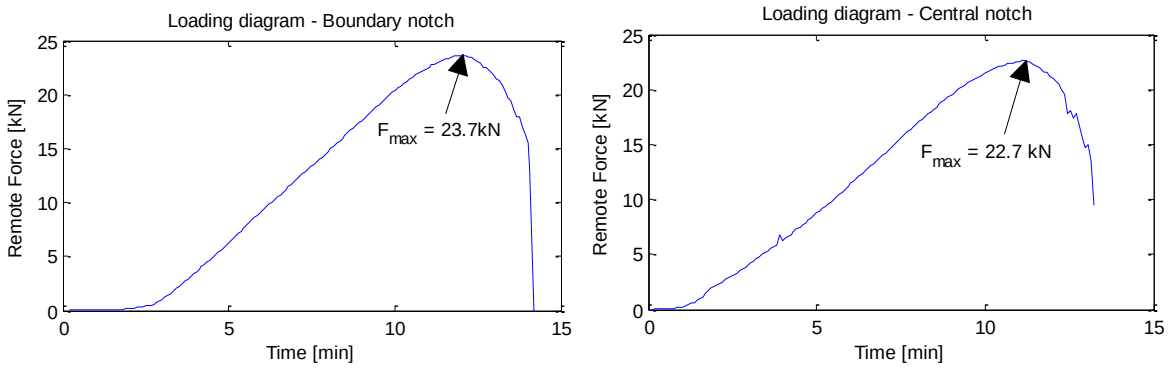

Fig. 4 Loading diagrams: Specimen with boundary notch (left), specimen with central notch (right).

Speckled pattern in the vicinity of the notch (only one half due to the symmetry) was optically observed during the test. The images were acquired by a 15 MPixel camera (Canon EOS500D, Canon Inc., Japan) and a macro-lens (Canon Ultrasonic EF 180mm f/3.5 L, Canon Inc., Japan) with frequency 1 image per 5 sec. during loading until the macroscopic fracture occurred. The surface of the specimen was illuminated by circular diffusion light due to avoidance of reflection artifacts. Images were stored in 3168x4752px RAW format and transformed to gray-scale color space.

2.3. STRAIN EVALUATION

Our own Digital Image Correlation (DIC) system [2] was employed for evaluation of the full-field displacements. A triangular mesh was generated in the ANSYS system using linear triangular (PLANE42) elements. Vertices of the triangular mesh were used as the input points at which displacements were measured using the DIC algorithm. The mesh was adjusted to reflect the presence of the stress concentrator, see Fig. 3 (middle). From the known nodal displacements, strain tensor at every triangular element was computed. For more accurate evaluation of the strains from measured displacements which are unavoidable noisy, a smoothing procedure based on spline function approximation was used. Due to the presence of relatively large strains at the vicinity of the notch tip, the finite Green-Lagrange strain tensor was used instead of conventional infinitesimal (small) strain tensor. Finally, the resulting strains were corrected using values of measured strains from the strain gage rosettes.

2.4. RESULTS

The resulting contour plots of the evaluated principal strains ε_1, ε_2 and its direction angle θ in the vicinity of the notch at maximal remote force for both specimens are shown in Fig. 5 (boundary config.) and Fig. 6 (Central config.). The plots are scaled in the same range so it is clearly visible that specimen with the central notch exhibits higher strains at the state of maximal force which is in consistent with the theory. In other words specimen with the boundary notches exhibits higher constraint factor.

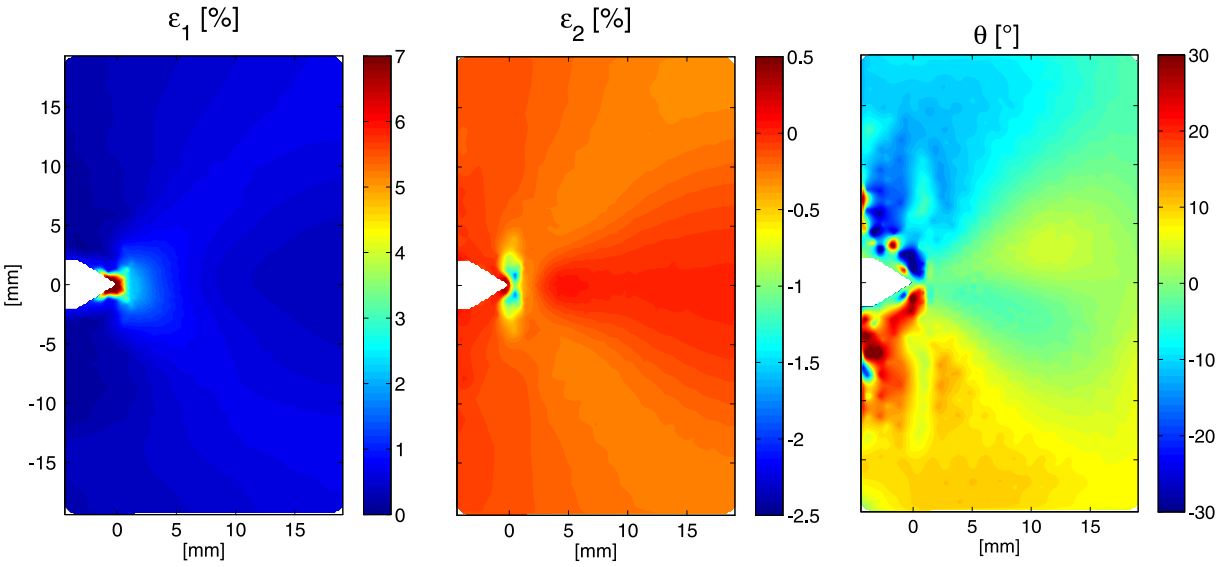

Fig. 5 Resulting principal strains and its direction angle in the vicinity of the boundary notch at maximal remote force F = 23.7kN.

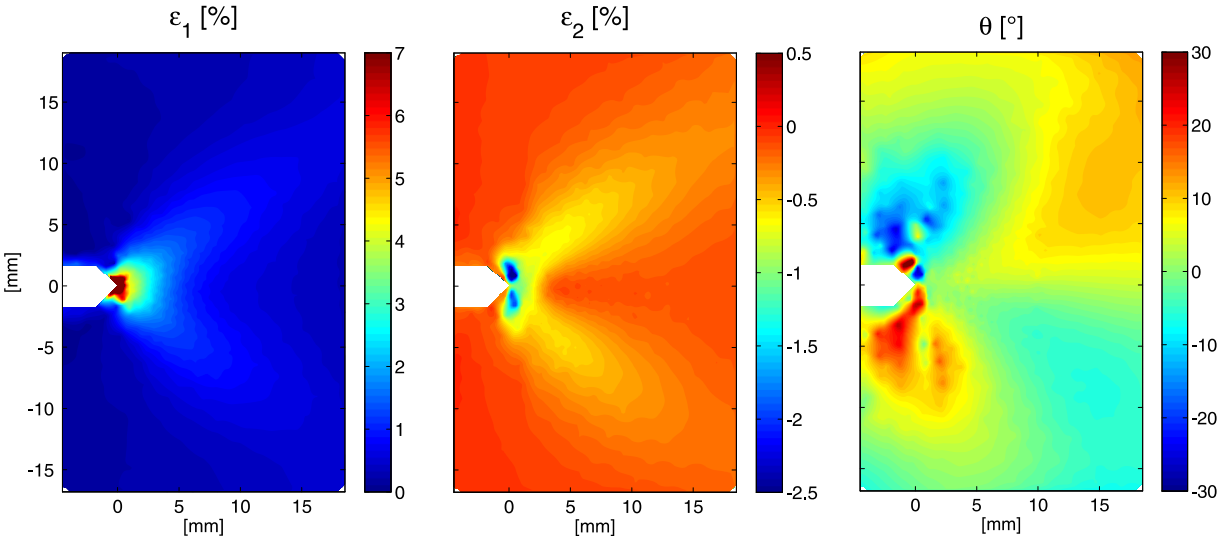

Fig. 6 Resulting principal strains and its direction angle in the vicinity of the central notch at maximal remote force F = 22.7kN.

3. CONCLUSION

It can be concluded, that the above described enhanced DIC method in conjunction with the strain gage measurement enables precise measurement of the full-field strains. The full-field strains were successfully evaluated in the vicinity of the V-Notch in two different geometry configurations. With the help of three non-collinear strain gage rosettes the measurements were corrected for the rigid body movements. Correlation for the rigid-body movement of the specimen during the experiment was found to be very important and limiting aspect of such measurements when strains are measured using DIC. Displacements were measured in a triangular FE mesh to enable direct comparison with FEM results. The comparison of two notch geometry configurations showed that specimen with the boundary notches exhibits less strains (higher constraint factor) and thus less plasticity. However, by using the equivalent stress intensity based on the von Misses yield criterion it was found, that the entire ligament of the specimen was fully plasticized even before the crack initiation in the both cases. Therefore conventional energetic elastic-plastic parameters such as J integral cannot be used and other approaches have to be applied.

ACKNOWLEDGEMENT

The research has been supported by the Grant Agency of the Czech Republic (grant No. P103/09/2101) and by the Grant Agency of the Czech Technical University in Prague (grant No. SGS12/116/OHK1/2T/11).

REFERENCES

[1] Peters, W.H. - Ranson, W.F. *Digital imaging techniques in experimental stress analysis*. Optical Engineering 21, 1982, p.427-431, ISSN 0091-3286

[2] Jandejsek, I. - Valach, J. - Vavřík, D. *Optimization and Calibration of Digital Image Correlation Method*, Proc. Experimental Stress Analysis 2010, Olomouc, 2010, p.121-126, ISBN: 978-80-244-2533-7

[3] Jandejsek, I. - Vavřík, D. *Experimental Methods for Evaluation of the Energy Balance in Vicinity of the Crack*, Proc. Experimental Stress Analysis 2011, Olomouc, 2011, p.135-138, ISBN 978-80-214-4275-7

COMPARISON OF OPTIMAL DESIGNS OF EXPERIMENTS IN APPLICATION TO SENSITIVITY AND INVERSE ANALYSIS

Eliška JANOUCHOVÁ[1], **Tomáš MAREŠ**[2],
Anna KUČEROVÁ[3]

Abstract: *Nowadays the numerical models of structures and materials are more precise, but still time-consuming. Despite the growth of a computational effort, the exploration of model behaviour requires some basic tools. One of them is the sensitivity analysis investigating the sensitivity of the model to its inputs. Another tool often used in inverse analysis is meta-modelling replacing an exhaustive simulation by an approximation. Strategies to assess the sensitivity and/or build an approximation are usually based on a finite set of simulations for a given sets of input parameters, i.e. the design of experiments. This paper reviews criteria defining optimal designs of experiments and compares their quality in sampling-based sensitivity analysis and in neural network training process.*

Keywords: *Design of experiments, optimality criterion, Latin Hypercube Sampling, sampling-based sensitivity analysis, artificial neural network*

1. INTRODUCTION

The increasing complexity of structural or material numerical models makes the exploration of a model response an important area of investigation. Sensitivity analysis (SA) provides some information about the contributions of individual system parameters/model inputs to the system response/model outputs. The presented contribution is focused on sampling-based sensitivity analysis [1], a widely used strategy to assess the sensitivity based on a set of simulations for a given sets of input parameters. These combinations of inputs parameters represent coordinates of points in the design space. An estimate of the sensitivity can be then obtained by computing Spearman's rank correlation coefficient (SRCC) between the input parameters and the corresponding response of the model. The accuracy of the sensitivity prediction depends on the choice of design points called the design of experiments (DoE).

To minimize the number of time-exhaustive simulations, reliable meta-models are usually constructed [2]. The meta-models represent the approximation/interpolation of a model response over the

[1]Bc. Eliška Janouchová , Department of Mechanics, Faculty of Civil Engineering, Czech Technical University in Prague, eliska.janouchova@fsv.cvut.cz

[2] Tomáš Mareš, Department of Mechanics, Faculty of Civil Engineering, Czech Technical University in Prague, tomas.mares.1@fsv.cvut.cz

[3]Ing. Anna Kučerová, Ph.D., Department of Mechanics, Faculty of Civil Engineering, Czech Technical University in Prague, anicka@cml.fsv.cvut.cz

domain of model parameters, the so-called design space. Among frequently used techniques of meta-modelling belong artificial neural networks (ANNs) [3], popular for their simple implementation. They are usually obtained by minimization of their error in a set of design points. The predictability of the resulting meta-model is then driven by the choice of the design points.

In a case of some computationally exhaustive numerical model, the number of samples to be performed within some reasonable time is rather limited. Randomly chosen sets of input parameters do not ensure appropriate estimation of related sensitivities or suitable meta-model approximating a model response. Therefore the design points must be chosen carefully. There are different approaches to generate DoE [4]. This contribution focuses on designs obtained by optimization of some optimality criterion. The aim of the presented paper is to review available criteria for generating DoE and compare suitability of their optimal designs for application in sampling-based sensitivity analysis and in an artificial neural network training process.

2. OPTIMALITY CRITERIA

A number of different criteria for assessing the quality of particular DoE can be found in literature. In general, they can be organized into groups with respect to the preferred DoE property. The most widely preferred features are the *space-filling* property, which is needed in order to allow for evaluation of sensitivities valid for the whole given domain of admissible input values, and the *orthogonality*, which is necessary to assess the impact of individual input parameters.

2.1. SPACE-FILLING CRITERIA

Audze-Eglais objective function (AE) proposed by Audze and Eglais [5] is based on a potential energy among the design points. The points are distributed as uniformly as possible when the potential energy E^{AE} proportional to the inverse of the squared distances among points is minimized, i.e.

$$E^{\mathrm{AE}} = \sum_{i=1}^{n} \sum_{j=i+1}^{n} \frac{1}{L_{ij}^2}\,, \qquad (1)$$

where n is the number of the design points and L_{ij} is the Euclidean distance between points i and j.

Euclidean maximin (EMM) distance is probably the best-known space-filling measure [6]. It states that the minimal distance $L_{\min,ij}$ between any two points i and j should be maximal. In order to apply the minimization procedure to all presented criteria, we minimize the negative value of a minimal distance E^{EMM}, i.e.

$$E^{\mathrm{EMM}} = -\min\{..., L_{ij}, ...\}, \quad i = 1...n, \quad j = (i+1)\,...\,n\,. \qquad (2)$$

Modified L_2 discrepancy ($\mathbf{ML_2}$) is a computationally cheaper variant of a discrepancy measure, which is widely used to assess precision for multivariate quadrature rules [7]. Here, the designs are

normalized in each dimension to the interval $[0, 1]$ and then, the value of ML_2 is computed according to

$$E^{\mathrm{ML}_2} = \left(\frac{4}{3}\right)^k - \frac{2^{(1-k)}}{n} \sum_{d=1}^{n} \prod_{i=1}^{k} (3 - x_{di}^2) + \frac{1}{n^2} \sum_{d=1}^{n} \sum_{j=1}^{n} \prod_{i=1}^{k} [2 - \max(x_{di}, x_{ji})] \,, \qquad (3)$$

where k is the number of input parameters, i.e. the dimension of the design space and x_{di} and x_{ji} are the i-th coordinates of the d-th and j-th points, respectively. To achieve the best space-filling property of DoE, the value of ML_2 should be minimized.

D-optimality criterion (Dopt) was proposed by Kirsten Smith in 1918 [8] as a pioneering work in the field of DoE for regression analysis. This criterion maximizes the determinant of the so-called information matrix ($\mathbf{Z^T Z}$). Again, in order to apply a minimization procedure, we can minimize negative value of the determinant of the information matrix, i.e.

$$E^{\mathrm{Dopt}} = -\det(\mathbf{Z^T Z}) \,, \qquad (4)$$

where $\mathbf{Z}$ is a matrix with evaluated regression terms in the design points.

It is known that under certain conditions, D-optimality criterion leads to the designs with duplicated points. To overcome this problem, the results presented further in this paper are obtained by an approach based on Bayesian modification of an information matrix proposed in [9].

2.2. ORTHOGONALITY-BASED CRITERIA

Conditional number (CN) is commonly used in numerical linear algebra to examine the sensitivities of a linear system [10]. Here, we use conditional number of $\mathbf{X}^T\mathbf{X}$, where $\mathbf{X}$ is a matrix of the design points' coordinates, so-called design matrix

$$\mathbf{X} = \begin{bmatrix} x_{11} & x_{12} & \cdots & x_{1k} \\ x_{21} & x_{22} & \cdots & x_{2k} \\ \vdots & \vdots & & \vdots \\ x_{n1} & x_{n2} & \cdots & x_{nk} \end{bmatrix} , \qquad (5)$$

where n is the number of the design points and k is the dimension of the design space and the columns are centred to sum to 0 and scaled to the range $[-1, 1]$. The conditional number is then defined as

$$E^{\mathrm{CN}} = \mathrm{cond}(\mathbf{X^T X}) = \frac{\lambda_\mathbf{1}}{\lambda_\mathbf{n}} \,, \qquad (6)$$

where λ_1 and λ_n are the largest and smallest eigenvalues of $\mathbf{X}^T\mathbf{X}$, respectively, therefore the E^{CN} is greater or equal to 1. Values closer to 1 correspond to more orthogonal DoE..

Pearson product-moment correlation coefficient (PMCC) is a standard measure of a linear dependence between two variables. In order to obtain orthogonal DoE in a multi-dimensional design space, the PMCC needs to be evaluated for each pair of columns in the design matrix *(5)*. As a result, one obtains a $k \times k$ symmetrical correlation matrix $\mathbf{C}$. In the case of an orthogonal DoE, the correlation

matrix is equal to identity matrix. To achieve an orthogonal DoE, one can, for instance, minimize the sum of squares of the elements above the main diagonal of $\mathbf{C}$ as it is done in engineering software [11] as well as in presented results, i.e.

$$E^{\mathrm{PMCC}} = \sqrt{\sum_{i=1}^{k} \sum_{j=i+1}^{k} c_{ij}^2}\,. \tag{7}$$

Spearman's rank correlation coefficient (SRCC) can be used to capture a nonlinear but monotonic relationship between two variables and therefore, it can be efficiently applied for estimation of correlations in sampling-based SA [1]. The idea is to replace the coordinates by their corresponding ranks. The orthogonality of the DoE can be achieved similarly to *(7)*.

Kendall tau rank correlation coefficient (KRCC) is an alternative measure of a nonlinear dependence between two variables. In particular, it is based on the number of concordant and discordant pairs of samples. The orthogonal DoE can be again obtained similarly to *(7)*.

3. GENERATION OF OPTIMAL DoE

Since the optimization of DoE defined on real domains becomes computationally exhaustive, practical applications are usually restricted to the optimization of the so-called Latin Hypercube (LH) designs [12], where the real domain is divided into disjoint intervals of equal probability and one value is selected from each interval. The discretization itself is quite useful for simplification of the optimization process. Therefore, we focus our attention mainly to the optimization of DoE in discrete domains assuming that continuous domains are usually also discretized so as to make the optimization process manageable. However, it is not obvious, whether such restriction excludes the best solutions regarding the objective of SA or ANN. Hence we compare the LH optimal designs with the free (unrestricted) optimal designs in order to investigate the impact of the LH restriction to results of SA and ANN.

In order to estimate the quality of individual criteria in SA and ANN, we obtained designs having 10 points in two-dimensional discrete domain. Both variables are defined in ten discrete values. Since the designs are not excessively complex, the Simulated Annealing method [13] was applied to optimize each criterion. The optimization process was performed 100 times for each criterion and both types of DoE. Of course, there is no guarantee that the global optimum is achieved, nevertheless, more frequent falls to local extremes also reflect the shortcoming of a particular criterion. Hence, we decided to present the obtained results without any deeper search for more robust and reliable optimization method.

4. MODELS

In engineering practice, the majority of the numerical models fulfil the condition of a monotonic relationship between the model parameters and the model response. Therefore, to support the study of optimal DoE quality in sampling-based SA and ANN training process, we performed the same comparison for a list of nonlinear but monotonic models. In particular, we consider the two-parametric models

with discrete parameters, both with 10 feasible discrete values. The shapes of the chosen models plotted are shown in Fig. 1.

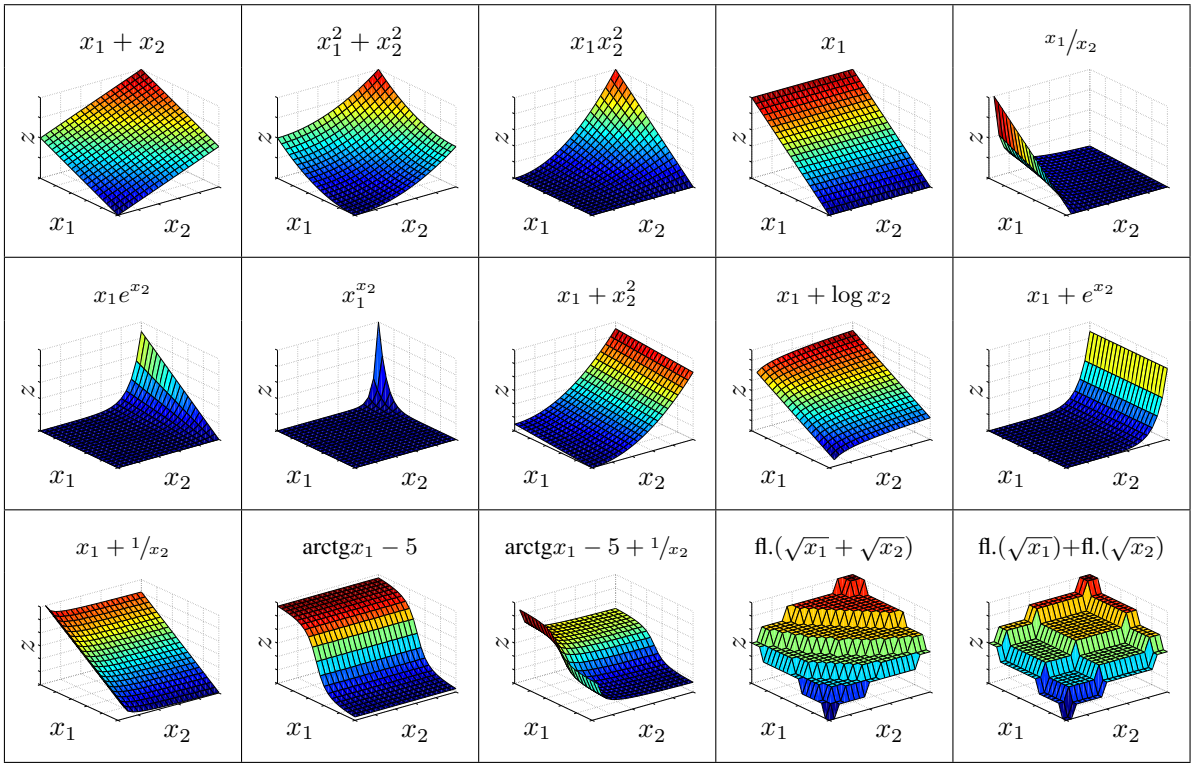

Fig. 1 Shapes of 15 mathematical functions for sensitivity and inverse analysis.

5. SENSITIVITY ANALYSIS

Having the numerical model $z = f(x_1, x_2, \ldots, x_k)$ relating the model response z and the model parameters x_i, the impact of the parameter x_i to the model response z can be estimated by evaluating their Spearman's rank correlation $\rho_{x_i,z}$ [1] according to

$$\rho_{x_i,z} = 1 - \frac{6 \sum_{a=1}^{n} \left(r(x_{ai}) - r(z_a)\right)^2}{n(n^2-1)}\,, \tag{8}$$

where x_{ai} are values of particular model parameter corresponding to points in DoE and z_a are values of model responses corresponding to these points.

Then, the parameter-response correlations were estimated using the all optimal designs and the differences among correlations $\tilde{\rho}$ obtained by the optimal designs and correlations ρ obtained by the full design (consisting of all 100 feasible design points) are stored. The error measure ϵ in the parameter-response correlations evaluated for a given function is considered as an average difference between each parameter and model response correlation obtained by an optimal and a full design, i.e.

$$\epsilon = \frac{1}{k} \sum_{i=1}^{k} \left| \tilde{\rho}_{x_i,z} - \rho_{x_i,z} \right|. \tag{9}$$

The statistics over the obtained values of errors ϵ is presented in Fig. 2 using the box plots.

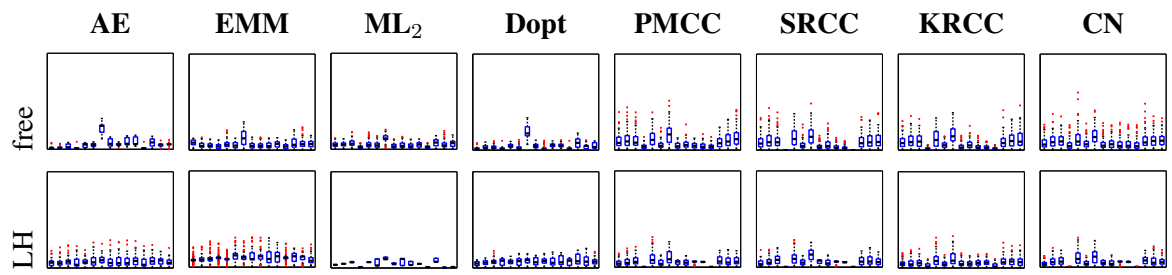

Fig. 2 Statistics on results of criteria in estimating parameter-response correlations. Each rectangle contains 15 *box plots representing the distribution of errors in correlation prediction for particular models depicted in Fig. 1. The scale is* 0 *at the bottom and* 1 *at the top per rectangle. Furthermore, each rectangle refers to the optimal designs according to one criterion associated with the corresponding column and to the chosen type of restriction applied associated with the corresponding row.*

6. INVERSE ANALYSIS - ARTIFICIAL NEURAL NETWORK TRAINING PROCESS

The inverse analysis is based on the combination of a stochastic simulation and an artificial neural network (ANN) [14]. ANN consists of many simple processing elements connected together to multi-layer perceptron. In particular, we used a fully conected feedforward neural network with logistic sigmoid transfer functions. Obtained designs constituted the training data used for calibration of the synaptic weights of the ANN. Simple adaptation algorithm was employed in order to achieve appropriete number of nodes in hidden layer. It starts with one hidden node, performs 10-fold crossvalidation loop and adds another node. This procedure continues until overfitting occures or synaptic weigt limit is met. Resulting architecture was the one with lowest average error on validation sets.

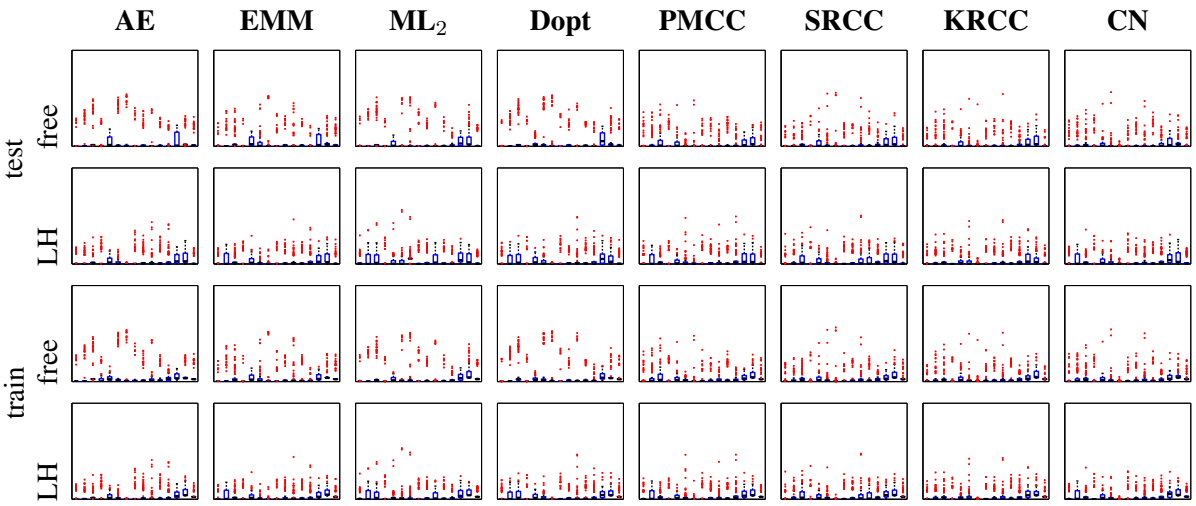

Fig. 3 Statistics on results in NN training process. The box plots are organized similarly as in Fig. 2.

In order to evaluate the quality of created ANNs, the relative errors ε are computed according to

$$\varepsilon = \frac{\sum_{i=1}^{I} |O_i - T_i|}{I(T_{\max} - T_{\min})}, \tag{10}$$

where O_i are the ANN outputs, T_i are the target values, I is the number of samples in a given data set and $T_{\max} - T_{\min}$ is difference of the maximal and minimal target values in testing data set. The statistics over the errors ε is presented in Fig. 3.

7. CONCLUSION

This paper reviews eight optimality criteria defining DoE and compares suitability of their optimal DoEs for usage in sampling-based SA and ANN training process on 15 theoretical models. For an easier evaluation of particular criteria, the mean and maximal errors ϵ in SA and ε in ANN over all models multiplied by 100 are listed in Tab. 1.

Tab. 1 Mean and maximal errors in correlation predictions and neural network training process.

		AE		**EMM**		**ML$_2$**		**Dopt**		**PMCC**		**SRCC**		**KRCC**		**CN**	
		mean	max	mean	max	mean	max	mean	max	mean	max	mean	max	mean	max	mean	max
free	SA	5.9	32.0	6.2	29.4	5.1	20.5	4.5	33.6	8.4	51.4	7.3	48.5	7.5	46.5	8.6	59.9
	NN tr	4.3	54.1	3.6	52.2	3.5	51.2	4.3	53.1	3.0	47.8	2.7	55.9	2.7	54.4	2.8	56.4
	NN test	4.7	53.6	3.6	51.9	3.8	50.9	4.4	52.3	3.5	47.8	3.2	56.4	3.2	50.9	3.3	54.3
LH	SA	6.7	28.9	9.8	31.1	4.5	11.2	6.8	20.3	5.5	31.4	5.8	28.4	5.6	33.0	5.3	30.7
	NN tr	3.2	43.5	3.1	46.4	4.0	56.3	3.3	48.9	3.1	49.4	3.4	50.3	3.0	45.6	3.3	35.9
	NN test	3.2	41.0	3.1	44.1	3.6	53.2	3.2	46.5	3.2	46.4	3.4	47.5	3.1	43.1	3.3	33.0

The overall results can be summarized in several following conclusions:

- The orthogonality-based criteria (CN, PMCC, SRCC and KRCC) provide the free designs with very bad results in SA. The LH designs are more successful, but their results in SA suffer from higher variances. The optimal designs of AE and EMM criteria achieve good results in sensitivity predictions. While the results of EMM criterion are in SA worse than the those of AE criterion. The best results in sensitivity predictions were obtained using the designs optimized with respect to the Dopt and ML$_2$ criteria. The LH restriction has improving effect on ML$_2$ designs in SA, but significantly worsening effect on the Dopt designs.
- The free optimal designs of AE and Dopt criteria have slightly worse results in ANN training process than the designs of other criteria. In contrast to the results in SA, the designs of the orthogonality-based criteria are successful in ANN training process. The results of ANN training process are similar for almost all the criteria in the case of LH designs. The ML$_2$ LH designs surprisingly achieve the worst results.

ACKNOWLEDGEMENT

The financial support of this work by the Czech Science Foundation (project No. 105/11/P370) is gratefully acknowledged.

REFERENCES

[1] Helton, J. C. - Johnson, J. D. - Sallaberry, C. J. - Storlie, C. B. *Survey of sampling-based methods for uncertainty and sensitivity analysis.* Reliab Eng Syst Safe, 2006, Vol 91, pp 1175-1209, ISSN 0951-8320.

[2] Simpson, T. W. - Poplinski, J. D. - Koch, P. N. - Allen, J. K. *Metamodels for Computer-based Engineering Design: Survey and recommendations.* Eng Comput, 2001, Vol 17, No. 2, pp 129-150, ISSN 0177-0667.

[3] Gurney, K. N. *An introduction to neural networks*, UCL Press, London, 2002, ISBN 1857285034.

[4] Janouchová, E. *Návrh experimentů pro stochastickou citlivostní analýzu*, Bakalářská práce, Fakulta stavební ČVUT v Praze, 2012, 85 s.

[5] Audze, P. - Eglais, V. *New approach for planning out of experiments.* Problems of Dynamics and Strengths, 1977, Vol 35, pp 104-107, Zinatne Publishing House.

[6] Johnson, M. - Moore, L. - Ylvisaker, D. *Minimax and maximin distance designs.* J Stat Plan Infer, 1990, Vol 26, No. 2, pp 131-148, ISSN 0378-3758.

[7] Fang, K. T. - Wang, Y. *Number-theoretic Methods in Statistics*, Chapman & Hall, London, 1994, ISBN 0412465205.

[8] Smith, K. *On the standard deviations and interpolated values of an observed polynomial function and its constants and the guidance they give towards a proper choice of the distribution of observations.* Biometrika, 1918, Vol 1/2, pp 1-85.

[9] Hofwing, M. - Strömberg, N. *D-optimality of non-regular design spaces by using a Bayesian modification and a hybrid method.* Struct Multidiscip O, 2010, Vol 42, pp 73-88, ISSN 1615-147X.

[10] Cioppa, T. M. - Lucas, T.W. *Efficient Nearly Orthogonal and Space-Filling Latin Hypercubes.* Technometrics, 2007, Vol 49, No. 1, pp 45-55.

[11] Novák, J., 2011. *Generator of optimal LHS designs SPERM v. 2.0* [online]. [2011] [cit. 2012-03-31]. CIDEAS, CTU in Prague. Available from WWW: <http://www.cideas.cz/ke_stazeni/sperm/>

[12] Iman, R. L. - Conover, W. J. *Small sample sensitivity analysis techniques for computer models, with an application to risk assessment.* Commun Stat Theor M, 1980, Vol A9, No. 17, pp 1749-1842.

[13] Kirkpatrick, S. - Gelatt, Jr. C. - Vecchi, M. P. *Optimization by Simulated Annealing.* Science, 1983, Vol 220, pp 671-680.

[14] Novák, D. - Lehký, D. *ANN inverse analysis based on stochastic small-sample training set simulation.* Eng Appl Artif Intel, 2006, Vol 19, pp 731–740, ISSN 0952-1976.

CONCRETE BRIDGE PIER SUBJECTED TO TRUCK IMPACT

Pavel JIŘÍČEK[1], **Marek FOGLAR** [2]

Abstract: *The paper presents determination of impact loading for the bridge substructure according to European standard EN 1991-1-7. These two methods based on static and dynamic analysis are evaluated and compared with outcomes of the detailed non-linear FEM model of truck impact of a concrete bridge pier. The outcomes are analyzed and conclusions are drawn.*

Keywords: *impact loading, numerical modeling*

1. INTRODUCTION

The European design standard EN 1991-1-7 prescribes two methods for determination of vehicle impact loading. The first simplified method is based on an equivalent static force. The second method is based on accurate input data and requires a special dynamic analysis for evaluating impact loading; therefore, it is ignored in the most cases of the structural arrangement.

Main principles of both methods are described and compared. As an alternative to these methods, a detailed non-linear FEM model of a real truck impact is prepared with usage of AUTODYN software.

2. VEHICLE IMPACT LOADING ACCORDING TO EN 1991-1-7

The European standard EN 1991-1-7 [1] provides procedures for assessing load from impact of road vehicles, trains, vessels etc.

The load can be obtained by:

- Equivalent static load
- Dynamic analysis

[1] Ing. Pavel Jiříček, Department of Concrete and Masonry Structures, Faculty Of Civil Engineering, CTU in Prague; pavel.jiricek@fsv.cvut.cz

[2] Ing. Marek Foglar, Ph.D., Department of Concrete and Masonry Structures, Faculty Of Civil Engineering, CTU in Prague; marek.foglar@fsv.cvut.cz

In the first case, the equivalent static loads are given in a table for transverse and longitudinal direction of traffic, where these forces do not act simultaneously. In the second case, the impact loading should be determined from dynamic analysis which allows getting more accurate value of impact loading. With similar input data the impact loading from the dynamic analysis is 2x higher compared to equivalent static load approach.

3. NUMERICAL MODELING

This part of the paper is focused on application of the procedures described in the previous paragraphs. The utilization of the equivalent static force and the use of the dynamic analysis are compared to a 3D FEM model of a truck impacting a bridge pier.

3.1. DESCRIPTION OF THE ANALYZED BRIDGE

The impact loads are applied on a typical prestressed concrete two span bridge (see Fig. 1 a Fig. 2). The superstructure is connected to a frame pier which is located in the median of a motorway. This bridge was built in 2005 by the joint venture of the companies STRABAG and SMP Construction as a part of the D3 motorway in south from Prague in the Czech Republic. Both the substructure and the superstructure are made of concrete C30/37. The span lengths are 25.750 and 21.735m. The middle pier is assessed to vehicle impact, the effect of the safety barriers is neglected.

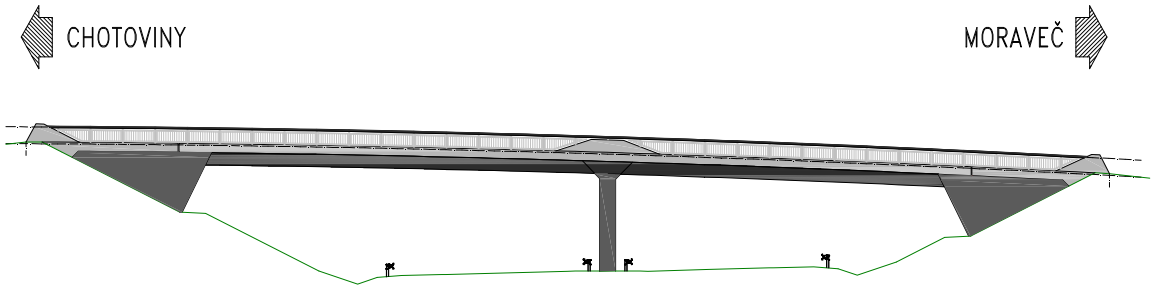

Fig. 1 View of the assessed bridge near Chotoviny

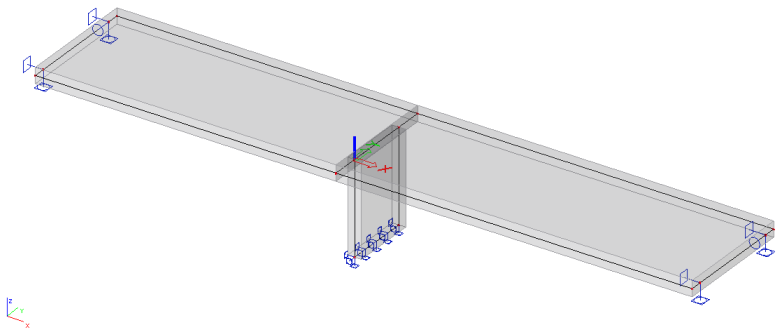

Fig. 2 Schematic slab FEM model of the bridge near Chotoviny

3.2. APPLICATION OF THE EQUIVALENT STATIC FORCE

When using the equivalent static force for assessing a bridge pier subjected to impact load [1], the forces are placed in the most adverse position, but do not act simultaneously. The impact forces are distributed on the center-line of the slab which is modeling the bridge pier.

The effect of the equivalent impact load on the bridge pier is assessed by a linear FEM analysis. The accidental load combination according to EN 1990 [2] is used for combining the effects of self-weight, dead load and traffic load (LM1 according to EN 1991-2 [3]) if it acts adversely.

The shear combined with the effect of torsion is the decisive load case, utilization of the cross-section is 60%, see Table 1.

Tab. 1 Summary of truck impact modeled with the use of the equivalent static force

	Impact direction	Decisive loading	Maximal impact force	Utilization	Dynamic coefficient
Truck Impact	longitudinal	shear	1000.00 kN	60%	×
	transverse	shear	500.00 kN	60%	×

3.3. DYNAMIC ANALYSIS

When using the Appendix C for assessing a bridge pier subjected to impact load [1]. The impact force acts in the direction of the traffic on the motorway.

In the following step, the dynamic system with two degrees of freedom is set up (Fig. 3).

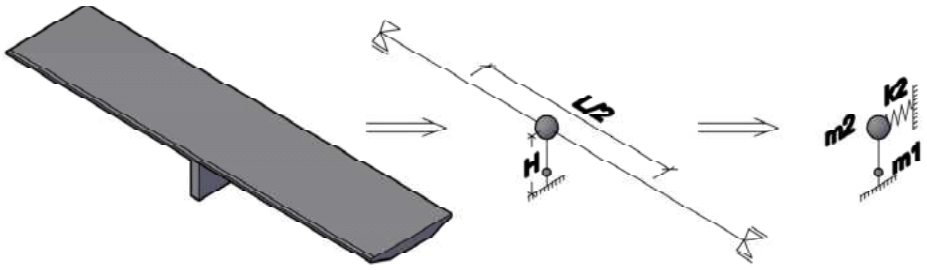

Fig. 3 Setting up the dynamic system of the bridge pier subjected to truck impact

The bridge pier is modeled by a cantilever which is supported by spring on its free end. The stiffness of the spring $k2$ corresponds to the lateral bending stiffness of the superstructure supported at bridge bearings. The mass $m2$ is taken as the mass of the upper half of the bridge pier and the middle part of the superstructure (self-weight + dead load). The mass $m1$ is taken as the mass of the lower part of the bridge pier and is located in the spot of the vehicle impact (1.5 m above the motorway). In the next step, the matrix of docility and the matrix of damping of the dynamic system are prepared

(Rayleigh's damping, damping coefficient taken 7% for reinforced concrete). From the known input values, the dynamic response of the system is obtained with the use of direct integration of the equation of motion (Fig. 4).

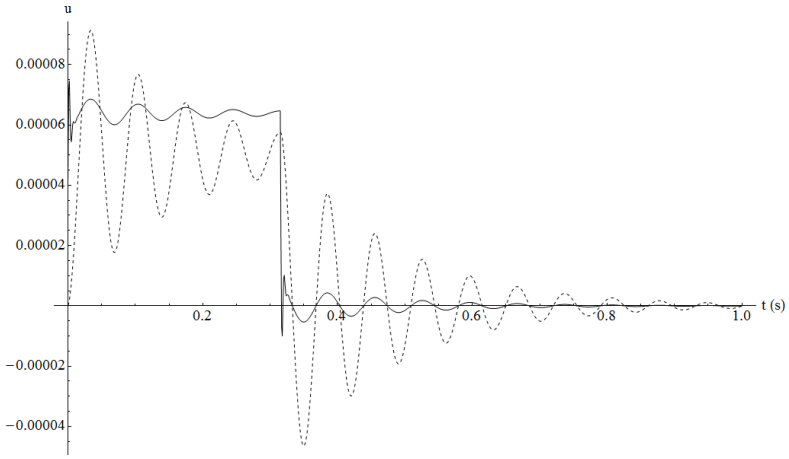

Fig. 4 Dynamic response of the system to the impact load, - - deflection at the top of the bridge pier, — deflection at the spot of the impact

The force couple causing the maximal deflection is determined reversely from the matrix of docility (3038.82;-337.28) [kN]. The 2D model of the bridge pier is then loaded by these forces and the resultant internal forces are determined.

The initial impact force in the direction of the traffic is 2371.7 kN, but the force causing the maximum deflections is 3038.82 kN; the resulting dynamic coefficient is 1.3.

The shear is the decisive load case, utilization of the cross-section is 80%, see Table 2.

Tab. 2 Summary of truck impact modeled with the use of the dynamic analysis

	Impact direction	Decisive loading	Maximal impact force	Utilization	Dynamic coefficient
Truck Impact	longitudinal	shear	3038.82 kN	80%	1.3
	transverse	N/A	N/A	N/A	N/A

3.4. NONLINEAR NUMERICAL ANALYSIS

Unlike both of the procedures for assessing a bridge pier subjected to vehicle impact incorporated in the EN 1991-1-7 [1] which (based on simplifying assumptions) provide impact loading for the structure, the method described in this part aims to model a real truck hitting a bridge pier in full scale and then obtain the impact load reversely. The truck impact model is prepared in the ANSYS AUTODYN software [5].

The truck IVECO Trakker ADN140T50 (Fig. 5) was taken as the hitting vehicle. The 3D computational model was prepared in the RHINOCEROS 4.0 software using 2D and 3D finite elements which represent the decisive structural parts of the vehicle.

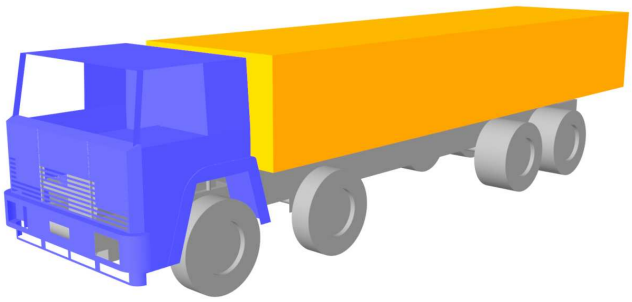

Fig. 5 Computational model of the truck

The FE-model is composed of a main frame carrying the motor, a cab with the bumper and the load of the truck (for achieving the maximum allowable load 32 tons). The material model used for the truck is linear steel without damage (material model with damage would increase the computing time, which is already now at approximately 96hrs). The geometrical model (Fig. 5) is meshed using the Lagrange's network with an element size of 50mm. The vehicle is moved with a speed of 90km/h towards the bridge pier.

The material of the bridge pier was chosen to illustrate its behavior when subjected to blast; the two main aspects are:

- Damage of the material when subjected to ultimate loading

- Increase of the strength (both tensile and compressive) depending on the speed of loading (dynamic increase factor)

The material model RHT for materials with damage was chosen for concrete [4], [5]. This model incorporates the strain-rate effect, which describes the increase of strength with the speed of loading. The concrete bridge pier is modeled without reinforcement; the concrete strength class was taken C30/37. The effect of the safety barriers is neglected. The elements of the pier erode when reaching 100% damage. The elements of the vehicle erode when reaching the ultimate deformation; the erosion increases the energetic instability of the system with the use of Lagrange's network, which sets boundaries to the used element size.

The truck speed at the moment of the impact together with the speed of the vehicle during the impact was taken from the FE model. The total duration of the impact was 334 ms. The acting impact force was obtained from the change of the momentum (Fig. 6), the unlikely local extremes were neglected. The maximum impact force is 5762.65 kN (9707.76 kN local extreme).

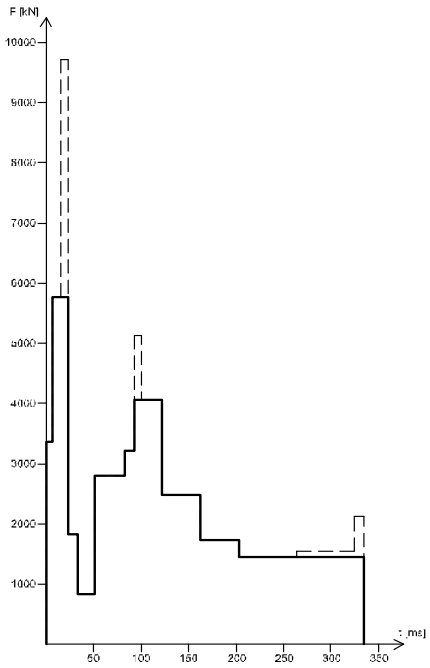

Fig. 6 The acting impact force during the impact, — real time dependence, — the time dependence used in the assessment

With the known course of the impact force the same procedure as in the previous part is used.

From the known input values, the dynamic response of the system is obtained with the use of direct integration of the equation of motion. The force couple causing the maximal deflection is determined reversely from the matrix of docility (6471.64;-580.75) [kN] (Fig. 7). The 2D model of the bridge pier is then loaded by these forces and the resultant internal forces are determined.

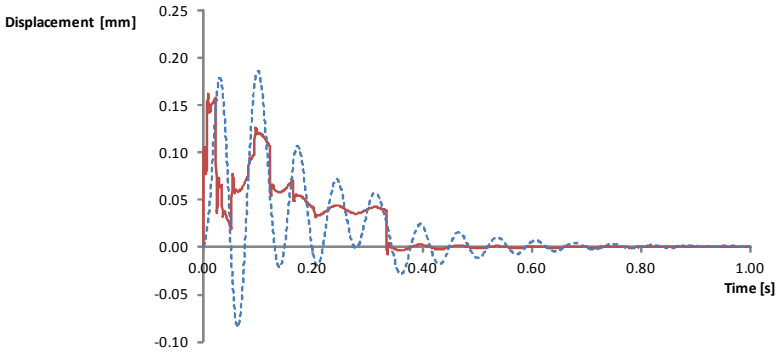

Fig. 7 Dynamic response of the system to the real truck impact load, — deflection at the top of the bridge pier, — deflection at the spot of the

The initial impact force in the direction of the traffic is 5762.65kN (9707.76 kN local extreme), but the force causing the maximum deflections is 6471.64 kN (10802.05 kN local extreme); the resulting dynamic coefficient is 1.12).

As in the previous chapter, shear is the decisive load case, utilization of the cross-section is 170% (280% for the local extreme), *see Table 3.*

Tab. 3 Summary of truck impact modeled with the use of a real vehicle

	Impact direction	Decisive loading	Maximal impact force	Utilization	Dynamic coefficient
Truck Impact	longitudinal	shear	6471.64 kN	170%	1.12
	transverse	N/A	N/A	N/A	N/A

This method compiles two completely different approaches, non-linear FEM model with cross-sectional assessment according to current design standards. Therefore FEM model in ANSYS AUTODYN was modified to get more precise impact process. After the main impact (the velocity of the vehicle is 0 km/h), damaged pier was loaded with traffic load LM1. Under LM1 loading damage of the pier slightly progresses, but stops at approximately 50% (Fig. 8). It means that damaged pier resists incidental traffic on the bridge.

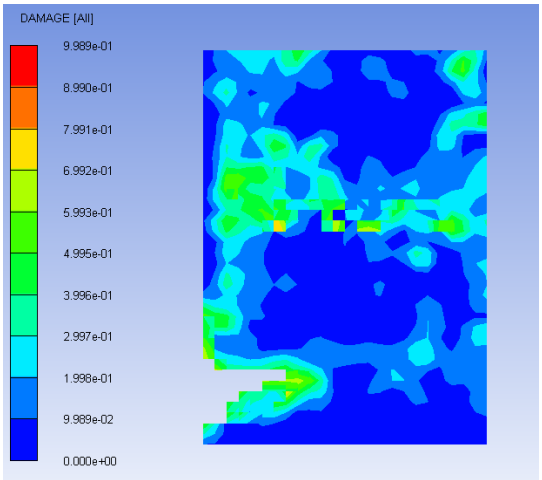

Fig. 8 Damaged pier loaded with traffic after impact

4. COMPARISON AND DISCUSSION

This paper describes three different methods of evaluating vehicle impact of bridge substructure. The first two prescribed by design standard EN 1991-1-7 are based on determination of equivalent static loading and dynamic analysis. In both cases resistance of the pier cross-section to impact loading is satisfactory. Simplified approach based on equivalent static loading provides impact force three times smaller than obtained by dynamic analysis.

As an option for these two methods, a full-scale non-linear FEM model of impacting truck was prepared. From change of momentum during the 334 ms long impact the acting loading was

calculated. Impact force obtained by detailed FEM model is two times higher than in case of dynamic analysis and six times higher than equivalent static force. Resistance of concrete cross-section of bridge pier is not satisfactory in case of loading bridge pier with force obtained by FEM model.

It is obvious that compiling non-linear and linear approaches is not suitable, therefore damaged pier was subsequently loaded with traffic load case LM1. In this case, its residual bearing capacity was verified, resistance of damaged bridge pier is satisfactory.

5. CONCLUSION

Full scaled model of impact compared to dynamic analysis described in modern design standards leads to approximately similar results. Time of impact itself is in both cases about 325 ms, deceleration could be taken as linear. Therefore the value and time dependence are about the same. Generally speaking, more precise method described in current design code corresponds more to real vehicle impact than simplified method based on equivalent static force.

ACKNOWLEDGEMENT

This paper was supported by the Czech Ministry of Industry and Trade project FR-TI3/531 and Czech Technical University project No. 12/029/OHK1/1T/11.

REFERENCES

[1] ČSN EN 1991-1-7, Zatížení konstrukcí, Obecná zatížení – Mimořádná zatížení, Praha: ÚNMZ, 2007.

[2] ČSN EN 1990, Zásady navrhování konstrukcí, Praha: ÚNMZ, 2007.

[3] ČSN EN 1991-2, Zatížení konstrukcí, Zatížení mostů dopravou, Praha: ÚNMZ, 2005.

[4] CEB-FIP Model Code 1990. Comité Euro-International du Béton, 1993

[5] AUTODYN Manuals, Chapter 9: Material models. Sam Ramon, 2009.

[6] Rossi, P., van Mier, J.G.M., Toutlemonde, F., Effect of loading rate on the strength of concrete subjected to uniaxial tension, Mater. Struct., 27, 1994, pp. 260-264.

[7] Rossi, P., Strain rate effects in concrete structures: LCPC experience, Mater. Struct., 1997, pp. 54-62.

[8] Brannon, R.M., Leelavanichkull, S., Survey of four damage models for concrete, Sandia National Laboratories, 2009.

[9] Georgin, J.F., Reynouard, J.M., Modeling of structures subjected to impact: concrete behaviour under high strain rate, Cement & Concrete Composites, 25, 2003, pp. 131-143.

BIOMECHANICAL EFFECTS OF THE INTERACTION SURFACES OF DENTAL IMPLANTS WITH VITAL TISSUE

Alice KAPKOVÁ[1]

Abstract: *Biomechanical attribute of the implant and his surface on the interface with vital tissue has significant role with covering his long-term stability. Improvement of the interaction with tissue, speed-up of the healing process and long-term quality integration of the implant in the bone tissue could be reached for example with using suitable material of the stem, application of the microporous surface lamella and biodegradable layers with culture of the bioactive compounds, or different kinds of plasma modifications.*

Keywords: *Implant, Titanium, Biocompatibility.*

1. INTRODUCTION

Dental implantology is specialization which deals with implement of the biocompatible material on the bone surface or into the upper or bottom jawbone, with holding of this material in this environment and with production of the special constructed fixed or removable denture which are used for the teeth function recovery and for the returning of the comfort and original look for partly or completely toothless patients [1]. It's known, that for human organism it is difficult to accept foreign substance and this is the reason for strive the approach to the origin material in the denture composite development. Implant has to be made from the acceptable material for the human body. One of the most serious problems is immune reaction of the organism which cause healing or non-healing of the implant. The most important presumption of the successful healing is biocompatibility of the material. This means that the material attribute with specific application has to be tolerated by living organism. Living organism always recognizes presence of the foreign substance and reacts on it with safety reactions led by immune system. The highest biocompatibility between implantation materials has the ceramic materials. Their nature in the human body is bio-inert or even bio-active. We can differentiate in bio-active materials implanted into the bone tissue osseoinductive and osseoconductive substances. For dental implants which are exposed to the high chewing pressure and to the extract-power effect meets the requirement on the mechanical endurance especially metals. But metals aren't mostly able to meet the chemical requirements. One of the possibilities how to combine advantageous attributes of the particular materials is to cover the metal material with protective layer. Then we can use advantageous mechanical attributes of the metals with optimal chemical attributes of BioCeramics.

[1] Ing. Alice Kapková, Department of Mechanics, Faculty of Civil Engineering, CTU in Prague; alice.kapkova@fsv.cvut.cz

One of the most known BioCeramics is calcium hydroxyapatite. Coating with hydroxyapatite is still contested so the new solutions of the physical technology or chemical modification of titanium which should increase the quality of osseointegration and speed up its creation are in development. Objections against coating with hydroxyapatite are due to behaviour of the coating in the long-term aspect. The main question is the stability of the hydroxyapatite in biological environment. Theses authors conclude after consideration of the information published in available literature, that the quality of the hydroxyapatite coating aren't enough analyzed yet so the current level of knowledge doesn't authorize to pronouncing the final judgment. It can't be excluded, that the negative rating of the coated implants has also significant commercial context. Coating brings undisputed advantages, but also covers risk. It can't be clearly determined without detailed analysis and introduction of the context, which surface is the right one. In any case, it is clear on the base of the published studies, that the micro-structured surfaces of the new age implants has important role in the osseointegration process.

2. MATERIAL CLASSIFICATION

Material aspect is important and defining in the dental implantology. Selection of the implant material is limited by mechanical and physical attributes which are currently quite clearly specified and evaluable. The general problem of metallic materials intended for compensation of human hard tissues is a high modulus of elasticity compared to the bone. A significant difference in modulus of elasticity can cause insufficient tension transfer to the surrounding tissue ("stress shielding effect"), which may lead to the later bone resorption and ultimately to loss of the implant. Efforts to eliminate the "stress shielding effect" is accompanied by a longer period of development both in material area and in technology area, where new methods and procedures for the production of modified materials and their surfaces including setting appropriate geometrical parameters are searched [2 - 7].

There were set following requirements for dental implants material based on long experience and systematic research:

- It has to be harmless for the tissue and the whole body (non-toxic, free antigens, non-radioactive).
- It may be biologically tolerant and stable. It can't interfere the metabolism and cause the resorption of the bone nest, cause the reaction of the organism on the foreign substance or be subject of biodegradation.
- It may be enough strong in terms of mechanical and physical and it may be electrochemically stable.
- It has to be radiopaque and satisfactory in terms of aesthetics and oral hygiene.
- There may be not any technical obstructions with shaping and sterilization.
- All these requirements may be fulfilled while keeping affordability.

There are three groups of materials in terms of dental implants:

1. hydroxyapatite ceramics
2. tri- and tetra-calcium ceramics
3. bioactive glass ceramics

3. BIOCOMPATIBILITY

Implantation is defined as a surgery, in which inorganic or organic material, dead and living tissue is transferred. Biological effect is besides mechanical and physical attributes also important for implant materials, which means reactions of the organism from molecular to macroscopic level. Mutual reaction between non-autogenous material and vital biological tissue is called biocompatibility. Implant material is divided in terms of biocompatibility for bio-tolerant, bioactive and bio-inert. The biological response of a bone is the most important in terms of dental implantology.

It applies a number of processes:

- Osseogenesis – origin, evolution, growth and the remodeling of the bone
- Osseoinduction – initiation of osseogenesis
- Osseoaffinity – the bone adhesion during osseogenesis
- Osseoconduction – leading of the osseogenesis in certain way
- Distance Osseogenesis – the healing of the implant leads to the surface resorption of the bone and to creation of the variously thick connective fibrous tissue, which leads to fibrointegration
- Contact Osseogenesis – there isn't creation of the connective fibrous layer typical for distance osseogenesis, occurs to osseointegration
- Detention Osseogenesis – there is creation of the chemical bond between implant and tissue without interstitial connective layer [1]

4. THE SURFACE OF INTRAOSSEAL PART

One of the most studies areas in dental implantology is the issue of surface treatment of dental implants. The purpose of the research teams and manufacturers have begun to actively deal with implants surface is clearly an effort to influence the rate of formation active bone-implant interface and to ensure maximum stability of the implant at an early stage of implementation. The aim of researchers is to find the perfect system with quality osseointegration and long-term functionality. Trend in the area of surface modifications is bioactive materials that accelerate the healing process and ensure actively the creation of strong connections between bone tissues and implant surface. The original, alkali-treated bioactive surface accelerates the creation of functional bone-implant interface and provide to the implant increasing secondary stability in the earliest stages of healing. This

phenomenon reduces healing time and allows safe, early and immediate workload. The implant surface modification is moving in two directions, either we will supply the coating – additive modification (titanium plasma spraying, electrochemical coating with bioactive materials), or we will form the surface remove microscopic particles with etching or sandblasting (subtractive modification).

The problem with additive method is the joint imperfection between the added material with the original surface – when roughening the surface by taking, there is a contamination of the microstructures with the particles of the material used for the roughening – that means the abrasives and acids. After the abrasion a precise phase of decontamination must be performed in order to remove all chemical components involved in each phase of production. If the decontamination wouldn't be performed precisely, the amount of titanium molecules on the surface would be so reduced that the oseointegration couldn't perform on an acceptable level due to the contamination. The opinion on the best implant surface varies a lot. The structure of contact with the bone may not be the same in all the area. The success of implementation is highly influenced by the surface of the fixture, but the quality and the reliability can be evaluated after a long term period (years) with clinical studies.

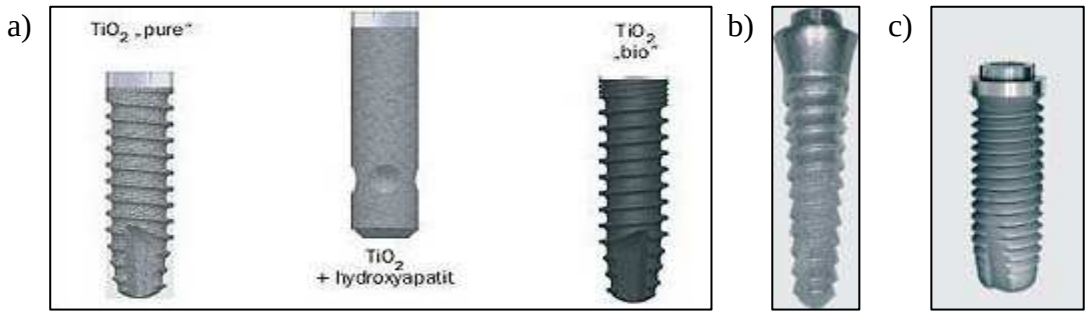

Fig.1. a) Different surface modification of enosseal implants [8]; b) Compress Implant System – the surface modified by coating with hydroxyapatite [9]; c) Hexatec Implant System – the surface is modified with combination of sandblasting with high quality corundum (>99% AI203 = aluminum oxide) and etching [9].

5. TITANIUM

Titanium is the first choice in materials used for dental implantology mainly for its biocompatibility and mechanical qualities. Machine cut and seamless titanium is considered as bio-inert material where the soft tissues encapsulates it and has direct contact with the bone (osseointegration) only in specific conditions and after a long time period. Since the discovery of osseointegration the history of dental implantology has been guided with the attempt to modify the surface of titanium with the aim to bring the reactivity closer to the bio-active materials and make the creation of functional interface between the dental implant and bone possible in the fastest way [10]. Titanium is used in production of detachable prosthetics, root pins etc. It is also highly resistant against corrosion as it forms a stable layer of oxides in its surface – the passivation layer that is able to regenerate in nanoseconds after it

has taken some damage. Pure titanium and alloys with aluminum and vanadium (Ti-6Al-4V) have very good mechanical properties (high strength, low module of flexibility, low weight). Pure titan can be found in 4 grades (grade 1-4) on the market, which differ in the content of oxygen (0.18-0.40%) and iron (0.20-0.50%). The amount of these admixtures has a significant impact on the properties of titanium material. Titanium is the most respected metal bio-material nowadays. Bio-active materials form a biologically active apatite layers and ensure a quicker healing to the implanted replacement, which is desirable by the patient.

Experimental and mainly clinical widely documented results have confirmed that for example dental implants with bio layer significantly speed up and improve the process of osseointegration and optimize the stability of the implant in the early critical period of healing, which leads to a more accurate prediction and success of the treatment and enables the usage of new progressive clinical methods, which can reduce the time needed for treatment. Surface modifications used in the process of preparation of bio-surface significantly increase the density of hydroxyle groups on the surface of the implants and therefore they increase the level of hydration of bio surface when compared to other similar commercial products. Chemical modification of bio surface on a nano level changes the surface to be highly hydrophilic and enables an active interaction with the blood plasma much sooner than the first osteogenetic cells settle down on the surface. Excellent wettability of the surface enables a quick penetration of blood in the complex structure of bio surface. The company LASAK developed an original 3-dimensional modification of the surface that combines mechanical and chemical modifications creating a unique micro macro and nano bio-active titanium surface. The bio surface stimulates the establishment of osteogenetic cells, supports the differentiation and synthesis of bone matrix, which leads to a higher contact of the bone and the implant in reduced time [10].

Fig.2. Bio surface (implant Impladent – Lasak Company, Czech Republic [10])

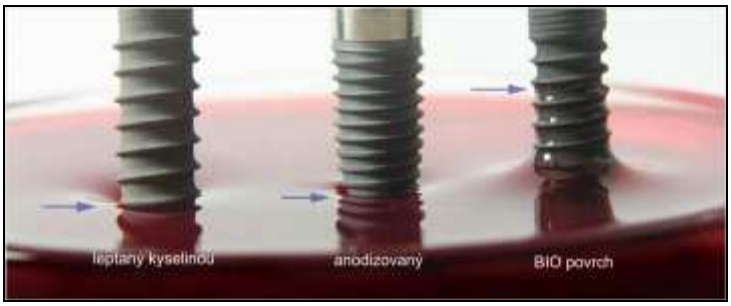

Fig.3. Hydrophilic BIO surface [10]

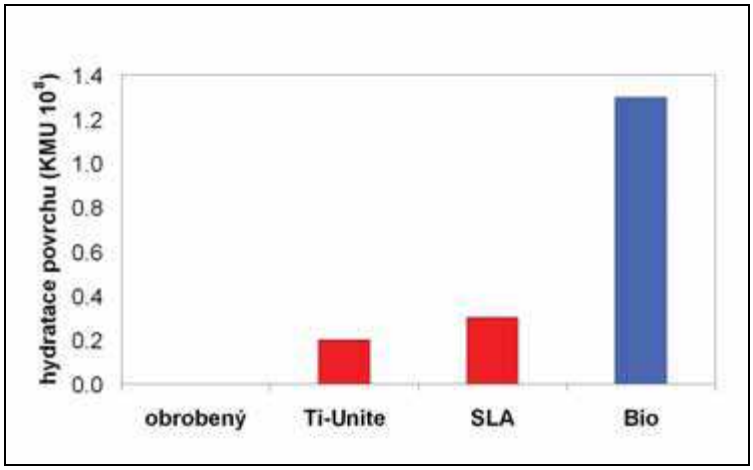

Fig. 4. Level of hydration Bio implant in comparison with other tested surfaces [10]

6. CONCLUSION

Dental implantology is young and became an undisputed part of stomatology. There are certain changes in the basis implantology techniques. For practical reasons there are more immediate or deferred implantations even by the multiroot teeth replacements. Some implant systems are based on a 1-phased implantation. The success of the healing phase is so high that it moved out of focus. A lot of attention is given to the surface structure of the fixtures.

Coating with hydroxyapatite is still challenged and new technologies of physical and chemical modifications of titanium are being developed to increase the quality of oseointegration and speed up its creation. Objections against coating are referring mainly to the behavior of the coating in longer period of time. The stability of hydroxyapatite in biological environment is challenged the most. Coating brings a lot of advantages but contains also some risks. The quality of coating material is not explored enough. Without a detailed analysis and detailed references there is no clear statement which surface (layer) is the most suitable. In any case, on the basis of published studies it is clear that microstructured surfaces of the new generation are very important in the process of oseointegration.

The overall success of oseoimplantation is influenced by many factors and the concrete surfaces cannot be evaluated before the final success. The state of the bone in the area of future implant is much more significant.

Not only the global, but the Czech dental market offers a lot of types of dental implants and implant systems. Implant systems can be divided into several concepts in regard to the method of implantation. There are systems used only for one period term protocol, double period term protocol or concepts enabling them both. Each implant system concept is represented also by the art of joining the fixture with the abutment.

Some implant systems are offering several types of fixtures with different shapes. Material is another attribute in line which is stated in every implant system. The vast majority of implants are

produced from titanium of a titanium alloy. A new product is in development – a nanostructured technically pure titanium (nTi), that excels with the mechanical properties e.g. high strength and a high level of gliding. Pure titanium is also marked with additional information (e.g. Grade 2, Grade 4 etc.) that classifies the material in regard to its composition [9].

ACKNOWLEDGEMENT

The financial support of this experiment by the Faculty of Civil Engineering, Czech Technical University in Prague (SGS project No. SGS12/117/OHK1/2T/11) is gratefully acknowledged.

REFERENCES

[1] Summer, D.R., Turner, T.M., Igloria, R., et al., Functional adaptation and ingrowth of bone vary as a function of hip implant stiffness, Journal of Biomechanics, 31, 1998, pp. 909-917, ISSN 0021-9290.

[2] Di Narda, F., In vitro testing with osteoblastic cellular lines in order to evaluate adhesion, proliferation and differentiation on the synthegra surface compared to surfaces roughened through traditional methods, [online], [cit. 20-9-2012], available from: <http://www.synthegra.it/uploads/files/countdown3.pdf>

[3] Hubálková, H., Krňoulová, J., Materiály a technologie v protetickém zubním lékařství. Praha: Galén, 2009, ISBN 978-80-7262-581-9.

[4] Huiskes, R., Weinans, H., van Rietbergen, B., The relationship between stress shielding and bone resorption around total hip stem and the effects of flexibile materials, Clinical Orthopaedics and Related Research, 1992, pp. 124-134, ISSN 0009-921X.

[5] Ihde, S., Goldman, T., Himmlova, L., et al., The use of finite element analysis to model bone – implant contact with basal implants, Oral Surgery Oral Medicine Oral Pathology Oral Radiology and Endodontology, 106, 2008, pp. 39-48, ISSN 1079-2104.

[6] Kong, L., Zhao, Y.Z., Hu, K.J., et al., Selection of the implant thread pitch for optimal biomechanical properties: A three – dimensional finite element analysis, Advances in Engineering Software, 40, 2009, pp. 474-478, ISSN 0965-9978.

[7] Sumner, D.R., Turner, T.M., Igloria, R., et al., Functional adaptotion and ingrowth of bone vary as a fiction of hip implnant stiffness, Journal of Biomechanics, 31, 1998, pp. 909-9l7, ISSN 0021-9290.

[8] Mazánek, J., Holakovský, J., Dentální implantologie, [online], [cit. 21-6-2006], available from:<http://zdravi.e15.cz/clanek/priloha-lekarske-listy/dentalni-implantologie-173944>

[9] Kokšal, L., Implantologické systémy v zubnom lekárstve - Podrobné špecifikácie – IV, [online], [cit. 24-2-2009], available from: <http://www.stomateam.sk/index.php?clanek=209>

[10] Lasak, Implantáty a kostní regenerace, [online], available from: <http://www.lasak.cz/storage/get/357-2012-01_capability-brochure_cz_web.pdf>

[11] Šimůnek, A. a kol., Dentální implantologie, Nucleus Hradec Králové, 2008, 285 p., ISBN 978-80-87009-30-7.

[12] Apaticko, C.,Gil, F.J., Fonseca, C.,et al., Corrosion behaviour of commercially pure titanium shot blasted with different materials and sizes of shot particles for dental implant applications, Biomaterials, 2003,24, pp. 263-273, ISSN 0142-9612.

[13] Ellison, B., Cheney, N.A., Berend, K.R., et al., Minimal stress shielding with a Mallory – Head titanium femoral stem with proximal porous coating in total hip arthroplasty. Journal of Orthopaedics Surgery Research, 4, 2009, pp. 42, ISSN 1749-799X.

[14] Filip P.: *Progresivní typy biomateriálů*, Skripta VŠB - TU Ostrava, 1995, 118 p., ISBN 80-7078-273-0.

[15] Hench, L.L, Sprinter, R.J., Allen, W.C., Greenlee, T.K., Bonding mechanism at the interface of ceramic prosthetic materials, J.Biomed. Mater. Res. Symp. 2, 117, pp. 197, ISSN 15-16-1439.

[16] Krishna, B. V., Bose, S. and Bandyopadhyay, A., Low stiffness porous Ti structures for load – bearing implants. Acta Biomaterialia, 2007, 3, pp. 997-1006, ISSN 1742-7061.

[17] Massaro, C., Rotolo, P., De Riccardis, F., Milella, E., Napoli, A., Wieland, M., Textor, M., Spencer, N.D., Brunette, D.M., „Comparative investigation of the surface properties of commercial titanium implants. Part I: chemical composition", J. Mater. Sci.: Mater. Med, 13, 2002, pp. 535-548, ISSN 0957-4530.

[18] Meijer, G. J., Starmans, F. J. M., Deputter, C., et al., The Influence of a Flexibile Coating on the Bone Stress around Dental Implants. Journal of Oral Rehabilitation, 19995, 22, pp. 105-11, ISSN 0305-182X.

[19] Morra, M., Cassinelli, C., Bruzzone, G., Carpi, A., Di Santi, G., Giardino, R., Fini, M., "Surface chemistry effects of topographic modification of titanium dental implant surfaces: 1. Surface Analysis", Int. J. Oral Maxillofac. Implants, 18, 2003, pp. 40-45, ISSN 2158-3706.

[20] Piattelli, A., Trisi, P., Passi, P., Piattelli, M., Cordioli, G.P., „Histochemical and confocal laser scanning microscopy study of the bone-titanium interface: an experimental study in rabbits", Biomaterials, 15, 1994, pp. 194-200, ISSN 0142-9612.

[21] Šimůnek, A., a kol., Dentální implantologie, Nukleus, 2001, 192 p., ISBN 80-86225-15-1.

[22] Walboomers, X. F., Habraken, W. J. E. M., Feddes, B., et al., Stretch – mediated responses of osteoblast – like cells cultured on titanium – coated substrates in vitro, Journal of Biomedical Materials Research Part A, 69, 2004, pp. 131-139, ISSN 1549-3296.

[23] Petruželka, J., Dluhoš, L., Hrušák, D., Sochová, J., Nanostrukturní titan – nový materiál pro dentální implantáty, Česká stomatologie, 106, 2006, pp. 72-77, ISSN 1213-0613.

MODELING OF FRESH CONCRETE CASTING USING XFEM

Filip KOLAŘÍK[1], **Bořek PATZÁK**[2]

Abstract: *Modeling of fresh concrete flow is interesting problem from both theoretical and practical point of view and its application to self compacting concrete casting simulations is a subject of active research with important practical aspects. Practical importance is especially in application to self compacting concrete, which is highly actual. It is usually modeled in eulerian description of motion as a problem of two immiscible fluids (concrete as a Bingham fluid and air as a Newtonian fluid). Due to different physical properties of these fluids, there are discontinuities of velocity and pressure fields at the interface. In this paper, the eXtended Finite Element Method (XFEM) is used allowing the standard FE approximation space with tailor made functions across the interface to resolve the discontinuities.*

Keywords: *flow, concrete, XFEM, Bingham model, level set*

1. INTRODUCTION

This paper deals with eXtended Finite Element Method (XFEM) and its implementation in flow problems. Especially, it is focused on its application to fresh concrete flow. In modeling of flow problems using standard Finite Element Method (FEM) fluid is usually considered as a single homogeneous continuous medium. There are in principle three ways, how to describe the motion of continuous medium. In Lagrangian description, motion of each point is described in the framework of reference configuration. This approach, usually used in structural mechanics, is not suitable for fluid description, because of large deformations which require frequent re-meshing. In Eulerian description the motion is connected to actual configuration and therefore convective term is present and the Navier-Stokes equations governs the motion of the fluid. In this case, computation can be done on a fixed grid and no re-meshing is needed. On the other hand, one needs to use some stabilization due to convective terms and also LBB condition has to be satisfied. The advantages of both approaches have been combined in Arbitrary Lagrangian Eulerian formulation which is often used to model fluid-structure interactions. In the present work, Eulerian formulation is used. Modeling of fresh concrete flow in the context of Eulerian formulation is typically done using so called immiscible fluids concept (as a free surface flow), first proposed in [1]. For example, in case of fresh concrete flow, one fluid represents concrete and the other

[1]Ing. Filip Kolařík , Department of Mechanics, Faculty of Civil Engineering, CTU in Prague, Thákurova 7, 166 27, Prague; CZ, filip.kolarik@fsv.cvut.cz

[2]Prof. Dr. Ing. Bořek Patzák , Department of Mechanics, Faculty of Civil Engineering, CTU in Prague, Thákurova 7, 166 27, Prague; CZ, borek.patzak@fsv.cvut.cz

one represents air. Since both fluids are immiscible, the interface between them can be always captured. There are different possibilities, how to track the interface. In FEM context, Volume Of Fluid, see [2] and level-set method [3], [4] are suitable choices. Since the flow is modeled using XFEM, the level-set method is used in this work. The level-set method describes interface as a zero level set of higher dimensional function. Usually, that function is chosen as a signed distance function. Motion of the interface is then governed by simple convective equation. Extended Finite Element Method enriching the standard continuous approximation of velocity and pressure fields by discontinuous enrichment functions along the interface is then used to discrete governing equations.

2. GOVERNING EQUATIONS

As was mentioned before, problem is described by Navier-Stokes equations. In this work, only 2D flow is considered. Let $\Omega \subset R^2$ be open set with boundary $\partial\Omega$. Boundary $\partial\Omega$ is decomposed to four mutually disjoint parts Γ_D, Γ_N, $\Gamma_{SWF}$and Γ_{OUT}, on which we prescribe Dirichlet boundary condition, Neumann boundary condition, so called "slip with friction" boundary condition, "penetration with resistance" [5] and so called "do nothing" boundary condition. The whole problem can be formulated as follows:

$$\rho\frac{\partial \boldsymbol{u}}{\partial t} + \rho\left(\boldsymbol{u}\cdot\boldsymbol{\nabla}\right)\boldsymbol{u} - \boldsymbol{\nabla}\cdot\boldsymbol{\sigma} - \rho\boldsymbol{b} = \boldsymbol{0} \qquad \text{in } \Omega \tag{1}$$

$$\boldsymbol{\nabla}\cdot\boldsymbol{u} = 0 \qquad \text{in } \Omega \tag{2}$$

$$\boldsymbol{u} = \boldsymbol{g} \qquad \text{on } \Gamma_D \tag{3}$$

$$\boldsymbol{u} = \boldsymbol{h} \qquad \text{on } \Gamma_N \tag{4}$$

$$\boldsymbol{u}\cdot\boldsymbol{t} + \beta^{-1}\,\boldsymbol{n}\cdot(\boldsymbol{\tau} - p\boldsymbol{\delta})\cdot\boldsymbol{t} = 0 \qquad \text{on } \Gamma_{SWF} \tag{5}$$

$$\boldsymbol{u}\cdot\boldsymbol{n} + \alpha\,\boldsymbol{n}\cdot(\boldsymbol{\tau} - p\boldsymbol{\delta})\cdot\boldsymbol{n} = 0 \qquad \text{on } \Gamma_{SWF} \tag{6}$$

$$\boldsymbol{n}\cdot(\boldsymbol{\tau} - p\boldsymbol{\delta}) = 0 \qquad \text{on } \Gamma_{OUT}. \tag{7}$$

Unknown fields are then velocity $\boldsymbol{u}$ and pressure p. Density ρ, body forces $\boldsymbol{b}$ and functions $\boldsymbol{g}$ and $\boldsymbol{h}$ are prescribed. Parameters β and α in equations (5) and (6) are assumed to be constant. Outer normal vector to the boundary is denoted as $\boldsymbol{n}$, tangent vector as $\boldsymbol{t}$. Standard decomposition of stress tensor $\boldsymbol{\sigma}$ into deviatoric stress $\boldsymbol{\tau}$ and hydrostatic pressure p is used. Strain rate tensor (8) is defined as symmetric part of velocity gradient:

$$\boldsymbol{D} = \frac{1}{2}\left(\boldsymbol{\nabla}\boldsymbol{u} + (\boldsymbol{\nabla}\boldsymbol{u})^T\right). \tag{8}$$

Constitutive law for air can be considered as one-parameter (viscosity μ) Newtonian fluid (9). It is well known that fresh concrete flow can be described by at least two parameters. The first one is yield stress τ_0 which introduces minimal stress necessary for concrete flow. The second parameter, plastic viscosity, μ_{pl} governs the main flow. Despite its simplicity, practical simulations have proved, that it

is a suitable choice for describing fresh concrete behavior. The Bingham model (10) is described by following equations:

$$\boldsymbol{\tau} = \mu \boldsymbol{D} \tag{9}$$

$$\begin{cases} \boldsymbol{\tau} = \left[\mu_{pl} + \frac{\tau_0}{\sqrt{\boldsymbol{J_2^e}}} \right] \boldsymbol{D} & ; |\boldsymbol{J_2}| \leq \tau_0 \\ \boldsymbol{D} = \boldsymbol{0} & ; |\boldsymbol{J_2}| \geq \tau_0 \end{cases} \tag{10}$$

where $\boldsymbol{J_2^e}$ is the second invariant of deviatoric strain tensor and $\boldsymbol{J_2}$ is second invariant of deviatoric stress tensor, which is defined as:

$$\boldsymbol{J_2} = \frac{1}{2} \boldsymbol{\tau} : \boldsymbol{\tau} \tag{11}$$

The second invariant of strain rate tensor is defined similarly.

3. DESCRIPTION OF THE INTERFACE

Generally speaking, there are two major approaches for description of the interface. So called interface tracking and interface capturing methods. First group of methods uses deforming mesh to track the interface and describes the interface in explicit manner. As it was mentioned before, in flow problems it is usual to use fixed grid and describe the motion in eulerian sense. Therefore, interface capturing methods have been developed in [3].They describes the interface in some implicit sense. One of the most often used methods of this group is so called level-set method which is applied in this work as well. In this method, interface is represented as a zero level set of some scalar function ϕ. Here, ϕ has been chosen as a signed distance function, which is defined by following property:

$$\phi(\boldsymbol{x}) = \pm \min_{\boldsymbol{x}^* \in \Sigma} ||\boldsymbol{x} - \boldsymbol{x}^*|| \tag{12}$$

The sign in the definition depends on which fluid occupies the point x, Σ denotes the interface between both fluids. Since the interface is changing in time, the level-set representation has to be updated at each time step. Motion of the interface is governed by level-set transport equation:

$$\frac{\partial \phi}{\partial t} + \boldsymbol{u} \cdot \boldsymbol{\nabla} \phi = 0 \qquad \text{in } \Omega \text{ x } [0, T] \tag{13}$$

where $\boldsymbol{u}$ is convective velocity of the fluid. Of course, to solve (13), the proper boundary and initial conditions are needed.

4. SPATIAL DICRETIZATION AND XFEM

Since both fluids in our model have different physical properties (density and viscosity), there are discontinuities in velocity and pressure fields along the interface. In general, one can distinguish between two types of discontinuities: strong and weak discontinuities. Strong discontinuity is present when there is a jump in a function. Weak discontinuity arises, when there is a jump in derivative of the function. Example of both types of discontinuities is typically two phase flow with surface tension, where the jump in pressure field (strong discontinuity) and jump in derivative of velocity field, or jump in strain rate tensor (weak discontinuity) occur. Proper description of discontinuities in terms of standard FEM is impossible because functions from approximation space are continuous. It is possible to refine mesh in sub-domains where one expects some discontinuities in the solution. In the case of two phase flow, such a solution is not efficient because the interface is evolving in time and therefore frequent re-meshing would be necessary. Contrary to this, treatment of discontinuities is very easy and natural using XFEM. The main idea behind XFEM is to enrich approximation space with tailored global (defined in whole domain) functions which can describe discontinuities in the solution. Choice of these functions depends on solved problem and on our a priori knowledge of solution. In our case, approximation of unknown function in XFEM has following form:

$$\boldsymbol{u^h}(\boldsymbol{x},\boldsymbol{t}) = \underbrace{\sum_{i\in I} N_i(\boldsymbol{x})\boldsymbol{u_i}(\boldsymbol{t})}_{standard\ FE\ approx.} + \underbrace{\sum_{i\in I^*} M_i(\boldsymbol{x})\boldsymbol{a_i}(\boldsymbol{t})}_{enrichment} \tag{14}$$

where $N_i(\boldsymbol{x})$ is standard FE shape function belonging to node i, I is the set of all nodes in computational domain Ω, $M_i(\boldsymbol{x})$ is enrichment function belonging to node i and I^* is the set of enriched nodes (which is subset of I). Note, that enrichment function $M_i(\boldsymbol{x})$ is defined as multiplication of proper global shape function, which stores "the knowledge" behind enrichment and "partition of unity" (PU) function:

$$M_i(\boldsymbol{x}) = N_i(\boldsymbol{x})[\psi(\boldsymbol{x}) - \psi(\boldsymbol{x_i})] \qquad \forall \text{ i} \in I^* \tag{15}$$

In (15), ψ is so called global enrichment function, which is defined on whole domain Ω and $N_i(\boldsymbol{x})$ is standard FE shape function. In general, one can use any set of functions with PU property instead of FE shape functions. Note, that global enrichment function ψ is "shifted" to ensure Kronecker-δ property hold. In two phase flow, when interface is described by level-set method, the enrichment functions for strong (16) and weak (17) discontinuities can be constructed easily as:

$$\psi_{sign}(\boldsymbol{x}) = sign(\phi(\boldsymbol{x})) = \begin{cases} -1 & : \phi(\boldsymbol{x}) \leq 0 \\ 0 & : \phi(\boldsymbol{x}) = 0 \\ 1 & : \phi(\boldsymbol{x}) \geq 0 \end{cases} \tag{16}$$

for strong discontinuity and

$$\psi_{abs} = abs(\phi(\boldsymbol{x})) \tag{17}$$

for weak discontinuity. As was proposed in [6], enrichment function in form 17 can leads to sub-optimal convergence because of presence of parasite terms in blending elements (elements in which only some nodes are enriched). In this paper, so-called "Ramp function", first published in [6], is used to overcome problems in blending elements.

Modeling of fresh concrete flow is a two fluid problem without the surface tension. Therefore, both velocity and pressure fields are enriched by "abs-enrichment" function. Namely:

$$\boldsymbol{u^h(x,t)} = \sum_{i \in I} N_i(\boldsymbol{x}) \boldsymbol{u_i(t)} + \sum_{i \in I^*} N_i(\boldsymbol{x}) \left[abs(\phi(\boldsymbol{x})) - abs(\phi(\boldsymbol{x_i})) \right] \boldsymbol{a_i(t)} \tag{18}$$

$$p^h(\boldsymbol{x},t) = \sum_{i \in I} N_i(\boldsymbol{x}) p_i(t) + \sum_{i \in I^*} N_i(\boldsymbol{x}) \left[abs(\phi(\boldsymbol{x})) - abs(\phi(\boldsymbol{x_i})) \right] b_i(t) \tag{19}$$

Provided that proper function spaces are defined, see [7], weak formulation of (1) - (7) states as follows: find $\boldsymbol{u^h} \in S_u^h$ and $p^h \in S_p^h$ such that $\forall \boldsymbol{w^h} \in V_u^h, \forall q^h \in V_p^h$:

$$\begin{aligned} &\int_\Omega \rho \boldsymbol{w^h} \frac{\partial \boldsymbol{u^h}}{\partial t} d\Omega + \int_\Omega \rho \boldsymbol{w^h} \cdot (\boldsymbol{u^h} \cdot \boldsymbol{\nabla u^h}) d\Omega + \int_\Omega \boldsymbol{\nabla w^h} : \boldsymbol{\tau(u^h)} d\Omega - \int_\Omega \boldsymbol{w^h} \cdot p^h d\Omega \\ &- \int_\Omega \boldsymbol{w^h} \cdot \boldsymbol{b} d\Omega - \int_{\partial\Omega} \boldsymbol{w^h} \cdot (\boldsymbol{\tau} - p\delta) \cdot \boldsymbol{n} dS + \int_\Omega q^h \boldsymbol{\nabla} \cdot \boldsymbol{u^h} d\Omega \\ &+ \sum_{el} \left[\int_{\Omega_e} \tau_{SUPG} (\boldsymbol{u^h} \cdot \boldsymbol{\nabla w^h}) \cdot \left(\rho \frac{\partial \boldsymbol{u^h}}{\partial t} + \rho \boldsymbol{w^h} \cdot (\boldsymbol{u^h} \cdot \boldsymbol{\nabla u^h}) - \boldsymbol{\nabla} \cdot \tau(\boldsymbol{u^h}) + \nabla p^h - \boldsymbol{b} \right) d\Omega_e \right] \\ &+ \sum_{el} \left[\int_{\Omega_e} \tau_{PSPG} \frac{1}{\rho} \nabla q^h \cdot \left(\rho \frac{\partial \boldsymbol{u^h}}{\partial t} + \rho \boldsymbol{w^h} \cdot (\boldsymbol{u^h} \cdot \boldsymbol{\nabla u^h}) - \boldsymbol{\nabla} \cdot \tau(\boldsymbol{u^h}) + \nabla p^h - \boldsymbol{b} \right) d\Omega_e \right] \\ &+ \sum_{el} \left[\int_{\Omega_e} \tau_{LSIC} \boldsymbol{\nabla} \cdot \boldsymbol{w^h} \rho \boldsymbol{\nabla} \cdot \boldsymbol{u^h} d\Omega_e \right] = 0 \end{aligned} \tag{20}$$

Terms in the first two lines follows from standard Galerkin discretization, the third line represents stabilization term due to convection effects, the fourth line provides PSPG stabilization for elements not satisfying LBB condition and the last line provides another stabilization in higher velocity flow.

Stabilization parameters $\tau_{SUPG}, \tau_{PSPG}, \tau_{LSIC}$ are chosen according to [7]. Note, that in that work, finite elements linear in both velocity and pressure were used and therefore terms with $\boldsymbol{\nabla \cdot \tau}$ vanishes. Moreover, due to relatively small flow velocity of concrete, only PSPG stabilization is needed, because linear element does not satisfy the LBB condition.

Level-set function, as a scalar function, is discretized by the same shape functions as pressure:

$$\phi^h(\boldsymbol{x}) = \sum_{i \in I} N_i(\boldsymbol{x}) \phi_i \tag{21}$$

5. TEMPORAL DISCRETIZATION AND SOLUTION SCHEME

After spatial discretization, we have system of non-linear ordinary differential (in time) equations, which has in general form:

$$(\boldsymbol{M} + \boldsymbol{M_\delta})\,\boldsymbol{a} + (\boldsymbol{N(u)} + \boldsymbol{N_\delta(u)}) + (\boldsymbol{K} + \boldsymbol{K_\delta})\,\boldsymbol{u} + \boldsymbol{K_\mu u} + (\boldsymbol{G} + \boldsymbol{G_\delta})\,\boldsymbol{p} = \boldsymbol{F} + \boldsymbol{F_\delta} \tag{22}$$

$$\boldsymbol{G^T u} + \boldsymbol{M_\epsilon a} + \boldsymbol{N_\epsilon(u)} + \boldsymbol{K_\epsilon u} + \boldsymbol{G_\epsilon p} = \boldsymbol{E} + \boldsymbol{E_\epsilon} \tag{23}$$

Terms $\boldsymbol{M}, \boldsymbol{N(u)}, \boldsymbol{K}, \boldsymbol{G}, \boldsymbol{F}, \boldsymbol{E}$ in (22) and (23) follows from standard Galerkin discretization and represents time dependent term, convective term, diffusive term, term connected to pressure and terms represents boundary conditions. Terms with δ subscript are due to the SUPG stabilization, terms with ϵ are due to the PSPG stabilization and $\boldsymbol{K_\mu}$ follows from LSIC stabilization.

5.1. IMPLEMENTATION ASPECTS

As an example of implementation, construction of mass matrix and diffusion matrix will be presented. The acceleration term (see (20)) can be rewriten using (18) at the element level into matrix form as:

$$\int_\Omega \rho \boldsymbol{w^h} \frac{\partial \boldsymbol{u^h}}{\partial t} d\Omega \quad \rightarrow \quad \int_\Omega \boldsymbol{N^T} \rho \boldsymbol{N} d\Omega \boldsymbol{r_a} \tag{24}$$

where $\boldsymbol{N}$ is extended matrix of shape functions at the element. Assuming we have a linear element and that all nodes of are enriched. Than $\boldsymbol{N}$ has the following form:

$$\begin{pmatrix} N_1 & 0 & N_2 & 0 & N_3 & 0 & \vdots & M_1 & 0 & \vdots & M_2 & 0 & \vdots & M_3 & 0 \\ 0 & N_1 & 0 & N_2 & 0 & N_3 & \vdots & 0 & M_1 & \vdots & 0 & M_2 & \vdots & 0 & M_3 \end{pmatrix} \tag{25}$$

In this extended aproximation matrix, $\boldsymbol{N_i}$ represents standard FE shape function and $\boldsymbol{M_i}$ represents additional aproximation to capture the discontinuity. In case of "abs-enrichment", $\boldsymbol{M_i}$ has the following form:

$$M_i(\boldsymbol{x}) = N_i(\boldsymbol{x})\,[\psi(\boldsymbol{x}) - \psi(\boldsymbol{x_i})] = N_i(\boldsymbol{x})\,[abs(\phi(\boldsymbol{x})) - abs(\phi(\boldsymbol{x_i}))] \tag{26}$$

Similraly the diffusion term can be rewritten as:

$$\int_\Omega \boldsymbol{\nabla w^h} : \boldsymbol{\tau}(\boldsymbol{u^h}) d\Omega \quad \rightarrow \quad \int_\Omega \boldsymbol{B^T D B} d\Omega \boldsymbol{r_u} \tag{27}$$

where $\boldsymbol{B}$ is extended matrix containing derivatives of shape functions. Assuming again that we have linear approximation of velocity and two of the nodes are enriched, enriched $\boldsymbol{B}$ matrix looks as follows:

$$\begin{pmatrix} N_{1,\boldsymbol{x}} & 0 & N_{2,\boldsymbol{x}} & 0 & N_{3,\boldsymbol{x}} & 0 & \vdots & M_{1,\boldsymbol{x}} & 0 & \vdots & M_{2,\boldsymbol{x}} & 0 & \vdots & M_{3,\boldsymbol{x}} & 0 \\ 0 & N_{1,\boldsymbol{y}} & 0 & N_{2,\boldsymbol{y}} & 0 & N_{3,\boldsymbol{y}} & \vdots & 0 & M_{1,\boldsymbol{y}} & \vdots & 0 & M_{2,\boldsymbol{y}} & \vdots & 0 & M_{3,\boldsymbol{y}} \\ N_{1,\boldsymbol{y}} & N_{1,\boldsymbol{x}} & N_{2,\boldsymbol{y}} & N_{2,\boldsymbol{x}} & N_{3,\boldsymbol{y}} & N_{3,\boldsymbol{x}} & \vdots & M_{1,\boldsymbol{y}} & M_{1,\boldsymbol{x}} & \vdots & M_{2,\boldsymbol{y}} & M_{2,\boldsymbol{x}} & \vdots & M_{3,\boldsymbol{y}} & M_{3,\boldsymbol{x}} \end{pmatrix} \tag{28}$$

Here, $N_{1,\boldsymbol{x}}$ is derivative of standard shape function (with respect to $\boldsymbol{x}$) and $M_{1,\boldsymbol{x}}$ id derivative of enriched approximation.

5.2. SOLUTION SCHEME

Solution scheme introduced in [8] can be described as follows:

1. Temporal discretization by generalized mid-point scheme.

$$\begin{aligned} \boldsymbol{a^{t+\Delta t}} &= \boldsymbol{a^t} + \boldsymbol{\Delta a} \\ \frac{\boldsymbol{u^{t+\Delta t}} - \boldsymbol{u^t}}{\Delta t} &= \alpha \boldsymbol{a^{t+\Delta t}} + (1-\alpha)\boldsymbol{a^t} \\ \boldsymbol{p^{t+\Delta t}} &= \boldsymbol{p^t} + \boldsymbol{\Delta p} \end{aligned} \tag{29}$$

2. Evaluation (prediction)

$$\begin{aligned} \boldsymbol{u} &= \boldsymbol{u^t} + \boldsymbol{\Delta a^t} \\ \boldsymbol{a} &= \boldsymbol{a^t} \\ \boldsymbol{p} &= \boldsymbol{p^t} \end{aligned} \tag{30}$$

3. Computing of velocity and pressure increments

$$\begin{aligned} \boldsymbol{M^* \Delta a} - \boldsymbol{G^* \Delta p} &= \boldsymbol{R} \\ (\boldsymbol{G^T})^* \boldsymbol{\Delta a} + \boldsymbol{G_\epsilon \Delta p} &= \boldsymbol{Q} \end{aligned} \tag{31}$$

where

$$
\begin{aligned}
&\boldsymbol{M^*} = \boldsymbol{M} + \boldsymbol{M_\delta} + \alpha\Delta t \left(\frac{\partial \boldsymbol{N}}{\partial \boldsymbol{u}} + \frac{\partial \boldsymbol{N_\delta}}{\partial \boldsymbol{u}} + \boldsymbol{K} + \boldsymbol{K_\delta} \right) \\
&\boldsymbol{G^*} = \boldsymbol{G} + \boldsymbol{G_\delta} \\
&(\boldsymbol{G^T})^* = \boldsymbol{M_\epsilon} + \alpha\Delta t \left(\frac{\partial \boldsymbol{N_\epsilon}}{\partial \boldsymbol{u}} + \boldsymbol{K_\epsilon} + (\boldsymbol{G^T}) \right) \\
&\boldsymbol{R} = \boldsymbol{F} + \boldsymbol{F_\delta} - \left[(\boldsymbol{M} + \boldsymbol{M_\delta})\, \boldsymbol{a} + (\boldsymbol{N(u)} + \boldsymbol{N_\delta(u)}) + (\boldsymbol{K} + \boldsymbol{K_\delta})\, \boldsymbol{u} + \boldsymbol{K}_\mu \boldsymbol{u} + (\boldsymbol{G} + \boldsymbol{G_\delta})\, \boldsymbol{p} \right] \\
&\boldsymbol{Q} = \boldsymbol{E} + \boldsymbol{E_\epsilon} - \left[\boldsymbol{G^T u} + \boldsymbol{M_\epsilon a} + \boldsymbol{N_{\epsilon(u)}} + \boldsymbol{K_\epsilon u} + \boldsymbol{G_\epsilon p} \right]
\end{aligned}
\tag{32}
$$

4. Evaluation of velocity and pressure

$$
\begin{aligned}
\boldsymbol{a} &\leftarrow \boldsymbol{a} + \boldsymbol{\Delta a} \\
\boldsymbol{p} &\leftarrow \boldsymbol{p} + \boldsymbol{\Delta p} \\
\boldsymbol{u} &\leftarrow \boldsymbol{u} + \Delta t \alpha \boldsymbol{\Delta a}
\end{aligned}
\tag{33}
$$

5. Repeat steps 2.-4. until convergence is reached.

6. Solve the level set equation with computed velocity field $\boldsymbol{u}$. This is done using positive explicit scheme described for example in [9].

7. Proceed with next time step.

6. NUMERICAL EXAMPLE

Implementing of XFEM in combination with moving interface by level-set method is quite complicated task and there is a lack of suitable benchmark tests. To illustrate the prototype implementation of XFEM and its application, the application to structural behavior of composite cantilever with circular inclusions is presented. The geometry and structured FE mesh are shown in $Fig.1$ together with stress magnitude contours. Note, that the discretization is based on structured, regular grid and is not capturing the circular inclusion geometry which is captured by introducing weak discontinuity enrichment in velocity field with kinks located at material interfaces. Material of cantilever is linear elastic with Young modulus $E = 3 \cdot 10^4 MPa$, weakened holes have Young modulus $E = 0.1 MPa$. Poisson ratio is equal to 0.3. Since there are different material properties, so-called "abs enrichment" was used, because of weak discontinuity in displacement (or strong discontinuity in strains and stresses). Constant continuous load with intensity 1 kN/m has been prescribed on the top surface of the beam. In $Fig.1$, contours of stress magnitude are shown. It can be seen, that in weakened holes the stress is nearly zero as the material has very small Young Modulus. In $Fig.2$, normal stress profiles at the restraint, resp. at the cut through each hole center is plotted shown. Again, it can be seen, that the stress is concentrated near the hole, while the hole itself is not under the stress.

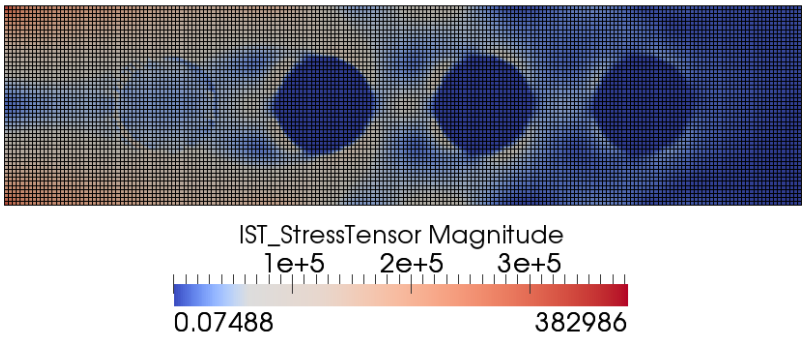

Fig. 1 Cantilever with weakened holes - stress magnitude contours

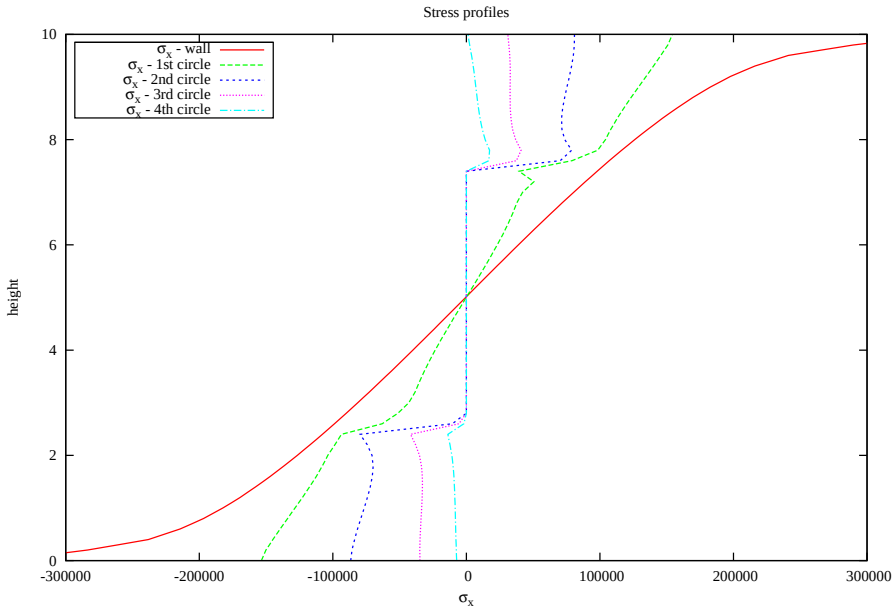

Fig. 2 The stress profile

7. CONCLUSION

In this paper, the numerical model for fresh concrete casting simulations was presented. The problem is treated as flow of a two immiscible homogeneous fluids with different physical properties. The concrete is considered as two-parametric Bingham fluid, the air is modeled as a standard Newtonian fluid. The interface between both fluids is descrideb in sense of level-set method. Extended finite element method is then used to resolve description of discontinuities in velocity and pressure fields across the interface. Since there is no surface tension in this problem, presenting discontinuity is only weak and therefore, so-called ”abs enrichment” is used. The prototype XFEM implementation is illustrated on structural

analysis of composite cantilever with circular inclusions.

ACKNOWLEDGEMENT

This work was supported by the Grant Agency of the Czech Technical University in Prague, grants No. SGS12/026/OHK1/1T/11 and New Industrial Technologies for Tailor-made Concrete Structures at Mass Customized Prices – „TailorCrete“, č. 7E10055.

REFERENCES

[1] Chessa, J. - V. - Belytschko, T. *An extended finite element method for two phase flow*, In: ASME J. Appl. Mech. 2003, Vol 70, 10-17.

[2] Gopala, V. - Van Wachem, B. Gopala, V. - Van Wachem, B. *Volume of fluid methods for immiscible-fluid and free-surface flows*, In: Chemical Engineering Journal 2008, Vol 141, pp 204-221.

[3] Sethian, J. *Level Set Methods and Fast Marching Methods*, second ed., Cambridge University Press 1999, Cambridge, ISBN-13 978-0-521-64557-7 .

[4] Osher, S. - Fedkiw, R. *Level Set Methods and Dynamic Implicit Surfaces*, Springer, 2003, Berlin, ISBN 0-387-95482-1

[5] Volker, J. *Slip with friction and penetration with resistance boundary conditions for the Navier–Stokes equations—numerical tests and aspects of the implementation* In: Journal of Computational and Applied Mathematics 2002, Vol 147, No.2, pp 287-300.

[6] Fries, T. *A corrected XFEM approximation without problems in blending elements*, In: Int. J. Numer. Methods Eng. 2008, Vol 75, 530-532.

[7] Tezduyar, T. - Osawa, Y. *Finite Element Stabilization parameters computed from element matrices and vectors* In: Computer Methods in Applied Mechanics and Engineering 2000, Vol 190, is. 3-4, pp 411 - 430.

[8] Patzák, B. - Bittnar, Z. *Modeling of fresh concrete flow*, In: Computers and Structures 2009, 87 (15), pp 962-969.

[9] Barth, T. - Sethian, J.A. *Numerical Schemes for the Hamilton–Jacobi and Level Set Equations on Triangulated Domains*, In: Journal of computational physics 1998, 145 1-40.

SEISMIC PERFORMANCE OF TIMBER FRAMES

Jan KOLEŠ, Stanislav POSPÍŠIL, Shota URUSHADZE[1]

Abstract: *A series of dynamic experiments was performed on one-story timber frame. In comparison with the previous frames [1, 2], improved connection between column and girder was used here. The tests included sinusoidal sweeps in two directions, arbitrary signals simulation earthquake loads in three directions, and snapback tests. Various parameters were measured, for example tension on columns and slabs, rotation between columns and beams, displacement of columns and acceleration of columns and beams. All these parameters lead to classification of the frame behavior with designed type of connection, for example the natural frequencies, eigenmodes and other dynamic properties of the structure. Parameter description will allow us to design and improve mathematical model of the timber frame.*

Keywords: t*imber frames, dynamic test*

1. INTRODUCTION

The performance of heavy wood frames in earthquakes has been studied both experimentally and analytically, while examples of timber frame buildings in seismically active areas are rare. This is primarily due to difficulties in design efficient moment – transmitting timber connections. Large inter-story drifts of wood-based moment resisting frames are caused by the low stiffness of the semi-rigid beam-to-column connections. In general, the serviceability limit state check will be the limiting criteria in the design process, leading to over-designed cross-sections of beams and columns. Apart from difficulties in balancing the moment capacities of members and connections, analysis and experiments showed that wood frames can perform well under dynamic loads due to the high strength and high energy dissipating capacity of the connections. The specific objectives of this work are:

- to study behavior of the frame under the cyclical load and the development of the cracks,
- to demonstrate feasibility of using high-strength screws in loaded connections of the frame,
- to study the performance of the frame, weakening of the joints and pinching of the screws.

2. TEST SETUP

The test was carried out on the simple one-story frame (see Fig. 1). Height of the entire structure was 3100 mm and dimensions of the upper floor were 4420 mm by 4420 mm. Most of the parts of the frame, like columns, beams and slab were made from glue-laminated timber. Wood of European

[1]Ing. Jan Koleš, doc. Ing. Stanislav Pospíšil, Ph.D., Ing. Shota Urushadze, Ph.D., Institute of Theoretical and Applied Mechanics AS CR, v.v.i.; koles@itam.cas.cz, pospisil@itam.cas.cz, urushadze@itam.cas.cz

spruce was used. Material had moisture content of 10 % and average density of 0.44 g/cm^3. Connection between column and beam was realized through 26 high strength lag screws. Additional timber block was placed in each corner between column and beam (see detail on Fig. 2). This block was predrilled so the screws could be screwed in the proper direction. It was also expected that it should increase the stiffness of the connection. Two types of screws were used, the first set with dimensions 300 mm (length) and 20 mm (diameter) and the second set with dimensions 300 mm (length) and 20 mm (diameter). Longer screws were of the diameter 20 mm and shorter of the diameter 12 mm. This measure was to fulfill required edge and end distances and spacing of the screws. There was a connection on each face of the column, since the beams were attached from all 4 sides and it was also above and below the beam. Screws were used rather than nails to avoid excessive nail withdrawal during repeating dynamics tests.

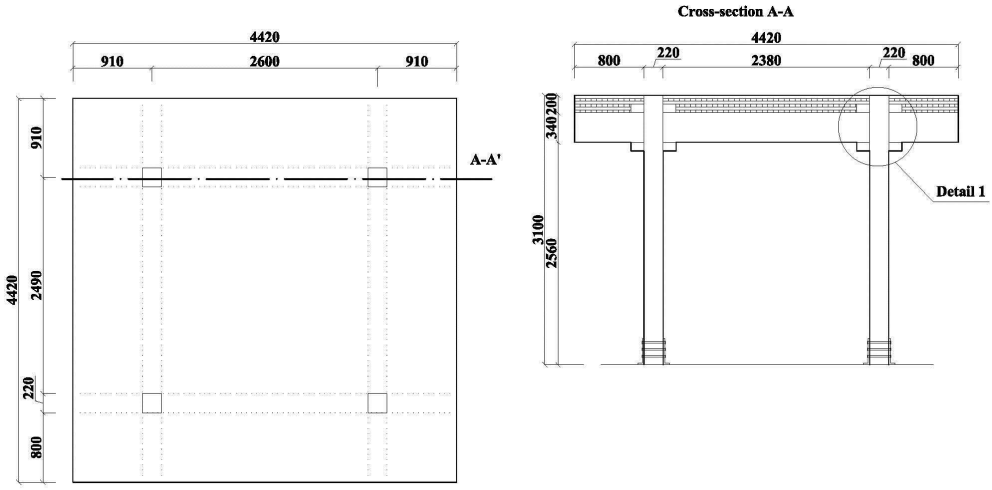

Fig. 1 Layout and cross-section of the frame

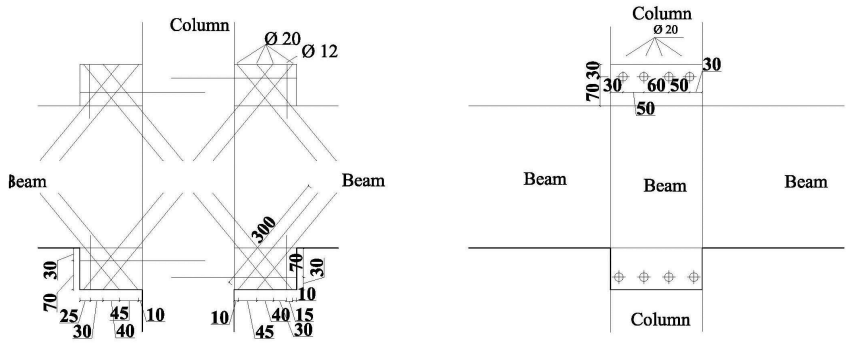

Fig. 2 Detail of the connection between column and beams

Every column was connected to the shaking table by angles from two opposite sides. Angles were tightened by 6 screws. This assembly allowed the connection to be fixed in X-direction and after few seismic tests and weakening of the connection due to pinching of the screws it also allows small rotation in the Y-direction.

3. TESTING PROCEDURE

Full scale shake table test was performed. Frame was loaded by 4 steel plates located above columns. Mass above each column was 250 kg, so total load was 1000 kg. Masses represented roughly live and dead load distributed above the floor. Full dead and live load were chosen to introduce maximum forces and also to induce maximum frame damage. Dimensions of the plates were 1000 mm × 1000 mm × 250 mm. The table was equipped with 16 accelerometers, 14 strain gauges glued on the structure, 6 potentiometric displacement sensors placed in two corners between beam and column and 4 potentiometric displacement sensors measuring displacement between table and beam. Frames were tested at University Walk Earthquake Engineering Research Centre, Bristol, United Kingdom. The experiment is shown in the Fig. 1 and the testing sequence is described in the Table 1. Structure has been subjected to a set of kinematical excitations with increasing level of intensity from peak ground acceleration 0.125 g to 1.3 g (g = 9.81 m/s^2). The synthetic earthquake was used as an excitation signal.

Each earthquake simulation was followed by modal testing to obtain natural frequencies of the frame. The modal parameters were obtained by low level sine sweep harmonic excitation with increasing frequency. Excitation for sine-sweep was from 0.01 g to 0.1 g. The sweep had logarithmical velocity 2 octave/min with frequency 1-16 Hz. Two snapback tests were used to describe the natural frequency.

Tab. 1Testing protocol for single story timber frame

Test number	*Test type*	*Excitation direction*	*Excitation level (g)*
1	Sine sweep	Y	*0.1*
2	Sine sweep	X	*0.05*
4	Snap back	Y	
5	Sine sweep	X	*0.01*
6	Sine sweep	Y	*0.01*
7	Sine sweep	Y	*0.01*
8	Sine sweep	Y	*0.1*
9	Snap back	Y	
10	Seismic	X & Y & Z	*0.05*
11	Seismic	X & Y & Z	*0.75*
12	Sine sweep	Y	*0.01*
13	Sine sweep	Y	*0.1*
14	Seismic	X & Y & Z	*1.3*
15	Snap back	Y	

4. RESULTS

During the experiment, accelerations of columns and beams, rotation between connections, displacement of the beams and tension in the columns were measured. We are able to extract from the measured data information about the changes in the natural frequencies. This helped us to describe

the degradation of the structure – weakening of the joints. Shift in the natural frequencies can be shown in the first natural frequency measured by accelerometer in Y-direction located in the middle of the upper slab. After the 1st seismic test frequency was 2.57 Hz, after the 2nd test frequency was 2.01 Hz and after the 3rd test it was 1.56 Hz.

The rotation in the connection between column and beam was measured. After the 1st seismic test the rotation was almost negligible, it reaches value 0.015 degrees. In the 2nd test rotation was 0.3 degrees, after the 3rd test it was 1 degree and after the significant cracks appeared, rotation was 4 degrees.

Also the strain on the column was important. For the strain gauge, glued in the middle of the column strain increases from 0.01 mm/m after the 1st test to 0.58 mm/m after the 2nd test and reached finally to 0.9 mm/m after the 3rd test.

5. CONCLUSION

This experiment was the first step in the assessment of the building behavior according to its natural frequencies and simulated earthquake. Research remains still in progress, another test only with joints were performed. Data from these experiments will be compared. The dissipation of the energy will be in the main interest. The obtained results may allow to predict the life-time of well-designed connections under the cyclic loading.

The results showed structural damage due to the earthquake progress. The value of the natural frequency decreased to about 60% of its original value. Damage was caused by plastic yielding in connections (both wood and screws). Beam to column connections can be designed in many different ways and the setup of our experiment represented one of the options. This frame was able to resist earthquake of 1.3 g while in nature earthquake reaches usually around 0.3-0.4 g.

6. ACKNOWLEDGEMENT

The financial support of this experiment by the Faculty of Civil Engineering, Czech Technical University in Prague (SGS project No. SGS12/117/OHK1/2T/11) is gratefully acknowledged.

REFERENCES

[1] Kasal, B., Pospíšil, S. Jirkovský, I., Heidusche, A., Drdácký, M., Haller, P., Seismic performance of laminated timber frames with fiber-reinforced joints, Earthquake Engineering and Structural Dynamics, 33, 2004, pp. 633-646.

[2] Kasal, B., Pospíšil, S., Heidusche, A., Urushadze, S., Shake table tests of a three-story spatial timber frame with moment connections, In: World conference on timber engineering, 2010.

[3] Evins, D.J., Modal testing, theory and application, Great Britain: SRP Ltd., Exeter, 2004.

[4] Meriam, J.L., Kraige, L.G., Engineering Mechanics – Dynamics, New York: John Wiley and Sons, Inc., 2008.

MODELING OF FRC SLABS LOADED BY BLAST LOADING

Martin KOVÁŘ[1]

Abstract: *The paper presents methods of numerical modeling of RC and FRC slabs subjected to blast loading. The models are based on experiments performed in the military training area Boletice with the cooperation of the Czech Army Corps. The use of fracture energy as the key quantity in the modeling of FRC in comparison to RC is studied.*

Keywords: *blast loading, fiber concrete, reinforced concrete*

1. INTRODUCTION

This paper presents numerical modeling of experiments of two sets of field tests of blast performance of reinforced concrete specimens and reinforced concrete specimens with plastic fibers. The tests were performed in cooperation with the Czech Army corps and Police of the Czech Republic at the military training area Boletice using real scale precast slabs and 25 kg of TNT charges placed in distance from the slab for better simulation of real in-situ conditions.

2. FIELD TESTS OF BLAST PERFORMANCE OF REINFORCED CONCRETE AND REINFORCED CONCRETE SPECIMENS WITH PLASTIC FIBRES

For description of the field tests see [1].

Fig. 1 Layout of the experiments

[1] Ing. Martin Kovář, Department of Concrete and Masonry Structures, Faculty of Civil Engineering, CTU in Prague; martin.kovar@fsv.cvut.cz

3. NUMERICAL MODELING

A numerical model of the experiment was prepared for the purpose of further research. The process of model set-up is described in the following text. The model was calibrated according to the outcomes of the experiments described in the previous chapter.

Fast dynamic phenomena can be solved by the method of explicit time integration (finite difference method, differential method, see Fig. 2) the equation of motion can be expressed as

$$M_n \cdot u_n'' + C_n \cdot u_n' + K_n \cdot u_n = p_n \tag{1}$$

equation is solved in time t_n, hence at the start of fixed time step.

The method is based on linear displacement change. The velocity

$$u'_{n+1/2} = \frac{1}{\Delta t_{n+1/2}}(u_{n+1} - u_n) \tag{2}$$

is inserted into equation of acceleration

$$u'' = \frac{1}{\Delta t_n}(u'_{n+1/2} - u'_{n-1/2}) \tag{3}$$

u_{n+1} remains unknown in Eq. (1). The displacement in time t_{n+1} is

$$\begin{aligned}&(\frac{1}{\Delta t^2}M_n + \frac{1}{2\Delta t}C_n)\cdot u_{n+1} = \\ &p_n - (K_n - \frac{2}{\Delta t^2}M_n)\cdot u_n - (\frac{1}{\Delta t^2}M_n - \frac{1}{2\Delta t}C_n)\cdot u_{n-1}\end{aligned} \tag{4}$$

The matrixes M and C are diagonal; the solution is fast and simple.

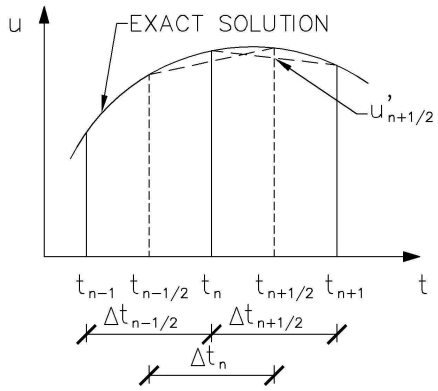

Fig. 2 The explicit time integration method (finite difference method)

In the method of explicit time integration, the system is in equilibrium only at time t_n, but not at time t_{n+1}. The time step depends on the highest natural frequency of the structural system. If the time step is adequately small, the method is numerically stable. The method of explicit time integration solves small number of equations in very small time steps in duration of approximately 10^{-6} – 10^{-8} s. The method of explicit time integration is suitable only for processes of a very short duration.

4. NUMERICAL MODELING OF THE EXPERIMENTS

LS-DYNA solver was developed for non-linear analysis of fast dynamic phenomena like blast or impact. Within the calculation, the FEM mesh can adapt by deleting elements whose resistance was depleted; these FEM elements "erode".

The model composes of several parts. The air forms boundaries of the model; the explosive (e.g. TNT) transfers the energy from the blast to FE elements of the air, where the blast wave propagates. The concrete specimen is modeled by solids, reinforcement by beam elements.

The air is modeled using the 009-Null material and forms the undeformable FE network. The concrete specimen is modeled by the 159-CSCM_Concrete material model (brittle material model with damage [4]; similar approach to concrete modeling is used by [2]. The explosive is modeled by the 008-High explosive burn material model. The blast overpressure is calculated by the JWL equation of state (EOS):

$$p = A\left(1-\frac{\omega}{R_1 V}\right)e^{-R_1 V} + B\left(1-\frac{\omega}{R_2 V}\right)e^{-R_2 V} + \frac{\omega E}{V} \qquad (5)$$

The material parameters of the used model (including strain-rate dependent response) were automatically generated in the LS-DYNA from the particular concrete compressive strength. The material properties of the FRC (fracture energy and others) are currently tested, see below.

As the first step, a 2Dmodel was prepared. Its goal was to show basic characteristics of the experiment, e.g. the time when the blast overpressure wave reaches the surface of the specimen, the time when the elements at the soffit the specimen start to erode, etc. The blast overpressure wave reaches the surface of the specimen at 0.25 ms, the first finite elements start to erode at 0.4 ms, see Fig. 3.

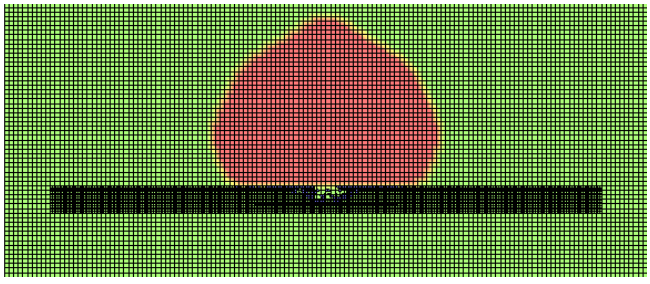

Fig. 3 Blast overpressure wave at 0.5 ms

4.1. 3D MODEL OF REINFORCED CONCRETE SPECIMENS

The 3D reinforced concrete model was prepared to mitigate the weaknesses of the plain concrete model using real dimensions of longitudinal and transverse reinforcement incl. links (steel reinforcement modeled as beam elements). The mesh size was chosen 30mm for concrete and reinforcement and 50mm for air [2].

The first elements erode when the blast overpressure wave reaches the surface under the hypocenter at 0.25 ms.

In the following phase, more FE erode, the damage of the specimen increases and spalling at the soffit takes place. Fig. 4 shows plastic strain (crack development) for plain concrete.

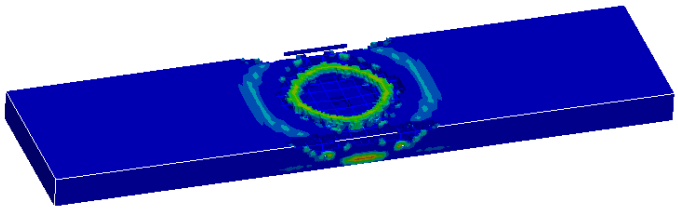

Fig. 4 Top view of the plain concrete specimen after the blast (t = 1 ms)

The results of numerical modeling show good agreement with the experiments for reinforced concrete specimens.

4.2. 3D MODEL OF REINFORCED CONCRETE SPECIMENS WITH PP FIBERS

The behavior of fiber concrete subjected to blast load is quite different from the behavior of plain (respectively reinforced) concrete specimens. At plain concrete, the specimen fails in tension after reaching its tensile strength. At fiber concrete, the stiffness of the specimen decreases after the tensile strength is reached (strain softening). The fibers take over the tensile stress during strain softening and the material performs with a residual tensile strength (approximately 1/3 of the original tensile strength according to fiber type, dosage and geometry). The difference between stress-strain diagrams of plain concrete and fiber concrete can be seen in Fig. 5.

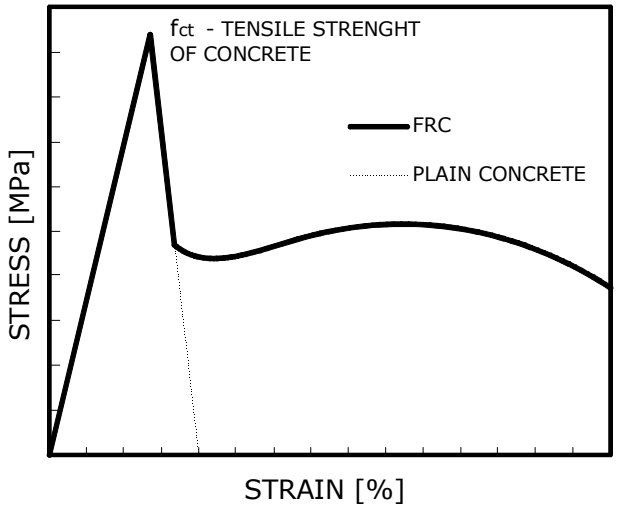

Fig. 5 Stress-strain diagram of concrete material model with damage

The material model of plain concrete MAT159_CSCM (material model with damage and plasticity, [3, 4]) used in LS-DYNA solver has to be recalibrated to perform according to the presented description, i.e. to provide ductile behavior. For the analytical description of the MAT159_CSCM material model, see Fig. 6.

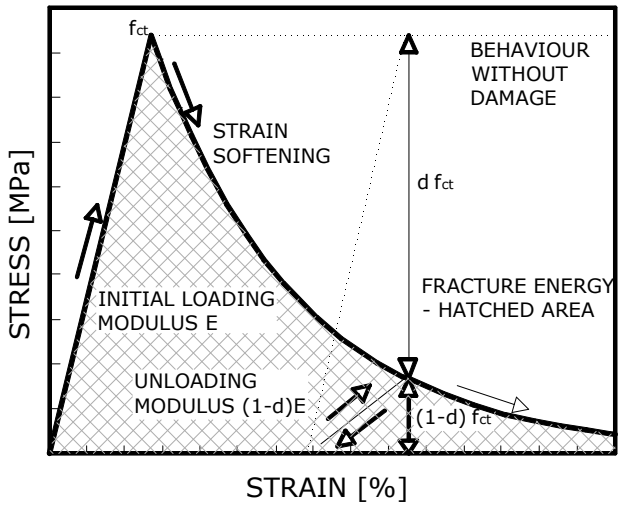

Fig. 6 Stress-strain diagram of concrete material model with damage

The key to MAT159_CSCM material model recalibration lies in tuning its unloading part to describe behavior of fiber concrete while the loading part can remain unchanged (the difference of plain concrete and fiber concrete can be neglected). The fracture energy G_f can be can be expressed as an integral of the area below the stress-strain diagram:

$$G_f = \int_0^{\infty} (1-d)\, f_{ct}\, dx \tag{6}$$

where: d is the damage (from 0 to 1) and f_{ct} is the tensile strength.

According to this approach, the integral of the fracture energy is used for verification of the value of the fracture energy.

The FRC material model was calibrated according to experiments described by [5]. The experiments studied the strain-rate effect of FRC specimens (700 ×150 × 150 mm) subjected to four point bending (see Fig. 7). The concrete mix properties and fiber dosage were the same as in the field experiments. The finite elements size in the numerical model used for evaluation of the experiments was chosen the same as in the full scale 3D models described in the preceeding paragraphs, as the blast modeling is highly scale-sensitive.

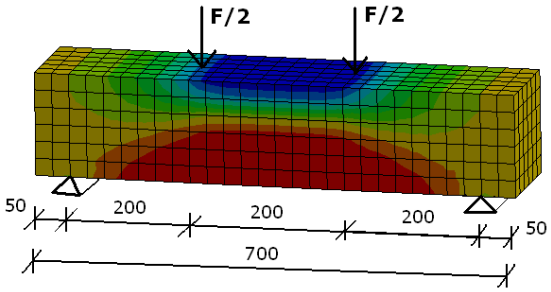

Fig. 7 Layout of the control experiment (mm)

The calibration models were prepared using LS-DYNA for plain concrete and both dosages of PP fibers. The fracture energy in tension and shear of the material model of plain concrete was modified to obtain similar integral of the fracture energy both from the experiments and the numerical evaluation.

For comparison of the force-deflection (F-δ) diagrams of plain concrete, 4.5 kg/m^3 and 9 kg/m^3 PP fibers FRC both experimental and numerical, see Fig. 8. The area of the force-deflection diagram was limited to the deflection of 8 mm.

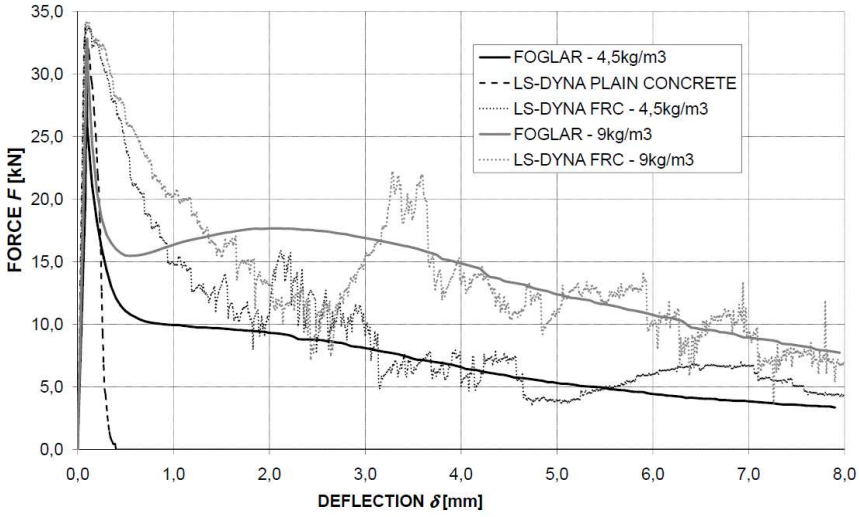

Fig. 8 Force – deflection diagram of material models

The obtained values of the fracture energy for various concrete strength classes and fiber dosages can be seen in Table 1.

Tab. 1 Fracture energy of various specimens

Specimen	Fracture energy [N/m]
LS-DYNA – plain concrete	5.6
FOGLAR C30/37 – 4.5 kg/m^3	62.0
LS-DYNA FRC – 4.5 kg/m^3	68.6
Foglar C30/37 – 9 kg/m^3	109.3
LS-DYNA FRC - 9 kg/m^3	102.9

The calibrated material model was used in the 3D models described in the previous chapter. For example of the result of the modeling, see Fig. 9.

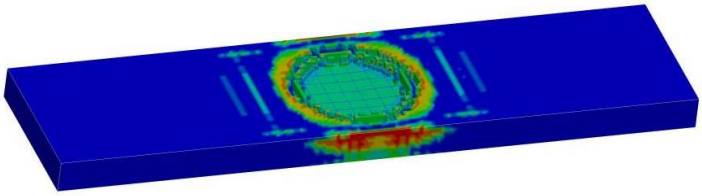

Fig. 9 Top view of the FRC specimen after the blast (t = 1 ms)

4.3. MATERIAL MODEL WITH SMEARED REINFORCEMENT

Another way to fiber reinforcement concrete modeling is to use smeared reinforcement as being made in [6]. The same experiment with concrete beams has been modeled in ATENA solver. Material model of plain concrete with smeared reinforcement with PP fiber characteristics has been used.

This material model shows good agreement with real experiments.

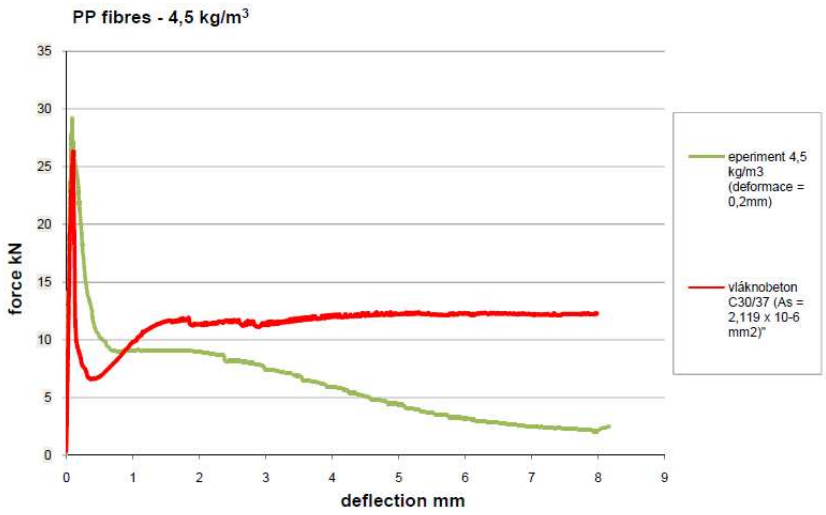

Fig. 10 Force-deflection diagram of smeared reinforcement model [6]

5. CONCLUSION

The experiments showed beneficiary effect of added fibers on blast performance of the specimens. The experiments also showed beneficiary effect of increased concrete compressive strength on blast performance of the specimens. Combination of fibers and increased compressive strength proved itself to be very effective for improving the blast performance.

The way of modeling of fiber concrete subjected to blast loading by increasing the facture energy of plain concrete MAT159_CSCM material model was presented and evaluated. The model calibration was performed according to small scale experiments. The results of numerical modeling show very good agreement with the experiments for specimens with added fibers.

Other ways of modeling of fiber concrete subjected to blast loading lie in using smeared reinforcement or in modeling of the dispersed reinforcement. These methods require much more effort to be invested, yet the result remains questionable.

ACKNOWLEDGEMENT

This paper was supported by the Czech Ministry of Industry and Trade project FR-TI3/531 and the CTU project No. SGS12/029/OHK1/1T/11.

REFERENCES

[1] Foglar M., Sochorová E., Kohoutková A., Field tests of blast performance of reinforced concrete and fibre reinforced concrete specimen, In: Engineering mechanics, 2011, pp. 143-146, ISBN 978-80-87012-33-8

[2] Coughlin A.M., Musselman E.S., Schokker A.J., D.G. Linzell, Behavior of portable fiber reinforced concrete vehicle barriers subject to blasts from contact charges, International Journal of Impact Engineering, 37 (5), 2010, pp. 521-529, ISSN 0734-743X

[3] Murray, Y.D., Evaluation of LS-DYNA Concrete Material Model 159, US Department of transportation, 2007, FHWA-HRT-05-063

[4] Murray, Y.D., User Manual for LS-DYNA Concrete Material Model 159, US Department of transportation, 2007, FHWA-HRT-05-062

[5] Drahorád M., Foglar M., Smiřinský S., Veselý M., Užití dynamického faktoru nárůstu pevnosti betonu pro zkrácení doby zkoušek vláknobetonových vzorků, Beton TKS, 1, 2012, pp. 74-79, ISBN 978-80-87158-30-2

[6] Lišková, K., Adjustace materiálového modelu vláknobetonu, Bakalářská práce, Fakulta stavební ČVUT v Praze, 2012, 87 p.

ALUMINIUM FOAM: PREDICTION OF MACROSCOPIC ELASTIC PROPERTIES USING NANOINDENTATION AND UP-SCALING MODEL

Vlastimil KRÁLÍK[1], **Jiří NĚMEČEK**[2]

Abstract: *This paper is focused on the prediction of macroscopic elastic properties of highly porous aluminium foam. The material is characterized by a closed pore system with very thin pore walls and large air pores. Intrinsic material properties of cell wall constituents are assessed with nanoindentation whereas analytical homogenizations are employed for the assessment of the cell wall elastic properties. Very good agreement was found between the various analytical estimates. Two-dimensional microstructural FEM model was applied to obtain effective elastic properties of the upper material level for which the Young's modulus ranges from 1.11 GPa to 1.4 GPa depending on the size of the evaluated area. The estimated range of values was lower in comparison with experimental results obtained from experimental compression tests. It follows from the 2-D approximation that the 2-D model underestimates the stiffness, compared to the real case constrained in 3-D. Therefore, more appropriate 3-D model based on microCT data will be prepared in the future work.*

Keywords: *metal foam, porous system, nanoindentation, micromechanical properties, homogenization*

1. INTRODUCTION

Structural materials (like cement, lime or gypsum composites as well as metals, wood or plastic) often exhibit large variation in the microstructure of their solid phases. They are also often characterized by a closed or open pore system. Porosity is usually smaller than the solid phase content but in case of lightweight materials the situation is opposite. An exceptional example is metal foam which typically exhibits porosity around 90% of the sample volume. Its cellular structure is analogous to the natural materials like wood or bones. On the other hand, many structural materials based e.g. on cement are characterized with open porosity. Also, the size of the pores differs a lot.

Metal foams belong to the group of modern structural materials with high potential to many engineering applications ranging from automotive and aerospace industries to building industry (e.g. sound proofing panels) [1]. This highly porous material with a cellular structure is known for its attractive mechanical and physical characteristics such as high stiffness in conjunction with very low

[1] Ing. Vlastimil Králík, Department of Mechanics, Faculty of Civil Engineering, CTU in Prague; vlastimil.kralik@fsv.cvut.cz

[2] doc. Ing. Jiří Němeček, Ph.D., Department of Mechanics, Faculty of Civil Engineering, CTU in Prague; jiri.nemecek@fsv.cvut.cz

weight, high strength, excellent impact energy absorption, high damping capacity and good sound absorption capability. The usual source material for the production of metal foams is aluminium and aluminium alloys because of low specific density (~2700 kg/m^3), low melting point (~660 °C), nonflammability, possibility of recycling and excellent corrosion resistivity.

In this study, micromechanical analysis of a commercially available aluminium foam Alporas® (Shinko Wire Co., Ltd) was performed. Nanoindentation technique was applied to access elastic properties of the distinct phases within the cell walls. Based on these results, overall effective elastic properties (Young's modulus) of the solid phase were evaluated by several homogenization schemes. To calculate the effective elastic properties at the whole structural level (including the air pores) microstructural FEM model was applied.

2. MATERIAL CHARACTERIZATION

2.1. STRUCTURE OF AL-FOAM

The Alporas foam is characterized by a hierarchical microstructure with the system of closed pores. An internal structure of the aluminum foam is shown in Fig. 1. The properties of Al-foam depend directly on the shape and structure of the cells, therefore description of its structure is very important. The most important structural characteristic of a cellular solid is its relative density, $\rho / \rho s$ (where ρ is the foam density and ρs is the density of the solid, i.e. Al). The fraction of pore space in the foam can be defined by its porosity ($1- \rho / \rho s$) [2].

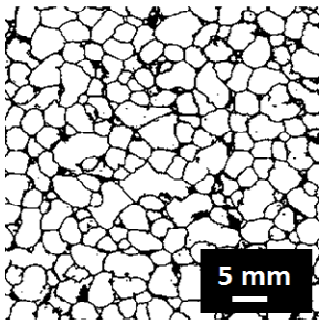

Fig. 1 Overall view on a typical structure of aluminium foam

The porosity was detected by weighing of a sufficiently large foam sample and by taking into account the density of pure aluminum (2700 kg/m^3). The relative density was assessed as 0.0859 and porosity reached 0.914, i.e. 91.4%.

Other important parameters for the description of the internal foam structure are both distribution of cell wall thicknesses and pore size and shape characteristics. These geometric parameters of the cell structure are crucial for the selection of the homogenization schemes and modeling mechanical performance. A high resolution optical image of the foam surface on a cross-section embedded to

blackwashed gypsum was prepared. Prior to imaging the specimen was mechanically polished with fine SiC papers to receive smooth and flat surface. Size of the scanned area was 125 × 149 mm (which is sufficiently large to represent a structural level of the material).

A characteristic size of each pore was estimated with the help of image analysis. Some small corrections and noise filtering in the binary image was necessary to help the algorithm automatically identify all individual pores. The pores are almost spherical or polyhedral shape due to a high foaming ratio. In the analysis, the pores were replaced by equivalent ellipses. Further, a shape factor computed as the ratio between the longer and shorter axes of the ellipse was obtained. Distribution of the values of shape factor is shown in Fig. 2. In our sample, the mean value of shape factor was 1.15 and indicates that the shape of the pores is nearly circular with a small flattening.

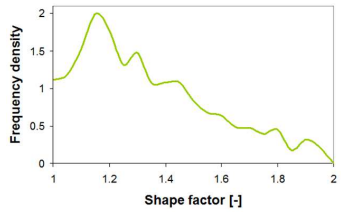

Fig. 2 Distribution of shape factor

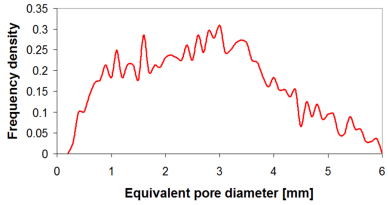

Fig. 3 Distribution of equivalent diameter

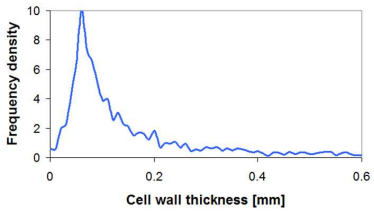

Fig. 4 Distribution of cell wall thickness

An equivalent pore diameter assuming circular pores was also calculated. The distribution of these equivalent pore diameters can be seen in Fig. 3. The equivalent diameters of pores are distributed over a range of 0.2 mm to 6 mm and the mean value of the equivalent diameter is 2.9 mm.

The cell wall thickness assessed as the minimum distance between neighboring pores was evaluated using image analysis. Distribution of the cell wall thicknesses is shown in Fig. 4. The distribution shows a significant peak, i.e. a characteristic thickness, around L~61 μm. The majority of cell wall thicknesses lies between 20 to 200 μm.

2.2. DEFINITION OF THE MODEL

At least two characteristic length scales can be distinguished for the material: the cell wall level and the foam level. Therefore, two-scale microstructural model for the prediction of macroscopic elastic properties on the whole foam level is proposed based on the utilization of nanoindentation data received on cell walls [3]. The model covers:

- **Level I** (the cell wall level).

In this level, characteristic dimension of the cell wall defined by the mean midspan wall thickness is L~61 μm. This level consists of prevailing aluminium matrix (Al-rich area) with

embedded heterogeneities in the form of Ca/Ti-rich areas. Distinct elastic properties of the microstructural constituents were assessed using nanoindentation at this level.

- **Level II** (the foam level).

At this level, the whole foam containing large pores with an average diameter ~2.9 mm is considered. Cell walls are considered as homogeneous having the properties that come from the Level I homogenization.

3. LEVEL I HOMOGENIZATION

Firstly, intrinsic elastic properties of the microstructural constituents were assessed by nanoindentation at this level. Detailed description of the experimental part can be found in [3]. Two-phase system (major Al-rich and minor Ca/Ti-rich phase) was assumed in the statistical deconvolution algorithm [4] to obtain Young's moduli and volume fractions of the two phases (Tab. 1). Poisson's ratio 0.35 was considered for both phases. Based on these results, effective elastic properties (Young's modulus) of the solid phase were evaluated by selected analytical homogenization schemes, namely Voigt and Reuss bounds, Mori-Tanaka method and self-consistent scheme. The homogenized elastic modulus for the cell wall is summarized in Tab. 2. Very close bounds and insignificant differences in the elastic moduli estimates by the schemes were found.

Tab. 1 Elastic moduli and volume fractions of the two microstructural phases from deconvolution

Input values from nanoindentation	Mean E (GPa)	St.dev. (GPa)	Volume fraction
Al-rich zone	61.9	4.6	0.638
Ca/Ti-rich zone	87	17	0.362

Tab. 2 Effective values of Young's modulus computed by different homogenization schemes at Level I

Scheme	Mori-Tanaka	Self-consist. scheme	Voigt bound	Reuss bound
$E_{eff,\ Level\ I}$ (GPa)	70.076	70.135	71.118	69.195

4. LEVEL II HOMOGENIZATION

At this level, cell walls are considered as a homogeneous phase having the properties that come from the Level I homogenization. The cell walls create a matrix phase and the large air pores can be considered as inclusions in this homogenization.

At first, effective elastic properties of the Level II were estimated with the same analytical schemes used in Level I. The volume of air pores was evaluated experimentally (Section 2.1) on our samples as 91.41 %. The analytical methods do not give appropriate results, because the basic assumptions following from Eshelby's solution of an ellipsoidal inclusion in an infinite body and volume fraction

restrictions are not fulfilled. List of results of Level II homogenization using analytical schemes is described in detail in [3].

At second, the more appropriate two dimensional microstructural FEM model was applied. The model geometry was generated from high resolution optical images of Al-foam cross-section, whose preparation is described in section 2.1. Resulting area with a size of 120 × 120 mm was thus created to represent a higher structural level of the material. At this image, pore centroids were detected, Delaunay triangulation applied and Voronoi cells created. Then, an equivalent 2D-beam structure was generated from cell boundaries (Fig. 5). As a first estimate, uniform cross-sectional area was prescribed to all beams (~8.59 % of the total area).

In this analysis, prescribed macroscopic strain $\mathbf{E}$ is imposed on the boundaries of the RVE and microscopic strains and stresses are solved in the RVE. Volumetric averaging of microscopic stresses leads to the assessment of an average macroscopic stress and finally estimation of effective stiffness parameters.

The key issue of the computation is the size of RVE and application of boundary conditions around the domain. Since the RVE size is always smaller than an infinite body, any constraints can strongly influence the results. Application of the kinematic boundary conditions leads to the overestimation of effective stiffness and it can give an upper bound, whereas the static boundary conditions give a lower bound [5]. The best solution is usually provided by applying periodic boundary conditions to RVE which are, however, difficult to implement into commercial codes.

Nevertheless, the influence of the boundary conditions on microscopic strains and stresses in the domain decrease in distant points from the boundary. The size of our domain (120×120 mm) allowed us to solve the problem with kinematic boundary conditions. For homogenization, considerably smaller region was used. Microscopic strains and stresses were computed inside this smaller area which was still sufficiently large to describe the material inhomogeneities and to serve as material RVE.

To determine the minimum size of the smaller area was used a rule of thumb mentioned e.g. in [6], which states that the ratio of sample size to cell size should be greater than 6 to 7. This rule is based on experimental tests, where the value of Young's modulus increased with increasing ratio of sample size to cell size. Mean cell size of our sample was calculated to 2.9 mm, as described in section 2.1. The minimum size of the region was therefore set to 20 × 20 mm (Fig. 5).

The whole domain (120 × 120 mm) was subjected to homogeneous macroscopic strain in one axial direction ($\mathbf{E}$={1, 0, 0}T) by imposing prescribed displacement to one domain side (Fig. 5). The test was performed using OOFEM software package [7] and microscopic strains and stresses solved in the domain. Strains and stresses (structural forces for the case of beams, respectively) inside the smaller

area (20 × 20 mm) were averaged and used for computation of the homogenized stiffness matrix (one column in the matrix, respectively). Assuming material isotropy, the (1, 1) member at the material stiffness matrix is given by:

$$L_{11} = E\frac{(1-v)}{(1+v)(1-2v)} \tag{1}$$

in which E is the Young's modulus and v Poisson's ratio, respectively. Since the Poisson's ratio of the whole foam is close to zero (as confirmed by experimental measurements) the L11 member coincides with the Young's modulus E. For the tension test in x-direction (Fig. 5), the homogenized Young's modulus was found to be E_{hom} = 1.11 GPa. The influence of increasing size of the smaller area to Young's modulus was also studied. The size of smaller area was increased from 20 × 20 mm to 40 × 40 mm for 5 mm and from 40 × 40 mm to 60 × 60 mm for 10 mm. Young's modulus dependence on the size of the area is shown in Fig. 6. Calculated values of Young's modulus oscillate around the fitted logarithmic curves and converge to a value of 1.4 GPa for the largest evaluated area. In the calculation of larger areas can occur influence of boundary conditions. Thus, a more accurate assessment is necessary to enlarge the size of the domain.

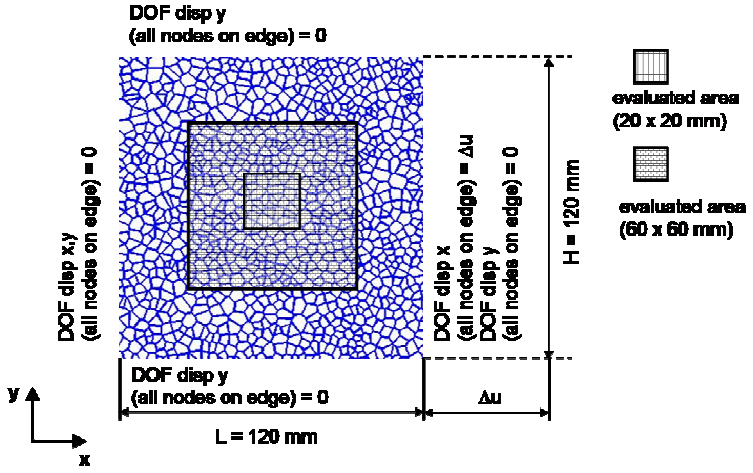

Fig. 5 2D-beam structure with prescribed boundary conditions.

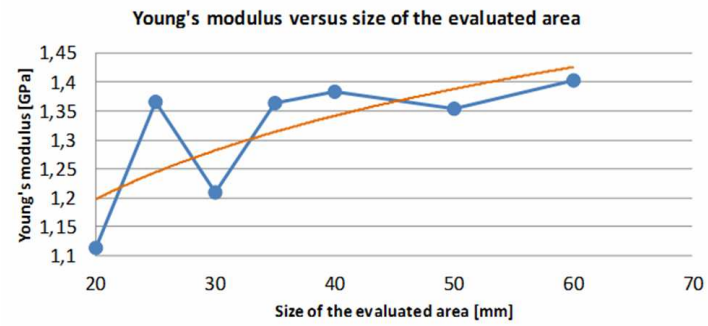

Fig. 6 Young's modulus versus size of the evaluated area.

Such stiffnesses are comparable with the range of experimental values (0.4−1 GPa) reported for Alporas® e.g. by [6]). It is lower than the first results obtained from our currently running experimental measurements (uniaxial compression test on 30×30×60 mm Alporas blocks) that indicate E≈1.45 GPa. The lower stiffness obtained from two-dimensional model can be explained by the lack of additional confinement appearing the three-dimensional case. Therefore, the results of the simplified 2-D model can be treated as the first estimate of the Level II material properties which need to be refined. The real confinement of a 3-D cell structure can hardly be captured in 2-D computation and leads to the necessity of the 3-D computation.

5. CONCLUSIONS

The microstructure of Al-foam was studied by image analysis and phase properties assessed with nanoindentation. Important parameters such as relative density (0.0859), porosity (0.914), distribution of cell wall thicknesses, distribution of equivalent pore diameters and shape factors of pores were determined. Two-scale micromechanical model was proposed for the assessment of foam effective elastic properties. Elastic parameters of cell walls (Level I) were obtained from statistical nanoindentation results from which one dominant and one minor mechanical phase were separated by the deconvolution algorithm. Application of analytical homogenization schemes showed very similar results of effective cell wall elastic properties (ELevel-I ≈ 70 GPa). This value together with corresponding volume fraction of cell walls and large pores were used in micromechanical up-scaling to the upper level (Level II). Effective elastic properties of the Level II were estimated with the same analytical schemes used in the Level I. However, the analytical methods do not give satisfactory results in this case. Therefore more appropriate two dimensional microstructural FEM model was applied. Homogenized Young's modulus ranges from 1.11 GPa to 1.4 GPa depending on the size of the evaluated area. The estimated range of values was lower in comparison with experimental results (1.45 GPa). It is primarily due to the three dimensional effects (cell shape, additional confinement) that cannot be captured in the two dimensional model. Therefore, further development of the numerical model (influence of beam stiffness variations and extension to 3-D) and extending an experimental program is planned in the near future.

ACKNOWLEDGEMENT

The financial support of this experiment by the Faculty of Civil Engineering, Czech Technical University in Prague (SGS project No. 12/116/OHK1/2T/11) and Czech Science Foundation (GAČR P105/12/0824) is gratefully acknowledged.

REFERENCES

[1] Banhart, J., Manufacture, Characterisation and Application of Cellular Metals and Metal Foams, Progress in Materials Science, 46 (6). 2001, pp. 559-632.

[2] Gibson, L.J., Ashby, M.F., Cellular Solids – Structure and Properties, Cambridge: Cambridge University Press, 1997, ISBN 0-521-49911-9

[3] Němeček, J., Králík, V., Vondřejc, J.. Němečková, J., Identification of micromechanical properties on metal foams using nanoindentation, In: Proceedings of the Thirteenth International Conference on Civil, Structural and Environmental Engineering Computing, Edinburgh: Civil-Comp. Press, 2011, pp. 1-12.

[4] Constantinides, G., Ravi Chandran, K.S., Ulm, F., Van Vliet, K.J., Grid Indentation Analysis of Composite Microstructure and Mechanics: Principles and Validation, Materials Science & Engineering: A, 430 (1), 2006, pp. 189-202.

[5] Šmilauer, V., Elastic Properties of Hydrating Cement Paste Determined from Hydration Models, Doctoral thesis, CTU in Prague, 2005, ISBN 978-80-01-03741-6.

[6] Ashby, M.F., et al., Metal Foams: A Design Guide, Oxford: Butterworth-Heinemann, ISBN 0-7506-7219-6.

[7] Patzák, B., Bittnar, Z., Design of Object Oriented Finite Element Code, Advances in Engineering Software, 32 (10-11), 2001, pp. 759-767.

INFLUENCE OF THE HIGH TEMPERATURE ON THE PROPERTIES OF CEMENT PASTE WITH ADDITION OF FLY ASH

Romana LOVICHOVÁ[1], **Pavel PADEVĚT**[2]

Abstract: *This paper is focused on the description of the change of material properties of cement paste with addition of fly ash due to the influence of exposure to high temperatures. In the cement paste with fly ash, the effect of high temperature causes the changes of content in physically bound water and the change in the material structure. Changes are reflected in the material properties of the cement paste as compressive strength, tensile strength in bending.*

Keywords: *cement paste, creep, fly ash, compression strength, tension strength in bending.*

1. INTRODUCTION

Nowadays, products that are not only made from genuine materials have been applied more and more. In building industry a lasting trend of using inexpensive, readily available, high-quality materials and raw materials is observable. Such material is the concrete respectively the cement paste, in which the fly ash is used.

The fly ash is a waste material that results from the combustion of black or brown coal. Combustion method determines the type of the fly ash which is produced. The fly ash can be divided into two basic groups, classical and fluidized. The classical fly ash has different properties than the fluidized one. The chemical inertness of the classical fly ash, low SO_3 content and fine granulometry to 1mm can be mentioned as its main advantages. The main disadvantage may be the content of heavy metals, which depends on the type of the burned coal. The type of the fly ash added to concrete is mostly classical. The fly ash adds to concrete other positive characteristics that are applied to the selected structures. These properties are, the lower heat of hydration development, lower density, comparable to or better than the material properties of concrete without the fly ash, secondary CSH gels hydration arising in concrete.

[1] Bc. Romana Lovichová, Department of Mechanics, Faculty of Civil Engineering, CTU in Prague; romana.lovichova@fsv.cvut.cz

[2] Ing. Pavel Padevět, Ph.D., Department of Mechanics, Faculty of Civil Engineering, CTU in Prague; pavel.padevet@fsv.cvut.cz

The fly ash is generated by coal combustion at high temperature. The cement is also produced at high temperature. These characteristics may predetermine the use of concrete with the fly ash in the fire-resistant structures. The porous structure of the cement paste with the fly ash can better drain free water from the material. So there is no rapid expansion of a steam in a fire and the structure is not damaged by this process quickly. The work deals with the influence of high temperatures in the cement paste on the moisture status.

2. MATERIAL PROPERTIES

As has been discussed in the introduction, the important material properties are compressive strength, tensile strength and elastic modulus. Changes in the properties of the cement paste [1] with fly ash to pure cement paste can be documented on those parameters. Density of the fly ash is significantly lower than the density of cement. It moves around 900 kg/m^3.

Compressive strength is a property determined from the uniaxial compressive tests, the specimen is loaded by the centric force. Maximum compressive strength and loaded areas of specimen determines the size of the compressive strength.

Tensile bending strength is determined from another type of the material test. The most commonly used test is the three-point bending test. The specimen with defined cross section area is loaded in the middle of the span by the increasing force to the failure. Tensile bending strength is calculated from the dimensions of specimen, distance of the supports and achieved load.

The modulus of elasticity is significant characteristic determined from the compressive stress and the deformation during loading. It is most often determined from pressure tests, as the secant value in the 1/3 of the strength and the corresponding strain.

Fracture energy is a property of a given size of the energy required to breach the specimen. It is determined from the three-point bending test. There are several methods for its determination. All methods are based on measurement of deformation and vertical forces on the specimen. Each specimen has the notch in the middle of the span. These properties are important for the design of structures in terms of capacity [3].

Its outstanding features are the water absorption and porosity. The fly ash is a porous material of high hardness. The paper compares the above-mentioned material properties of the dried and saturated specimens.

3. MATERIAL TESTS

The cement paste containing the fly ash is a homogeneous material. Homogeneity of the material allows the use of small specimens for testing. The size of the specimens 20 × 20 × 100 mm was

chosen for the experiments. For production, the cement paste made from water and Portland cement CEM I 42.5 R was chosen initially. Water-cement ratio for the preparation of the cement pastes was selected 0.4. The consistency of the cement paste is liquid, well-workable and does not need a plasticizer used for preparation.

The same water-cement ratio was used for the production of the cement paste with the fly ash. The ratio between the amount of cement and the fly ash was 1:1. Specimens were produced in the steel molds with precise dimensions.

After concreting, all specimens were stored in a water bath. Testing was performed at the age of one and three months. The article presents the results of the test after 28 days. By the time the test specimen was stored in a water bath. Before testing, specimens were removed from the water bath and divided into two groups – dried specimens and water saturated specimens. All specimens were loaded by high temperatures. They were selected for testing at 20, 150, 200, 250, 300 and 450 °C. After removing specimens from the water bath followed by thermal loading, the specimens were heated to a specific temperature at 100 °C / hour. Subsequently, the temperature was defined by specimen heated for 24 hours and then the temperature was naturally cooled to 20 °C.

Saturated specimens were brought back into the water bath and left there two days before testing. The compression strength was tested on six specimens. The specimens were prepared from the three solids, they were cut into two equal parts of the height 50mm. Specimens for the test in tension in bending were used in the original size and they were marked by the number 5. The modulus of elasticity was measured when the compressive strength test was realized.

Each specimen was loaded 3 times to 1/3 of the expected strength and then the compression test was carried out. The fracture energy tests were carried out during the experiments. Four specimens in each group were provided with the notch to half of the height of the cross-section.

4. COMPARISON OF PROPERTIES

First of all it is possible to compare the volume density. Table 1 shows the volume density of the cement pastes without admixture and with admixture of the fly ash.

The table shows a gradual reduction in volume density of the cement paste without the fly ash. The heating of the specimen at 300 °C will reduce the volume density of 400 kg/m^3. Conversely dried specimens containing fly ash still have the same density, although the temperature was raised to 300 °C. The Table 2 shows the change of volume density of solids, which were heated to the specified temperature and then refunded for 2 days in the water.

Volume density of saturated solids mixed with fly ash was 1750 kg/m^3.

Tab. 1 Properties of specimens before testing.

Temperature (°C)	Volume density of pure cement paste (kg/m^3)	Volume density of cement paste with fly ash (kg/m^3)
20	2058	1322
150	-	1339
200	1700	1303
250	-	1340
300	1604	1324
450	1625	1305

Significant reduction of volume weight is seen for cement paste containing the fly ash. A very significant difference is obtained by comparing the values for the pure cement paste and the paste mixed with the fly ash in the dry state. The difference reaches almost 700 kg/m^3.

The compressive strength of the specimen can be divided into two groups according to the content of the fly ash. In Table 2, we can see a comparison between the cement paste tested after heating and the cement paste with the fly ash, which was tested in the water-saturated state and in the dried state.

Tab. 2 Compression strength of the dried specimens.

Temperature (°C)	Pure cement paste (MPa)	Cement paste with fly ash – dried (MPa)	Cement paste with fly ash – saturated (MPa)
20	60.03	34.33	24.68
150	86.85	28.39	22.42
200	86.92	29.19	20.08
250	-	27.82	27.62
300	66.49	24.57	30.83
450	15.73	14.11	23.27

The cement paste shows increase of the strength at 200 °C. Change comes at increasing temperatures up to 450 °C, which significantly decreases the compressive strength of 75 % of the strength of 66.49 MPa at 300 °C.

Table 2 shows the compressive strength of saturated specimens and specimens prepared with the fly ash too. The saturated specimens have initially lower strength of 10 MPa in comparison with the desiccated specimens. At a temperature of 250 °C, the strengths of dried and saturated specimens mutually correspond. For saturated material the strength at 300 °C was increased compared to the values at 200 °C. Conversely dried specimens show sustained slight decrease of the strength from the outset. A significant change occurs at 450 °C, the dried paste has a significantly lower compressive strength than the saturated paste.

A very interesting result can be seen from comparison of the strength of the cement paste and the cement paste mixed with the fly ash. The tested saturated paste with the fly ash has the strength 7.5 MPa higher than the pure cement paste.

Comparison of the development of the compressive strength of the cement paste containing the fly ash is shown in Figure 1.

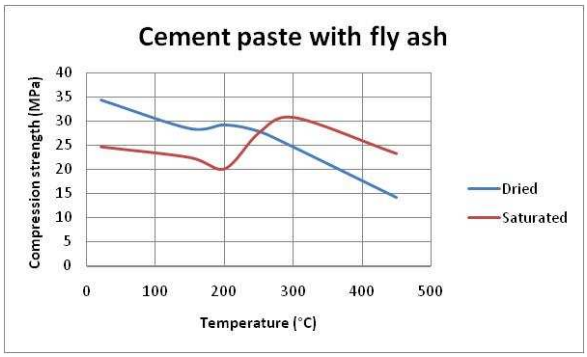

Fig. 1 Compression strength of the cement paste with the fly ash.

The results of the tensile strength in bending are shown in Table 3. The table compares the strength of the dry cement paste tested at high temperature and the dry cement paste mixed with the fly ash.

Tensile strength in bending of the cement paste culminates at a temperature of 200 °C. Conversely dried cement paste with fly ash has consistently decreasing character of the tensile strength. Initially, the strength value for pastes with the fly ash is higher than in case of the pure cement paste.

Tab. 3 Tensile strength in bending of the cement paste, and the cement paste with the fly ash – dried specimens.

Temperature (°C)	Pure cement paste (MPa)	Cement paste with fly ash – dried (MPa)	Cement paste with fly ash – saturated (MPa)
20	2.69	7.48	5.70
150	-	6.36	4.19
200	6.06	5.52	3.79
250	-	5.08	3.98
300	1.89	5.56	3.13
450	0.30	-	2.48

The ratio between the compressive strength and the tensile strength in bending is very interesting. For example, at 200 °C, the compressive strength of the pure cement paste is 14 times

greater than the tensile strength in bending. For the dried cement paste with the fly ash, this ratio is significantly lower, namely 4x.

As shown in Table 3, the declining trend in the tensile strength in bending is observable also in the saturated specimens with the fly ash. In this case, the ratio of the compressive strength and flexural strength is slightly higher than for the dried specimens, specifically 5 times.

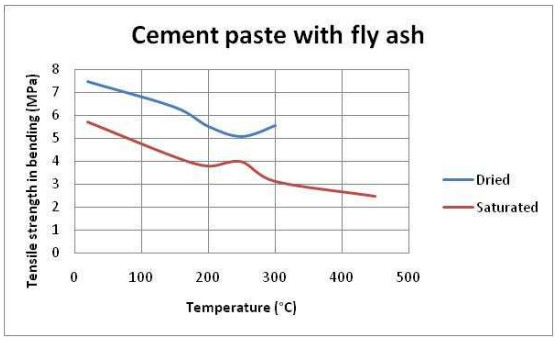

Fig. 2 Tensile strength in bending of cement paste with fly ash.

5. SUMMARY

The fly ash as a waste material in the construction industry has consolidated. As shown in the paper, the material made from the fly ash reaches comparable parameters such as the cement paste made from the Portland cement. The positive trend is reflected in the long term, when the properties of the cement paste with addition of the fly ash are improving. The cement paste mixed with the fly ash changes material properties with increasing temperature. These changes are not as dramatic as in the case of the cement paste without any additions. The perspective of the use of the fly ash in the structures of fire protection is very interesting when the cement material with the fly ash reaches the same or better properties than the pure cement paste at elevated temperature.

ACKNOWLEDGEMENT

The financial support of this experiment by the Faculty of Civil Engineering, Czech Technical University in Prague (SGS project No. 12/117/OHK1/2T/11) is gratefully acknowledged.

REFERENCES

[1] Padevět P., Mechanical Properties of Cement Pastes, International Conference 70 Years SvF STU, Bratislava, 2008.

[2] Van Mier, J.G.M., Fracture Processes of Concrete, CRC Press, 1997, ISBN 0-8493-9123-7.

[3] Bahar Demirel, B., Kelestemur, O., Effect of elevated temperature on the mechanical properties of concrete produced with finely ground pumice and silica fume, Fire Safety Journal, 45, 2010, pp. 385–391, www.elsevier.com/locate/firesaf.

CALIBRATION OF AFFINITY HYDRATION MODEL USING ARTIFICIAL NEURAL NETWORKS

Tomáš MAREŠ[1], **Eliška JANOUCHOVÁ**[2],
Anna KUČEROVÁ[3]

Abstract: *This contribution presents different strategies for application of neural networks in calibration of affinity hydration model and discusses their possible advantages and drawbacks. Precision of described methods is illustrated on simulated as well as experimental data.*

Keywords: *artificial neural networks, model calibration, affinity hydration model, cement paste*

1. INTRODUCTION

Development in numerical modelling provides the possibility to describe a lot of complex phenomena in material or structural behaviour. The resulting models are, however, often highly nonlinear and defined by many parameters, which have to be estimated so as to properly describe the investigated system and its behaviour. Basically, there are two modes of parameter identification - forward and inverse. Forward tends to be more robust. Advantage of inverse mode is computing efficiency and ease of use, however approximation of inverse mapping from model output to its parameters is hard task, since its existence is not guaranteed. Within the several last decades, a lot of attention was paid to soft computing methods such as artificial neural networks (ANNs). ANN can be applied in both modes of parameter identification, in inverse mode as approximation of mentioned inverse mapping. In forward mode as approximation of numerical model itself, in order to increase computational efficiency.

2. ARTIFICIAL NEURAL NETWORK

Artificial neural networks (ANNs)[1] are powerful computational systems consisting of many simple processing elements - so-called neurons - connected together to perform tasks analogously to biological brains. Their main feature is the ability to change their behaviour based on an external information that flows through the ANN during the learning (training) phase.

In particular, type of ANN we used was a fully connected feedforward neural network with logistic

[1] Tomáš Mareš, Faculty of Civil Engineering, Department of Mechanics, Czech Technical University in Prague, tomas.mares.1@fsv.cvut.cz

[2]Bc Eliška Janouchová, Faculty of Civil Engineering, Department of Mechanics, Czech Technical University in Prague, esikblesik@post.cz

[3]Ing Anna Kučerová, PhD, Faculty of Civil Engineering, Department of Mechanics, Czech Technical University in Prague, anicka@cml.fsv.cvut.cz

sigmoid transfer function. Parameters of ANN - so called synaptic - were optimized by conjugate gradients. Simple adaptation algorithm was employed in order to achieve appropriate number of neurons in hidden layer. It starts with one hidden node, performs learning with several restarts, chooses ANN with lowest validation error and adds another node. This procedure continues until overfitting occurs or synaptic weight given by number of training data limit is met. Finally, the resulting architecture with the lowest average error on validation set is chosen. The overfitting was indicated by fulfilling following inequality:

$$\frac{E_{v,n}}{E_{v,n-1}} > 0.99, \tag{1}$$

where $E_{v,n}$ is average error on validation set with n hidden nodes, $E_{v,n-1}$ is error on the same data, calculated in the same way, but with $n-1$ hidden nodes.

2.1. Affinity hydration model

The affinity model provides a simple framework describing all stages of cement hydration. The rate of hydration can be expressed by the temperature-independent normalized chemical affinity $\tilde{A}(\alpha)$ [2]

$$\frac{\mathrm{d}\alpha}{\mathrm{d}t} = \tilde{A}(\alpha) \exp\left(-\frac{E_a}{RT}\right), \tag{2}$$

where α stands for the degree of hydration, T is an arbitrary constant temperature of hydration, R is the universal gas constant (8.314 Jmol^{-1}K^{-1}) and E_α is the apparent activation energy.

For the hydration heat prediction, an analytical form presented in [3] is used:

$$\tilde{A}(\alpha) = B_1 \left(\frac{B_2}{\alpha_\infty} + \alpha\right)(\alpha_\infty - \alpha) \exp\left(\bar{\eta}\frac{\alpha}{\alpha_\infty}\right), \tag{3}$$

where B_1 and B_2 are coefficients related to chemical composition, α_∞ is the ultimate hydration degree and $\bar{\eta}$ represents microdiffusion of free water through formed hydrates. Then a curve of the degree of hydration development α can be obtained by the numerical integration of equation (3).

2.2. Data preparation

Since the bounds for model parameters vary in orders, one can employ the expert knowledge about the parameter meanings and before preparation of training data transform them into standardised parameters $p_i \in [0;1]$. The bounds for affinity model parameters together with theie relations to the standardised parameters p_i are given in Tab. 1.

In the space of standardised parameters we prepare a design of experiments having 100 samples based on Latin Hypercube Sampling optimised with respect to modified L_2 discrepancy. In [4] it is shown that such an experimental design has a good space-filling property and is nearly orthogonal. For each design point we perform a model simulation to obtain a bundle of 100 curves for the degree of hydration $\alpha(t)$, see Fig. 1.

Tab. 1 Bounds for affinity model parameters.

Parameter	Minimum	Maximum	Relation
B_1	10^6	10^7	$p_1 = \log B_1 - 6$
B_2	10^{-6}	10^{-3}	$p_2 = (\log B_2 + 6)/3$
$\bar{\eta}$	-12	-2	$p_3 = (-\bar{\eta} - 2)/10$
α_∞	0.7	1.0	$p_4 = (\alpha_\infty - 0.7)/0.3$

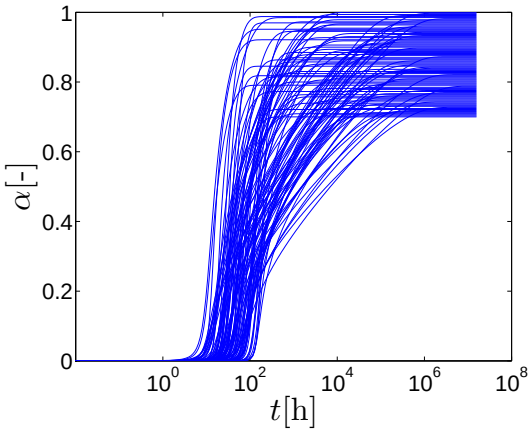

Fig. 1 Bundle of degree of hydration curves obtained for design points.

Since the model response is represented by the degree of hydration being a function of the time, the time domain is discretized into 199 steps uniformly distributed with the logarithm of the time.

Results of the described 100 simulations are also used as training data for ANNs. Then, the last preparatory step concerns the generation of validation data for evaluation of particular ANN's architecture (i.e. number of hidden nodes) and testing data for final assessment of resulting ANNs. For each of these data sets we run 50 simulations for randomly generated sets of input parameters.

2.3. Neural network application

In overall, there are two main philosophies for application of ANN in identification problems. In a forward mode/direction, the ANN is applied to approximate the model response. The model calibration then turns into a minimisation of distance between the ANN's predictions and experimental data. The efficiency of this strategy relies on the evaluation of the trained ANN to be significantly much faster than the full model simulation. Here the aim is to approximate the curve of hydration degree. This can be done in two different ways. First is based on approximation of model as a whole, i. e. mapping from parameters accompanied by time to degree of hydration. Second uses several networks to approximate

degree of hydration for given values of time (this scenario will be called fowardSplit in further text). In particular, the sequence of 10 time steps used in our experiments is $t_i = (15, 30, 45 \ldots, 195)$

In the inverse mode, there is problem how to represent curves, since usage of 199 dimensional vector as ANN input is impractical. There are again several options how to deal with this fact. Straightforward way is to make expert choice of some important time steps based on the result of sensitivity analysis. Here we have chosen the following time steps $t_i = (38, 58, 78, \ldots, 178)$. More sophisticated approach is to employ some dimensionality reduction method, for example principal component analysis, but some expert choice is needed here as well. In order to preserve intrinsic influence of model parameters to its response, the data are only mean centred and not normalised. For our task, the PCA produced only six components with relative variance higher then 0.5% and thus only these components were used as inputs for inverse mapping approximation.

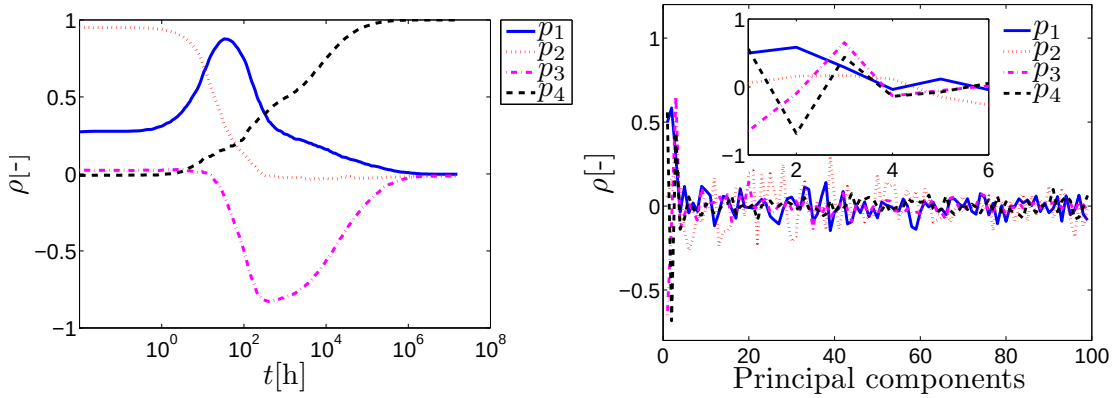

Fig. 2 Sensitivity analysis results.

2.4. Verification of model calibration

In order to evaluate the quality of particular ANNs, the relative errors ε are computed for training, validation and testing data according to

$$\varepsilon = \frac{\sum_{i=1}^{I} |O_i - T_i|}{I(T_{\max} - T_{\min})}, \tag{4}$$

where O_i are the ANN outputs, T_i are the target values (i.e. α in case of the forward mode and p_i in case of inverse mode), I is the number of samples in a given data set (training, validation or testing) and $T_{\max}$, $T_{\min}$ are the maximal and minimal target values in training data set, respectively. The validation and testing data sets consist of 50×199 samples.

We also have to compare the quality of identification procedures. While in the inverse mode the ANNs predict directly the values of model parameters, in the forward mode we have to perform an optimisation of the parameters minimising the distance between the ANN prediction and target model

response:

$$\sum_{m=1}^{M} (O(t_m) - \alpha(t_m))^2 \,, \tag{5}$$

where $M = 199$ is the number of model response components. The optimisation process is governed by the GRADE evolutionary algorithm, see [5] for details about this method[4]. The optimisation process was performed for all validation and testing data and the relative errors ε according to equation (4) for parameter predictions were then computed for all the identification modes. The obtained results are listed in table 2. To assess the quality of identification procedure in terms of model response, the model simulations were performed for all sets of identified parameters and the relative error ε was computed between the obtained responses and the original target responses. These results can be seen in Tab. 2.

Tab. 2 Results of identification procedure in relative errors ε [%]

	p_1		p_2		p_3		p_4		α	
	valid	test	valid	test	valid	test	valid	test	valid	test
Forward	7.70	7.39	11.56	14.83	4.52	3.61	1.88	1.86	0.60	0.52
ForwardSplit	2.03	1.78	0.54	0.75	1.30	1.04	0.05	0.06	0.18	0.16
InvPCA	5.95	6.57	7.98	13.25	2.22	2.34	0.23	0.31	0.63	0.74
InvExpert	1.40	1.26	1.09	2.63	2.90	2.72	0.10	0.16	0.39	0.35

It can be seen, that easier and more straightforward approaches achieved better results especially in terms of parameter values

2.5. Validation of model calibration

The previous section was focused on mutual comparison of the presented identification strategies on simulated data. However, a complete comparison has to include their validation on experimental data. To that purpose we used the curve of hydration degree obtained by isothermal calorimetry for a cement "Mokra" CEM I 42.5 R taken directly from Heidelberg cement group's kiln in Mokrá, Czech Republic [3].

In general, validation does not allow for a comparison in terms of parameters value, because these are not known a priori. Nevertheless, the simplicity and the fast simulation of affinity hydration model permit a direct optimisation of model parameters without any incorporated approximation and the result-

[4]The parameters of GRADE algorithm were set to pool_rate = 4, radioactivity = 0.33 and cross_limit = 0.1. The algorithm was stopped after 10000 cost function evaluations.

ing optimal parameter values can be compared with the results obtained using the ANN approximations.

Cost functions were formulated in following way:

$$F_1 = \sum_{m=1}^{M} (\alpha(t_m) - \alpha^{\mathrm{Mokra}}(t_m))^2 , \quad (6)$$

$$F_2 = \sum_{m=1}^{M} |\alpha(t_m) - \alpha^{\mathrm{Mokra}}(t_m)| , \quad (7)$$

where $M = 199$ stands again for number of discretized values of hydration degree, $\alpha(t_m)$ is the model response and $\alpha^{\mathrm{Mokra}}(t_m)$ are the interpolated experimental data. We applied again the GRADE algorithm with the same setting as in the previous section to minimise the both cost functions (6) and (7). The obtained parameter and cost functions values are written in Tab. 3 and the resulting degree of hydration

Tab. 3 Parameter values identified on experimental data obtained for "Mokra"cement.

Method	p_1	p_2	p_3	p_4	F_1	F_2
Direct1	0.856	1.000	0.208	0.053	0.002	0.336
Direct2	0.858	1.000	0.208	0.050	0.002	0.271
Forward	0.922	0.911	0.339	0.051	0.135	2.333
ForwardSplit	1.000	0.859	0.380	0.070	0.145	2.85
InversePCA	0.875	0.740	0.133	0.052	0.102	1.898
InverseExpert	0.736	1.100	0.124	0.051	0.023	2.850

curves can be compared with experimental data in Fig. 3.

Subsequently, the both forward and inverse modes of identification were applied to the experimental data using the prepared ANNs. The identified parameters are again written in Tab. 3 and corresponding simulated degrees of hydration are plotted in Fig. 3.

Surprisingly, validation results do not correspond fully to verification results. There is obvious error increase in both forward identification approaches. By detail comparison, we found out, that part of experimental data lies outside bounds defined by data used for ANN. This problem was solved by introducing 5 time steps offset, which moved experimental data back to boundaries. Resulting parameters and errors can be seen in Tab. 4 and on Fig. 4, one can easily observe increased precision of all identification procedures.

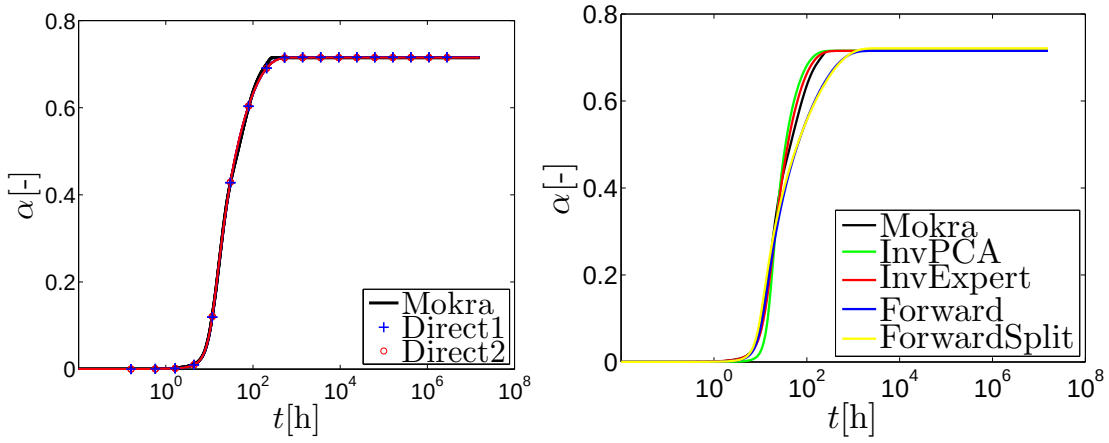

Fig. 3 Comparison of experimentally obtained degree of hydration for "Mokra" cement with simulations for directly optimised model parameters (left). Results obtained with varios usages of ANN (right)

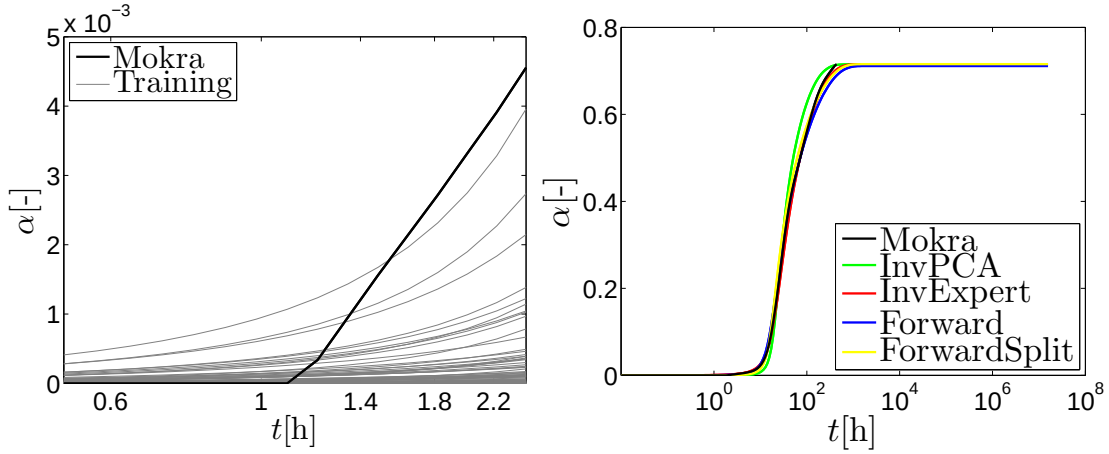

Fig. 4 Part of original data for "Mokra" out of bounds (left). Resulting curves after moving original data 5 steps forward

3. CONCLUSIONS

The presented paper tries to review possible applications of artificial neural networks in calibration of numerical models. The basic identification modes are described in details: the forward and the inverse. Their advantages and drawbacks are illustrated on calibration of affinity hydration model. Verification of the procedures is performed using 50 independent testing data obtained from numerical simulations and experimental data obtained for cement "Mokra" CEM I 42.5 R are subsequently employed for the validation of the presented methods. The main advantage of the inverse approach is an easy application to new measurements. The computationally consuming and difficult part concerns the ANN development which has to be done only once. However the validation on experimental data revealed the importance of knowing a priori the parameter bounds because of ANNs poor extrapolation abilities.

Tab. 4 Parameter values identified on experimental data obtained for adjusted experimental data

Method	p_1	p_2	p_3	p_4	F_1	F_2
Direct1	0.647	1.000	0.208	0.053	0.002	0.332
Direct2	0.650	1.000	0.207	0.050	0.002	0.268
Forward	0.718	0.958	0.255	0.038	0.017	1.114
ForwardSplit	0.816	0.757	0.265	0.052	0.021	0.891
InvPCA	0.768	0.706	0.173	0.050	0.077	1.619
InvExpert	0.571	1.098	0.186	0.050	0.005	0.423

ACKNOWLEDGEMENT

The financial support of this work by the Czech Science Foundation (project No. 105/11/P370) is gratefully acknowledged.

REFERENCES

[1] Gurney, K. N. *An introduction to neural networks* UCL Press, London, 2002, ISBN 1857285034

[2] Gawin D., and Pesavento F. and Schrefle B. *Hygro-thermo-chemo-mechanical modelling of concrete at early ages and beyond. Part I: Hydration and hygro-thermal phenomena* International Journal for Numerical Methods in Engineering vol 67, number 3, 2006, ISSN 1097-0207

[3] Šmilauer V. *Multiscale Modeling of Hydrating Concrete* Saxe-Coburg Publications, Stirling, 2012, ISSN 1759-3158

[4] Janouchová E. and Kučerová A. *Competitive Comparison of Optimal Designs of Experiments for Sampling-based Sensitivity Analysis* Computers & Structures, arXiv/1201.0942, 2011, ISSN 0045-7949

[5] Kučerová A. *Identification of nonlinear mechanical model parameters based on softcomputing methods* PhD thesis, Ecole Normale Supérieure de Cachan, Laboratoire de Mécanique et Technologie, 2007

COMPARISON OF MAXIMIN LHS DESIGN STRATEGIES

Eva MYŠÁKOVÁ[1], Matěj LEPŠ[2]

Abstract: *The paper is focused on methods for designs of experiments (DoEs). We are interested in LHS designs of experiments in multidimensional regular design spaces within hypercubes. The main objective placed on the designs is their space-filling property. The quality of resulting designs is measured by Euclidean Maximin distance (EMM). The paper presents several methods that use hill climbing or simulated annealing algorithms. It also provides a comparison of their computational demands and quality of resulting designs.*

Keywords: *design of experiment, space-filling, Latin Hypercube Sampling, maximin, simulated annealing*

1. INTRODUCTION

The designs of experiments (DoEs) constitute an essential part of the development of any meta-model (surrogate) [1, 2]. The aim is to gain maximum knowledge from a given system with a minimum number of evaluations. Since we assume that the final meta-model is *a priori* unknown, the design should be spread over the domain as uniformly as possible. The effectiveness of such DoE can be measured by several criterions aiming mainly at orthogonality or space-filling properties. See references [3, 4] for orthogonal and sources [5, 6] for space-filling criterions. We have selected the *Euclidean Maximin distance* (*EMM*) for its simplicity and easiness in visualization. The *EMM* is the minimal distance out of all distances between any two design points and is to be maximized. The use of this metric is suitable for classical real (physical, chemical, biological, etc.) experiments as well as for virtual experiments called simulations (e.g. army's combat scenarios). We introduce several methods that create designs with a fixed, predetermined number of design points in Section 2. Section 3 then presents results and conclusions.

2. METHODS

In this section several methods are presented. Note that designs are created in a unitlesss domain $\langle 0, 1\rangle^n$, where n is the number of dimensions; the real designs are created by linear transformation to user-specific bounds.

[1]Bc. Eva Myšáková , Faculty of Civil Engineering, Czech Technical University in Prague, eva.mysakova@fsv.cvut.cz

[2]Ing. Matěj Lepš, Ph.D., Faculty of Civil Engineering, Czech Technical University in Prague, leps@cml.fsv.cvut.cz

2.1. METHOD `STANDARD_LHS`

The Latin Hypercube Sampling (LHS) is one of the most popular space-filling algorithms, although its resulting space-filling properties can be very low. In the LHS, each variable (dimension) is divided into n intervals, where n is a number of desired design points. In each interval, a point is placed randomly (property `smooth on`) or in the middle of the interval (property `smooth off` in MATLAB.), independently for each variable. There is only one point in each interval of each variable (dimension). This leads to a regular DoE, see e.g. Figure 1. The worst LHS design is such that all points lie on a diagonal (Figure 2). This design has bad both, space-filling properties as well as high correlation. To solve this deficiency, the simplest solution is to create a brand new LHS design, i.e. an application of "a brute force method". This is used for example in MATLAB environment within the `lhsdesign` routine[3]. Hereafter, we denote this method as `standard_LHS`.

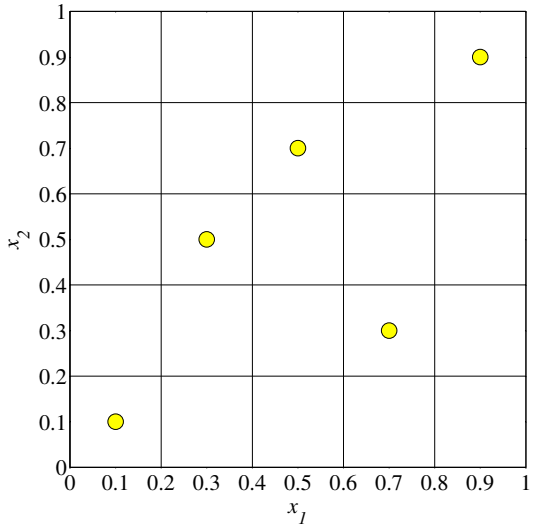

Fig. 1 LHS design - 2 variables and 5 points.

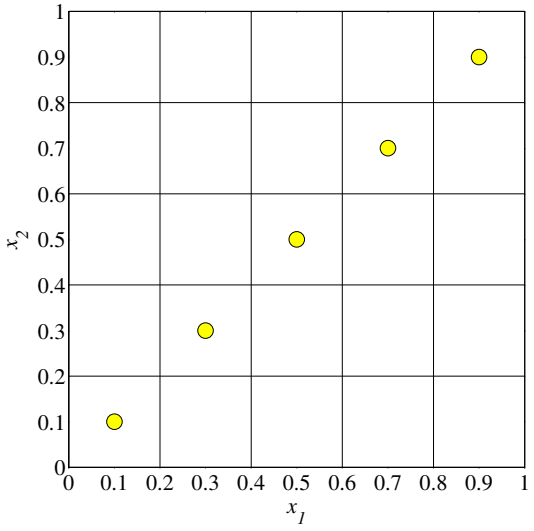

Fig. 2 Improper LHS design.

2.2. METHOD `RANDOM_RANDOM_EXCHANGE`

A bad LHS design (from the view of *EMM* metric) can be also improved by changing the positions of individual points (with preservation of LHS properties - i.e. "sudoku rules" in 2D), see e.g. references [5, 7] for more details. Two points and one variable are selected and then the corresponding coordinates of selected points are exchanged. All three selections are random. At each iteration, we accept only a successful step (rise of *EMM* value), and therefore, we can denote this method as the random Hill Climbing algorithm. As we can see in Figure 3, only exchange with one of critical points (points with minimal interpoint distance - *EMM*) can be successful - this is guaranteed in the next method.

[3]With the default settings, MATLAB generates 5 samples and the best is introduced to a user.

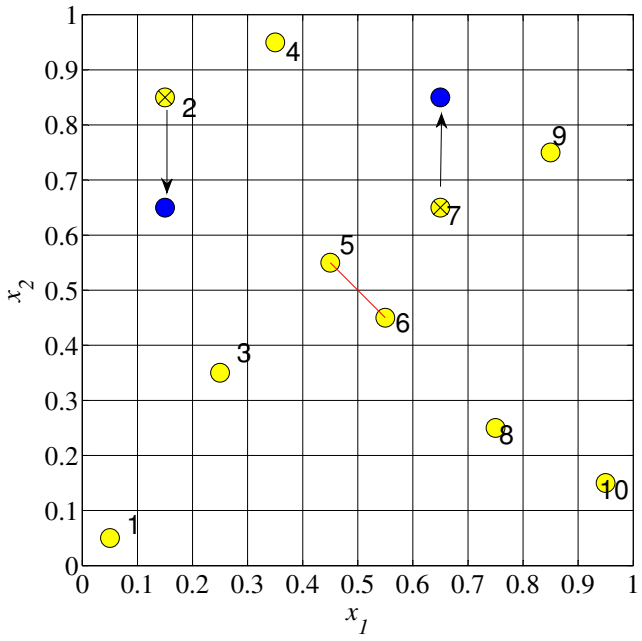

point	coordinates x_1	x_2
1	0.05	0.05
2	0.15	***0.85*** $\rightarrow$ ***0.65***
3	0.25	0.35
4	0.35	0.95
5	0.45	0.55
6	0.55	0.45
7	0.65	***0.65*** $\rightarrow$ ***0.85***
8	0.75	0.25
9	0.85	0.75
10	0.95	0.15

Fig. 3 An exchange of two random sample points (here in coordinate x_2). Red line shows EMM. This change does not lead to a rise of EMM value, therefore it will not be accepted.

2.3. METHOD `RANDOM_CMIN_EXCHANGE`

Since we know, which pair of points (or more pairs of points - particularly with property `smooth off`) creates the worst value within the *EMM* metric, we have applied heuristic procedure, where we try to change the position of these critical points (i.e. to destroy the existence of that too much close pairs). The algorithm is changing one (randomly chosen) coordinate of a critical point (it is chosen randomly, which point from the pair is going to exchange) and one randomly chosen point until an improvement occurs - the *EMM* value rises. After that new critical points are found and the process is repeated.

2.4. SIMULATED ANNEALING (SA)

Simulated annealing is frequently used algorithm [8, 7, 9], which seams to be suitable for the use with above described methods. The algorithm is based on an analogy with annealing of steel to remove the imperfections in its structure. It is efficient for its ability to leave the local optimum. The algorithm enables acceptance of a worse then the best so far reached solution. Then better local optimum or even global optimum can be found. A worse solution is accepted with certain probability which depends on a parameter called temperature. In accordance to the speed of convergence the temperature is reduced which also reduces the probability of acceptance of a worse solution. Figure 4 shows the example of the history of one run of the algorithm.

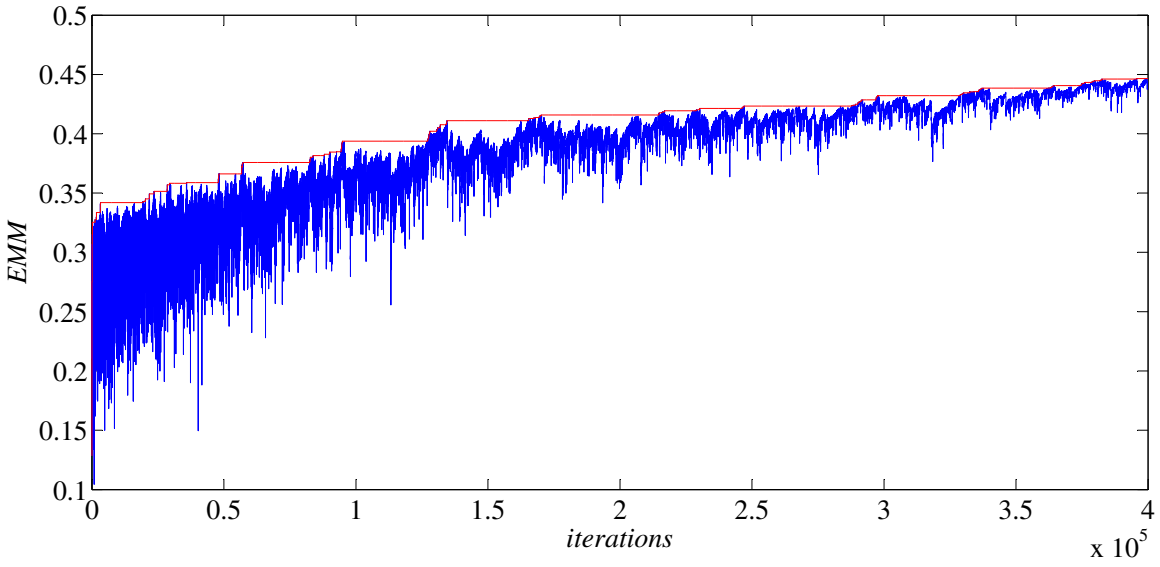

Fig. 4 Simulated Annealing. Red line shows the best EMM value reached during the run.

2.5. ITERATED LOCAL SEARCH WITH PERTURBATIONS

This method presented and described in [10] is also based on changing of design points coordinates. However, points and coordinates for exchange are not chosen randomly but systematically in a "local search" part of the algorithm. When all possibilities of successful exchanges are exhausted the pertur-

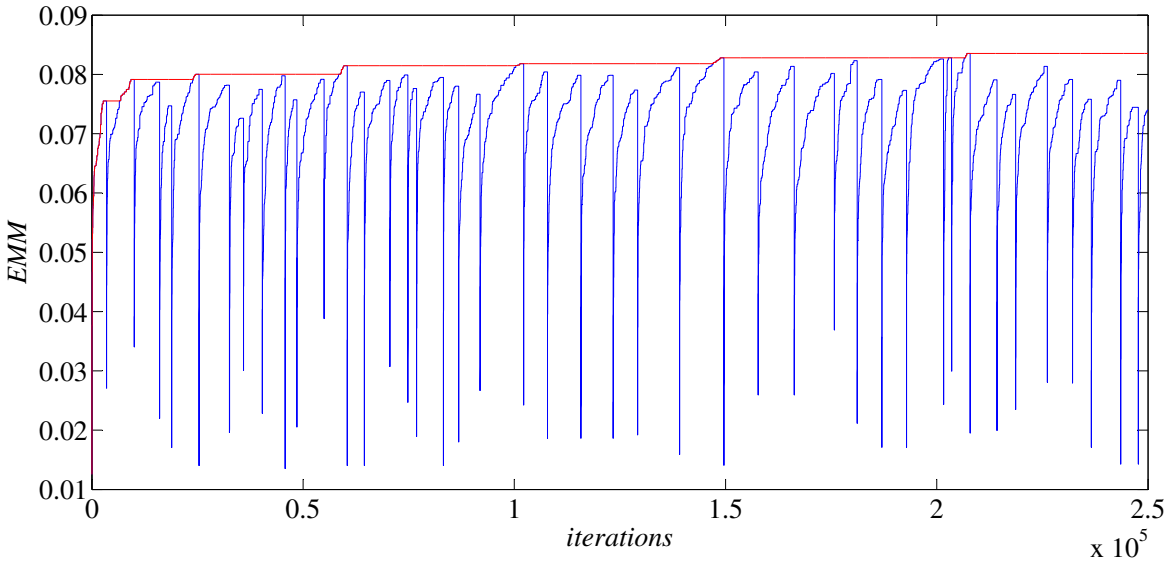

Fig. 5 Iterated local search with perturbations in 2D. The figure shows actual EMM value in each iteration. It is clear that quality of design right after perturbation is very low. It rises during running of the local search. Red line shows the best reached EMM value.

bation phase is started. In this random part of the method, the design matrix (matrix of design points coordinates) is slightly modified. One coordinate and a subset of consecutive design points are chosen and the chosen coordinates of these points are "circshifted". The motivation is to leave local optimum reached by the local search. When perturbation is done, a new local search is applied again on that slightly modified design. The progress of the method is illustrated in Figure 5.

3. RESULTS AND CONCLUSIONS

The algorithms were implemented in MATLAB and we present a statistic from 10 runs of each algorithm. All designs have 100 design points. We use functions `lhsdesign` which is included in MATLAB's statistical toolbox. Interpoint distances and the *EMM* values were computed by an effective algorithm from the MATLAB function `lhsdesign`.

It is evident from Figures 6 and 7 that the `standard_LHS` cannot compete with other methods. The methods `random_random_exchange` and `random_Cmin_exchange` reached similar values after a sufficient number of iterations. However the `random_Cmin_exchange` method is better in cases of the restricted number of iterations. Simulated annealing provides improvement in all examples, especially for designs with property `smooth off`. Iterated local search with perturbations produces very good designs. However it needs to be mentioned that only few perturbations were done in case of 5D and 10D designs in results presented here (with these numbers of iterations).

Our contribution has shown results for rectangular domains. Our next research will focus on designs in constrained and/or irregular design spaces.

Legend for Figures 6 and 7:

	`standard_LHS`	100000 it.
	`random_random_exchange`	400000 it.
	`random_random_exchange` - SA	400000 it.
	`random_Cmin_exchange`	400000 it.
	`random_Cmin_exchange` - SA	400000 it.
	`ILS + perturbations`	250000 it.
	minimum for LHS with property `smooth off`	
	2D - theoretical maximum for LHS [11]	
	5D - maximum for LHS reached by a periodical design [7]	
	10D - maximum for LHS reached by ILS + perturbation [10]	

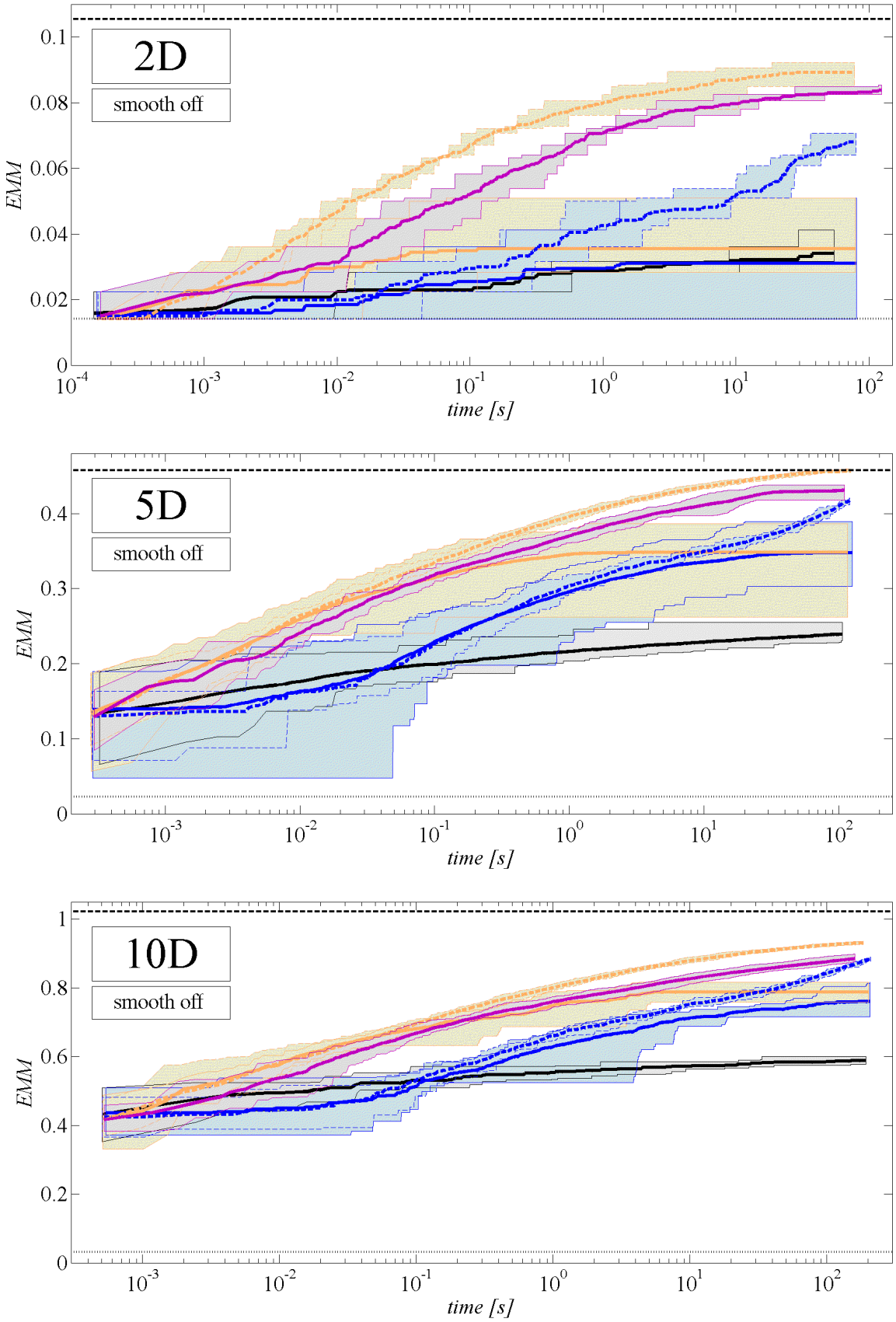

Fig. 6 The comparison of speed (time) and quality (EMM - higher is better) of presented methods. `smooth off` *- the design points are placed in the middle of intervals.*

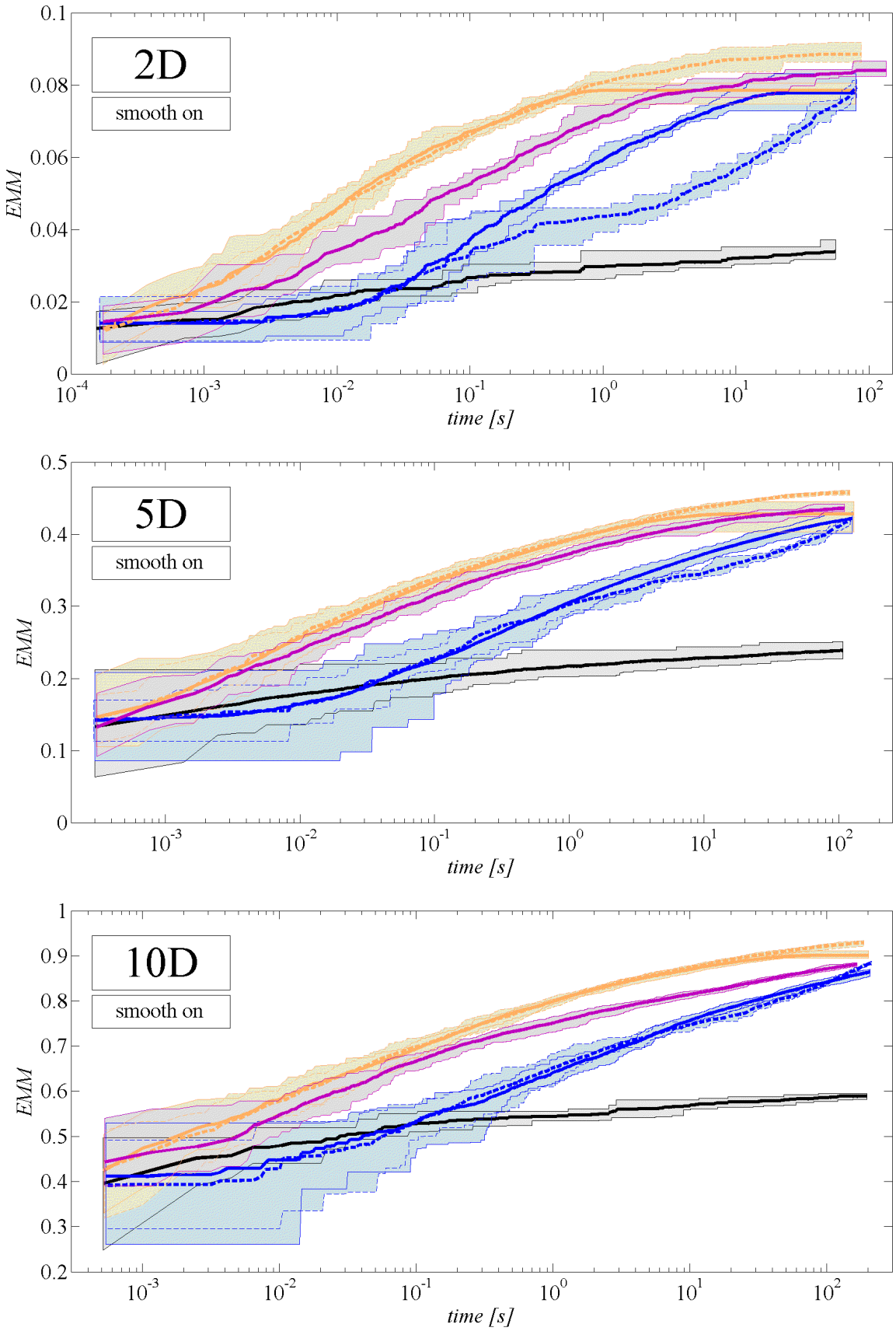

Fig. 7 The comparison of speed (time) and quality (EMM - higher is better) of presented methods. `smooth on` *- the design points are placed randomly within intervals.*

ACKNOWLEDGEMENT

We acknowledge the financial support from the Grant Agency of the Czech Republic - Project No. P105/12/1146 and from the Technology Agency of the Czech Republic through the project TA01030733.

REFERENCES

[1] Simpson, T. W. - Peplinski, J. D. - Koch, P. N. - Allen, J. K. *Metamodels for Computer-based Engineering Design: Survey and recommendations*, Engineering with Computers, 2001, 17:129-150.

[2] Jin, Y. *A comprehensive survey of fitness approximation in evolutionary computation*, Soft Computing, 2005, 9:3-12.

[3] Cioppa, T. M. - Lucas, T.W. *Efficient Nearly Orthogonal and Space-Filling Latin Hypercubes*, Technometrics, 2007, 49(1):45-55.

[4] Janouchová, E. - Kučerová, A. *Competitive Comparison of Optimal Designs of Experiments for Sampling-based Sensitivity Analysis*, Computers & Structures, Sent for publication, 2011.

[5] Morris, M. D. - Mitchell, T. J. *Exploratory designs for computational experiments*, Journal of Statistical Planning and Inference, 1995, 43:381-402.

[6] Bursztyn, D. - Steinberg, D. *Comparison of designs for computer experiments*, Journal of Statistical Planning and Inference, 2006, 136(3):1103-1119.

[7] Husslage, B. G. M. *Maximin designs for computer experiments*, PhD thesis, Universiteit van Tilburg, 2006.

[8] Novák, D. - Lehký, D. *ANN inverse analysis based on stochastic small-sample training set simulation*, Engineering Applications of Artificial Intelligence, 2006, 19(7):731-740.

[9] Kučerová, A. *Identification of nonlinear mechanical model parameters based on softcomputing methods*, PhD thesis, Ecole Normale Supérieure de Cachan, Laboratoire de Mécanique et Technologie, 2007.

[10] Grosso, A. - Jamali, A.R.M.J.U. - Locatelli, M. *Finding maximin latin hypercube designs by Iterated Local Search heuristics*, European Journal of Operational Research, 2009, 197(2):541-547.

[11] van Dam, E. R. - Rennen, G. - Husslage, B. *Bounds for Maximin Latin Hypercube Designs*, Operations Research, 2009, 57(3):595-608.

VERIFICATION OF COCCIOPESTO MORTAR MICROMECHANICAL MODEL

Václav NEŽERKA[1], Jan ZEMAN[2], Pavel TESÁREK[3]

Abstract: *In order to study the behavior of traditional lime-based mortars containing crushed bricks or other clay products, known as cocciopesto, a micromechanics-based model had been proposed. The Mori-Tanaka homogenization scheme seems to be suitable for such type of composite. The mortar components were modeled as spherical inhomogeneities, coated by C-S-H gel in case of crushed brick particles or by a layer having reduced stiffness (interfacial transition zone) around the particles of sand. The calculated effective stiffness of the cocciopesto mortar samples was compared with the experimentally obtained data. The study indicated how important is to know the mortar microstructure and material properties of the individual components.*

Keywords: *cocciopesto, C-S-H coating, ITZ, stiffness homogenization, micromechanical modeling*

1. INTRODUCTION

Cocciopesto is a traditional historic lime-based mortar containing, beside lime and sand, also the pieces of crushed bricks or other clay products, such as pottery. The use of mortars manufactured according to traditional recipes and procedures proved to be better solution than exploiting new incompatible materials. Authorities dealing with cultural heritage encourage using strictly the materials compatible with the original ones [1].

Crushed bricks were added to mortar first by Phoenicians, who were ignorant of the chemical processes in the mortar, but they knew by experience that addition of burnt clay products can increase the mortar durability and strength. Romans called such material *cocciopesto* and used it in areas where other natural pozzolans were not available. The non-linear behavior of the mortar allows for a better energy dissipation and that explains the extraordinary durability of some ancient structures [2].

It was found that cocciopesto exhibits a hydraulic character due to formation of C-S-H gel on the lime-brick interface — the thin layer of the gel was reported by many papers. However, the bricks must be made of clay and burnt at the appropriate firing temperature (which is about 600-900°C [3]).

[1]Ing. Václav Nežerka, Faculty of Civil Engineering, Czech Technical University in Prague, vaclav.nezerka@fsv.cvut.cz

[2]Doc. Ing. Jan Zeman, Ph.D., Faculty of Civil Engineering, Czech Technical University in Prague, zemanj@fsv.cvut.cz

[3]Ing. Pavel Tesárek, Ph.D., Faculty of Civil Engineering, Czech Technical University in Prague, tesarek@fsv.cvut.cz

The goal of this work is to verify the micromechanical model proposed in [4], only with a slight change that the concentration factors for the coated particles are found using Herve-Zaoui scheme [5]. Works of Pichler and Hellmich [6], Smilauer et al. [7] and Vorel et al. [8], provided an inspiration for the development of micromechanical models as they exploited the Mori-Tanaka method [9, 10] on micro- and mesoscale to estimate the effective stiffness of concrete.

2. MODEL

The mortar microstructure can be modeled as a composite consisting of a matrix, voids (v), inert materials (I), such as sand, and chemically active materials (A), such as crushed bricks. All the inhomogeneities embedded in a matrix are assumed to be spherical. The chemically active phases are covered by a coating that represents various hydration products, such as C-S-H gel. The imperfect bond between the sand particles and the matrix is introduced into the model as Interfacial Transition Zone (ITZ), which is formed around the aggregates also in concrete [11] (see Fig. 1). ITZ is characterized by a lower stiffness compared to the surrounding matrix.

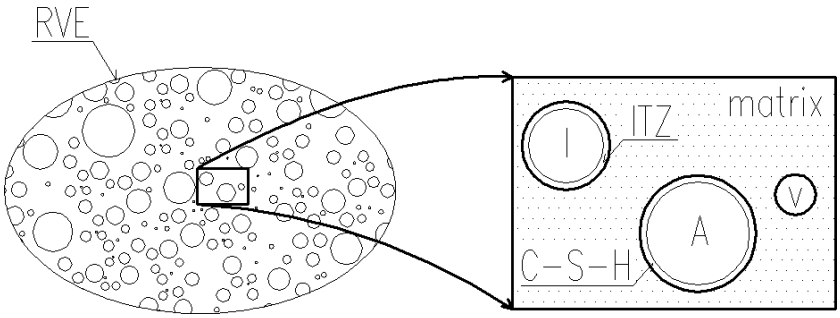

Fig. 1 Simplified microstructure in representative volume element (RVE) of mortars

The effective mortar properties are estimated using Mori-Tanaka method for which the dilute concentration factors representing the coated particles (bricks and sand) and their coating (C-S-H and ITZ) are calculated using the Herve-Zaoui solution [5].

2.1. MORI-TANAKA SCHEME

In Mori-Tanaka scheme ([9, 10]) the strain in individual inhomogeneities is not directly dependent on the externally applied load (macroscopic strain), but rather on a strain in the matrix, which is approximated by a constant field.

In the special case of an isotropic matrix containing spherical inhomogeneities, the Mori-Tanaka method also yields an isotropic overall behavior, irrespective of the spatial arrangement of the phases. Therefore, the dilute concentration factors and the effective elasticity tensor can be decomposed into their volumetric and deviatoric parts as follows:

$$A^{(r)}_{\mathrm{dil,K}} = \frac{K^{(0)}}{K^{(0)} + \alpha^{(0)}(K^{(r)} - K^{(0)})} \tag{1a}$$

$$A^{(r)}_{\mathrm{dil,G}} = \frac{G^{(0)}}{G^{(0)} + \beta^{(0)}(G^{(r)} - G^{(0)})} \tag{1b}$$

and

$$K^{\mathrm{eff}} = \frac{c^{(0)}K^{(0)} + \sum_{r=1}^{n} c^{(r)}K^{(r)}A^{(r)}_{\mathrm{dil,K}}}{c^{(0)} + \sum_{r=1}^{n} c^{(r)}A^{(r)}_{\mathrm{dil,K}}} \tag{2a}$$

$$G^{\mathrm{eff}} = \frac{c^{(0)}G^{(0)} + \sum_{r=1}^{n} c^{(r)}G^{(r)}A^{(r)}_{\mathrm{dil,G}}}{c^{(0)} + \sum_{r=1}^{n} c^{(r)}A^{(r)}_{\mathrm{dil,G}}} \tag{2b}$$

where the superscripts (0) and (r), represent the matrix and general inhomogeneity, respectively; individual phases in the equations above are represented by their volumetric fractions, and by their bulk, $K^{(r)}$ and shear moduli, $G^{(r)}$. The parameters $\alpha^{(0)}$ and $\beta^{(0)}$ represent the volumetric and deviatoric part of Eshelby tensor and can be for the spherical inhomogeneities embedded in an isotropic matrix calculated as

$$\alpha^{(0)} = \frac{1+\nu^{(0)}}{3(1+\nu^{(0)})} \quad \text{and} \quad \beta^{(0)} = \frac{2(4-5\nu^{(0)})}{15(1-\nu^{(0)})} \tag{3}$$

In such case, these parameters depend only on the matrix Poisson's ratio, $\nu^{(0)}$.

2.2. HERVE-ZAOUI SCHEME

Herve and Zaoui [5] found an analytical solution for the elastic strain and stress fields in an infinite medium constituted of an n-layered isotropic spherical inclusion, embedded in a matrix subjected to uniform stress or strain conditions at infinity. The integration constants were found using the continuity conditions and equilibrium of stresses on the interface of individual phases. The dilute concentration factors for the coated inclusions can be found separately by means of their volumetric and deviatoric parts.

The dilute concentration factors for individual layers of the spherical inclusion can be found as

$$A^{(i)}_{\mathrm{dil,K}} = F_i \tag{4}$$

representing the volumetric part while the deviatoric part of the dilute concentration factor for the inner sphere ($i = 1$) can be found as:

$$A^{(1)}_{\mathrm{dil,G}} = A_1 - \frac{21}{5}\frac{{r^{(1)}}^2}{1-2\nu^{(1)}}B_1 \tag{5}$$

and for the other layers as

$$A^{(i)}_{\mathrm{dil,G}} = A_i - \frac{21}{5}\frac{{r^{(i)}}^5 - {r^{(i-1)}}^5}{(1-2\nu^{(i)})({r^{(i)}}^3 - {r^{(i-1)}}^3)}B_i \tag{6}$$

for $i = 2, ..., n$. The formulation of the matrices needed for the calculation of the concentration factors, $A^{(i)}_{\mathrm{dil,K}}$ and $A^{(i)}_{\mathrm{dil,G}}$, can be found in the paper by Herve and Zaoui [5].

3. MATERIALS

There were two mixes prepared and tested for the verification of the model, labeled as CI and CII (standing for cocciopesto I and cocciopesto II). These two mortars are identical, except for the binder to aggregate mass ratio, which was 1 : 4.5 in case of CI and 1 : 3 in case of CII mortar. At the day of testing the samples were approximately six months old.

The amount of water was just roughly calculated for each mixture and then adjusted to fulfil the flow table workability test (slump test) requirement, which was prescribed as 15±1 cm in diameter (according to DIN 85555). Both, CI and CII, samples had the values of flow table workability test 14.5× 14.5 cm, satisfying the requirement. The volume of air in the fresh CI and CII mortar samples was 4.4 % and 3.6 %, respectively.

3.1. MATRIX

The binder was identical for both mixes, CI and CII, and it consisted of pure lime and metakaolin in a mass ratio 7 : 3. The used white air-slaked lime (CL90) Čertovy schody has a great purity, 98% of CaO + MgO (97.4% CaO, 0.6% MgO, 0.13% SO_3 and 0.1% SO_2) [12]. Finely ground, highly reactive metakaolin (Mefisto L05), manufactured in ČLUZ a.s. Nové Strašecí, was used. Main components of the metakaolin Mefisto L05 are SiO_2 (58.7%) and Al_2O_3 (38.5%), K_2O (0.85%), Fe_2O_3 (0.72%), TiO_2 (0.5%), MgO (0.38%), and CaO (0.2%) [12].

Alongside with the mixes CI and CII also the pure lime / metakaolin paste without aggregates was prepared to investigate its porosity, stiffness and mass development. It was found that from 1 g of lime / metakaolin powder (mass ratio 7 : 3) produces 1.43 g of paste (i.e. the matrix). From the preliminary nanoindentation results it was estimated that the average paste stiffness (after recalculation due to microporosity) is approximately $E^{(0)} = 11000$ MPa. Porosity of the paste was determined from the bulk (1066 kg/m^3) and matrix density (2298 kg/m^3), obtained using pycnometers and its value is 53.6 %.

3.2. AGGREGATES

The aggregates were composed of two components – crushed bricks and sand. The size distribution and mass ratios are summarized in Tab. 1.

Tab. 1 Aggregate size distribution of sand and crushed bricks

fraction [mm]	0.063-0.125	0.125-0.25	0.25-0.5	0.5-1.0	1.0-2.0	2.0-4.0
crushed bricks (mass portion)	1	4	7.5	10	11	25
sand (mass portion)	10.8	43	80.6	107.5	118.3	29.9

The bulk densities of brick and sand were experimentally determined as 2277 kg/m^3 and 2720 kg/m^3, respectively. Their Young's moduli and Poisson's ratios were found in the literature, see Tab. 2.

3.3. C-S-H GEL COATING

A thickness of the C-S-H layer at the brick interface is assumed to be about 20 μm for the calculations; the backscattered electron image of the interface can be seen in Fig. 2, which is reproduced from [13].

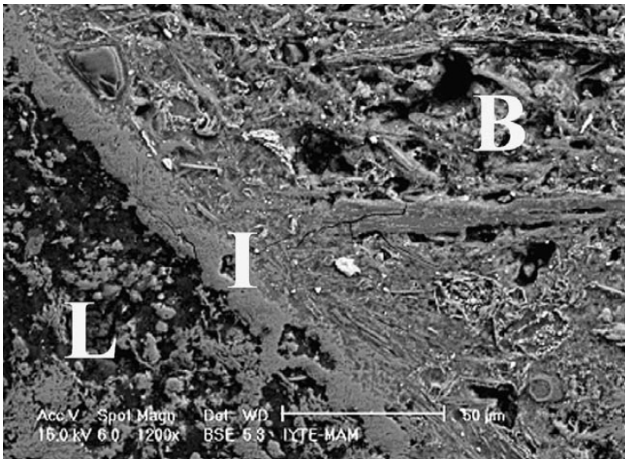

Fig. 2 Brick interface (I) between lime matrix (L) and brick aggregate (B), reproduced from [13]

The estimate of the thickness and elastic stiffness of C-S-H gel coating was based on literature study. For the calculation of the effective properties of cocciopesto mortars, values representing the low-density C-S-H gel [14] were considered. The nanoindentation results showed that the low-density C-S-H phase has a mean stiffness of about 22000 MPa [15], the density of the gel in calculation was considered as 2000 $\mathrm{kg/m^3}$, as suggested in [16] and Poisson's ratio as 0.20. It is assumed that the created C-S-H gel around the brick particles only fills the voids and does not consume any matrix or brick. It is in agreement with works of Velosa et al. [17], Vejmelková et al. [12], or Baronio et al. [2], who found a reduction in porosity in hydraulic mortars, if the hydration products were created.

3.4. INTERFACIAL TRANSITION ZONE (ITZ)

The cohesion (bond) between the round-shaped river sand grains and the matrix is probably far from perfect. This fact together with the difference in elastic moduli of the matrix and sand results in formation of ITZ having significantly lower stiffness compared to the surrounding matrix.

In case of concrete Yang [11] proposed the thickness of ITZ around the aggregates in thickness 20 μm and having the elastic modulus about 20 % to 40 % of the surrounding matrix. However, in case of lime-based mortars and round-shaped sand the reduction of the modulus in ITZ is probably higher and in our study we estimate its value to be approximately 200 MPa. This value gives a satisfactory agreement between the calculated effective moduli and those obtained from experiments.

Tab. 2 Properties of individual components used for calculations

	density [kg/m^3]	E [MPa]	ν [-]	source	mass portion [-]	note
matrix	2298	12500	0.25	-	1.014 (CI), 1.521 (CII)	-
sand	2720	70000	0.17	[8]	2.718	-
clay brick	2270	2400	0.17	[18]	0.408	-
voids	-	0	0.25	-	-	30 % of volume
C-S-H gel	2000	22000	0.20	[16, 15]	-	thickness 20μm
ITZ	2298	200	0.25	-	-	thickness 20μm

4. RESULTS AND DISCUSSION

The effective elastic mortar stiffness was determined from the experimentally measured strain during the compression test. The test was performed on prismatic samples, having approximately following dimensions: 160 × 40 × 40 mm. The length of the samples was sufficient for placement of an extensometer and the loading was performed in three cycles. The samples exhibited slight hardening and reading from the third loading cycle was considered in the evaluation of the effective elastic mortar stiffness.

Because of an insufficient amount of samples, the results cannot be considered as exact but they only indicate that the sample CII is stiffer in comparison with CI (richer in aggregates). The experimentally obtained Young's moduli for CI and CII mortar samples are $E_{\mathrm{CI}}^{\mathrm{eff,exp}}$ = 5227 MPa and $E_{\mathrm{CII}}^{\mathrm{eff,exp}}$ = 6534 MPa, respectively. This corresponds to the results of three point bending tests performed few months before the testing in compression, where the stiffness of notched beams was also higher in case of CII mortar.

Considering the material properties of individual components as indicated in Tab. 2 the microme-

chanical model predicts the effective stiffness of the mortar samples CI and CII to be $E_{\mathrm{CI}}^{\mathrm{eff,cal}}$ = 5703 MPa and $E_{\mathrm{CII}}^{\mathrm{eff,cal}}$ = 6279 MPa, respectively. All the calculations were done in MATLAB environment and the code can be downloaded at `mech.fsv.cvut.cz/~nezerka/software`.

5. CONCLUSION

The study confirms that the micromechanical modeling can despite a few simplifications, mainly in geometry, predict the properties of cocciopesto mortars.

The authors are aware that more samples should be experimentally tested and another set of experiments will be carried out soon. The mortar samples should be also composed of a smaller amount of components for easier identification of their influence on the effective properties.

Also the properties of individual constituents, mainly their stiffness, should be further investigated to obtain more accurate results from the calculations. Comprehensive input data should be obtained by means of nanoindentation, including the stiffness of sand particles. Also the mercury intrusion porosimetry should be exploited for estimation of the pore size distribution in the matrix. Consequently, the elastic stiffness of the matrix could be estimated with a significantly higher accuracy.

The model indicated that the layers around the particles, i.e. C-S-H coating of bricks and ITZ around the sand, plays a crucial role in determination of the effective mortar stiffness. Therefore the areas close to grains should be also carefully investigated.

ACKNOWLEDGEMENT

The authors would like to thank for the financial support by the grant no. SGS12/027/OHK1/1T/11.

REFERENCES

[1] D. Michoniová. *Questions about renovation plasters (in czech).* Zprávy památkové péče, 65:313–316, 2005.

[2] G. Baronio, L. Binda, and N. Lombardini. *The role of brick pebbles and dust in conglomerates based on hydrated lime and crushed bricks.* Construction and Building Materials, 11:33–40, 1997.

[3] A. Moropoulou, A. Bakolas, and K. Bisbikou. *Characterization of ancient, Byzantine and later historic mortars by thermal and X-ray diffraction techniques.* Thermochemica Acta, 269/270:779–995, 1995.

[4] V. Nežerka, M. Somr, and J. Zeman. *Micromechanics-based models of cocciopesto mortars.* Proceedings of the 18th International Conference Engineering Mechanics, 2012, ISBN 978-80-86246-40-6.

[5] E. Herve and A. Zaoui. *n-layered inclusion-based micromechanical modelling.* International Journal of Engineering Science, 31:1–10, 1993.

[6] B. Pichler and Ch. Hellmich. *Upscaling quasi-brittle strength of cement paste and mortar: A multi-scale engineering mechanics model.* Cement and Concrete Research, 41:467–476, 2011.

[7] V. Šmilauer, P. Hlaváček, F. Škvára, R. Šulc, L. Kopecký, and J. Němeček. *Micromechanical multiscale model for alkali activation of fly ash and metakaolin.* Journal of Materials Science, pages 1–11, 2011.

[8] J. Vorel, V. Šmilauer, and Z. Bittnar. *Multiscale simulations of concrete mechanical tests.* Journal of Computational and Applied Mathematics, in press, 2012.

[9] Y. Benveniste. *A new approach to the application of Mori-Tanaka theory in composite materials.* Mechanics of Materials, 6:147–157, 1987.

[10] T. Mori and Tanaka K. *Average stress in matrix and average elastic energy of materials with mixfitting inclusions.* Acta Metallurgica, 21:571–574, 1973.

[11] C.C. Yang. *Effect of the transition zone on the elastic moduli of mortar.* Cement and Concrete Research, 28:727–736, 1998.

[12] E. Vejmelková, M. Keppert, Z. Keršner, P. Rovnaníková, and R. Černý. *Mechanical, fracture-mechanical, hydric, thermal, and durability properties of lime-metakaolin plasters for renovation of historical buildings.* Construction and Building Materials, 31:22–28, 2012.

[13] H. Böke, S. Akkurt, B. Ípekoğlu, and E. Uğurlu. *Characteristics of brick used as aggregate in historic brick-lime mortars and plasters.* Cement and Concrete Research, 36:1115–1122, 2006.

[14] P.R. Selvam, V.J. Subramani, S. Murray, and K. Hall. *Potential Application of Nanotechnology on Cement Based Materials.* Mack-Blackwell Rural Transportation Center, 2009.

[15] G. Constantinides and F.J. Ulm. *The effect of two types of C-S-H on the elasticity of cement-based materials: Results from nanoindentation and micromechanical modeling.* Cement and Concrete Research, 34:67–80, 2004.

[16] J.T. Jeffrey and M.J. Hamlin. *A colloidal interpretation of chemical aging of the C-S-H gel and its effects on the properties of cement paste.* Cement and Concrete Research, 36:30–38, 2006.

[17] A.L. Velosa, F. Rocha, and R. Veiga. *Influence of chemical and mineralogical composition of metakaolin on mortar characteristics.* Acta Geodynamica et Geomaterialia, 153:121–126, 2009.

[18] R. Hendricx et al. *Observation of the failure mechanism of brick masonry doublets with cement and lime mortars by X-ray CT.* Technical report, Katholieke Universiteit Leuven, 2009.

MULTI-OBJECTIVE IDENTIFICATION OF NONLINEAR MATERIAL MODEL

Adéla POSPÍŠILOVÁ[1], **Matěj LEPŠ**[2]

Abstract: *A multi-objective formulation of a nonlinear material model identification is presented. Since the material is tested on the basis of several tests, the multi-objective optimization with objectives for errors in individual tests' identification is a logic solution. Two optimization algorithms are implemented and compared. The first one is based on mean error function and an application of the single-objective genetic algorithm GRADE. In the second approach, for each test an error function will be defined, which allows to emphasize individual contributions of those tests. To optimize this problem, the multi-objective genetic algorithm NSGA-II is employed.*

Keywords: *parameter estimation, multi-objective optimization, NSGA-II, GRADE, clustering, data mining*

1. INTRODUCTION

Parameter estimation is a branch of study everywhere, where some model of natural phenomena is investigated. The aim is to fit the obtained test results with the outputs of the model. In this paper, the identification of a nonlinear viscoplastic material model is introduced. The detailed description of the model will not be presented because of non-disclosure treaty applied to the model; however, it is not necessary for the presentation of the optimization results.

The target of parameter estimation process is to obtain unknown input parameters for the model from known outputs (experimental or model results), i.e. to find a set of parameters which provides the desired outputs. Four main approaches for this task can be distinguished [1]:

- *A hand fitting method*, called also *guru method*, can be used if the input parameters are directly related to experimental results (or the user is experienced enough). Then, the fitting procedure can be performed *by hand*. Unfortunately, such relation usually does not exist in modern complex models.
- *A trial and error method* can be used for any inverse problem and no development of a special estimation procedure is needed. It is an intuitive and easy iterative search process: the input parameters are estimated until the desired outputs are found. The estimation procedure is very time demanding in this case and a finding of a good solution cannot be guaranteed.
- *An inverse mode* assumes the existence of inverse relation between outputs and inputs and searches for this relation or its approximation. If such relationship exists and is established, then the desired

[1]Ing. Adéla Pospíšilová , Faculty of Civil Engineering, CTU in Prague, adela.pospisilova@fsv.cvut.cz

[2]Ing. Matěj Lepš, Ph.D., Faculty of Civil Engineering, CTU in Prague, leps@cml.fsv.cvut.cz

inputs are obtained easily and fast even if executed repeatedly. On the contrary, the searching process is very time demanding and often unsuccessful.

- *A forward mode* is based on minimization of a function determining the difference between desired and estimated outputs. This approach can be used universally, i.e. if the model is capable to provide the desired outputs, with enough time the solution will be always found.

The last method is used in this paper. Traditionally, this problem has been solved by gradient-based optimization methods, but, nowadays, the model is often created in a program where the code visibility is limited and therefore, the knowledge of derivatives is missing even if the function is differentiable. Hence, the artificial intelligence methods, e.g. evolutionary algorithms, can be successfully applied here. However, the objective functions are often multi-modal and these algorithms tend to converge to the local optima.

There are two ways to solve this problem: the algorithm can be improved towards solving multi-modality or the objective function can be changed. The example of the first way, strategy CERAF, is presented in the next section. One possible approach for the second way is solving the original optimization problem in the multi-objective space [2]. This approach for parameter estimation is inspired by an idea of *multi-objectivization* presented in [3], where authors suppose that expanding the single-objective problem to the multi-objective space gives an algorithm more freedom to explore and less probability to be trapped in local minima. The original objective is replaced with a set of new objectives or new objectives are added to the original one. In our approach, the viscoplastic model is tested using several experimental setups, using e.g. tensile, compressive, cyclic or relaxing tests. Then, the multi-objective problem is easily created by forming one objective for each of the tests.

The remainder of the paper is organized as follows: The algorithms are described in next sections, particularly, the genetic algorithms GRADE and NSGA-II are presented. Algorithm GRADE represents the "classical" way to the forward mode of inverse analysis and strategy CERAF helps to overcome the multi-modal problem. Algorithm NSGA-II is multi-objective genetic algorithm used to demonstrate the pros and cons of the multi-objective methodology. Results are presented in the fourth section together with cluster analysis to study the results obtained by the two mentioned methods. The last section contains concluding and future work remarks.

2. GRADE UTILIZING CERAF STRATEGY

GRADE [4] is a real-coded stochastic optimization algorithm combining principles of genetic algorithms and differential evolution [5]. CERAF (from French *CEntre RAfioactiF*) is a tool for obtaining diversity among solutions [6]. Both algorithms are available for free downloading in MATLAB and C++ versions in the given references.

The short description of GRADE utilizing CERAF strategy is as follows. The initial population

is created randomly within the size $2N$. The modified tournament strategy is used for selection of two parents. The two chromosomes are chosen randomly and the one with worse fitness value (the combination of objective and constraints functions values) is discarded. This approach called elitism allows that the best solution cannot be lost. The routine is repeated as long as the number of population has N size. Afterwards the mutation operator and crossing operator are used to create population with N size. Mutation operator is applied to the parent chromosome and is used with explicit probability - *radioactivity* to create a new offspring. The number of new offsprings is not the same in each generation therefore in average this number should converge to N * *radioactivity parameter*. The crossing operator is used to create the rest of the N number of a new population. Two parent chromosomes are randomly chosen, their difference is computed and multiplied by *cross_rate* parameter (a random number from given interval in advance specified by user) and added to the one with better fitness function. Afterwards the selection follows and the whole routine is repeated with the number of generation specified in advance.

3. NONDOMINATED SORTING GENETIC ALGORITHM II

Nondominated Sorting Genetic Algorithm II (NSGA-II) was firstly published in [7]. It is an improved approach of NSGA where the main disadvantages were high computational complexity of non-dominated sorting. In this version of the algorithm, there is no need to sort the population in every generation; also the original version has lack of elitism and need for specifying the sharing parameter for obtaining wide variety of solutions. This algorithm deals with all of these disadvantages for obtaining better solution much faster [8].

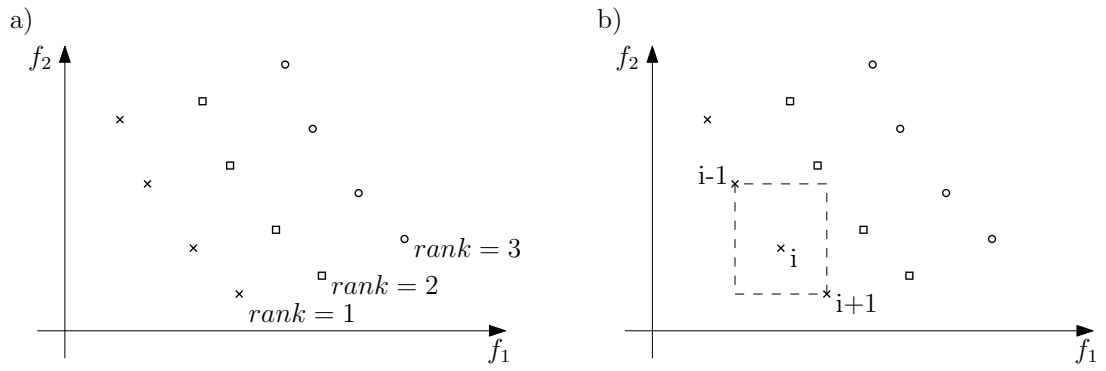

Fig. 1 Calculation for NSGA-II of a) Nondominated rank, b) Crowding distance

The first population is randomly created with a given distribution. In this work, the uniform distribution within the given range (lower and upper bounds of the parameters) is used. All individuals are sorted into each front (see Fig. 1a). For each individual p the number of solutions n_p which dominate the solution p and a set of solutions S_p that the solution p dominates are calculated. Afterwards, for every individual with $n_p = 0$ the $rank = 1$ is assigned. These solutions are called nondominated and create the first front. This procedure is repeated until each individual has assigned its own rank. This means that all individuals are placed into the fronts. Solutions with $rank = 1$ are dominated by solutions with

$rank = 0$, are nondominated to each other and dominates all solutions with $rank$ higher than 1. The same rule is applied to individuals with higher ranks. To maintain diversity within the optimal fronts the crowding distance attribute is used for all nondominated solutions. This parameter designates how close the other solutions in the neighbourhood (see 1b) are. The bigger the crowding distance is, the better diversity in the solutions is.

The tournament selection for choosing individuals is used afterwards. The quality of the individual is identified with very low rank and with the very high crowding distance. The more superior the individual is, the better chance to create an offspring with its properties is. Consequently, the crossover and mutation operators are used for creating new offspring population.

The parent as well as the offspring population are sorted again and the $rank$ and crowding distance are assigned to each individual. Only the N number of individual comes into the tournament selection. This procedure is stopped after the given number of generations is evaluated.

In our work, we are using an algorithm that was implemented in MATLAB by Reiner Schulz [9]. This implementation is based on the reference [8] mentioned above.

4. RESULTS

The identification of the viscoplastic model is in the presented formulation composed of four experimental test setups. Therefore, the multi-objective version is created by four objectives, with one mean square error term for each test. The single-objective counterpart is then created by the mean of all four objectives. The next section discusses the obtained results from the multi-objective point of view, whereas the following section is devoted to the data analysis with the obtained non-dominated points coupled with the clustering analysis.

4.1. COMPARISON OF SINGLE AND MULTI OBJECTIVE IDENTIFICATION

When simultaneously optimizing several error functions an experimenter is usually interested in the solutions closest to the origin. Although not exactly precise, this will be the solution with the minimal mean value of all objectives that is also used as a measure of the quality in the single-objective formulation. From this view, the best solution was found with the GRADE method

$$F_{best} = [3.5750, 3.2631, 2.6103, 3.1798] \qquad (1)$$

attaining mean value 3.1571. The best solution from NSGA II algorithm gets only to the mean 3.3776. However, when inspecting the whole Pareto front created from all solutions inspected during the whole run of both algorithms, see Fig. 2, the NSGA II produced much uniform and wider set of solutions, which is an aim in multi-objective optimization. Nevertheless, interesting part is the cardinality of both fronts, NSGA II found approximately 1700 non-dominated solutions, whereas GRADE algorithm results are composed from more than 6000 points. Such behavior can be explained by the ability of the GRADE operators to find different solutions, however this cannot be generalized and can be problem dependent.

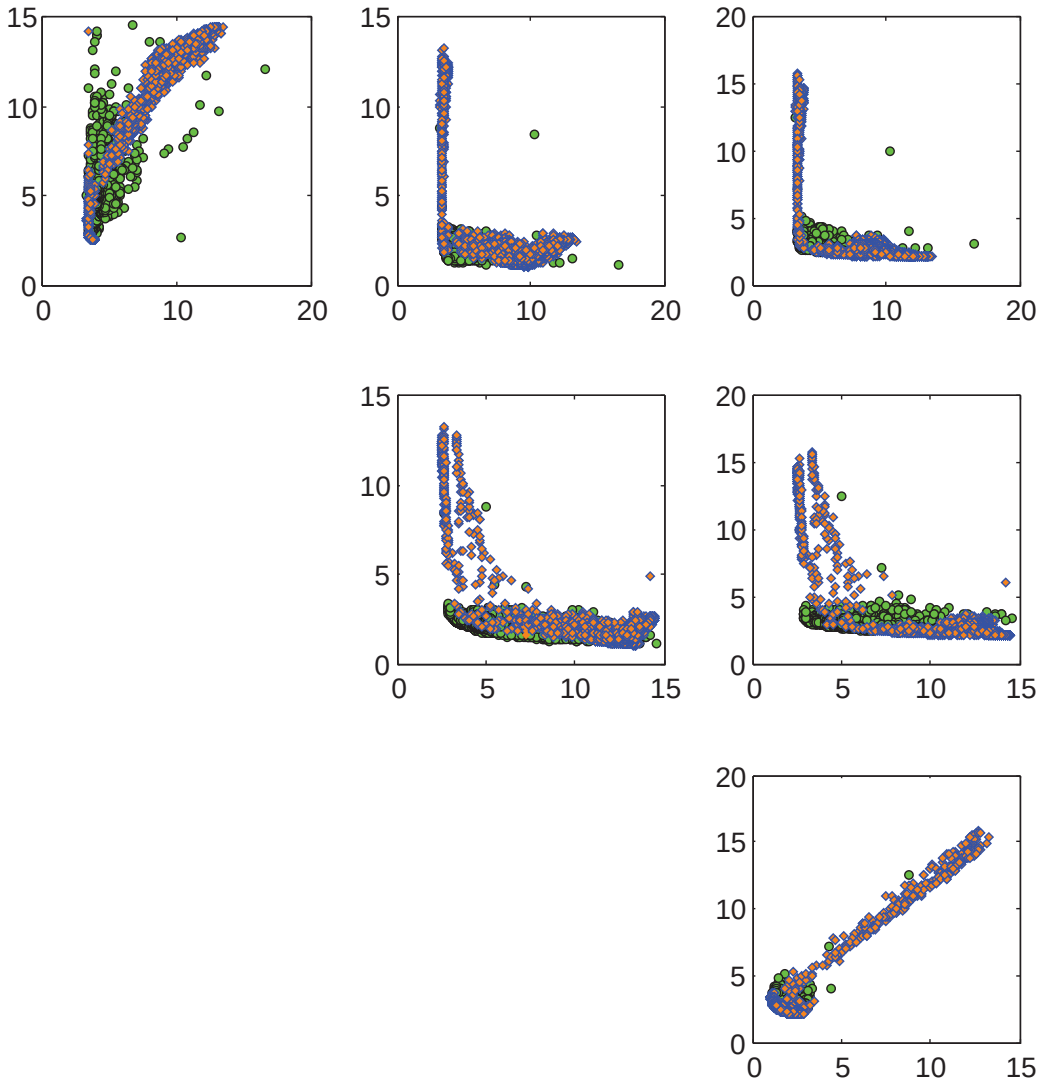

Fig. 2 Plot of Pareto fronts obtained from multi-objective NSGA-II (orange diamonds) and single-objective GRADE algorithms (green circles); individual boxes show two-dimensional projections, i.e. the first box is the plot of f_1 vs f_2, the second is f_1 vs f_3, etc.

4.2. DATA ANALYSIS

Next, we analyze the union of results obtained by both methods to gain more knowledge of the given identification problem. Firstly, the so-called *ideal objective vector* can tell us, how far we can get on individual objectives. The ideal objective vector is created by coordinates of minima of all objectives, i.e. $F_{ideal} = [min(f_1), \cdots, min(f_4)]$, here $F_{ideal} = [3.281, 2.5573, 1.055, 2.0970]$. The first coordinate which is closed to the first coordinate of F_{best} reveals that we cannot expect bigger improvement by optimizing the first objective. This is also nicely documented by the almost straight part of Pareto front projections in the first line in Fig. 2. Other objectives offer a place for improvements, with the attractive

third objective, where the minimum is more than twice lower than the value in the best point. Another interesting point is the shape of Pareto front projections. Upper left corner and lower right corner of Fig. 2 suggest that the first and the second objectives are slightly and the third and the fourth objectives are highly correlated. Opposite is true for the first and the second against the third and the fourth objectives, respectively, where the projections show typical antagonistic shapes of Pareto fronts.

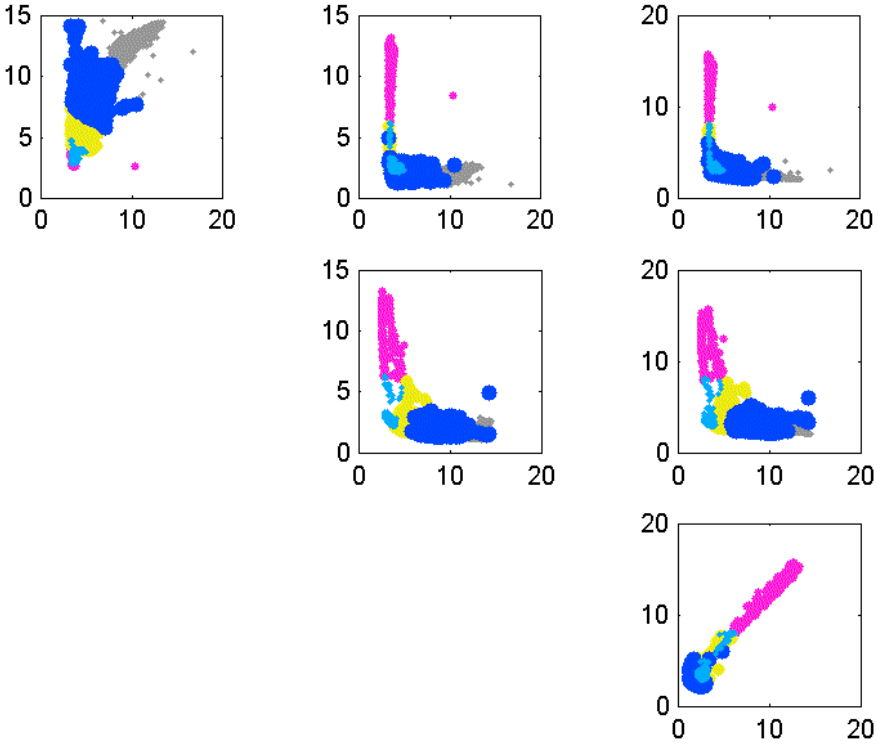

Fig. 3 Pareto front of clusters; light blue is the cluster closest to the origin.

4.3. CLUSTER ANALYSIS

Next, we investigate properties of resulting solutions using a k-means clustering analysis [10] available in Matlab. Clustering is a tool for data mining that tries to find similarities among data and to sort huge amount of data into categories. Since the important part is formed by the solutions closest to the origin, the k-means clustering have been performed in the objective space, see Fig. 3. The light blue cluster is the cluster closest to the origin. The plot of the histograms of individual variables forming this cluster, see 4, reveal that the majority of the solutions are on the boundary of the admissible domain, particularly at x_1, x_9 and x_{12}. The plots also show that the best single-objective solution is rather isolated, which is nicely visible on the histogram of x_1 variable.

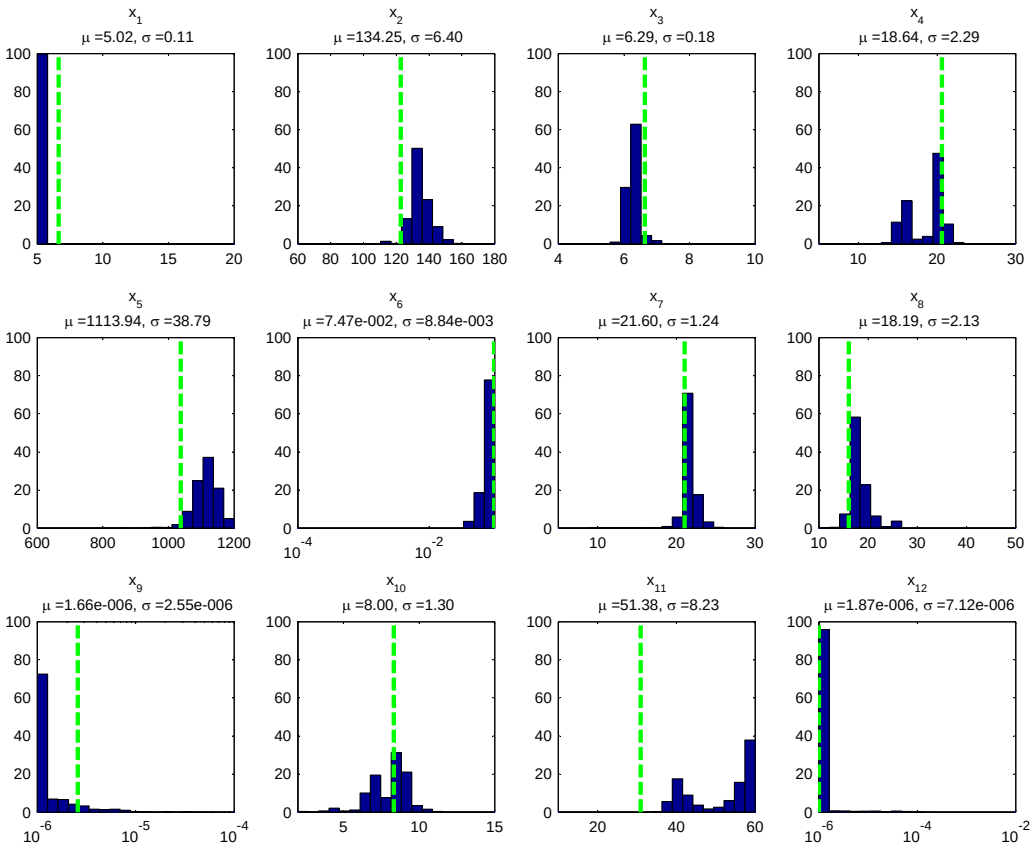

Fig. 4 Histograms of the best cluster from Fig. 3 together with the highlight of the best solution (green dashed line).

5. CONCLUSION

The comparison of the single-objective and multi-objective identification of the material parameters for a viscoplastic model has been presented in this work. The classical single-objective genetic algorithm GRADE was compared with the multi-objective algorithm NSGA-II. It was expected that the best solution closest to the origin will be found by the GRADE algorithm and that the NSGA-II will produce wider Pareto front. Both statements were confirmed. However, the richness of the Pareto-front produced by the GRADE algorithm was surprising. This is mainly caused by the aim of the NSGA-II to cover as wide space as possible and by withdrawing of too closed solutions from the front. Finally, the investigation of the resulting histograms of the cluster of solutions closest to the origin suggest to widen the given bounds since a majority of the solutions lie on the boundary of the admissible space. To sum it up, the single-objective optimization approach is recommended for the search for the best solution, whereas the multi-objective for the deep search through the space to obtain diverse solutions.

ACKNOWLEDGEMENT

The financial support of this work from the Grant Agency of the Czech Technical University in Prague (SGS project No. 12/027/OHK1/1T/11) and from the Technology Agency of the Czech Republic through the project TA01030733 is gratefully acknowledged.

REFERENCES

[1] R. Mahnken. *Identification of Material Parameters for Constitutive Equations*, chapter 19, pages 637–656. Encyclopedia of Computational Mechanics Part 2. Solids and Structures. John Wiley & Sons, Ltd., 2004. ISBN 0-470-84699-2.

[2] Vitingerová, Z. *Evolutionary Algorithms for Multi-Objective Parameter Estimation*, Ph.D. thesis, Czech Technical University in Prague, Faculty of Civil Engineering, 2010.

[3] Knowles, J. D. - Watson, R. - Corne, D. W. *Reducing local optima in single-objective problems by multi-objectivization*, In: *First International Conference on Evolutionary Multi-Criterion Optimization*, 2001, pp. 269–283. Springer-Verlag. Lecture Notes in Computer Science No. 1993. ISBN 978-3-540-41745-3.

[4] Kučerová, A. *Identification of nonlinear mechanical model parameters based on softcomputing methods*, Ph.D. thesis, Ecole Normale Supérieure de Cachan, 2007, 156 p.

[5] Kučerová, A. *Stochastic optimization tool: GRADE algorithm* [online]. [2012] [cit. 2012-07-28]. Available from WWW: <http://klobouk.fsv.cvut.cz/ anicka/grade/grade.html>.

[6] Kučerová, A. *Stochastic optimization tool: CERAF strategy* [online]. [2012] [cit. 2012-07-28]. Available from WWW: <http://klobouk.fsv.cvut.cz/ anicka/ceraf/ceraf.html>.

[7] Deb, K. - Agrawal, S. - Pratap, A. - Meyarivan, T. *A Fast Elitist Non-Dominated Sorting Genetic Algorithm for Multi-Objective Optimization: NSGA-II*, In: Lecture Notes in Computer Science, 1917/2000, pp. 849–858. ISSN 0302-9743.

[8] Deb, K. *A Fast and Elitist Multiobjective Genetic Algorithm: NSGA-II*, In: IEEE Transactions on Evolutionary Computation, 2002, Vol. 6, No. 2, pp. 182–197. ISSN 1089-778X.

[9] Schulz, R. 2004. *A Matlab implementation of NSGA-II* [online]. [2004] [cit. 2012-07-28]. Available from WWW: <https://atlas.genetics.kcl.ac.uk/∼rschulz/homepage/NSGA_II.tar.gz>.

[10] Jain, A. - Murty, M. - Flynn, P. *Data clustering: A review*, In: ACM Computing Surveys, 1999, Vol. 31, No. 3, pp. 264–323. ISSN 0360-0300.

EVALUATION OF MATERIAL PARAMETERS FROM THREE POINT-BENDING TEST ON NOTCHED BEAMS

Michal PŘINOSIL[1], **Petr KABELE**[2]

Abstract: *Three-point bending test performed on notched beam is a standard method for evaluation of fracture energy of materials. For evaluation of other material parameters, like Young's modulus of elasticity and tensile strength, it is necessary to perform other tests. This article deals with the estimation of tensile material parameters of lime mortar from just three-point bending test on notched beam using numerical simulations.*

Keywords: *three-point bending test, notched beam, fracture energy, tensile strength, LHS method*

1. INTRODUCTION

At the present time there is a lot of building materials on the market. Their effective utilization depends on information about their properties and conditions for which the materials were developed. Development of materials and testing methods go hand in hand and with a little exaggeration there are so many test methods as materials. These are often very specific experiments designed for evaluating one or two material parameters. One example is three-point bending test on notched beams proposed by RILEM [1], which is proposed to obtain fracture energy of quasi-brittle materials. The experiment consists in bending of a beam in which the crack starts to spread from a notch and fracture energy is calculated as the total work required to break the beam divided by the cross-sectional area of the beam above the notch.

Although the experiment is based on crack propagation due to tensile effects in nature, we don't get information about other tensile characteristics, such as tensile strength and Young's modulus of elasticity. To obtain these important parameters it is necessary to perform other experiments. Each such experiment is time consuming and to perform it, it is necessary to prepare tens of specimens. This corresponds to the demands on material, storage and testing machines. However, if it is possible from one experiment to derive more material parameters using numerical tools, the entire process will be simplified, which could bring obvious benefits. The objective of this work is to determine tensile characteristics like fracture energy, tensile strength and Young's modulus of elasticity of lime mortar from the three-point bending test with notched beam using numerical tools.

[1] Ing. Michal Přinosil, Department of Mechanics, Faculty of Civil Engineering, CTU in Prague; michal.prinosil@fsv.cvut.cz

[2] prof. Ing. Petr Kabele, Ph.D., Department of Mechanics, Faculty of Civil Engineering, CTU in Prague; petr.kabele@fsv.cvut.cz

2. THREE-POINT BENDING TEST WITH NOTCHED BEAMS

In our research we are interested in development of new lime based mortar reinforced with short fibers, which is applicable for the repair and maintenance of historical monuments. Material design is based on the concept that the strength of fiber bridging is higher than the tensile strength of the lime matrix and material fractures in the form of fine distributed cracks. This effect is known as multiple cracking. In order to fulfill the conditions of multiple cracking [2], during material design it is necessary to know the micromechanical parameters of individual components of composite, especially those characterizing the reinforcing fibers, lime matrix and the interface between these two components. This work is further focused on the evaluation of material parameters of the lime matrix.

2.1. TESTING SET-UP

Design composition of lime mortar is based on the previous research of lime composites [3] and on the methodology and material engineering of tensile hardening composites ECC [4]. As the binder, hydrated air lime powder was selected and fine quartz sand was used as the filler. The granulometric curve corresponds to design by Dinger-Funk [5] with maximum particle size D_{max} = 0.3 mm. The volume ration of binder and filler was 1:3 and the water/binder ratio was 0.24 l/kg. From this mixture, a set of prism beams was made with size 40×40×160 mm. Before testing they had been stored for 7 months in room conditions in order to reach full carbonation and material parameters were stabilized on their final value [6]. After that the beams were cut into specimens with dimensions of 12×12×80 mm. A notch 1 mm wide was cut into each specimen. The notch length corresponded to 35÷50% of the specimen‘s height. All dimensions were measured and recorded for further processing. The support span was 59 mm (Fig. 1). The experimental procedure was based on the work of fracture method, which is also used in the RILEM recommendation [1]. The tests were performed by means of the MTS Alliance RT/30 machine. Loading was controlled by the crosshead displacement, which was applied at the constant rate of 0.025 mm/min. The applied force and the crosshead displacement were continuously recorded.

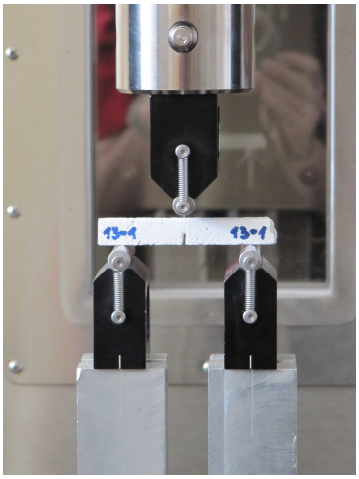

Fig. 1 Testing set-up

2.2. EVALUATION OF FRACTURE ENERGY BY THE WORK OF FRACTURE METHOD

Figure 2 shows results of the three-point bending test with notched beams in the form of the load-displacement diagrams. From these results the fracture energy G_f was determined as follows. First, the tails of the load-displacement curves were extrapolated to the point where they intersect the horizontal axis with displacement u_0. Then the work W_f of external force P was calculated as:

$$W_f = \int_0^{u_0} P du \tag{1}$$

and the fracture energy in the ligament is defined as:

$$G_f = \frac{W_f}{A_{lig}} = \frac{W_f}{b(a - a_0)} \tag{2}$$

where A_{lig} is a cross-sectional area of ligament and b is width of beam, a is height of beam and a_0 is depth of notch. Due to the small size of specimens, the effect of self-weight was neglected. From the results shown on Fig. 2 we obtained the average value of fracture energy G_f = 2.41 J/m^2.

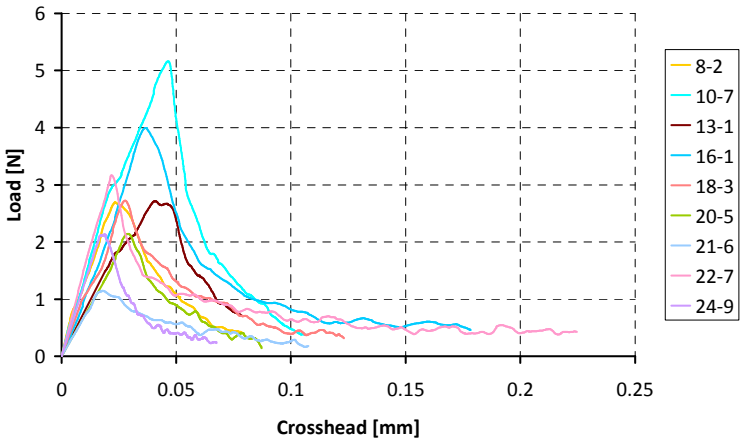

Fig. 2 Load-displacement diagrams from the three-point bending tests with notched beams

3. NUMERICAL MODELING

In order to evaluate the tensile strength f_t, the cohesive traction-separation relationship and Young‘s modulus of elasticity E_m a numerical model was created in finite element software Atena [7]. Individual cracks were represented using the crack band approach. Cohesive relationship, which relates a bridging stress to a crack opening displacement, was considered as bilinear (Fig. 3) and was represented by parameters f_t, δ_2, pX and pY (Fig. 3). Geometry of the model and boundary conditions corresponded to the experiment and plane stress was assumed. Cracking was allowed only in a 1-element wide band above the notch.

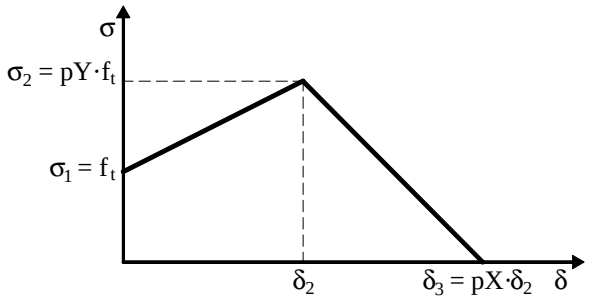

Fig. 3 Cohesion relationship

3.1. EVALUATION OF MODULUS OF ELASTICITY

Young's modulus of elasticity E_m is a material parameter, which can be evaluate straightforward from elastic part of load-displacement diagrams. It is necessary to find out the load level in which all tested specimens behave linearly elastically. The load level of approximately P = 0.28 N with average displacement u = 0.0026 mm was found to meet this criterion for all tested specimens (Fig. 2). The first numerical simulation of the test was performed with estimated modulus E_m = 1000 MPa. The calculated load corresponding to displacement u = 0.0026 mm was approximately P = 0.32 N. Assuming the linear elasticity and by comparing the calculated load P to the measured one, we obtained the corrected modulus of elasticity E_m = 900 MPa.

3.2. EVALUATION OF TENSILE STRENGTH AND COHESIVE RELATION

Evaluation of the tensile strength f_t and the shape of the cohesive law represented by δ_2, pX and pY is more complex and there is no straightforward way to evaluate these parameters directly from the notched three-point bending test. For this reason we decided to determine these parameters using optimization. To this end, random sets of these parameters were generated using the LHS (Latin Hypercube Sampling) method in software FREET [8]. Individual responses calculated with the numerical model of the fracture specimen using the sampled parameters were then compared with experimentally measured data, and the set providing the least difference was selected.

All random parameters were generated using rectangular distribution without any correlation between the parameters themselves. The lower and upper limits of the distribution were chosen based on experience from previous simulations (Table 1). The average fracture energy evaluated by interpreting from corresponding traction-separation laws (G_f = 2.444 J/m^2) is close to the experimental data. We performed 20 simulations. The parameters of individual simulations are shown in Table 2.

Tab. 1 The limits of rectangular distribution

	f_t [MPa]	pY [-]	δ_2 [mm]	pX [-]
Lower limit	0.25	0.8	0.0001	1
Upper limit	0.45	2	0.0002	2

For the defining the optimization criterion three variables describing the structural response were selected. The first two variables correspond to the horizontal and vertical position of the peak on load-displacement diagram. Averaged over all experimental data, the peak has coordinates F_{max} = 3.09 N and w_{max} = 0.03 mm (Fig. 4). The third variable is the work of external force. We consider only the work up to the deflection which corresponds to three times w_{max}:

$$W_f^* = \int_0^{3w_{\max}} P du \tag{3}$$

Calculations was performed for individual tests and then averaged. This restriction was introduced to avoid inaccuracies resulting from extrapolation of the load-deflection curves (since neither the experiments nor in the testes were possible to conduct up to zero force). It was found through the numerical simulations that at deflection corresponding to three times the peak deflection, the remaining ligament reaches about 1/3 of the initial length and begins to act as a hinge.

After calculation, the absolute values of differences in variables between the data of numerical simulations ($F_{max,sim}$, $w_{max,sim}$, $W^*_{f,sim}$) and experiment ($F_{max,exp}$, $w_{max,exp}$, $W^*_{f,exp}$) were calculated:

$$dF_{\max} = \left|F_{\max,sim} - F_{\max,\exp}\right|,\ dw_{\max} = \left|w_{\max,sim} - w_{\max,\exp}\right|,\ dW_f^* = \left|W_{f,sim}^* - W_{f,\exp}^*\right| \tag{4}$$

These values were further normalized using the values from the experiment:

$$dF_{\max,norm} = \frac{dF_{\max}}{F_{\max,\exp}},\ dw_{\max,norm} = \frac{dw_{\max}}{w_{\max,\exp}},\ dW_{f,norm}^* = \frac{dW_f^*}{W_{f,\exp}^*} \tag{5}$$

Finally, the optimization criterion is defined as:

$$N = \sqrt{dw_{\max,norm}^2 + dF_{\max,norm}^2 + dW_{f,norm}^{*2}} \tag{6}$$

The values of the optimization criterion of individual simulations are shown in Table 2.

Tab. 2 The random parameters of individual simulations and value of optimization criterion

	f_t [MPa]	pY [-]	δ_2 [mm]	pX [-]	N [-]
LHS001	0.255	1.67	0.0001625	1.925	0.478
LHS002	0.265	0.95	0.0001825	1.525	0.321
LHS003	0.275	1.97	0.0001025	1.275	0.267
LHS004	0.285	1.13	0.0001225	1.125	0.467
LHS005	0.295	0.83	0.0001275	1.875	0.410
LHS006	0.305	1.43	0.0001775	1.175	0.315
LHS007	0.315	1.01	0.0001375	1.825	0.238
LHS008	0.325	1.55	0.0001325	1.425	0.212
LHS009	0.335	1.61	0.0001675	1.225	0.450
LHS010	0.345	1.49	0.0001925	1.675	0.913
LHS011	0.355	1.85	0.0001425	1.325	0.493
LHS012	0.365	1.91	0.0001975	1.475	1.264
LHS013	0.375	1.25	0.0001475	1.025	0.212
LHS014	0.385	1.31	0.0001075	1.725	0.186
LHS015	0.395	1.19	0.0001875	1.775	0.879
LHS016	0.405	1.37	0.0001175	1.375	0.191
LHS017	0.415	1.73	0.0001725	1.625	1.219
LHS018	0.425	1.07	0.0001575	1.575	0.505
LHS019	0.435	1.79	0.0001125	1.975	0.785
LHS020	0.445	0.89	0.0001525	1.075	0.246

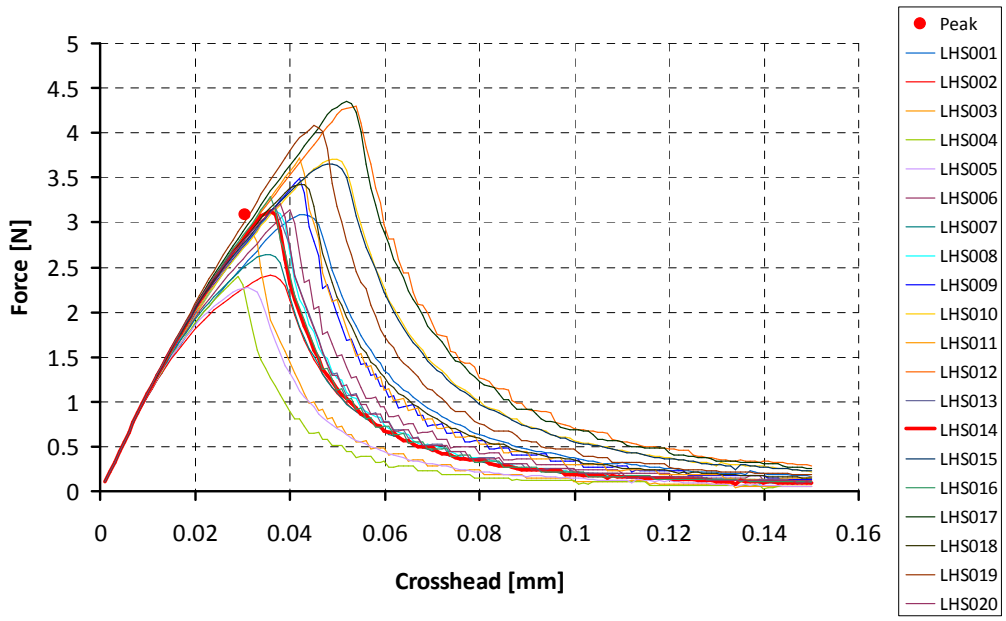

Fig. 4 Load-displacement diagrams from numerical simulation

In Figure 4 results of numerical simulation in the form load-displacement diagrams are shown. The best match for the proposed criteria is for simulation LHS014 (red bold line in Fig. 4). This simulation corresponds to the tensile strength f_t = 0.385 MPa with slightly hardening cohesion relationship (Tab. 2) and G_f = 2.02 J/m^2.

4. VERIFICATION

To verify the results we performed the three-point bending experiment on beams without notch. Testing set-up, material and geometry were same as in the case of notched beams. In this case, the specimens had been stored for 11 months in room conditions, but we assumed that the material parameters were same as in the case of notched specimens [6]. Figure 5 shows results in form of the load-displacement diagrams. The Young‘s modulus of elasticity was calculated from slope of initial elastic part of curves and the tensile strength was calculated from the load level where the individual curves begin to clearly diverge from the initial slope. From these results we get the averaged values E_m = 850 MPa and f_t = 0.4 MPa. These results are in a very good agreement with those obtained by the method proposed in section 3.2.

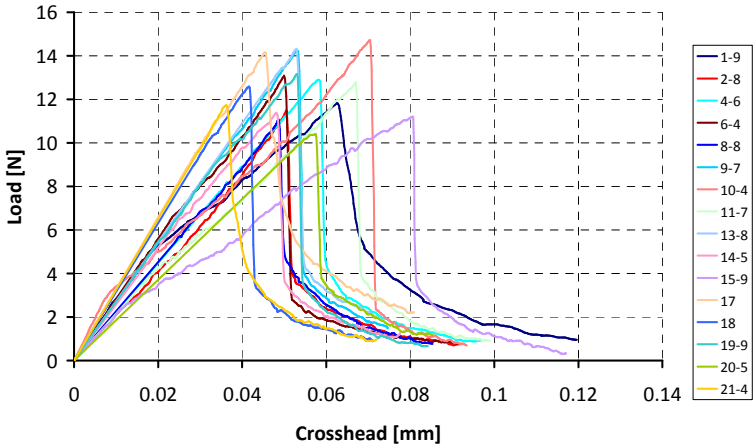

Fig. 5 Load-displacement diagrams from the three-point bending tests

5. CONCLUSION

According to the results, the numerical simulation (with randomly generated material parameters using LHS method) is a useful tool to evaluate Young‘s modulus of elasticity, tensile strength and shape of cohesive relationship. Tensile strength and Young‘s modulus of elasticity determined using the proposed method are in a good agreement with results obtained experimentally. It should be also noted that the fracture energy evaluated by integrating the traction-separation law with the optimum parameters (set LHS014, section 3.2) is lower than that determined by the work of fracture method applied to the experimental results (section 2.2). This may be due to two reasons associated with the evaluation of fracture energy from experiment. The first reason may be inaccuracy introduced by extrapolation of the load-deflection curve. The second reason may be that when calculating the crack area A_{lig} in Eq. (2), the fracture plane was always assumed to be perfectly straight and vertical. In reality, though, propagation of the crack in inclined direction, which resulted in larger fracture area, was often observed (Fig. 6).

Fig. 6 Crack propagation from the notch at an inclination

ACKNOWLEDGEMENT

Financial support of the Czech Technical University in Prague under project SGS12/027/OHK1/1T/11 is gratefully acknowledged.

REFERENCES

[1] RILEM Technical Committee 50 (Draft Recommendation), Determination of the fracture energy of mortar and concrete by means of three-point bend tests on notched beams, Materials and Structures, 18 (4), 1985, pp. 287-290, ISSN 1359-5997

[2] Marshall, D.B., Cox, B.N., A J-integral method for calculating steady-state matrix cracking stresses in composites, Mechanics of Materials, 7 (2),1987, pp. 27-133, ISSN 0167-6636

[3] Drdácký, M.F., Michoinová, D., Procházka, P.P., Maltovinové směsi vyztužené vlákny pro obnovu a záchranu uměleckých památek, The final report of the research project of the Czech Ministry of Culture no. PK00-P04-OPP15., Prague, 2002.

[4] Li, V.C., On Engineered Cementitious Composites – A review of the material and its applications. Journal of Advanced Concrete Technology, 1 (3), 2003, pp. 215-230, ISSN 1347-3913

[5] Novák, L., Mix design and experimental investigation of durability of fiber reinforced cementitious composites, Ph.D. thesis, CTU in Prague, Prague, 2010.

[6] Izaguirre, A., Lanas, J., Alvarez, J.I., Effect of a polypropylene fibre on the behaviour of aerial-lime-based mortars, Construction and Building Materials, 25 (2), 2011, pp. 992-1000, ISSN 0950-0618.

[7] Červenka, V., Jendele, L., Červenka, J., ATENA Program Documentation, Part 1: Theory, Prague: Červenka Consulting, 2012.

[8] Novák, D., et. al., FREET Program Documentation, Part 1: Theory, 2002.

DESIGN OF THE BEARING BUILDING ENVELOPE WALL FROM CAST GYPSUM

Josef ŘÍHA[1], **Tomáš PLACHÝ**[2], **Pavel TESÁREK**[3]

Abstract: *The paper focuses on the use of modified gypsum on the envelope bearing walls of buildings. Modified gypsum will be presented in the form of load-bearing block walls and prefabricated walls. Usage analysis and perspective gypsum will be made for bearing element of buildings. Modified gypsum and its use will be presented on a sample construction of a real building. Static and structural design will be carried out. The design must meet all requirements for an envelope.*

Keywords: *gypsum block, building envelope, mechanical proprieties*

1. INTRODUCTION

Gypsum for building industry is obtained in two possibilities [1]. The first possibility is the production of natural gypsum, where dehydration of gypsum on plaster according endothermic equation is used. Then we distinguish two different approaches and the so-called dry process that produces β-gypsum and the wet process that produces α-gypsum. The second possible source of gypsum is getting gypsum as a secondary element in a chemical production or flue gas desulfurization of coal power plants. If we appreciate the necessary solution of this waste handling appears next using in form of a product usable in construction as an environmentally and cost effective solution.

As a building material, it is known for use in interiors of buildings in the form of different plasterboard, a mixture for plaster and floors, racking blocks and possibly an excellent imitation of marble. Improvement of mechanical properties is achieved by modification of gypsum and adding reinforcement elements (glass fiber). This enables the production of ceiling and wall systems based on plaster. [2]. The largest expansion of gypsum element production was in the middle of the 20th century. The aim was to maximize the use of gypsum for construction elements of buildings.

[1]Bc. Josef Říha, Department of Mechanics, Faculty of Civil Engineering, CTU in Prague; rihajos4@fsv.cvut.cz

[2]Ing. Tomáš Plachý, Ph.D., Department of Mechanics, Faculty of Civil Engineering, CTU in Prague; plachy@fsv.cvut.cz

[3]Ing. Pavel Tesárek, Ph.D., Department of Mechanics, Faculty of Civil Engineering, CTU in Prague; tesarek@fsv.cvut.cz

The production focuses more on the additional elements and the main supporting elements disappear from the market in recent years. At present time, the blocks only for interior non load bearing walls are used in Poland (Mutigips, Promont). In Singapore, there were made weather resistant blocks reinforced with glass fiber (Plasterceil). These blocks are non-load bearing. These are then used for external wall of buildings [3]. In Australia, they specialize on production of prefabricated gypsum panels with dimensions 12×3×0.124 m (Rapidwall) (Fig. 1). The panels are reinforced with glass fiber around the circumference. Prefabrication greatly accelerates construction and labor intensive. If it is necessary, cavities of panel are filled with thermal insulation or concrete. It was calculated that unfilled cavities of panel can be used in a conventional house with two floors at maximum [4]. It is necessary to fill the space with concrete from 2 floors above (climatic conditions for Australia). Resistance in pressure is around 100 kN/m for the unfilled concrete walls. The load capacity depends on the type of concrete by the walls filled with concrete. And move around a value of 800 kN/m.

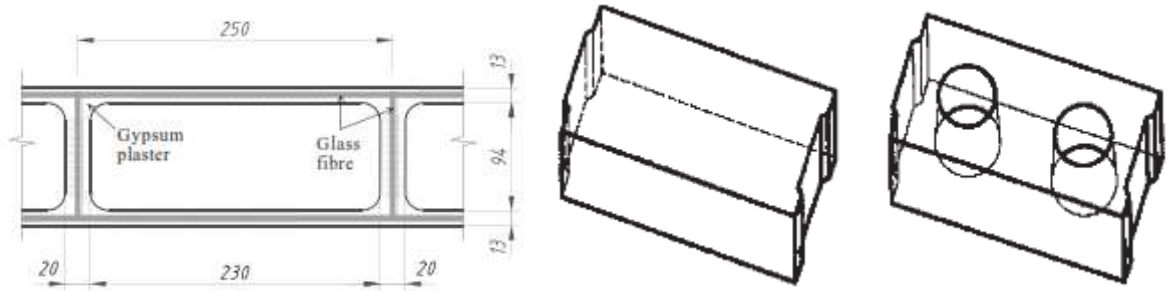

Fig. 1 Ground plan (Rapidwall) (left) [4], gypsum blocks 600×300×150 mm (Gypstrend) (fight) [6]

1.1 REQUIREMENTS FOR THE ENVELOPE

The external wall is an integral part of any structure. It is one of the main elements characterizing the architectural design of the building. The main requirements for the carrier envelope are sufficient mechanical resistance and stability against applied loads. Envelope should have enough ability to resist the effects of fire. It must be made appropriately for future users. This means that it must be hygienic, non-toxic and not harm the environment. The envelope must be energy efficient and sufficiently resistant to noise propagation. The envelope in the form of bricks fittings (Fig. 2) meets the above requirements.

For the application of gypsum on the supporting elements, envelopes deal with two basic problems. Firstly, it is necessary to ensure that the temperature will not exceed 70 °C because of decomposition of hardened gypsum. Secondly, it must prevent or slow down the degradation caused by moisture and frost.

Fig. 2 Prefabricated walling panel (Rapidwall)

The first problem can be eliminated by suitable modification of compounds for the production blocks. The second problem can be solved by the addition of hydrophobic additives into the mixture [5]. Additives ensure that blocks are water prove and they prevent degradation. That will help to thermal insulation of facades. Thermal insulation is equally necessary if we construct residential buildings.

1.2. MATERIAL SPECIFICATIONS

Composition for the production of blocks is based on previous experiments and knowledge. The blocks modified by hemihydrate of calcium sulphate show to be most suitable for the production. Mixture of calcium sulphate hemihydrate, aeration and hydrophobic additives, water and heat-insulating additives such as expanded perlite or vermiculite are used to achieve optimum properties. Blocks with dimensions advantageous for masonry work and handling [3] are cast from these mixtures. The optimal ratio appears to be in the ratio 1: 0.5: 0.25, which corresponds to the dimension 600×300×150 mm e.g. It is also possible to produce the block with openings. Block is made with tongue and groove due to accurate and fast walling. Bed joints shall be affixed with glue and vertical joints are dry.

Walls of gypsum blocks + standard insulation system made of mineral wool thickness 100 mm reported according to CSN 73 0540 heat transfer coefficient around 0.23 W/m^2K. Values characterizing the energy-efficient building are obtained by using thicker insulation. Gypsum blocks have in most aspects the same or better properties compared with aerated concrete blocks.

The main advantages of masonry blocks of cast gypsum are fire resistance, low weight (bulk density), thermal and acoustic insulation, handling and workability, health harmless, suitability for allergy sufferers and low price.

Tab. 1 Technical parameters of the modified gypsum blocks (Gypstrend) [6].

Technical parameters	unit	value
bulk density	kg/m^3	550 – 650
compressive strength (28 d)	MPa	2.5 – 5.5
moisture absorptivity	weight %	3.15
open porosity	% volume	57
Frost rezistence	freezing cycles	25
water vapour diffusion resistance factor	-	10
moisture diffusivity	m^2s^{-1}	$3.1*10^{-10}$
thermal conductivity	$Wm^{-1}K^{-1}$	0.156
Reaction to fire	class	A1
fire resistance	min	over 180
airborne sound insulation	dB	49
modulus of elasticity	GPa	1.74
drying shrinkage	$mm.m^{-1}$	0.1
radioactivity of 226Ra	$Bq.kg^{-1}$	25

2. DESIGN OF THE OFFICE BUILDING ENVELOPE

The main point of this work is to focus on the design of bearing envelope extensions to an office building factory in Kobeřice near Opava (Gypstrend Ltd.). The proposal will be based on EN 1996 Eurocode 1 – Actions on structures [7] and EN 1996-1-1 Eurocode 6 – Design of masonry structures [8].

2.2. TECHNICAL DESCRIPTION OF THE OBJECT

The existing office building of the factory is a reinforced concrete wall system, which is made from double-aisle roofed prefabricated reinforced concrete panels. Ground plan dimensions are 36.25 × 12.3 m, height 9.1 m. The building has 3 floors and is covered with a flat roof (Fig 3). The proposed extension presents the possibility of using gypsum blocks on the envelopes [9].

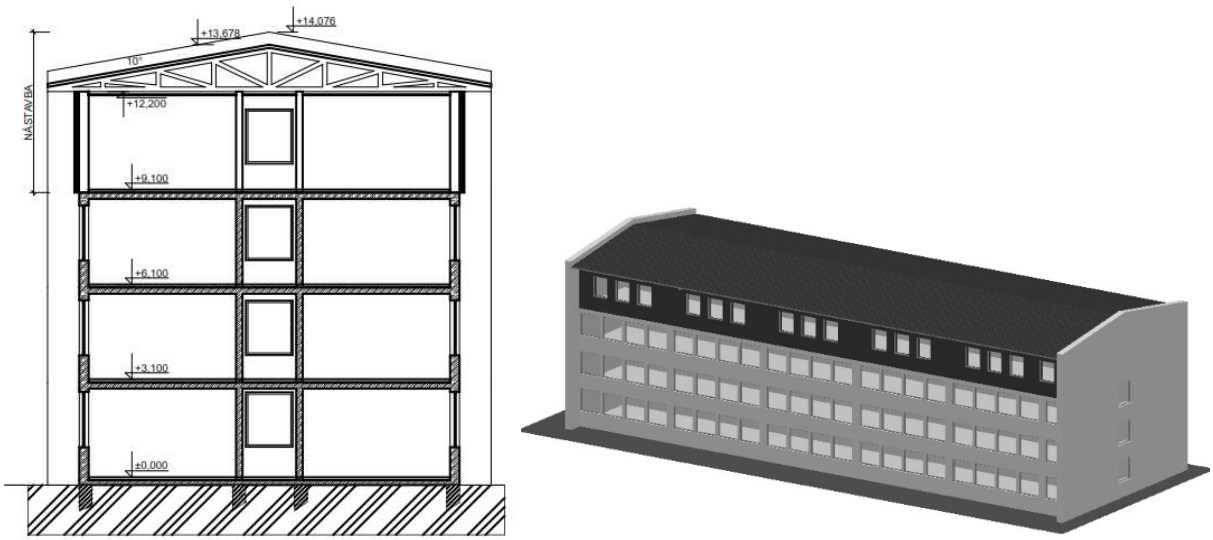

Fig. 3 Schematic section (left) and axonometric view of the building (right)

2.3. VERTICAL LOAD STRESS

Resistance to centric pressure was determined by static calculation taking into account the material properties of modified gypsum. Only random eccentricity can be considered by using roofing trusses. It does not consider the influence of glue strength in the joint. Slenderness ratio is within the limits, when there is no need to consider creep. The design strength of the walls was determined by the Eurocode and it is around 0.95 MPa. Resistance to pressure was determined in the heel and in the middle fifth of the height of the wall. The reserve of load bearing capacity of the blocks were 70%. From these facts it results that the static calculation of the superstructure of the building is acceptable. It should be noted that the smallest dimension of the pillar is 300 mm. It was found by next calculation that it is possible to make also two floors building of classical object from the blocks with need to resolve details ceiling joints. Trusses will be anchored to the wall plate through chemical anchor in a concrete reinforcing rim.

If we consider the imposition of stiffening trusses on a rim, this solution can be calculated as concentrated loads. Local failure is unlikely to be in this type of roofing. Masonry has sufficient capacity.

3. CONCLUSION

Blocks of cast gypsum, respectively prefabricated wall panels, are suitable as supporting elements for the buildings envelopes. Buildings comply with all requirements and can usefully complement the global market in the field of construction. Blocks are particularly suitable for the construction of houses, small buildings and superstructures buildings. Gypsum blocks with lower density are used to minimize the size of the load on the existing building. Prefabricated wall panels made of reinforced

gypsum is applied to larger and more extensive construction of buildings. After installation of the prefabricated wall, it will be poured by concrete mixture with a specific strength,

ACKNOWLEDGEMENT

The financial support of this experiment by the Faculty of Civil Engineering, Czech Technical University in Prague (SGS project No. 12/117/OHK1/2T/11) is gratefully acknowledged.

REFERENCES

[1] Černý, R., Keršner, Z., Rovnaníková, P., Tesárek, P., Toman, J., Tydlitát, V., Vimmrová, A., Vyšvařil, M., Wagner, P., Properties of modified gypsum, (In Czech), Brno: CERM, 2009. 134 p. ISBN 978-80-214-3988-7

[2] Tesárek, P., Jiřičková, M., Černý, R., Rovnaníková, P., Mechanical, thermal and hygric properties of FGD gypsum modified by plasticizers, (In Czech), Stavební obzor, 15 (4), 2006, pp. 114-117.

[3] Zdravkov, B., Pelovski, Y., Extruded building materials from FGD gypsum, Journal of Environmental Protection and Ecology, 7 (1), 2006, pp. 129-136

[4] Rice, G., How an emerging glass-fibre gypsum plaster walling system and improved calcining technology can stimulate profit for the gypsum industry can stimulate, Global Gypsum Magazine, 2009, pp. 22-27.

[5] Tesárek, P., Černý, R., Rovnaníková, P., Mechanical, thermal and hygric properties of FGD gypsum modified by hydrophobizers. (in Czech), Stavební obzor, 15 (5), 2006, pp. 141-143.

[6] Černý, R., Peringer, F., Rovnaníková, P., Tesárek, P., Wagner, P., Material on the basis of calcium sulfate hemihydrates, in particular for production of blocks for building envelope walls, Utility model n. 20478 (Czech national database), 2010.

[7] EN 1996 Eurocode 1 - Actions on structures, Part 1-1 General actions, Prague: CNI 211, 8 p.

[8] EN 1996-1-1 Eurocode 6 - Design of masonry structures. Part 1-1 General rules for reinforced and unreinforced nasonry structures, (In Czech), Prague: CNI, 2007, 106. p

[9] ČSN 722301, Gypsum binders, (In Czech) Prague, ČNI, 1978, 17 p., ISBN 778-72-87111-45-7

RESPONSE OF GRANDSTANDS LOADED BY ACTIVE CROWD AS GAUSSIAN PROCESS

Ondřej ROKOŠ[1], **Jiří MÁCA**[2]

Abstract: *During numerical MC simulation of structure response convergence in distribution of output time functions describing deflections at selected point was observed. Note that the structure was loaded by active crowd only with almost negligible damping and that the asymptotic distribution was normal. With the fact that input processes are non-Gaussian, this is useful property that would simplify structure response estimation. Conditions under which convergence is reached are described and discussed with attempt for explanation.*

Keywords: *grandstands, active crowd, stochastic processes, convergence*

1. INTRODUCTION

Response of grandstands is quite simple question when neglecting all randomness in the model and assuming deterministic load. For more accurate description, uncertainties mainly in forcing terms and passive human crowd parameters together with it's spatial distribution over the structure arises. Mathematical model is written as a set of hyperbolic differential equations

$$\boldsymbol{M}(\lambda)\ddot{\boldsymbol{v}}(t,\lambda) + \boldsymbol{C}(\lambda)\dot{\boldsymbol{v}}(t,\lambda) + \boldsymbol{K}(\lambda)\boldsymbol{v}(t,\lambda) = \boldsymbol{f}(t,\lambda), \qquad (1)$$

where λ and t denotes random and time parameter. This model could be also generalized with nonlinearities in biodynamic human models. Uncertainties in equation *(1)* are described in words as

- right hand side—forcing terms due to jumping of active crowd $\boldsymbol{f}(t,\lambda)$,
- uncertainties in biodynamic model parameters—randomness of $\boldsymbol{K}(\lambda)$, $\boldsymbol{M}(\lambda)$ and $\boldsymbol{C}(\lambda)$ matrices,
- size and spatial distribution of active/passive crowd.

For simplicity, material parameters of the structure are assumed to be deterministic and forcing terms stationary. Set of equations *(1)* represents quite general mathematical model of physical reality. Unfortunately this problem is too complex and cannot be resolved easily at once. Article is thus aimed only at the partial question concerning a structure response under the assumption that only active crowd is occupying the structure.

[1]Ing. Ondřej Rokoš , Faculty of Civil Engineering, CTU in Prague, ondrej.rokos@fsv.cvut.cz

[2]Prof. Ing. Jiří Máca, CSc., Faculty of Civil Engineering, CTU in Prague, maca@fsv.cvut.cz

2. MC SIMULATION

Probability distributions of the structure response at selected point can be acquired employing Monte Carlo simulation (MC). This is possible only when appropriate generator of artificial load is available. Such can be found for example in [1] for discrete frequencies of jumping 1.5, 2.0, 2.67, 3.5 Hz or [2], which is more difficult for implementation but covers frequency range 1.4-2.8 Hz. Generating many input processes and numerically solving eq. *(1)* we arrive to statistical properties of output functions. A few typical input processes together with typical spectral image and histogram are depicted in fig. 1. Clearly, histogram is non-Gaussian, thus we can expect also non-Gaussian response distribution. Led

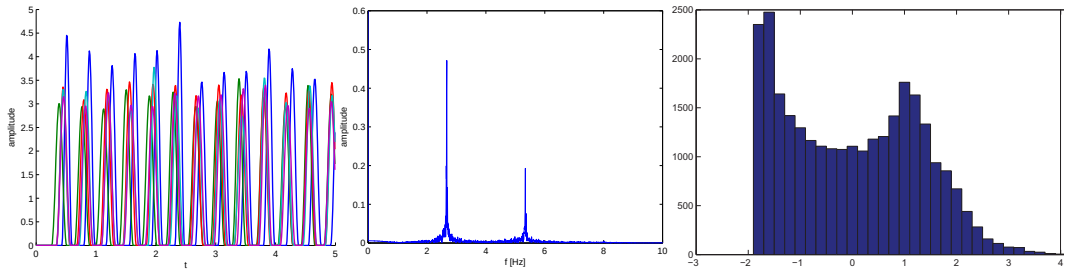

(a) Realizations *(b)* Typical spectral image *(c)* Centered histogram, $\mu = 1$

Fig. 1 Five realizations of the input process, typical histogram and spectral image; functions are normalized with weights of the spectators; frequency of jumping $\bar{f} = 2.67$ *Hz*

by central limit theorem and fact that the response of the structure at selected point results from linear combination of many forcing terms, we can assume that the response distribution shall converge to normal. By intuition the more complex structure, the more forcing terms, the less damping, the better convergence will be. This intuition is supported by numerical simulation, but under reservation as will be apparent later. Let us have three different structures depicted in fig. 2. Red arrow determines chosen point with direction of measured displacement. Structures are fully occupied by active crowd jumping at frequency $\bar{f} = 2.67$ Hz, Rayleigh proportional damping used with $\xi_1 = 0.005$ and $\xi_2 = 0.008$ for the first two vertical bending modes in all cases. First vertical eigenfrequencies are in tab. 1. Histograms

Tab. 1 First eigenvalues corresponding to vertical bending modes [Hz]

Structure	f_1	f_2	f_3	f_4	f_5	f_6	f_7	f_8
(a)	7.5	22.8	41.1	—	—	—	—	—
(b)	5.4	7.0	8.2	25.1	28.4	—	—	—
(c)	2.5	2.6	3.8	4.5	4.8	4.9	5.4	6.0

of output processes for each structure based on 1000 MC simulations of 160 s lengths are depicted in

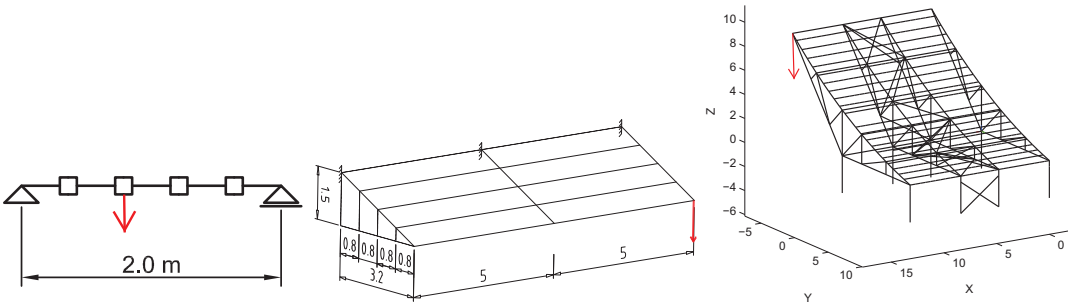

(a) Simply supp. beam, 4 pos. *(b)* Cantilever grandstand, 78 pos. *(c)* Complex structure, 630 pos.

Fig. 2 Three different structures, their geometry and total number of positions for spectators

fig. 3 together with maximum likelihood estimate of normal probability density function. Let us choose

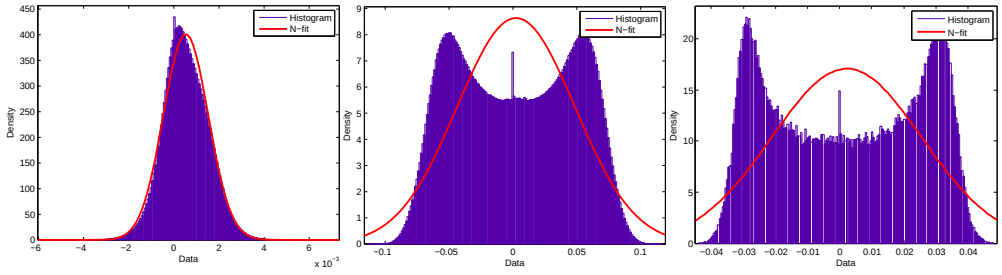

(a) *(b)* *(c)*

Fig. 3 Histograms of tested structures based on 1000 MC simulations; jumping frequency $\bar{f} = 2.67$ *Hz*

structure *(a)* and change material properties to reach given lower eigenfrequency and follow changes in histograms. Results are outlined in fig. 4. Similarly, changes of histograms due to damping alteration are depicted in fig. 5 for frequencies $f_i = 2.7, 8.1, 14.5$ Hz.

Let us briefly discuss some results. From fig. 4 is obvious that in the case of resonance response distribution is far from normal. This is also the case in fig. 3 *(b), (c)*, where in *(b)* the second harmonic $2 \cdot 2.67 = 5.34$ Hz is in resonance with the first eigenfrequency $f_1 = 5.4$ Hz, cf. tab. 1. Structure *(b)* has more resonant eigenfrequencies with applied load. From fig. 5 is apparent that vanishing damping contributes positively to normal distribution. It should be also noted that displacements of the structure are too large due to undamped resonance.

Gaussian random variable X is completely described by two parameters, mean value μ_X and variance $\mathrm{var}X = \sigma_X^2$. Similarly Gaussian continuous random process $X(t) = X_t$, $t \in T \subset \mathbb{R}^+$ is described by mean value $\mathrm{E}X_t = \mu(t) = \mu_t$ and autocovariance function $\mathrm{E}(X_s - \mu_s)(\overline{X}_t - \overline{\mu}_t) = R(s,t)$. When forcing terms are normal stationary processes, differential equation linear and no uncertainties in equation parameters (left hand side in eq. *(1)*), response is also Gaussian and stationary. Theory of linear

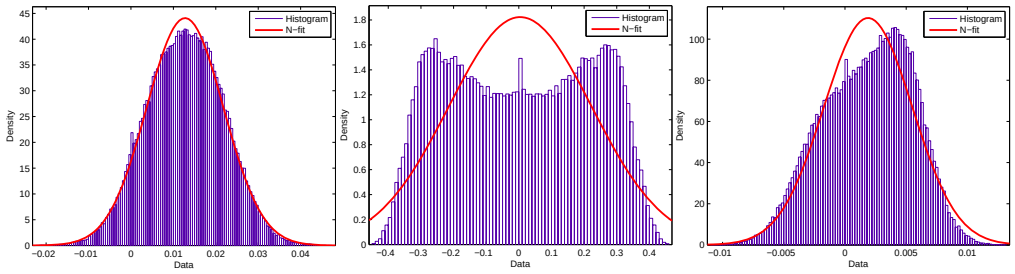

(a) $f_i = 1.5, 4.6, 8.3$ Hz *(b)* $f_i = 2.7, 8.1, 14.5$ Hz *(c)* $f_i = 4, 12.1, 21.8$ Hz

Fig. 4 Histograms of the structure (a), response with changed eigenfrequencies, cf. tab. 1 and fig. 3

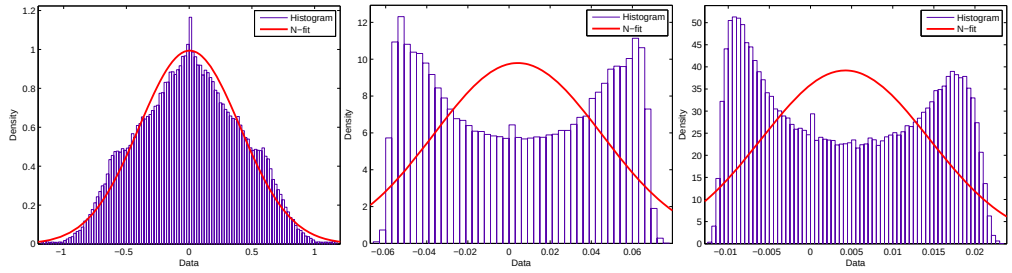

(a) $\xi_i = 0, 0$ *(b)* $\xi_i = 0.05, 0.1$ *(c)* $\xi_i = 0.2, 0.3$

Fig. 5 Histograms of the structure (a), response with changed damping, frequencies $f_i = 2.7, 8.1, 14.5$ Hz, cf. fig. 3

filters can be employed to obtain parameters describing output random functions. When inputs are non-Gaussian, but output as a sum of many non-Gaussian terms converge in distribution to normal, we are talking about asymptotic solution. Also it is possible to solve non-Gaussian response, but theory is much more demanding. Let us mention translation processes, Gaussian processes scaled by random parameters and other conditional Gaussian processes, processes defined by stochastic differential equations etc., for example see [3], chap. 7.4.1.2.

3. CONVERGENCE IN DISTRIBUTION

Let us first explain, what does convergence in distribution mean, [4] §10 Definition 4.

The sequence $\xi_1, \xi_2, \ldots$ of random variables *converges in distribution* to the random variable ξ (notation: $\xi_n \xrightarrow{d} \xi$) if $\mathrm{E}f(\xi_n) \to \mathrm{E}f(\xi)$, $n \to \infty$, for every bounded continuous function $f(x)$. Condition is equivalent to the convergence of the distribution $F_{\xi_n}(x)$ to $F_\xi(x)$ at each *point x of continuity* of $F_\xi(x)$.

Thus, if distribution function $F_\xi(x)$ is absolutely continuous, probability density exists, and convergence in distribution also means that density as it's derivative converges.

From figs. 3 and 4 it is obvious that the response histograms are influenced mainly by eigen-frequencies of the structure. Explanation can be based on fact that spectral density has several peaks corresponding to deterministic periodic function. Almost "constant" remainder is spectral density standing for additional noise. That the noise is almost Gaussian can be verified by filtering the spectra in near vicinities of each harmonic. Such spectra with consecutive inverse Fourier transform together with its histogram are depicted in fig. 6, see original data in fig. 1. In the case that peak of the transfer

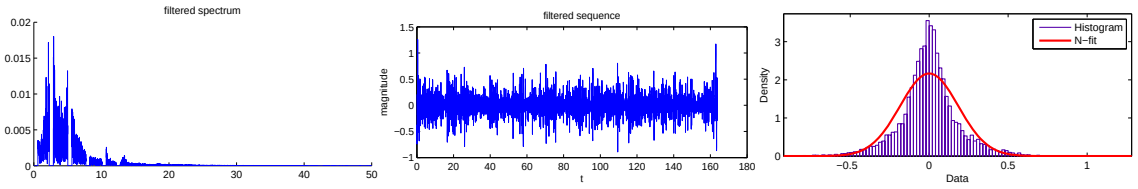

(a) Filtered spectral density *(b)* Filtered realization *(c)* Histogram of filtered realization

Fig. 6 Filtered spectra, it's inverse Fourier transform and histogram of sequence, cf. fig. 1

function magnify noise, response is mor or less normal. Conversely, in the case of resonance with some of the harmonics, histogram is close to one that has sine function which is almost identical with one in fig. 3 *(c)*. Situation is depicted in fig. 7, where only transfer functions corresponding to node marked in fig. 2 *(a)* by red arrow are depicted. Remaining functions are similar because response is driven by the first eigenmode in this simple case.

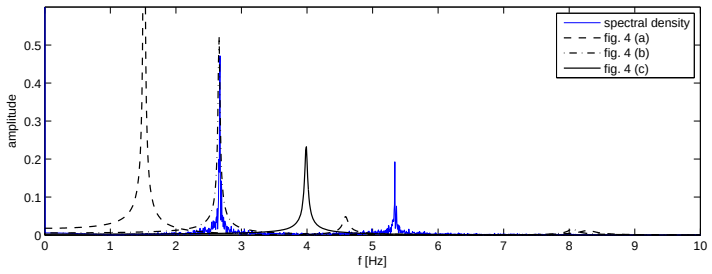

Fig. 7 Spectral density with several transfer functions corresponding to fig. 4 (a), (b) and (c); magnification factor of transfer functions is 4

4. GAUSSIAN PROCESSES AND LINEAR FILTERS

From the previous section it follows that input process can be decomposed into non stationary mean value μ_t and stationary noise, that is

$$X_t = \sum_{k=1}^{p} a_k e^{\mathbb{i}t\omega} + Y_t = \mu_t + Y_t, \qquad (2)$$

where $a_1, \ldots, a_p$ are constants, $\omega_1, \ldots, \omega_p$ are mutually distinct numbers and Y_t is white noise with mean zero and constant variance $\sigma^2 > 0$. This kind of process is called covariance stationary. For

description of input process, mean value μ_t and spectral density $f(\omega)$ are needed. Mean value can be estimated using Least Squares Method. Employing Euler formula and placing $\omega_k = k \cdot 2\pi\bar{f}$ in (2) yields

$$\mu_t = \alpha_0 + \sum_{k=1}^{p} \alpha_k \cos(k \cdot 2\pi\bar{f}t) + \beta_k \sin(k \cdot 2\pi\bar{f}t). \tag{3}$$

Then the vector $\hat{\boldsymbol{\alpha}}$ of estimated parameters $\hat{\alpha}_0, \hat{\alpha}_1, \ldots, \hat{\alpha}_p, \hat{\beta}_1, \ldots, \hat{\beta}_p$ can be evaluated as

$$\hat{\boldsymbol{\alpha}} = (\boldsymbol{\Phi}^T\boldsymbol{\Phi})^{-1}\boldsymbol{\Phi}^T\bar{\boldsymbol{X}}, \tag{4}$$

where

$$\boldsymbol{\Phi} = \begin{pmatrix} 1 & \cos(2\pi\bar{f}t_1) & \sin(2\pi\bar{f}t_1) & \ldots & \cos(p \cdot 2\pi\bar{f}t_1) & \sin(p \cdot 2\pi\bar{f}t_1) \\ 1 & \cos(2\pi\bar{f}t_2) & \sin(2\pi\bar{f}t_2) & \ldots & \cos(p \cdot 2\pi\bar{f}t_2) & \sin(p \cdot 2\pi\bar{f}t_2) \\ \ldots & \ldots & \ldots & \ldots & \ldots & \ldots \\ 1 & \cos(2\pi\bar{f}t_n) & \sin(2\pi\bar{f}t_n) & \ldots & \cos(p \cdot 2\pi\bar{f}t_n) & \sin(p \cdot 2\pi\bar{f}t_n) \end{pmatrix},$$

$t_1, \ldots, t_n$ are equidistant partitions of time interval and

$$\bar{\boldsymbol{X}} = \bar{\boldsymbol{X}}(t) = \frac{1}{N}\sum_{k=1}^{N} X_k(t),$$

is mean over an N realizations. Here $X_k(t)$ is k-th realization of forcing term. Generating 10 000 realizations leads to coefficients in tab. 2. From here it is obvious that constant term with the first two or three harmonics are sufficient.

Tab. 2 Coefficients for approximation of the mean value

Coeff.	$\hat{\alpha}_0$	$\hat{\alpha}_1$	$\hat{\beta}_1$	$\hat{\alpha}_2$	$\hat{\beta}_2$	$\hat{\alpha}_3$	$\hat{\beta}_3$	$\hat{\alpha}_4$	$\hat{\beta}_4$
Value	0.9958	0.2939	1.1770	−0.2471	0.0984	−0.0037	−0.0153	−0.0008	−0.0001

As a next step, estimate of spectral density $\hat{f}(\omega)$ of centered forcing term $X_t - \mu_t$ is needed. Because periodogram is biased, Parzen windowing will be used. By averaging

$$\hat{f}_{jj}(\omega) = \int_{-\infty}^{\infty} b(x-\omega) I_T(\omega)\,\mathrm{d}x, \tag{5}$$

where $I_T(\omega)$ denotes periodogram of centered forcing term

$$I_T(\omega) = \frac{1}{2\pi T}\left|\int_0^T X(t)e^{-\mathrm{i}t\omega}\,\mathrm{d}t\right|^2, \qquad -\infty < \omega < \infty. \tag{6}$$

For Parzen window special function $b(x)$ is used, for details see chap. VII and VIII in [5]. Except magnitudes, spectral density of centered forcing term is similar to original one in fig. 1 *(b)*. Cross spectral densities are obtained similarly as

$$\begin{aligned} \hat{f}_{jk}(\omega) &= \int_{-\infty}^{\infty} b(x-\omega) I_{jk}(\omega)\,\mathrm{d}x, \\ I_{jk}(\omega) &= \frac{1}{2\pi T}\int_0^T X_j(t)e^{-\mathrm{i}t\omega}\,\mathrm{d}t \overline{\int_0^T X_k(s)e^{-\mathrm{i}s\omega}\,\mathrm{d}s}, \qquad -\infty < \omega < \infty. \end{aligned} \tag{7}$$

Resulting histogram of centered process is closer to normal, cf. fig. 8 *(b)*. Procedure resembles filtering mentioned in section 1.2, but for discrete frequencies. Response of the structure to mean value can be

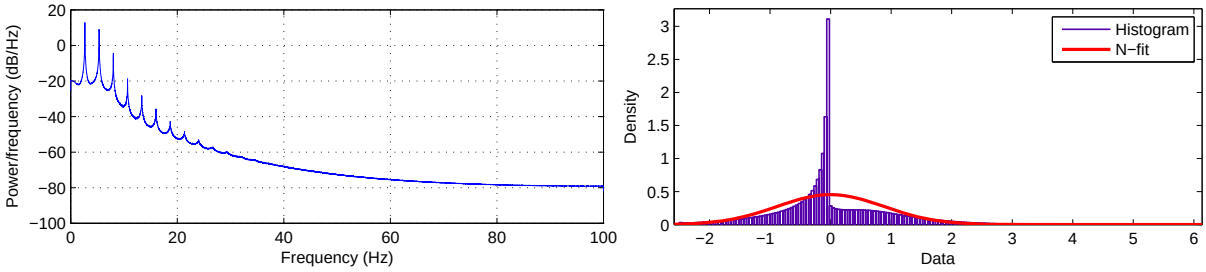

(a) Spectral density *(b)* Histogram

Fig. 8 Centered forcing terms—spectral density and histogram; $\bar{f} = 2.67$ *Hz*

computed employing common numerical integration methods such as Newmark, HHT, etc. To estimate asymptotic probability distribution of the structure response forced by stationary stochastic process, theory of linear filters will be used. Spectral densities of forcing terms are located in spectral density matrix $[\boldsymbol{S}_f(\omega)]_{jk}$. When processes are considered independent, off diagonal terms are zero. Further, this assumption will be implied. Employing transfer function of linear filter corresponding to the structure $\boldsymbol{H}(\omega)$, spectral density matrix of output processes is obtained as

$$\boldsymbol{S}_v = \boldsymbol{H}\boldsymbol{S}_f\boldsymbol{H}^H, \tag{8}$$

where $\boldsymbol{H}^H$ denotes Hermitian transpose. Transfer function is computed as

$$\boldsymbol{H}(\omega) = (-\omega^2\boldsymbol{M} + \mathbb{i}\omega\boldsymbol{C} + \boldsymbol{K})^{-1}. \tag{9}$$

Variance of centered stationary process with two sided spectral density $f(\omega)$ or one sided spectral density $g(\omega)$ is computed according to

$$\sigma^2 = \int_{-\infty}^{\infty} f(\omega)\,\mathrm{d}\omega = \int_0^{\infty} g(\omega)\,\mathrm{d}\omega. \tag{10}$$

Knowing spectral density matrix of the structure response, variance of arbitrarily chosen point can be estimated. Results computed for the aforementioned structures are depicted in fig. 9. These ought to be superposed with mean value μ_t response. As a next step approximation of centered forcing with ARMA process can be employed.

5. CONCLUSION

MC simulation proved that driving forces on the structure have non-Gaussian distribution. Statistical data processing of structure response based on MC simulation showed that in some situations convergence to normal is reached. This fact leads to covariance stationarity of input process. Mean value μ_t was approximated with trigonometric series employing least squares method. By centering, histogram

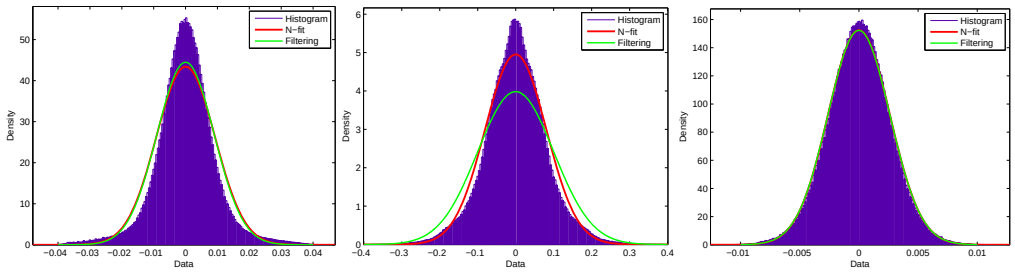

(a) *(a)*, $f_i = 1.5, 4.6, 8.3$ Hz *(b)* *(a)*, $f_i = 2.7, 8.1, 14.5$ Hz *(c)* *(a)*, $f_i = 4, 12.1, 21.8$ Hz

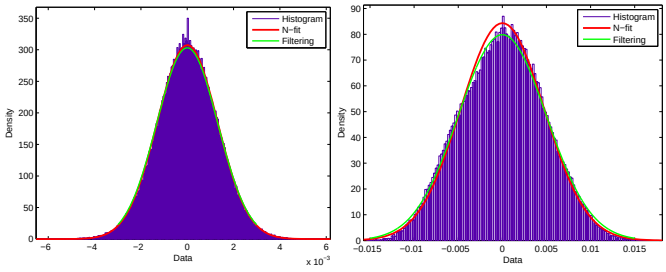

(d) structure *(b)* histogram *(e)* structure *(c)* histogram

Fig. 9 Histograms of structure (a), (b) and (c) response; structure (a) with changed eigenfrequencies, cf. fig. (4)

of driving forces was closer to colored Gaussian noise, which improved convergence to normal in distribution of output process.

ACKNOWLEDGEMENT

The financial support of this contribution by the Faculty of Civil Engineering, Czech Technical University in Prague (SGS project No. 12/027/OHK1/1T/11) is gratefully acknowledged.

REFERENCES

[1] J. H. Sim, *Human-structure Interaction in Cantilever Grandstands*, Doctor of Philosophy thesis at the university of Oxford, 2006

[2] V. Racic, A. Pavic, *Mathematical Model to Generate Near-periodic Human Jumping Force Signals*, Mechanical Systems and Signal Processing 24 (2010) 138–152, ISSN: 0888-3270

[3] M. Grigoriu, *Stochastic Calculus: Applications in Science and Engineering*, Birkhäuser, Boston, 2002, ISBN: 978-0817642426

[4] A. N. Shiryaev, *Probability (Graduate Texts in Mathematics v. 95), Second Edition*, Springer-Verlag, Berlin, 1989, ISBN: 978-0387945491

[5] J. Anděl, *Statistická analýza časových řad*, SNTL, Praha 1976, ISBN: 990000163X

INTEGRAL TRANSFORMS IN STRUCTURAL DYNAMICS

Vladimír ŠÁNA[1], **Michal POLÁK**[2]

Abstract: *Following text is focused on integral transforms in structural dynamics. It means especially FourierTransform (FT, DFT, FFT). There will be also discussed Wavelet Transform, which allows us to analyze signals in time and frequency domains with satisfying distinction.*

Keywords: *Fourier Analysis, Time-Frequency Analysis, Wavelet Transform, Integral Transforms*

1. INTRODUCTION

The reason why we apply integral transforms on the signals is that we need to find out what frequencies are in analyzed signal. This is very important e.g. in modal analysis, where we have to detect natural frequencies and natural mode of vibrations to verify computational model of the structure.

2. FOURIER ANALYSIS

2.1. FOURIER'S SERIES

Periodical functions can be expressed as sum of cosines and sines with different harmonic frequencies. It is also applicable to discontinuous functions with finite number of discontinuities and with finite number of local extremes.

The equation of complex Fourier's Series is:

$$\overline{f}_{(t)} = \sum_{k=-\infty}^{\infty} c_k e^{i\frac{2\pi}{T}kt} \qquad (1)$$

$$c_k = \frac{1}{T}\int_0^T f_{(t)} e^{-i\frac{2\pi}{T}kt}\, dt \qquad (2)$$

[1] Ing. Vladimír Šána, Department of Mechanics, Faculty of Civil Engineering, CTU in Prague; vladimir.sana@fsv.cvut.cz

[2] prof. Ing. Michal Polák , CSc., Department of Mechanics, Faculty of Civil Engineering, CTU in Prague; polak@fsv.cvut.cz

T - natural period, $f_{(t)}$ - original function, c_k are Fourier's coefficients, $\overline{f}_{(t)}$ - approximated function

2.2. CONTINUOUS FOURIER TRANSFORM

Generally, in dynamics and in the other branches of science, Fourier Transform is used, which is defined by equation (3). Inverse Fourier Transform is described by relation (4)

$$F_{(\omega)} = \int_{-\infty}^{\infty} f_{(t)} e^{-i\omega t} dt \qquad (3)$$

$$f_{(t)} = \frac{1}{2\pi} \int_{-\infty}^{\infty} F_{(\omega)} e^{i\omega t} d\omega \qquad (4)$$

where $f_{(t)}$ is real or complex function and $e^{-i\omega t}$ is the kernel, $F_{(\omega)}$ is transformed function in frequency domain.

This type of integral transform can be used in nonperiodic functions e.g. impulses. It provides us to get a continuous spectrum in frequency domain, but we cannot detect exact time, where the frequency appeared.

Continuous Fourier Transform can be used only if analyzed function accomplishes Dirichlet's conditions. As consequence, the transformed function has to be absolutely integrable. It means

$$\int_{-\infty}^{\infty} \left| f_{(t)} \right| dt < \infty \qquad (5)$$

2.3. DISCRETE FOURIER TRANSFORM

Discrete Fourier Transform converts vector of function's values in time domain to vector of Fourier's coefficients in frequency domain. Analyzed vector is given by sampling continuous function. DFT is defined as:

$$F_k = \sum_{n=0}^{N-1} f_n e^{-i\frac{2\pi}{N}kn} \qquad k = 0,1,2,...,N-1 \qquad (6)$$

and inverse DFT defined by:

$$f_n = \frac{1}{N} \sum_{k=0}^{N-1} F_k e^{i\frac{2\pi}{N}kn} \qquad n = 0,1,2,...,N-1 \qquad (7)$$

where f_n is sampled (digitalized) function, N is the number of samples, F_k - Fourier's spectral coefficients.

Function for FFT analysis, example:

$$f_{(t)} = \left\{3\sin(2\pi 20t) + 5\cos(2\pi 30t) + 6\sin(2\pi 40t) + 4\sin(2\pi 5t)\right\}e^{-5t}$$

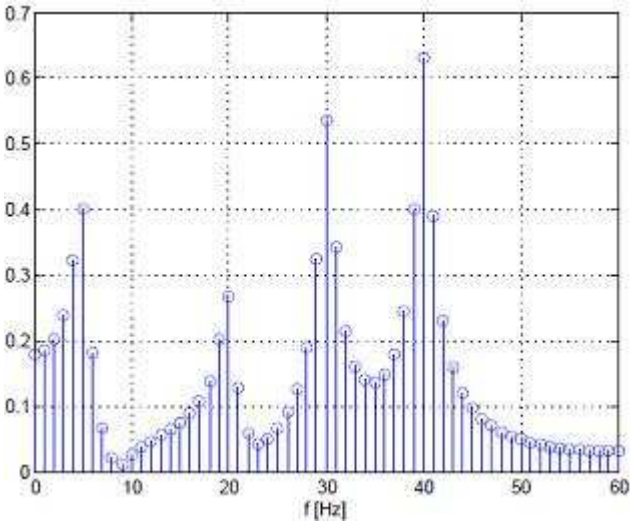

Fig. 1 Spectrum of analyzed signal

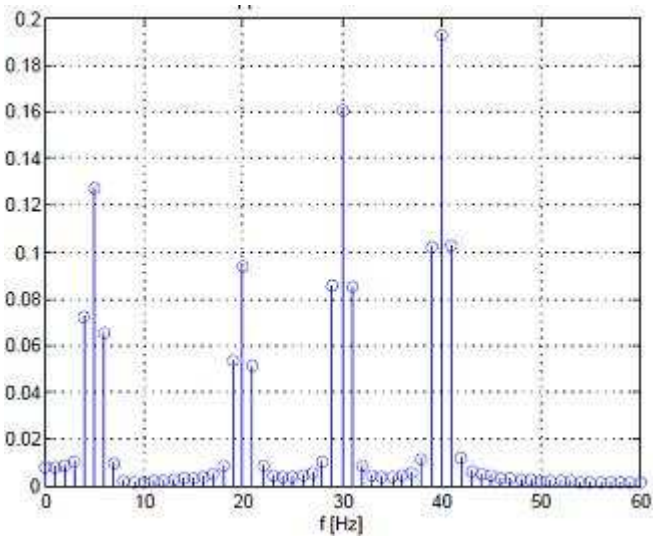

Fig. 2 Spectrum multiplied by Gauss window

2.4. SAMPLING

Discrete signal is created from continuous signal by sampling. This process is called digitalization of analog function. Important parameters are sampling frequency f_s and sampling period T_s. For correct reconstruction of original analog function it is necessary to keep conditions for choice of sampling frequency. This theorem is known as the Shannon-Nyquist condition: $f_s > 2 f_0$, f_0 : frequency of original function

If this condition is not kept, then effect called aliasing occurs, shown in figure 4.

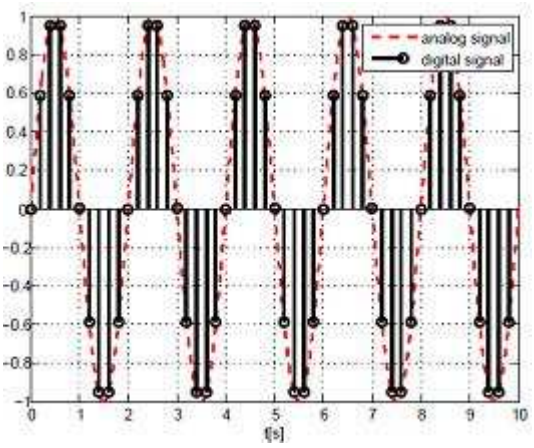

Fig. 3 Sampling

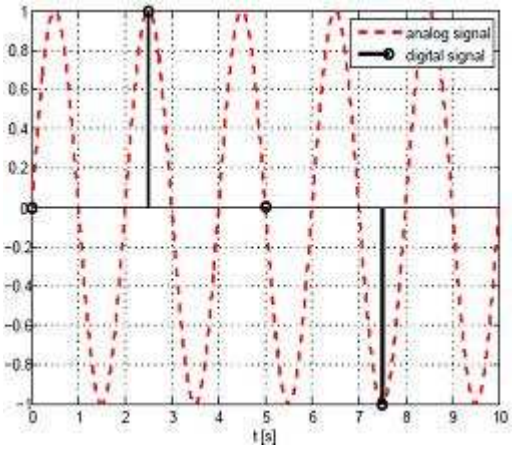

Fig. 4 Aliasing effect

Thus aliasing occurs, when the analog signal is subsampled. It is undesirable event and it looks like a different period is forced to the original function.

2.5. FAST FOURIER TRANSFORM

This algorithm is very effective for computer elaboration, because of reduced number of complex multiplicasions in the DFT from N^2 to $N \log N$. It has been developed by Cooley and Tukey in 1965.

The first step is to divide sequence into the even and odd figures. This procedure allows us compute just two N/2 – point DFT. The only requirement is on the quantity of points (*N)*, which has to be considered to FFT algorithm. FFT is applicable for $N = 2^m$, where *m* is the natural number.

3. TIME – FREQUENCY ANALYSIS

3.1. SHORT TIME FOURIER TRANSFORM

In previous procedures it is not possible to detect at which time frequencies have occurred. That is why Short Time Fourier Transform was introduced. It is defined by (8)**.**

At first it is analyzed function scalar multiplied by window function (fundamental window functions are shown in Figure 5) and time axis is divided into finite number of intervals, where it is assumed that the signal is stationary. Thanks to the Heisenberg's principle of uncertainty it is not possible to achieve same distinction in time and frequency domain.

$$F_{(\omega)} = \int_{-\infty}^{\infty} f_{(t)} w_{(t-\tau)} e^{-i\omega t} dt \tag{8}$$

Discrete STFT:

$$F_k = \frac{1}{\sqrt{N}} \sum_{n=0}^{N-1} f_n w_n e^{-i\frac{2\pi}{N}kn} \tag{9}$$

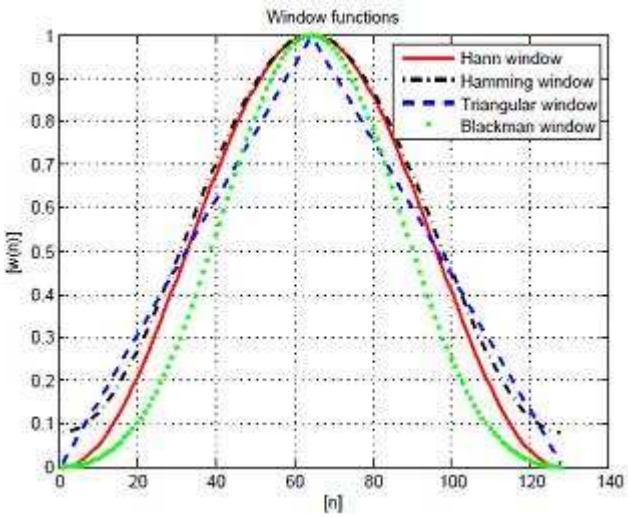

Fig. 5 Window functions

Function for STFT analysis, example:

$$f_{(t)} = \left\{3\sin\left(2\pi 250t\right) + 5\cos\left(2\pi 100t\right) + 6\sin\left(2\pi 20t\right) + 4\sin\left(2\pi 400t\right)\right\} e^{-2t}$$

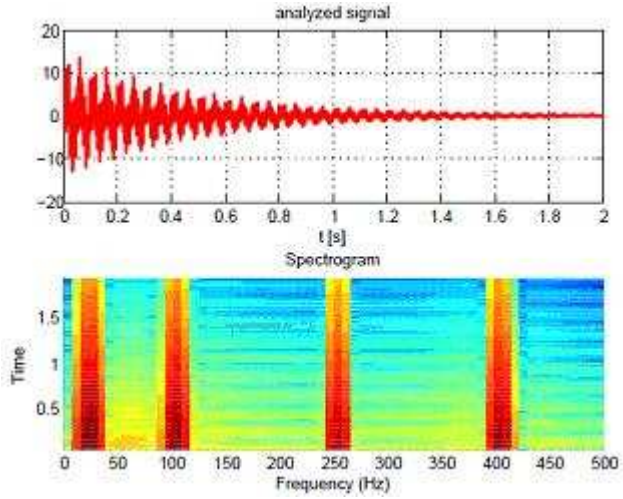

Fig. 6 Spectrogram of analyzed function

3.2. WAVELET ANALYSIS

This type of analysis transforms signals from time domain to time-frequency domain thanks to mother wavelets (shown in Figure 7). After application of Wavelet Transform to one-dimensional function, we obtain function of two variables, scale and shifting. Graphical representation of wavelet coefficient is called scalogram or wavelet map.

3.3. CONTINUOUS WAVELET TRANSFORM

Wavelet Transform is also effective for nonstationary signals and for signals, where high frequencies are in short time intervals, such as eartquake or speech registration. It is an alternative to STFT with higher distinction ability. Disadvantage of STFT is constant width of time window, but in WT the window width is variable. Continuous Wavelet Transform is defined by (10).

The aim of the CWT is to decompose signal to wavelet coefficient series. By contrast with the Fourier Transform mother wavelets are aperiodic functions. Mother wavelets simply oscillate around the point of localization.

$$W_{(a,\tau)} = \int_{-\infty}^{\infty} f_{(t)} \frac{1}{\sqrt{a}} \psi_{\left(\frac{t-\tau}{a}\right)} dt \qquad (10)$$

Inverse Wavelet Transform:

$$f_{(t)} = \frac{1}{C_\psi} \int_{0}^{+\infty} \int_{-\infty}^{+\infty} W_{(a,\tau)} \frac{1}{\sqrt{a}} \psi_{\left(\frac{t-\tau}{a}\right)} d\tau \frac{da}{a^2} \qquad (11)$$

where a is the scale, $f_{(t)}$ is analyzed function and $\psi_{(\frac{t-\tau}{a})}$ is the mother wavelet, kernel of transform, τ is time shifting of wavelet, C_ψ coefficient of admissibility

3.4. DISCRETRE WAVELET TRANSFORM

Continuous Wavelet Transform is not practical in computer processing due to infinite number of wavelet coefficients that is why DWT was introduced. In contrast with Fourier Transform, DWT has local character. Therefore, DWT provides better approximation of discontinuities.

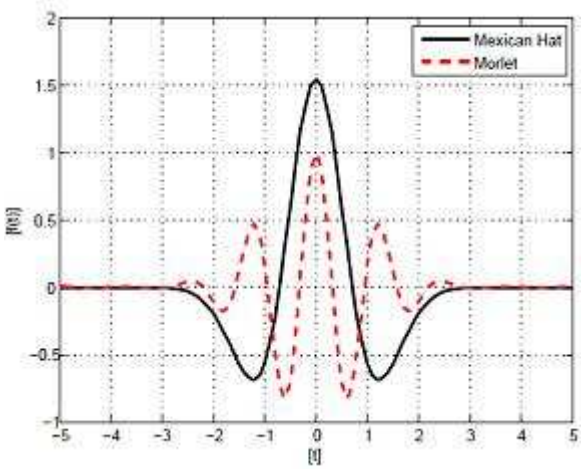

Fig. 7 Examples of mother wavelets

Function for Wavelet Analysis, example:

$$f_{(t)} = \left\{4\sin(2\pi 20t) + 5\sin(2\pi 50t) + 2\sin(2\pi 10t)\right\}e^{-2t}$$

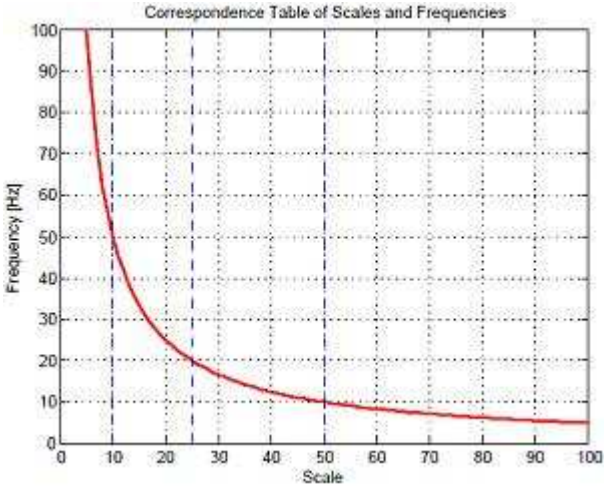

Fig. 8 Correspondence table of scales and frequencies

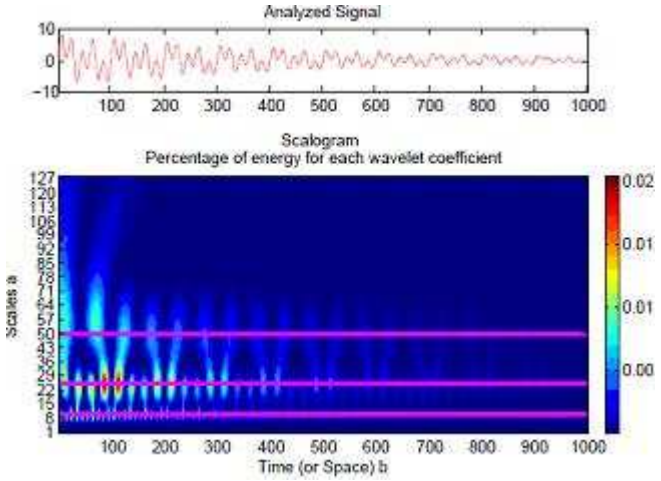

Fig. 9 Scalogram of analyzed function

ACKNOWLEDGEMENT

This paper has been created thanks to project SGS12/117/OHK1/2T/11 supported by Czech Technical University in Prague.

REFERENCES

[1] Boggess, A., Narcow, J.F., A First Course in Wavelets with Fourier Analysis, Prentice Hall, 2001, ISBN 0130228095

[2] Carslaw, H.S., Introduction to the theory of Fourier's Series and Integrals, 1921, ISBN 1418182729

[3] Hernandez, E., Weiss, G., A First Course on Wavelet, 1996**,** ISBN 0849382742

[4] Rektorys, K., et all.: Přehled užité matematiky I, Prometheus, Praha, 1995, ISBN 978-80-7196-180-2

[5] Tůma, J., Zpracování signálů z mechanických systémů užitím FFT, Praha, 1997, ISBN 80-901936-1-7

LOAD-BEARING LINTEL FROM MODIFIED GYPSUM

Ondřej ŠANDERA[1], Tomáš PLACHÝ[2], Pavel TESÁREK[3]

Abstract: *Gypsum is one of the oldest binders that people use. Due to its properties it has wide use not only in the construction industry at present time. It is used to carry out of plaster work, floor screeds and for production of industrially manufactured products in the construction. The aim of the paper is to design a load-bearing lintel from modified gypsum as a supplement to gypsum blocks for outer walls and create another possible variant of the walling system.*

Keywords: *modified gypsum, load-bearing lintel, tensile reinforcement*

1. INTRODUCTION

1.1. HISTORY

Gypsum is a historical binder, which was used for several thousand years B.C. In Syria there were discovered finishes of walls dating 7 000 years BC. Egyptians 5 000 years ago burnt gypsum in open fires, fired material crushed to powder and mixed it with water to prepare mortar for masonry blocks of pyramids. Romans used gypsum to produce decorative elements. In China and India they used gypsum for the inside plaster to achieve a smooth surface. In the Middle Age in Europe there was widespread use of decorative plasters, which has been used for interiors and exteriors since the 13th century [1].

In the 16th century, the specially treated gypsum was used as a substitute for natural colored marble. In the 2nd half of the 17th century after the great fire of London, the gypsum was used for finish layout of wooden buildings like a fire protection in Paris. The massive use of gypsum like a construction binder occurred in the 2nd half of the 19th century with the development of construction technologies and industrial production. At present time the gypsum is used in the interior in the form of gypsum boards or in different plaster systems. In Poland they used gypsum as a building material for outer walls [1]. In Australia they developed in early 90 of the 20th century hollow panels from the

[1] Bc. Ondřej Šandera, Department of Mechanics, Faculty of Civil Engineering, CTU in Prague; ondrej.sandera@fsv.cvut.cz

[2] Ing. Tomáš Plachý, Ph.D., Department of Mechanics, Faculty of Civil Engineering, CTU in Prague; plachy@fsv.cvut.cz

[3] Ing. Pavel Tesárek, Ph.D., Department of Mechanics, Faculty of Civil Engineering, CTU in Prague; tesarek@fsv.cvut.cz

modified gypsum reinforced with glass fiber intended for civil construction. The manufacturer states that the two-storey houses can be built from panels with empty cavities. For higher objects it is necessary to fill the cavities with concrete [2].

1.2. PRODUCTION OF GYPSUM AND ITS PROPERTIES

Gypsum is one of the airy inorganic binders. The raw material for the production is gypsum obtained from natural or industrial sources. Gypsum from industrial sources is further distinguished on "chemo-gypsum", formed as a waste of chemical production and "energo-gypsum", which is produced by desulphurization of flue gas in thermal power plants. The production process of gypsum is called calcination and it takes place dehydration of gypsum according to the equation:

$$CaSO_4 \cdot 2H_2O + heat \rightarrow CaSO_4 \cdot 0.5H_2O + 1.5H_2O \qquad (1)$$

The α- and β- modifications of gypsum are created depending on the dehydration conditions, which are different in grain shape and technological properties. Modification of α-gypsum shows greater strength after hardening slurry and it is generally considered for better binder.

Mechanical properties of gypsum depend on many factors. Its moisture has the biggest influence on it. It is necessary to pay attention to the humidity of the environment in which is located, because gypsum is very hydroscopic. Strength and modulus of elasticity decrease by wetting of the product. The additives may be added to the gypsum for improving some properties, for this reason. In terms of fire protection gypsum products are considered to be fire resistant [4], [5] and [6].

2. LOAD-BEARING GYPSUM LINTEL

The aim of designing load-bearing lintel from modified gypsum is complete the developing modified gypsum blocks for outer walls. The idea is develop next structural member from this material and create a complete system of masonry. The lintel size was chosen with regard to the size of blocks, the estimated clear opening width 1 500 mm and the finally weight of the lintel [6]. Additional requirement was easy to handle with it. The designed dimensions are following:

- length: L = 1 800 mm
- height: h = 300 mm
- width: b = 150 mm
- length of storage: t = 150 mm

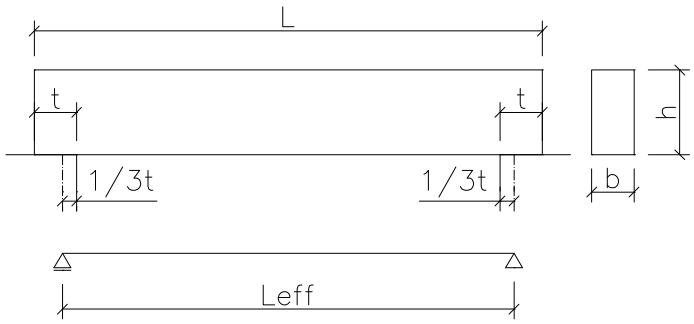

Fig. 1 Static scheme of lintel

2.1. SPECIFICATION OF USED MATERIAL

The gypsum binder G2BII grey (β- hemihydrate calcium sulphate) [7] – product of Gypstrend Ltd - will be used for the manufactory of lintel. Mixture is composed of gypsum binder, plasticizer-aerating additives, hydrophobic additives, thermal insulation additives and water. Exemplary composition of the mixture can be found in the utility model [8]. Material parameters based on calcium sulphate hemihydrate according to an exemplary composition are shown in Tab. 1.

Tab. 1 Material parameters

Interviewed property	Unit	The average value
Density of fresh mixture	kg/m^3	1159
Cake spilling	mm	120
Coefficient of water	kg/kg	0.8
Start hardening	min.	8
The end of hardening	min.	13
Compressive strength after 2 hours	MPa	1.9
Compressive strength after 24 hours	MPa	2
Compressive strength after 7 days	MPa	3.6
Compressive strength after 28 days	MPa	3.8
Flexural tensile strength after 7 days	MPa	2
Flexural tensile strength after 28 days	MPa	2.1
Absorptivity	% weight.	8
Density after drying	kg/m^3	680
Frost resistance	cycles of freezing	25
Coefficient of thermal conductivity l	W/m·K	0.156
Coefficient of thermal expansion a	K^{-1}	$7.22 \cdot 10^{-6}$
Mass activity ^{226}Ra	Bq/kg	25
Water vapor diffusion resistance factor	50/90% r.h.	16
Moisture absorption coefficient	kg/m^2s	0.007
Modulus of elasticity	GPa	1.74

The material is characterized by a relatively high compressive strength. Tensile strength in bending is on the other hand about half of the compressive strength value. Therefore it is necessary to place tension reinforcement to the underside of lintel [9].

2.2. REINFORCEMENT

As the tensile reinforcement, located on the underside of lintel, it is supposed concrete reinforcement steel B500 with a yield stress f_y = 500 MPa. There is expected to have two separate reinforcing bars of the same diameter. Interaction with gypsum binder is provided by ribbed surface of reinforcement. For improving the interaction between reinforcement and gypsum binder, it is possible to get rectangular or semicircular hooks at the end of the reinforcement.

There are considered two variants of reinforcement. The first alternative is uncoated concrete reinforcement. In the second alternative there is used epoxy coated reinforcement due to reinforcement corrosion protection. Thickness of epoxy layer is about 200 μm.

The coefficient of thermal expansion of steel is $\alpha = 1.2 \cdot 10^{-5}$ K^{-1}, which is an order of magnitude larger than the gypsum. The lintel will be hidden under the contact thermal insulation system and would not be exposed to the extreme temperature differences. It can be assumed that the temperature differences in summer and winter does not exceed 20 °C. This would not formed large additional stress from the different thermal expansion in the element and following damages to the lintel.

3. DESIGN OF THE GYPSUM LINTEL

Design of the lintel from modified gypsum is based on the standards CSN EN 1992-1-1 Designing of concrete structures and CSN EN 12 602 Prefabricated reinforced components of autoclaved aerated concrete. Lintel cannot be shortened or its cross section cannot be modified. It is deposited in a mortar bed. To create a window opening it is necessary to use two lintels.

3.1. VARIANT 1 – CONCRETE REINFORCEMENT

Static design of the lintel is based on an idealized rectangular stress distribution. It is assumed that the gypsum is active only in pressure and the steel reinforcement transfers whole tension. There are designed 2 rods with diameter ø 8 mm; the size of the cover is 20 mm. This design meets the condition of the minimum reinforcing and distance between the centres of the bars.

Value of the design moment resistance M_{Rd} = 10.45 kNm was calculated for this designed member. This approximately corresponds to the value of continuous load f = 32.7 kN/m (including the self-weight of the lintel) or the value F = 13 kN for the concentrated load. Shear reinforcement is not necessary because calculated value of the design shear resistance of the unreinforced section is $V_{Rd,1}$ = 192 kN.

3.2. VARIANT 2 – EPOXY COATED CONCRETE REINFORCEMENT

The first designed variant is not completely useful for use in gypsum binder because the ability of gypsum to absorb water will corrode the reinforcement in a lintel. Corrosion of reinforcement in gypsum materials is relatively high because moisture penetrates easily to the reinforcement due to high

porosity of the hardened gypsum. Gypsum binders also have not the ability to create an alkaline environment in which the steel was passivated. The gypsum has pH = 5 at a relative humidity higher than 60 %. This leads to corrosion of the reinforcement. Therefore, it is necessary to protect the reinforcement against the corrosion.

As prevention against corrosion we can use galvanized or stainless steel reinforcement. Another possibility is the use of non-metallic reinforcement from carbon, glass or propylene fibres. The wider applications of these variants are still precluded primarily by high price. That is the reason why the second variant was chosen epoxy coated reinforcement.

The disadvantage of this variant is smaller cohesion of reinforcement with gypsum binder compared to the first variant. Some sources introduce decrease cohesion about 20 %. For galvanized reinforcement, the cohesion is less only about 7 % [10].

4. CONCLUSION

Construction elements from modified gypsum, thanks to their properties and low energy demands for production, seem to be appropriate building material for the family construction and superstructures of buildings in the future. The wide application of these products depends only on the material properties of gypsum. If the possibility of reinforcing gypsum with epoxy coated reinforcement will be proved, we can get another potential walling system. This system from modified gypsum blocks could compete with walling system of aerated concrete widespread in our country due to their properties.

ACKNOWLEDGEMENT

The financial support of this experiment by the Faculty of Civil Engineering, Czech Technical University in Prague (SGS project No. 12/117/OHK1/2T/11) is gratefully acknowledged.

REFERENCES

[1] Rovnaníková, P., History and application of gypsum, (in Czech), In: Zpravodaj STOP - Sádra v památkové péči, 8 (2), 2006, pp. 4-5, ISSN 1212-4168

[2] Svoboda, L., et al., Building materials, (In Czech), Bratislava: Jaga group, 2007, ISBN 978-80-8076-057-1

[3] Wu, Y.F., The structural behavior and design methodology for a new building system consisting of glass fiber reinforced gypsum panels, In: Construction and Building Materials, 23, 2009, pp. 2905-2913.

[4] Černý, R., Keršner, Z., Rovnaníková, P., Tesárek, P., Toman, J., Tydlitát, V., Vimmrová A., Vyšvařil, M., Wagner, P., Properties of modified gypsum, (In Czech), Brno: CERM, 2009, ISBN 978-80-7204-665-2

[5] Vimmrová, A., Keppert, M., Svoboda, L., Černý, R., Lightweight gypsum composites: Design strategies for multi-functionality, In: Cement and Concrete Composites, 33, 2011, pp. 84-89.

[6] Zhaq, F.Q., Liu, H.J., Hao, L.X., Li, Q., Water resistant block from desulfurization gypsum, In: Construction and Building Materials, 27, 2012, pp. 531-533.

[7] ČSN 722301, Gypsum binders, (In Czech), Prague: ČNI, 1978, 17 p., ISBN 778-72-87111-45-7

[8] Černý, R., Peringer, F., Rovnaníková, P., Tesárek, P., Wagner, P., Material on the basis of calcium sulfate hemihydrates, in particular for production of blocks for building envelope walls, Utility model n. 20478 (Czech national database), 2010.

[9] Arikan, M., Sobolev, K., The optimization of a gypsum-based composite material, In: Cement and Concrete Research, 32, 2002, pp. 1725-1728, ISSN 0008-8846

[10] Kayyali, O.A., Yeomans, S.R., Bond and slip of coated reinforcement in concrete, In: Construction and building materials, 9, 1995, pp. 219-226.

DYNAMIC PACKING OF HETEROGENEOUS PERIODIC UNIT CELL

David ŠEDLBAUER[1]

Abstract: *In this contribution we would like to introduce a packing algorithm that deals with a dynamic model of heterogeneous periodic unit cells (PUCs). One PUC consists of two phases, hard discs with identical radii and matrix. Dynamic and time-varying features constitute random initial velocities, time growing radii as well as matrix dynamic attenuation and elastic discs collisions. A special focus will be given to avoid discs overlapping and to minimize anisotropy. A statistical descriptor together with so called "pseudo-optimization" is used to reach above mentioned goals. The obtained results are compared with previous works.*

Keywords: *dynamic packing, periodic unit cell, hard disc, isotropy*

1. INTRODUCTION

From the macroscopic and/or microscopic point of view, heterogeneous materials consisting of solid particles within matrix are very common in number of industrial sectors. For all let us mention civil engineering (concrete, mortar) or chemical industry (solid propellants). Mechanical characteristics of these materials such as tensile strength, compressive strength, fragility and its isotropy are strongly dependent on the deployment of particles within the unit cell.

Solid particles distribution with respect to the required properties could be described by various computer models. Random propellant packing is the issue of contributions [1], [2], [3], [4]. Some of models involve optimization algorithms. Kučerová in [5] presents random microstructure generators and application of genetic algorithm GRADE and Metropolis (Monte Carlo) algorithm used for their generation. Kumar et al. in [3] deal with reconstruction of periodic unit cells of particulate composites with genetic algorithms. Stroeven et al. in [6] present assessment of packing characteristics. Model used in the work [5] can be indicated as a static while contributions [1], [2], [3] include the dynamics.

2. MODEL AND ALGORITHM OF HETEROGENEOUS POC

In this work 2D heterogeneous POC is in the center of interest. POC represents main central cell surrounded by its nine images that guarantee periodic boundary conditions, see Fig. 1. Only if the disc center is within the cell, the disc is in the cell. Firstly, the number of time steps, during which whole process took place, has to be established. Another parameter that has to be set before the start of the

[1] Ing. David Šedlbauer, Department of Mechanics, Faculty of Civil Engineering, CTU in Prague; david.sedlbauer@fsv.cvut.cz

algorithm is a volume fraction. Then a given number of center of discs are randomly thrown into the basic medium – matrix. In the algorithm a matrix represents a deceleration coefficient that is shown and described in Eq. *2*. At the beginning (time step 0) disc radii have zero size. Over time, the radii increase constantly according to the volume fraction and the number of time steps. Next randomness elements are initial velocity vectors of each disc (disc centers).

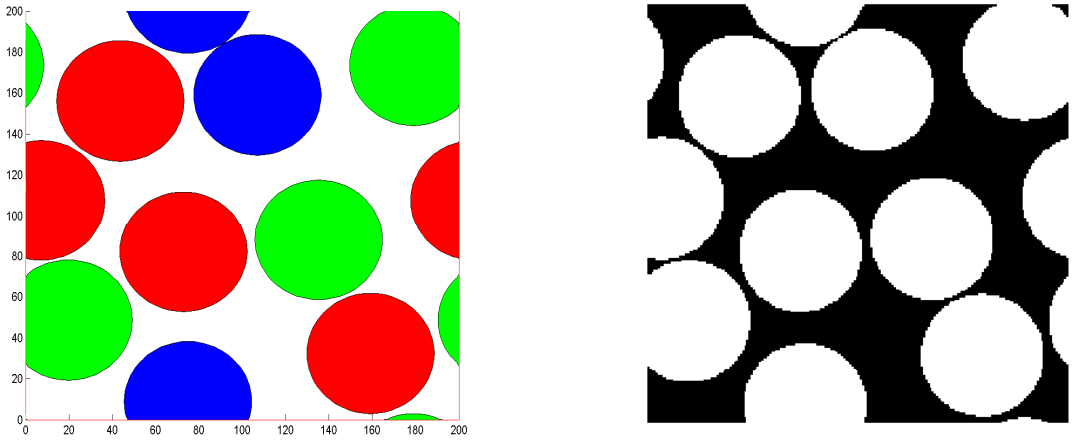

Fig. 1 Left – heterogeneous periodic unit cell, Right – corresponding bitmap, discs colors are only for clarity and have no other purpose

Discs position $\overrightarrow{ri}$ is in the course of time defined by

$$\overrightarrow{ri} = d\overrightarrow{ri} + dt \cdot \overrightarrow{vi} \qquad (1)$$

where $d\overrightarrow{ri}$ is position of the i-th disc in the time t, dt is a time step and $\overrightarrow{vi}$ is actual velocity determined by

$$\overrightarrow{vi} = dc \cdot (d\overrightarrow{vi} + con \cdot dt \cdot (o\overrightarrow{ri} - d\overrightarrow{ri})) \qquad (2)$$

where $d\overrightarrow{vi}$ is a velocity, $d\overrightarrow{ri}$ is a position and $o\overrightarrow{ri}$ is an optimal position in terms of isotropy of the i-th disc in the time t, dt is a time step, dc indicates matrix resistance and con is parameter that determine a speed of approaching to the optimal position.

Value of the parameter dc depends on the number of time steps. To get particles into positions in which cell has the highest isotropy is necessary to guarantee the movement of particles until the end of the algorithm. One way to ensure this is to set parameter dc with linear or quadratic dependence on time but with indirect proportion. Parameter dc decreases with increasing over time. But we opted for simplicity to set the parameter to a constant value. For a hundred time steps and due to the isotropy is the best value for parameter dc equal to 0.99.

The situation is similar with the parameter *con*, which represents the rate of approximation to the optimum position of each disc. This parameter can be linear or quadratic and directly proportional to the time. Again, for simplicity and clarity we have chosen a constant value for this parameter set to 1.05. It fits best with a hundred time steps after which the algorithm lasts.

2.1. ISOTROPY

To find a model with the greatest final isotropy it is firstly necessary to describe this phenomenon. As a statistical descriptor, we have used two-point probability function. There occurs simple Monte Carlo algorithm within the selected modification of the probability calculation, where two points are randomly thrown into the cell and a number of successful hits into one phases shall be recorded. Due to time demands of this algorithm the Discrete Fourier Transform (DFT) is assigned that will significantly speed up the calculation. Detailed description of the application of two-point probability for isotropy of heterogeneous periodic cell is presented in [5].

In order to be able to use DFT, it is necessary to convert unit cell image to the bitmap image, as shown in Fig. 1 and Fig. 2. Taking into account the shape of a circular disc, which does not correspond to the bitmap, there is need to establish certain approximation. One bit belongs to phase r only if its center lies within the disc or the disc edge. The result of the aforementioned procedure is the sum of errors on the isotropy that we are trying to minimize.

The sum of errors on the isotropy is valuated in each time step. However isotropy of a square or rectangular cell with circular particles is more dependent on particle diameter than on its composition. To be able to compare the sum of isotropy errors in each time step, the binary image of cell in each step is created by increasing radius of all particles to their final size, see Fig. 2. This is due to number of time steps, number of particles and the given volume fraction. Thus a reference, comparable cells are created.

Fig. 2 Unit cell, corresponding bitmap and reference bitmap

Therefore, if the isotropy error of referential bitmap in time t is smaller than the smallest isotropy error by that time, than the optimal position of particles in the calculation of velocity $\overrightarrow{vi}$ (see Eq. 2) is replaced by the current particles position. The initial pseudo-optimal particle positions have

random values. Manual optimization pitfalls might be undesirable particles overlap, which may appear in the bitmap due to introduction of the final (maximum) radii during the algorithm. In fact, the overlap with the calculated values of disc radii is prevented due to introduction of particle collisions.

2.2. EXIT AND COLLISION

During the algorithm there occur two phenomena that significantly affect the parameters defining the particles motion. The first is the exit of a disc from the PUC. At this event get particle centers out of the cell and vice versa its duplicate enters into the cell on the opposite side. To ensure the periodical conditions it is necessary to define a time when the above phenomenon happens and redefine disc coordinates. This time is defined as the smallest positive value of the four fractions:

$$\Delta t_e = min\{-x_i/vx_i\,;\,(X-x_i)/vx_i\,;\,-y_i/vy_i\,;\,(Y-y_i)/vy_i\} > 0 \qquad (3)$$

where Δte is time for which there will be another exit since the previous event or time step, x_i and y_i are coordinates of i-th disc center, X and Y are the cell dimensions and finally vx_i and vy_i are velocities of i-th disc in *x* and *y* direction, respectively. To find out the corresponding particle that gets out, it is necessary to carry out the calculation for each disc.

The next event is a collision where there is an elastic reflection of particles. This event occurs when the center distance is equal to the sum of the radii. As well as for exit it is necessary to determine the smallest (earliest) collision time. This is expressed by following relations.

$$(x_j - x_i)^2 + (y_j - y_i)^2 = (r_j + r_i)^2 \qquad (4)$$

$$x_i = x_i^t + vx_i^t \cdot \Delta\, t_c \qquad y_i = y_i^t + vy_i^t \cdot \Delta\, t_c \qquad r_i = r_i^t + dr \cdot \Delta\, t_c \qquad (5), (6), (7)$$

$$x_j = x_j^t + vx_j^t \cdot \Delta\, t_c \qquad y_j = y_j^t + vy_j^t \cdot \Delta\, t_c \qquad r_j = r_j^t + dr \cdot \Delta\, t_c \qquad (8), (9), (10)$$

where $x_i,\ y_i,\ x_j,\ y_j$ are collision discs coordinates, $x_i^t,\ y_i^t,\ x_j^t,\ y_j^t$ are discs coordinates $vx_i^t,\ vy_i^t,\ vx_j^t,\ vy_j^t$ are discs velocities at the time t, r_i, r_j are collision discs radii, r_i^t, r_j^t are discs radii at time t, dr is an increase of the step of the radius and $\Delta\, t_c$ is time elapsed since time t. Equation 4 is quadratic and can have two complex roots or two real roots with the same sign. Due to the variable type the nearest collision time is the minimum of positive real roots. Collision time and exit time shall be calculated at each time step and after some of the events because of recalculated velocities.

Discs velocities after the collision are calculated from the law of conservation of energy and the momentum conservation law. Firstly, we shall convert velocities into the collision coordinate system where we determinate the normal velocities (in the direction of the discs center connection) and tangential velocities that are perpendicular to the normal ones. Normal velocities after the collision have following form:

$$v'_{1N} = (v_{1N} \cdot (A_1 - A_2) + 2 \cdot A_2 \cdot v_{2N})/(A_1 + A_2) \quad (11)$$

$$v'_{2N} = (v_{2N} \cdot (A_2 - A_1) + 2 \cdot A_1 \cdot v_{1N})/(A_1 + A_2) \quad (12)$$

where v_{1N}, v_{2N} are velocities before collision in the collision coordinate system and A_1, A_2 are areas of discs that collide. Another problem occurs during the calculation of collision times. Numerical inaccuracies caused by floating point precision can lead to particles overlapping. Therefore, overlapping check is inserted into the algorithm. Each of the discs that overlap pushed away to ensure the mere discs touches.

3. COMPARISON OF RESULTS

In this part we would like to compare the results of heterogeneous microstructures generation using the above presented dynamic algorithm with the already known algorithms. The dynamic algorithm has the working title DYN12. Comparison is performed on a set of examples where we gradually change the required volume fraction for the given number of particles. Parameter *N* indicates the number of particles and takes values from the set 4, 9, 16 and 25 particles. Monitored variable is the sum of errors on isotropy. Selected algorithms are GRADE, METROPOLIS and modifications of these GRADE2 and METROPOLIS2. Description of the first algorithm GRADE is presented in [7], while the METROPOLIS algorithm can be found in [8]. The values of errors on isotropy of previously published algorithms are taken from [5]. The results are summarized in the Tab. 1. In the first column of the table is a graphical representation using the algorithm DYN12 for every single predefined volume fraction for N equal to 16. In the next columns volume fractions *vf* and numbers of particles N are shown. Then, the average isotropy errors for each algorithm among 100 runs follow.

Final sum of errors of isotropy dispersion is for a better assessment of the dynamic algorithm represented in Fig. 3. This is shown for selected particles numbers and volume fractions. Sums of errors are entered on the vertical axis. On the horizontal axis solution numbers for the first fifty generated solutions are plotted.

Tab. 1 Average values at the end of the algorithms for 100 runs

	vf	N	DYN12	GRADE	GRADE2	METROPOLIS	METROPOLIS2
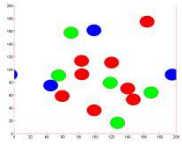	**0.1**	4	2.461	1.704	**1.695**	2.258	1.711
		9	1.713	1.099	0.969	1.825	**0.930**
		16	1.332	0.881	0.769	1.434	**0.672**
		25	1.080	0.624	0.546	0.995	**0.453**
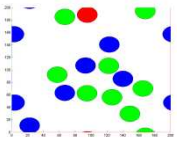	**0.2**	4	5.642	3.275	**3.237**	5.160	3.271
		9	4.028	2.555	2.253	3.539	**2.113**
		16	3.068	2.273	1.846	2.826	**1.544**
		25	2.410	1.802	1.409	2.031	**1.109**
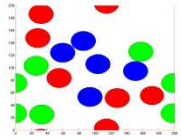	**0.3**	4	8.066	5.074	**5.038**	7.908	5.089
		9	5.790	3.939	3.432	5.582	**3.157**
		16	4.411	3.270	2.549	3.960	**2.096**
		25	3.587	380.778	2.129	3.051	**1.615**
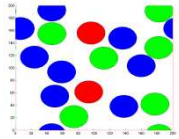	**0.4**	4	10.422	6.334	**6.287**	9.880	6.387
		9	7.237	4.918	4.193	6.805	**3.846**
		16	5.605	704.267	3.632	5.294	**2.790**
		25	4.367	3795.627	3.216	4.118	**2.139**
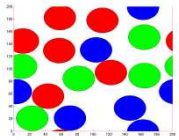	**0.5**	4	10.623	6.722	**6.683**	10.121	6.692
		9	7.759	83.953	4.960	7.688	**4.278**
		16	5.912	3602.860	5.032	5.993	**3.161**
		25	4.770	13636.924	5.642	4.791	**2.510**
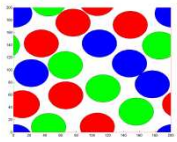	**0.6**	4	10.266	6.038	6.002	9.963	**5.978**
		9	7.115	424.561	5.993	7.985	**4.405**
		16	5.491	10667.807	8.384	6.045	**3.396**
		25	4.548	23131.964	7.809	5.263	**2.881**
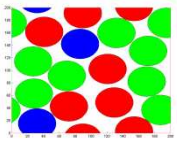	**0.7**	4	9.073	5.153	5.117	8.339	**5.142**
		9	6.827	2459.832	9.174	8.541	**5.170**
		16	**5.083**	30826.508	11.955	6.606	5.947
		25	**4.000**	55213.877	12.476	6.201	7.155

4. CONCLUSION

Before comparison of obtained results we must note that the function for calculating anisotropy (or isotropy errors) with optimization algorithms involves a substantial penalty for an overlap. That is fully demonstrated with algorithm GRADE especially for higher volume fraction and a higher number of particles. However in case of the presented algorithm DYN12 overlapping is eliminated by dynamical events. Therefore, there is no penalty. Even if pseudo-optimization was used in DYN12, when there is just better position in terms of isotropy remembered, DYN12 is comparable with METROPOLIS algorithm. That is mainly due to the motion of particles and dynamic phenomena. It is obvious that with increasing discs number discs evenly spread over the cell and the cell has a higher isotropy. With higher volume fraction there is not enough space for disc motion and this ensures that discs do not pack one cluster and thus, the resulting cell has again higher isotropy.

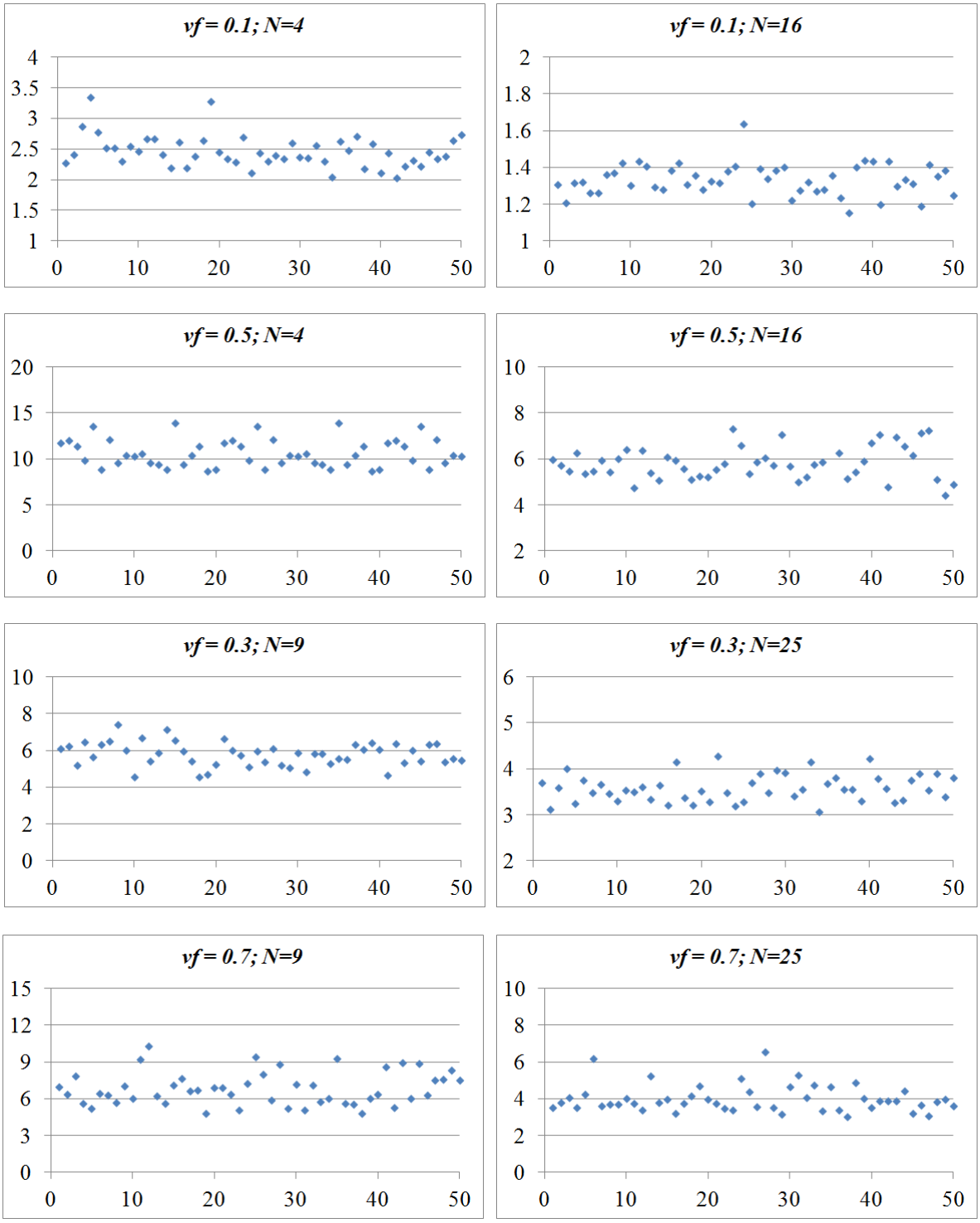

Fig. 3 Sum of errors on the isotropy dispersion

It is possible to read from the figure 3 that the dispersion of sum of errors on the isotropy is significantly influenced by the ratio of the disc number a volume fraction. The smaller number of discs the larger volume fraction, the higher dispersion is. Better results we can achieve by the larger number of time steps. With this there is a bigger chance to reach real optimal position during the motion.

Finally a parameter for the attenuation and parameter for achieving optimal position can be time-dependent or different for various disks numbers and for various volume fractions. In addition to these aspects we will in the future work focus on direct optimization with some of swarm intelligence method such as Particle Swarm Optimization [9] or Ant colony optimization [10].

ACKNOWLEDGEMENT

The financial support of this contribution by the Faculty of Civil Engineering, Czech Technical University in Prague (SGS project No. SGS12/027/OHK1/1T/11) is gratefully acknowledged. Author is indebted to A. Kučerová for supplying with isotropy measuring used in this paper.

REFERENCES

[1] Knott, G.M., Jackson, T.L., Buckmaster, J., The random packing of heterogeneous propellants, AIAA Journal, 39 (4), 2001, ISSN: 0001-1452

[2] Kochevets, S., Buckmaster, J., Jackson, T.L., Random propellant packs and the flames they support, Joint Propulsion Conference and Exhibit, Huntsville, 2000, AIAA 2000-3461

[3] Kumar, N. Ch., Matouš, K., Geubelle, P.H., Reconstruction of periodic unit cells of multimodal random particulate composites using genetic algorithms, Computational Materials Science, 42, 2008, pp. 352-367, ISSN: 0927-0256

[4] Matouš, K., Inglis, H.M., Gu, X., Rypl, D., Jackson, T.L., Geubelle, P.H., Multiscale modeling of solid propellants: From particle packing to failure, Composites Science and Technology 67, 2007, pp. 1694-1708, ISSN: 0266-3538

[5] Kučerová, A., Genetic algorithm-based generation of isotropic equal-sized hard-disk microstructures, In: The Proceedings of 4th International Conference on Advances in Structural Engineering and Mechanics, ASEM, 2008, pp. 1583-1593, ISBN: 978-89-89693-21-5

[6] Stroeven, P., Stroeven, M., Assessment of packing characteristics by computer simulation, Cement and Concrete Research, 29, 1999, pp. 1201-1206, ISSN 0008-8846

[7] Kučerová, A., Identification of nonlinear mechanical model parameters based on softcomputing methods, Ecole Normale Suprieure de Cachan, 2008, 141 p., ISBN 978-2-11-097464-8

[8] Torquato, S., Random heterogeneous materials, New York: Springer-Verlag, 2002, 701 p., ISBN 0-387-95167-9

[9] Kennedy, J., Eberhart, R.C., Particle Swarm optimization, In: IEEE International Conference of Neural Networks, 1995, pp. 1942-1948, ISBN 0-7803-2768-3

[10] Colorni, A., Dorigo, M., Maniezzo, V., Distributed Optimization by Ant Colonies, In: European Conference on Artificial Life, 1991, pp. 134-142.

EXPERIMENTAL AND NUMERICAL ANALYSIS OF VERTICAL SPLICE SKEW JOINT WITH KEY

Karel ŠOBRA[1], **Petr FAJMAN**[2], **Jiří MÁCA**[3]

Abstract: *Currently, for reconstruction of historical trusses traditional carpentry joints are used. For many years these joints are constructed in the same way. Unfortunately, the mechanical behavior of these joints and influence of their parts and geometry of joints to the joint stiffness are not well known. This paper describes a study recently completed on the vertical splice skew joint with a key. Experimental tests were performed and compared to the numerical results of three-dimensional finite element model created using ATENA 3D.*

Keywords: *historical trusses, vertical splice skew joint, carpentry joints, numerical modeling*

1. INTRODUCTION

In traditional timber trusses the carpentry joints are used to transfer forces between truss members. Forces are primary transferred by direct contact and by friction. Sometimes it is necessary to replace some parts of truss. To replace members which are bended, vertical splice skew joint has good application. Splice 80 – 120 cm long and edged on the opposite sides composes this joint [1].

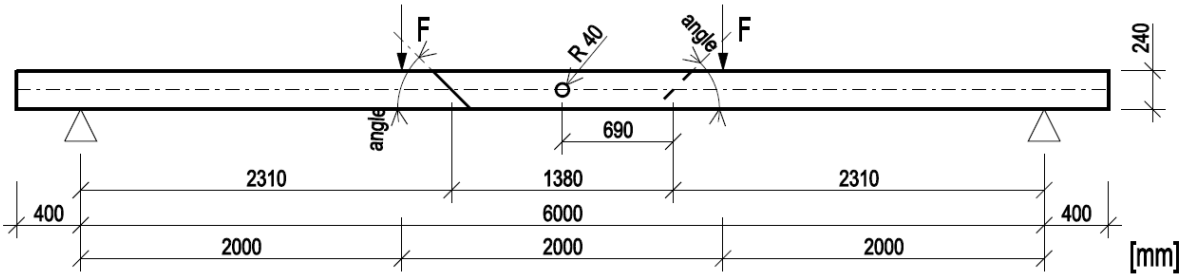

Fig. 1 Joint in the middle of the span

[1] Ing. Karel Šobra, Department of Mechanics, Faculty of Civil Engineering, CTU in Prague; karel.sobra@fsv.cvut.cz

[2] doc. Ing. Petr Fajman, CSc., Department of Mechanics, Faculty of Civil Engineering, CTU in Prague; fajman@fsv.cvut.cz

[3] prof. Ing. Jiří Máca, CSc., Department of Mechanics, Faculty of Civil Engineering, CTU in Prague; maca@fsv.cvut.cz

2. EXPERIMENTAL TESTS

For better understanding of mechanical behavior of wood and for setting the material characteristics of wood, the experimental tests were made. For measuring the basic material properties, four-point bending tests were made on two wood trusses without a joint. The arrangement of four-point bending test is shown in Fig. 2. These trusses had the same dimensions like a trusses with joint. Dimensions of a truss are shown in Fig. 1, cross section dimensions were 0.24 × 0.2 m.

Fig. 2 Arrangement of four-point bending test

In the next step the scaled models (1:4) were tested. The basic observation of joint's response to the loading and type of deformation was captured by this scaled models tests. Some characteristics like modulus of elasticity (MOE in Tab. 1), modulus of rupture (MOR) same as maximal force necessary to failure (F_{max}) and density of wood were set. Statistical evaluation of measured data is shown in Tab. 1. Overall, 48 measures on the scaled models were made. In the Tab. 1 *w* is the bending deflection measured in impact of maximal loading force, *x* is the mean number, *s* is the mean square error, *v* is the coefficient of variation, *min.* and *max.* are the minimal and the maximal measured values.

Tab. 1 Scaled model characteristics

	F_{max}	w - F_{max}	MOR	MOE	Density
	[N]	[mm]	[MPa]	[MPa]	[kg/m^3]
x	1599.3	6.02	68.62	7967.08	444
s	164.89	1.14	6.61	857.44	48
v	10.32	18.94	9.63	10.76	10,92
min.	1333.55	3.61	57.39	6910	369
max.	2012.88	9.24	86.29	10281.9	570

2.1. REAL SCALE MODELS

In the third round experimental tests of joints were made in real scale. The same as scaled models the real joints were broke in three- and four-point bending tests. Position of joint in the truss was various. There were two positions of the joint (Fig. 1, Fig. 3). In the first one the joint was in the middle of the

span and in the second one the joint was at the end of the span. For the maximal effect of moment of bending the first arrangement was set and for the maximal effect of shear force the second arrangement was made. To proof the measured data two trusses of each arrangement were tested.

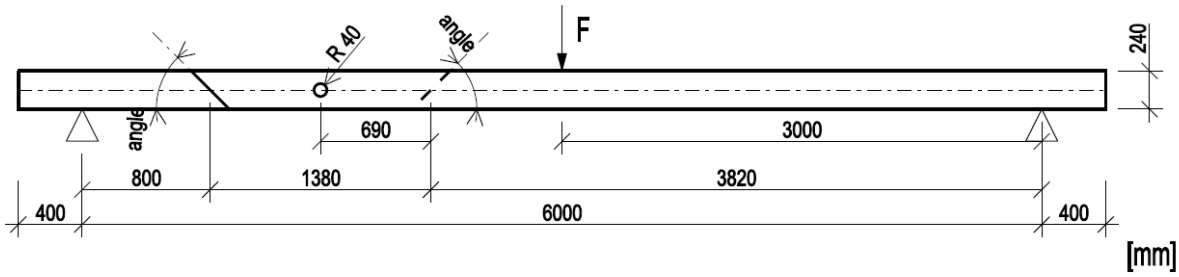

Fig. 3 Position of the joint at the end of the span

Two more various geometry types of skew joint were considered. The first one assumed skew angle of the joint end 45° and the second type assumed skew angle 63.3°. Currently, only the tests of model with 63.3° skew angle are made.

Interesting part of the joint is a key. At the beginning the joint with the wooden key was assumed. However only in gothic trusses all wooden carpentry joints were used and the utilization of these joints is rare in Czech Republic. On the basis of this observation the metal key was used for the experiments with full scaled model.

2.2. CONCLUSION OF EXPERIMENTAL TESTS

During the experimental tests some conclusions were made. There are big differences in behavior of scaled model and real model. During the scaled model experiments more, various types of collapses of the joint were observed. Some of the failures are shown in Fig. 4. Two main parameters influence this behavior. The first parameter is utilization of the wooden key. Metal key used in real scale models had better shear strength than wooden key used in scaled models. Wooden key is the weak part of a joint and it is disposed to shear failure.

Fig. 4 Damaged scaled joint

The second parameter which influences the behavior of a joint is quality of material. In real scale model initial drying crack was discovered on all tested trusses (Fig. 5). Depth of this crack was around 100 mm in vertical direction on both sides and approximately 70 mm in horizontal direction also on both sides of a truss. This crack debilitated the cross section and it was the primary source of failure. At the end of the experiment the second crack parallel with the initial one was evolved. The scaled model did not have initial damage like drying crack and its mode of deformation was more unpredictable.

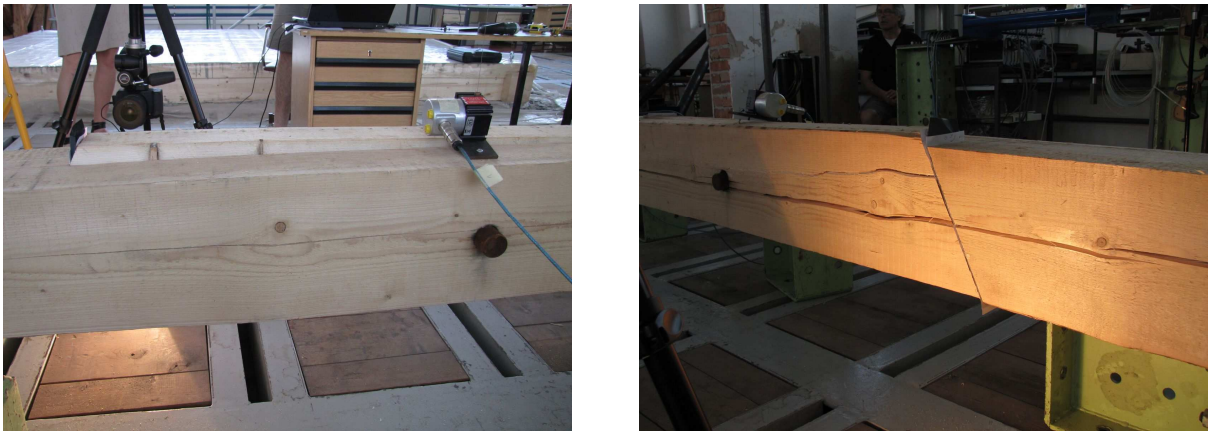

Fig. 5 Damaged joint with initial drying crack

3. NUMERICAL MODELING

The aim of the project, which solves the wooden joints, should be the pack of recommendations for design engineers. For set this package it is necessary to understand the basic behavior of the joints. However, experimental test of many models is complicated and time-intensive. Consequently, it is necessary to have strong tool for observation changes in the design of a joint. On the basis of complications with experimental tests the numerical model was made.

3.1. MATERIAL

For three-dimension finite element model ATENA 3D was chosen. ATENA is commercial software primary developed for calculating a material on the concrete base. Despite concrete and wood have pretty different material properties, ATENA 3D nonlinear cementitious material for the case of wood joint was chosen as a base material.

Concrete is homogeneous material with different compressive strength and tensile strength. On the other hand wood is anisotropic material with different properties in each direction. For simplification, wood may be reasonably modeled as orthotropic material with symmetric properties in directions perpendicular to the grain. Orthotropy would require set three values of Young's modulus E, three shear modules G and six Poisson's ratios ν. With symmetry, only nine independent parameters need to be defined [3 - 4]. Unfortunately, only one pack of the material properties, same for all directions, can be set up in ATENA cementitious material. It is possible to reach the orthotropic

properties from homogeneous material model using smeared reinforcement which can be add to the basal material and adjust some material properties in the direction of reinforcement.

To describe homogeneous material only one set of the material properties can be used in ATENA cementitious model. For wood basal material the lowest parameters, which are same for radial and transversal direction was used and to adjust grain direction material properties the smeared reinforcement was used. On the basis of experimental tests of scaled model the material properties of wood base material were set up. Namely the values were $E = 5$ GPa, $\nu = 0.2$, the tensile strength $F_t = 0.5$ MPa, the compressive strength $F_c = 1$ MPa (in ATENA cementitious model prescribes minimal ratio $F_c/F_t = 2$), on the basis of [2] the fracture energy $G_f = 3 \cdot 10^{-4}$ MN/m.

Whole construction was separated into 17 macroelements included two macroelements used as steel supports and two macroelements used as bearing plates under concentrated forces. Both, the brick elements and the tetrahedral elements, which ATENA provided, were used during the mashing. The dimension of finite elements was set to 0.05 m, on the surround of skew ends of joint, the mesh was refined. The finite element model as four-point bending test was performed, so the construction was loaded by two separate concentrated forces. Loading proceeded in the loading steps, in each step both the forces were risen by 1 kN.

4. CONCLUSION

There are big differences in the behavior of scaled model and real size construction as it was mentioned. One of the most visible factors, which influences this behavior, is quality of material. Longitudinal initial drying cracks were observed in the real size model. This crack is opening during the loading and causes breakdown of the joint. Another factor is type of the material of the key. The metal key is not weak part of construction in contrast to the wooden key, which is subject to the shear failure.

It is not easy to fit the cementitious material model to the wood material properties for numerical modeling. It is possible to get right material properties of wood using smeared reinforcement, but cementitious material does not have grained structure like wood. Cracks perpendicular to the grain was first observed during the loading (Fig. 6). This perpendicular crack did not correspond with real behavior of the wooden joints.

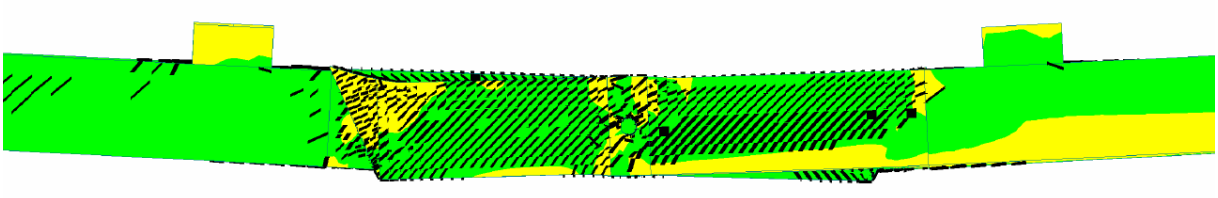

Fig. 6 Cracks perpendicular to the grain in FEM model

The ATENA cementitious material model does not assign satisfactory behavior (Fig. 7). On the basis of this, the material model will be tuned to get better match with measured data from the experiments. To compare the results, another commercial software will be used and the noncommercial software developed at the Department of Mechanics, FCE CTU in Prague for another calculating is going to be used.

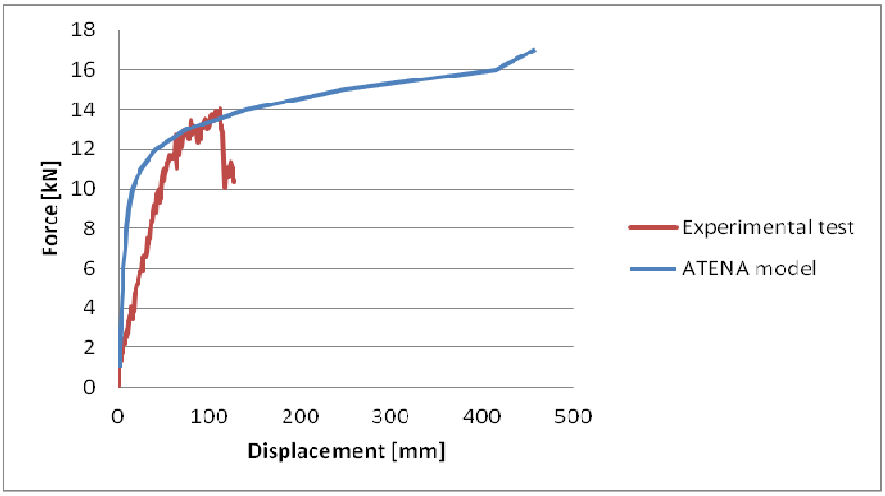

Fig. 7 Force – displacement in the middle of the span graph

ACKNOWLEDGEMENT

The financial support of this experiment by the Faculty of Civil Engineering, Czech Technical University in Prague (SGS project No. SGS12/027/OHK1/1T/11 – Numerical Modeling in Mechanics of Structures and Materials) is gratefully acknowledged.

REFERENCES

[1] Gerner, M., Tesařské spoje, Praha: Grada, 2003, 220 p., ISBN 80-247-0076-X.

[2] Majano, M.A., Hughes, M., Fernández-Cabo, J.L., Fracture Characteristics and Properties of Thermally Modified Timber made out of Beech, In: European Conference on Wood Modification [online], [2009], [cit. 2012-08-06], available from WWW: <http://www.holiwood.org/fileadmin/publications/2009/>.

[3] Parisi, M.A., Cordié, C., Mechanical behavior of double-step timber joints, In: Construction and Building Materials, [online], [2010], 24 (8), pp. 1364-1371, [cit. 2012-08-06], ISSN 09500618, available from WWW: <http://linkinghub.elsevier.com/retrieve/pii/>.

[4] Sangree, R.H., Schafer, B.W., Experimental and numerical analysis of a stop-splayed traditional timber scarf joint with key, In: Construction and Building Materials, [online], [2009], 23 (1), pp. 376-385, [cit. 2012-08-06], ISSN 09500618, available from WWW: <http://linkinghub.elsevier.com/retrieve/pii/>.

MODELING OF COLLAPSE CALDERAS

Michael SOMR[1]

Abstract: *Collapse calderas are one of the most remarkable volcanic structures. The reasons for that are not only negative, as for example the hazard for people and environment, but also positive due to their association with ore resources and generation of fertile soils. However, the processes leading to the collapse are very complex and to understand them requires cooperation of many scientific disciplines, including the numerical modeling. Therefore, the objective of this paper is to sum up the numerical methods and procedures (used in the investigation of the collapse calderas) in order to be able to develop a new and more realistic model.*

Keywords: *caldera, numerical modeling, fault, magma chamber, host rock*

1. INTRODUCTION

Collapse calderas are defined as the volcanic depressions that result from the disruption of the geometry of the magma chamber roof due to faulting during an eruption. The calderas are often confused with the apical craters. The difference is that craters result from the collapse and subsequent blocking of the volcanic conduit without affecting the roof of the magma chamber and they have many times smaller diameter than the calderas.

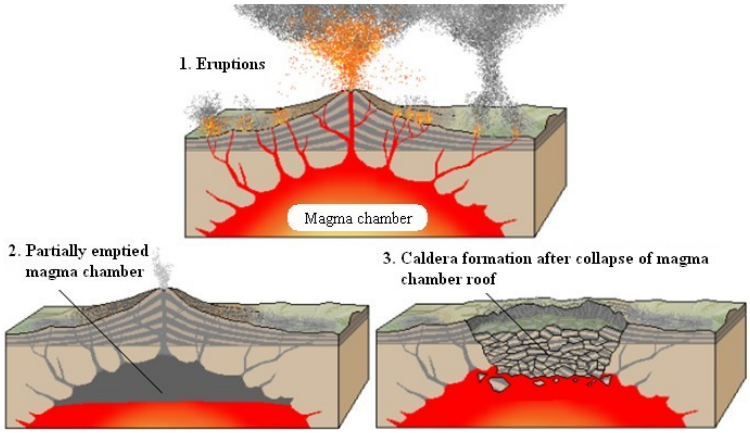

Fig. 1 Evolution of the collapse caldera (reproduced from [1])

The volcanic eruptions, which are necessarily connected with the origin of collapse calderas, are the most powerful and amazing displays of the force of the nature. This is also the reason why the eruptions are a huge natural hazard and even a single eruption can claim thousands of lives just in few

[1] Ing. Michael Somr: Faculty of Civil Engineering, Czech Technical University in Prague, Thákurova 7, 166 29 Praha 6, Czech Republic; e-mail: michael.somr@fsv.cvut.cz

moments, as described in e.g. [2] [3] [4] [5]. However, the volcanic processes can be also very beneficial for the mankind thanks to e.g. ore deposits and fertile soils (the erupted volcanic material generates some of the most fertile soils and agricultural areas in the world) [6] [7].

Despite a relatively low rate of occurrence of new calderas (approximately three new calderas per 100 years since 1783 [8]), the vast pyroclastic eruptions associated with the caldera collapse are one of the most catastrophic geologic events that have occurred on the Earth's surface.

The collapse calderas have not received a considerable attention of scientists only due to their link to the ore deposits and geothermal energy resources, but also because of their impact on the environment, climate, and the human society [9]. In addition, since the volcanoes and their eruptions are just a small surface manifestation of immense magmatic processes ongoing under the surface, the calderas can provide very important insights into the generation and evolution of large-volume silicic magma bodies [9]. The understanding to the collapse calderas is a highly interdisciplinary matter, most closely linked to geophysics [10] [11], petrology [12] [13], and geochemistry [12] [13].

2. METHODOLOGY

Since the investigation of the collapse calderas is very complex task, it is wise to use different approaches, which can complement and confirm each other in order to reach the most correct and realistic results. In the case of the calderas, the analogue models, theoretical models, and field studies are usually used and suitably combined.

2.1. ANALOGUE MODELS

Analogue and scale experiments are a tool to identify, investigate, and visualize processes that cannot be directly observed in nature using the analogue materials for the host rock (dry quartz sand, flour, etc.) and for the magma chamber (water of air filled balloons, silicone reservoirs, etc.). In some cases they establish guidelines for applying the theoretical models [14]. Generally, analogue models indicate how the process of caldera collapse takes place. Since they are not able to take into account the rock mechanics and fluid dynamics, the models cannot quantify and indicate when and why the collapse will take place.

2.2. THEORETICAL MODELS

The theoretical models based on the thermodynamics, solid and fluid mechanics, etc. have progressively become an indispensable tool to study caldera-forming processes. These models, on the contrary to analogue models, are useful to quantify variables. They are also an important tool for predicting semi-quantitative general conditions for fracture and fault formation. Furthermore, in contrast to the analogue models, numerical approximations are able to reproduce and take into account the physical properties of host rock and magma. Theoretical models are adequate to perform

parametric studies but an inappropriate knowledge of the system (i.e. rheology, geometry, boundary conditions) may lead to wrong conclusions [14].

2.3. FIELD STUDIES

Field studies are useful to adjust analogue and theoretical models and to check their veracity and reliability. However, the studies are more or less limited to surface phenomena. Nevertheless, the field studies can give us information about the caldera structure and in some cases it is also possible to determine pre-eruptive conditions of the magma and the most probable causes that triggered the eruption. The reconstruction of caldera collapses is a fundamental tool to understand the collapse mechanism of the calderas occurring nowadays [14].

3. COLLAPSE OF CALDERA

With respect to the pressure evolution inside the magma chamber during the formation of the caldera, there are two types of the collapse calderas.

3.1. UNDERPRESSURE CALDERA

The caldera-forming eruption begins under overpressure inside the chamber that triggers (once overcome the tensile strength of the host rock) magma injection into the host rock and finally the eruption. The magma withdrawal during these phases leads to a pressure decrease in the magma chamber. The collapse begins once the strength of the magma chamber roof is exceeded [14].

3.2. OVERPRESSURE CALDERA

These calderas are formed due to the overpressurization of the magma chamber in the presence of a large scale doming or underplating. When the tensile strength of the host rock is exceeded, ring fractures originate at the surface. The caldera-forming eruption starts due to the decompression of the magma chamber throughout the ring faults [14].

4. NUMERICAL MODELS

During several last decades, the theoretical models based on the thermodynamics, rock and fluid mechanics have become more and more important, because they are cheap, fast, and accurate in predicting and simulating the volcanic processes. Nevertheless, the mathematical expressions are, in most cases, so complex that they cannot be solved analytically but the numerical methods and computers must be employed.

Nowadays, the combination of the field studies, analogue, and numerical models is the best way how to understand and describe the whole sequence of the processes, which participate in the origin of the collapse caldera.

In general, the models dealing with volcanology can be either pre-eruptive, or eruptive. The pre-eruptive models are important to understand the processes (such as cooling, differentiation, mixing, degasification, overpressurization, magma chamber rupture, etc.) leading to the volcanic eruptions. Some models consider that the pressure increase in the magma chamber is caused by a volatile oversaturation due to cooling and crystallization processes [15] [18]. Some models assume that the overpressurization originates from the income of a fresh magma into the magma reservoir [15] [17]. Other models also take into account the stress fields around the chamber, the magma chamber rupture, and the subsequent dike injection [18] [19].

On the other hand, the eruptive models should consider the physical processes inside the magma chamber, in the conduit, during the magma discharge, and in the atmosphere, during the eruption. All these processes affect each other, but to couple them is extremely difficult task. Therefore, for simplicity's sake, the processes are solved separately as magma chamber models (variations of pressure inside the chamber), conduit models (degasification and magma fragmentation along the conduit), and atmospheric models (deposition of the volcanic material).

The papers dealing with the theoretical models of collapse calderas, which were published in the last two decades, can be divided into the three main groups (corresponding to the following sections) according to the tasks they are focused on.

4.1. PRESSURE EVOLUTION INSIDE MAGMA CHAMBER

These models are suitable for parametric studies concentrated on the magma composition, water content, some properties of host the rock, and the magma chamber geometry. They are based on simple fracture criteria. All models in this section assume that caldera collapses due to decompression of the magmatic reservoir.

The paper [20] contains the analysis of magma chamber pressure during the eruption and the estimate of erupted magma chamber volume fraction necessary for triggering the collapse.

To determine the mass, which may erupt from a chamber during the caldera-forming eruption until the critical underpressure, at which the walls fail, tries the work [21].

In the paper [22], there is a pressure evolution model during explosive caldera-forming eruptions and also a description of the pressure variation throughout the whole "central vent eruption – caldera collapse" cycle. The elastic behavior was assumed.

The failure criterion for piston collapse along reverse ring fault and comparison with experimental results, but also calculation of a volume fraction required to trigger the caldera collapse were investigated in the paper [23]. The Mohr-Coulomb criterion was applied.

4.2. STRESS CONDITIONS FOR NORMAL-FAULTS CALDERA INITIATION

The aim of the models in this section is to give information about the stress conditions leading to the initiation of the faults crucial for the collapse of the caldera. Specifically, we look for the location of the principal stress σ_3 and maximum value of $\sigma_1 - \sigma_3$. Assuming $\sigma_1 \geq \sigma_2 \geq \sigma_3$ means that we actually search for the maximum tension and the double of the maximum shear stress. These models enable to investigate, which geometrical configuration of the magma chamber will induce the stresses suitable to initiate the normal ring faults. The models do not take into account any pre-collapse fracturing. However, some of them consider the influence of regional tectonic stresses (regional doming).

The apical caldera collapse as a consequence of a domal deformation, using the elasto-plastic model with Von Mises criterion, is the topic of [24].

In the paper [25], there are investigated the caldera collapse, resurgence of a central dome and quasi-static evolution of thermally stratified continental crust near both, inflating and relaxating magma chambers. The author uses elastic-visco-plastic model.

The magma chamber subjected to different conditions (lithostatic equilibrium, overpressure, underpressure, horizontal tensile stresses, and vertical compressive stresses), employing elastic model with Griffith criterion under tensile strength, was a task of papers [18] and [26].

The paper [27] deals with the coupled thermomechanical model in order to find out the conditions for the caldera collapse due to the magma chamber underpressure, with help of the thermoelasticity, Mohr-Coulomb criterion, and Griffith criterion under tensile strength.

The quantitative discussion about the relationship between the caldera geometry and the magma chamber depth, which utilizes the elasto-plastic model and the Mohr-Coulomb criterion, is contained in the paper [28].

To sum it up, the papers [24] [25] and [28] considers the collapse of the caldera through magma chamber overpressure, the paper [27] through chamber underpressure, and the papers [18] and [26] work with both, over and underpressure in the magma chamber.

4.3. PREDICTION OF FAULT LOCATION ASSUMING INELASTIC BEHAVIOR

The main goal of the papers included in this section is to investigate the formation and deep geometry of the caldera faults and the relationships between the magmatic system and the surface features of ash flow calderas. The calculations provide the time-dependent stress and thermal regimes in the vicinity of the magma chamber, but also the prediction of the fault location and geometry, and the directions of the potential brittle failure zones around the magma reservoir. The main parameters considered in these models are the regional stress fields, magma chamber geometry and the roof aspect ratio R (R=h/w, where h is the thickness of the magma chamber roof and w is the roof width). All the following models consider the collapse through the magma chamber overpressure.

In the paper [19], there is a thermomechanical numerical model using a stationary temperature field without and with a regional extension, and also using a full time-dependent conduction and advection describing the caldera collapse and long-term post-collapse activity, considering the influence of the heat diffusion from the hot magma body and thermal blanketing by the ignimbrite cover. The authors used the elastic-plastic-ductile model, Mohr-Coulomb criterion, and also non-linear viscous model.

The caldera collapse with a pre-defined rectangular existing magma chamber and the steady-state geotherm without heat transport during the collapse are included in the paper [6]. And again, the author used the elastic-plastic-ductile model, Mohr-Coulomb criterion, and also non-linear viscous model.

The previous two models are able to study the thermal regime at depth, which may alter crustal rheology and physical properties of the rock, and consequently influence fracture formation and development [14].

The paper [29] contains numerical simulations of the formation of cracks under the tensile stresses or increasing magma chamber pressures. It also includes a fracture model that enables to follow the growth of fractures. The paper utilizes elasto-plastic model, Von Mises criterion, and Griffith criterion under tensile strength.

5. CONCLUSION

The numerical models provide the necessary information about the stress conditions which can initiate the collapse of the caldera, but also about the stress conditions in which the collapse will never occur. Nevertheless, there are still some limitations and restrictions, which should be diminished in order to make the numerical models more reliable. Namely, the problems are uncoupled fluid dynamics and rock mechanics, considering the homogeneity of the host rock, impossibility of the dike injection, absence of volcanic edifice, and ignoring the regional faults or previously formed structures. But the most serious problem is probably the way of modeling the behavior of the host rock. Majority of the models assume that the walls of the magma chamber are elastic. Of course, the elasticity cannot follow the deformation history of the magma chamber and the effects of the magma on the host rock. In spite of these limitations, the numerical modeling has brought a significant advance in understanding the processes of the caldera collapse.

ACKNOWLEDGEMENT

The financial support of this research by the Faculty of Civil Engineering, Czech Technical University in Prague (SGS project No. 12/027/OHK1/1T/11) is gratefully acknowledged.

REFERENCES

[1] Benítez, L.M. *Volcano caldera,* available from www: <http://es.wikipedia.org/wiki/-Archivo:Volcano_caldera_Lmb.png>.

[2] Sigurdsson, H. *Introduction,* In: Encyclopedia of Volcanoes, Sigurdsson, H. et al., Academic Press, San Francisco, 2000, p. 1-13, ISBN 978-0126431407.

[3] Blong, R.J. *Volcanic hazard and risk management,* In: Encyclopedia of Volcanoes, Sigurdsson, H. et al., Academic Press, San Francisco, 2000, p. 1215-1227, ISBN 978-0126431407.

[4] Blong, R.J. *Building damage in Rabaul, Papua New Guinea, 1994,* In: Bulletin of Volcanology 65(1), 2003, p. 43-54, ISSN 1432-0819.

[5] Witham, C. *Volcanic disasters and incidents: a new database,* In: Journal of Volcanology and Geothermal Research 148, 2005, p. 191-233, ISSN 0377-0273.

[6] Guillou-Frottier, L. - Burov, E.B. - Milési, J.P. *Genetic links between ash-flow calderas and associated ore deposits as revealed by large scale thermo-mechanical modeling,* In: Journal of Volcanology and Geothermal Research 102, 2000, p. 339-361, ISSN 0377-0273.

[7] Ping, C.L. *Volcanic soils,* In: Encyclopedia of Volcanoes, Sigurdsson, H. et al., Academic Press, San Francisco, 2000, p. 1259-1270, ISBN 978-0126431407.

[8] Walker, G.P.L. *Downsag calderas, ring faults, caldera sizes, and incremental growth,* In: Journal of Geophysical Research 89, 1984, p. 8407-8416, ISSN 2156 -2202.

[9] Lipman, P.W. *Calderas,* In: Encyclopedia of Volcanoes, Sigurdsson, H. et al., Academic Press, San Francisco, 2000, p. 643-662, ISBN 978-0126431407.

[10] Davy, B.W. - Caldwell, T.G. *Gravity, magnetic and seismic surveys of the caldera complex, lake Taupo, North Island, New Zealand,* In: Journal of Volcanology and Geothermal Research 81, 1998, p. 69-89, ISSN 0377-0273.

[11] Milner, D.M. - Cole, C.P. - Wood, C.P. *Assymetric, multiple-block, collapse at Rotorua caldera, Taupo Volcanic Zone, New Zealand,* In: Bulletin of Volcanology 64 (2), 2002, p. 134-149, ISSN 1432-0819.

[12] Francis, P.W. - Sparks, R.S.J. - Hawkesworth, C.J. - Thorpe, R.S. - Pyle, D.M. - Tait, S.R. - Mantovani, M.S. - McDermott, F. *Petrology and Geochemistry of Volcanic Rocks of the Cerro Galan Caldera, Northwest Argentina,* In: Geological Magazine 126, 1989, p. 515-547, ISSN 1469-5081.

[13] Edgar, C.J. - Wolff, J.A. - Nichols, H.J. - Cas, R.A.F. - Martí, J. *A complex quaternary ignimbrite-forming phonolitic eruption: the Poris member of the Diego Hernández Formation (Tenerife, Canary Islands),* In: Journal of Volcanology and Geothermal Research 118, 2002, p. 99-130, ISSN 0377-0273.

[14] Geyer, A. *Dynamics and structural evolution of collapse calderas: A comparison between field evidence, analogue and mathematical models*, doctoral thesis, Facultat de Geologia, Universitat de Barcelona, 2007, 438 p.

[15] Tait, S. - Jaupart, C. - Vergniolle, S. *Pressure, gas content and eruption periodicity of a shallow crystallizing magma chamber,* In: Earth and Planetary Science Letters 92, 1989, p. 107-123, ISSN 0012-821X.

[16] Martí, J. - Folch, A. *Anticipating volcanic eruptions,* In: Volcanoes and the Environment, J. Martí and G. Ernst, Cambridge University Press, Cambridge, 2005, p. 90-120, ISBN 978-0521592543.

[17] Folch, A. - Martí, J. *The generation of overpressure infelsic magma chamber by replenishment*, In: Earth and Planetary Science Letters 163, 1998, p. 301-314, ISSN 0012-821X.

[18] Gudmundsson, A. *Formation and development of normal-fault calderas and initiation of large explosive eruptions,* In: Bulletin of Volcanology 60, 1998, p. 160-171, ISSN 1432-0819.

[19] Burov, E.B. - Guillou-Frottier, L. *Thermomechanical behavior of large ash-flow calderas,* In: Journal of Geophysical Research 104(B10), 1999, p. 23081-23109, ISSN 2156 -2202.

[20] Druitt, T.H. - Sparks, R.S.J *On the formation of calderas during ignimbrite eruptions,* In: Nature 310, 1984, p. 679-681, ISSN 1476-4687.

[21] Bower, S.M. - Woods, A.W. *Control of magma volatile content and chamber depth on the mass erupted during explosive volcanic eruptions,* In: Journal of Geophysical Research 102, 1997, p. 10273-10290, ISSN 2156 -2202.

[22] Martí, J. - Folch, A. - Macedonio, G. - Neri, A. *Pressure evolution during caldera forming eruptions,* In: Earth and Planetary Science Letters 175, 2000, p. 275-287, ISSN 0012-821X.

[23] Roche, O. - Druitt, T.H. *Onset of caldera collapse during ignimbrite eruption,* In: Earth and Planetary Science Letters 191(3-4), 2001, p. 191-202, ISSN 0012-821X.

[24] Komuro, H. - Fujita, Y. - Kodama, K. *Numerical and experimental models on the formation mechanism of collapse basins during the Green Tuff orogenesis of Japan,* In: Bulletin of Volcanology 47, 1984, p. 649-666, ISSN 1432-0819.

[25] Chery, J. - Bonneville, A. - Villote, J.P. - Yuen, D. *Numerical modelling of caldera dynamical behavior,* In: Geophysical Journal International 105, 1991, p. 365-379, ISSN 1365-246X.

[26] Gudmundsson, A. - Martí, J. - Turón, E. *Stress fields generating ring-faults in volcanoes,* In: Geophysical Research Letters 24, 1997, p. 1559-1562, ISSN 1944–8007.

[27] Folch, A. - Martí, J. *Geometrical and mechanical constraints on the formation of ring-fault calderas*, In: Earth and Planetary Science Letters 221(1-4), 2004, p. 215-225, ISSN 0012-821X.

[28] Kusumoto, S. - Takemura, K. *Caldera geometry by the depth of the magma chamber,* In: Earth, Planets and Space 57, 2005, p. e17-e20, ISSN 1880-5981.

[29] Gray, J.P. - Monaghan, J.J. *Numerical modeling of stress fields and fracture around magma chambers,* In: Journal of Volcanology and Geothermal Research 135, 2004, p. 259-283, ISSN 0377-0273.

REVIEW ON EVALUATION OF EQUIVALENT STRESS TENSOR IN THE DISCRETE ELEMENT METHOD

Jan STRÁNSKÝ[1], **Milan JIRÁSEK**[2]

Abstract: *In this contribution, the theory of equivalent stress tensor derived from discrete forces and moments (which is a typical situation in the discrete element method) is reviewed. The stress tensor and couple stress tensor are derived based on equilibrium equations for both statics and dynamics. Asymmetry of the stress tensor is discussed as well. Finally, evaluation of the stress tensor is illustrated by simple examples.*

Keywords: *DEM, stress, couple stress, Cosserat continuum, stress asymmetry.*

1. INTRODUCTION

The discrete element method (DEM) is one of the most widely used numerical schemes for the description of solids. It represents a material body by rigid discrete units (discrete elements, which can displace and rotate) mutually interacting by contact forces and moments. This discrete representation is an essential feature of DEM. However, in some cases one would like to transform such discrete information (contact forces for instance) into its continuum counterpart (e.g. stress tensor). To give an example, consider a sample of sand, which is on the fine scale definitely discrete, thus discrete forces may be used as a model for description of mutual interaction between grains. On the other hand, on the coarse scale (e.g. the foundation of a building), investigation of each individual sand grain would not be meaningful (or even possible) and the same material is considered as a continuum.

The evaluation of equivalent stress from discrete forces is a topic much older than DEM itself [1], described in numerous papers [2, 3, 4], but it still remains a subject of debates in specialized literature [5, 6, 7, 8, 9]. The aim of this contribution is to summarize the current knowledge and present it to the general professional public.

[1]Ing. Jan Stránský , Faculty of Civil Engineering, Czech Technical University in Prague, jan.stransky@fsv.cvut.cz

[2]Prof. Ing. Milan Jirásek, DrSc., Faculty of Civil Engineering, Czech Technical University in Prague, milan.jirasek@fsv.cvut.cz

2. THEORY

We will work in a three-dimensional Cartesian coordinate system with basis vectors $\mathbf{e}_i$. Index notation and Einstein summation rule are used in tensorial equations. ∇_i denotes a spatial derivative, for example

$$\frac{a_{ij}}{\partial x_i} = \nabla_i a_{ij} \tag{1}$$

In the following text, we will exploit the divergence (Gauss-Ostrogradsky) theorem

$$\int_V \nabla_k a_{ikj} \,\mathrm{d}V = \int_{\partial V} n_k a_{ikj} \,\mathrm{d}\partial V \tag{2}$$

and the identity

$$\sigma_{ij} = \delta_{ik}\sigma_{kj} = (\nabla_k x_i)\sigma_{kj} = \nabla_k(x_i\sigma_{kj}) - x_i(\nabla_k \sigma_{kj}). \tag{3}$$

Here, δ_{ij} is the Kronecker delta symbol, V is the spatial domain occupied by the body of interest and ∂V is its boundary. The Levi-Civita permutation symbol will be denoted as ε_{ijk}. Overlined quantities stand for volume averages (e.g. $\overline{\sigma}_{ij}$ is the volume average of stress tensor).

2.1. CONTINUUM STRESS THEORY

The discrete elements in DEM possess 6 degrees of freedom, namely 3 displacements and 3 rotations. The classical (Boltzmann) continuum uses 3 degrees of freedom (3 displacements) in each material point. Because of this inconsistency, higher-order (e.g. Cosserat) models should be used for continuum approximation of DEM in its general form [2]. For readers not familiar with the Cosserat continuum, we quickly summarize the main ideas (see Fig. 1).

The material point can be represented by an infinitesimal cube with dimensions Δx_i. Such cube can be deformed by stretching and shearing, but also by bending and torsion. For more information about Cosserat kinematics see [10].

Each deformation mode has its force counterpart. The stress state of a material point is expressed by the second-order stress tensor σ_{ij} and the second-order couple stress tensor μ_{ij}. The ij component of the stress (couple stress) tensor represents the surface traction (moment couple) acting on the surface with normal $\mathbf{e}_i$ in direction $\mathbf{e}_j$. Surface traction t_j and surface couple m_j acting on a surface with a general normal n_i can be expressed as

$$n_i\sigma_{ij} = t_j, \qquad n_i\mu_{ij} = m_j \tag{4}$$

Equilibrium equations are expressed in terms of body forces f_i and body couples ϕ_i and can be derived from equilibrium on an infinitesimal cube considering its dimensions in the limit $\Delta x_i \to 0$.

For example, force equilibrium (2D) in direction 1 yields

$$-\Delta x_2\sigma_{11}(x_1) + \Delta x_2\sigma_{11}(x_1+\Delta x_1) - \Delta x_1\sigma_{21}(x_2) + \Delta x_1\sigma_{21}(x_2+\Delta x_2) + f_1\Delta x_1\Delta x_2 = 0$$

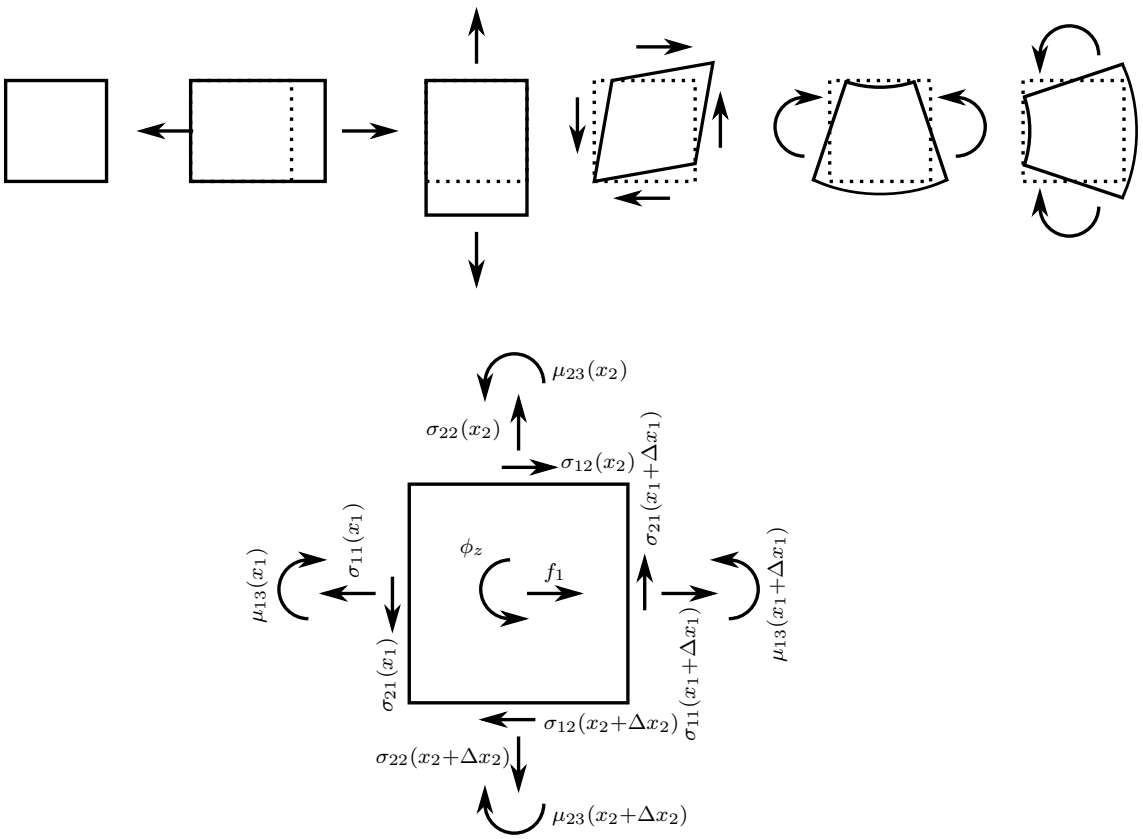

Fig. 1 Two-dimensional representation of Cosserat deformation modes and their force counterparts (top) and stresses and couple stresses on elementary cube (bottom)

$$\frac{\sigma_{11}(x_1+\Delta x_1)-\sigma_{11}(x_1)}{\Delta x_1}+\frac{\sigma_{21}(x_2+\Delta x_2)-\sigma_{21}(x_2)}{\Delta x_2}+f_1=0 \quad \xrightarrow{\Delta x_i\to 0}$$
$$\xrightarrow{\Delta x_i\to 0} \quad \nabla_1\sigma_{11}+\nabla_2\sigma_{21}+f_1=0 \tag{5}$$

and moment equilibrium yields

$$-\Delta x_2\mu_{13}(x_1)+\Delta x_2\mu_{13}(x_1+\Delta x_1)-\Delta x_1\mu_{23}(x_2)+\Delta x_1\mu_{23}(x_2+\Delta x_2)+$$
$$+\Delta x_2\sigma_{12}\Delta x_1-\Delta x_1\sigma_{21}\Delta x_2+\phi_3\Delta x_1\Delta x_2=0$$
$$\frac{\mu_{13}(x_1+\Delta x_1)-\mu_{13}(x_1)}{\Delta x_1}+\frac{\mu_{23}(x_2+\Delta x_2)-x_2\mu_{23}(x_2)}{\Delta x_2}+\sigma_{12}-\sigma_{21}+\phi_3=0 \quad \xrightarrow{\Delta x_i\to 0}$$
$$\xrightarrow{\Delta x_i\to 0} \quad \nabla_1\mu_{13}+\nabla_2\mu_{23}+\sigma_{12}-\sigma_{21}+\phi_3=0. \tag{6}$$

Generalization of (5) and (6) provides the full form of equilibrium equations (which can be derived more rigorously from linear momentum and angular momentum balance):

$$\nabla_i\sigma_{ij}+f_j = 0, \tag{7}$$
$$\nabla_i\mu_{ik}+\varepsilon_{ijk}\sigma_{ij}+\phi_k = 0. \tag{8}$$

If couple stresses and body couples are omitted (which is the case of the classical Boltzmann continuum), equation (8) reduces to

$$\varepsilon_{ijk}\sigma_{ij} = 0 \tag{9}$$

which implies symmetry of the stress tensor. In a general case, the stress tensor in the Cosserat continuum model may be asymmetric. In the following text, we exclude the external load contribution to f_i and m_i, and we will consider f_i and m_i as the inertial terms, related to the acceleration of a material point (e.g. $f_i = -\rho a_i$, where ρ is the mass density and a_i is the acceleration).

2.2. DISCRETE STRESS TENSOR

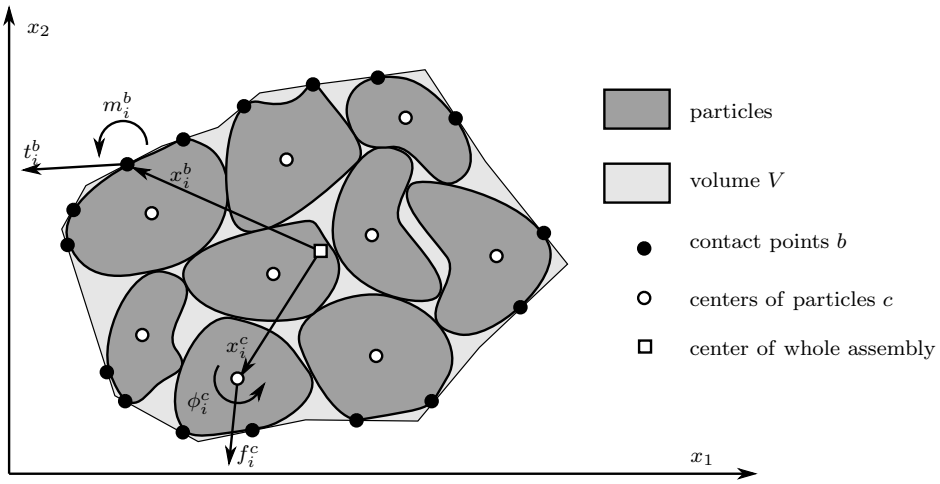

Fig. 2 Two-dimensional representation of investigated particle assembly

Consider a set of discrete *perfectly rigid* particles of generic shapes, mutually interacting by forces and moments (see Fig. 2). The assembly of investigated particles is embedded in a certain volume V. In the following text, we will use surface integrals of surface tractions and volume integrals of body forces. In the case of discrete forces and moments and perfectly rigid particles, we consider external and body loads as Dirac delta distributions transforming the boundary integral into a discrete sum over external inter-particle bonds b and the volume integral into a sum over the centers of mass c of particles:

$$\int_{\partial V} x_i t_j = \sum_b x_i^b t_j^b, \qquad \int_{\partial V} x_i m_j = \sum_b x_i^b m_j^b, \tag{10}$$

$$\int_V x_i f_j = \sum_c x_i^c f_j^c, \qquad \int_V x_i \phi_j = \sum_c x_i^c \phi_j^c. \tag{11}$$

Recalling equations (2), (3) and (8) we can write:

$$V\overline{\sigma}_{ij} = \int_V \sigma_{ij}\,\mathrm{d}V = \int_V \nabla_k(x_i\sigma_{kj}) - x_i(\nabla_k\sigma_{kj})\,\mathrm{d}V =$$

$$= \int_{\partial V} x_i n_k \sigma_{kj}\,\mathrm{d}\partial V - \int_V x_i(\nabla_k\sigma_{kj})\,\mathrm{d}V = \int_{\partial V} x_i t_j\,\mathrm{d}\partial V + \int_V x_i f_j\,\mathrm{d}V =$$

$$= \sum_b x_i^b t_j^b + \sum_c x_i^c f_j^c \tag{12}$$

$$V\overline{\mu}_{ij} = \int_V \mu_{ij}\,\mathrm{d}V = \int_V \nabla_k(x_i\mu_{kj}) - x_i(\nabla_k\mu_{kj})\,\mathrm{d}V =$$
$$= \int_{\partial V} x_i n_k \mu_{kj}\,\mathrm{d}\partial V - \int_V x_i(\nabla_k\mu_{kj})\,\mathrm{d}V = \int_{\partial V} x_i m_j\,\mathrm{d}\partial V + \int_V x_i(\phi_j + \varepsilon_{klj}\sigma_{kl})\,\mathrm{d}V =$$
$$= \int_{\partial V} x_i m_j\,\mathrm{d}\partial V + \int_V x_i\phi_j\,\mathrm{d}V + \int_V x_i\varepsilon_{klj}[\nabla_m(x_k\sigma_{ml}) - x_k(\nabla_m\sigma_{ml})]\,\mathrm{d}V =$$
$$= \int_{\partial V} x_i m_j\,\mathrm{d}\partial V + \int_V x_i\phi_j\,\mathrm{d}V + \int_{\partial V} x_i\varepsilon_{klj}n_m x_k\sigma_{ml}\,\mathrm{d}\partial V - \int_V x_i\varepsilon_{klj}x_k\nabla_m\sigma_{ml}\,\mathrm{d}V$$
$$= \sum_b x_i^b m_j^b + \sum_c x_i^c\phi_j^c + \sum_b x_i^b x_k^b\varepsilon_{klj}t_l^b + \sum_c x_i^c x_k^c\varepsilon_{klj}f_l^c \tag{13}$$

These equations are general expressions for the equivalent stress and couple stress tensor for an assembly of discrete particles. As already mentioned, in the general case the stress tensor may be asymmetric.

While equation (12) is independent of the reference point, equation (13) is not. This violates one of three conditions of equivalent stress stated in [3] and will be subjected to further investigation. In the following text, the center of the investigated volume is chosen as the reference point.

2.3. DISCRETE STRESS TENSOR OF ONE PARTICLE

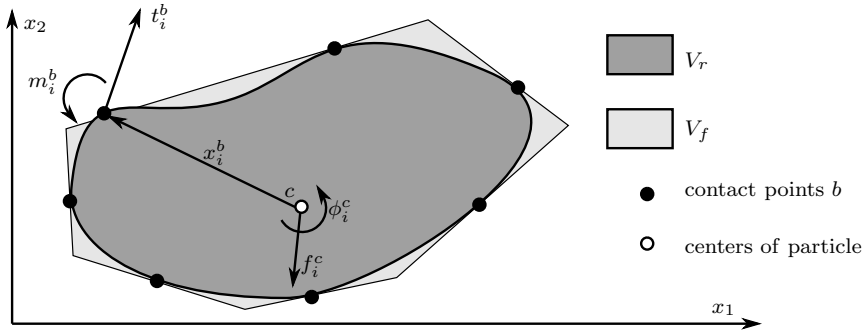

Fig. 3 Two-dimensional representation of one particle

Depending on the physical meaning of the particle (actual particle or just spatial discretization), V is equal to the real volume V_r or a fictitious volume V_f, see Fig. 3. The sum over centers of gravities is reduced to one term only. Furthermore, we can put the origin of coordinates into the center of mass, so that this term vanishes completely. The resulting formulas for the equivalent stress tensor and equivalent couple stress tensor are

$$V\overline{\sigma}_{ij} = \sum_b x_i^b t_j^b \tag{14}$$

$$V\overline{\mu}_{ij} = \sum_b x_i^b m_j^b + \sum_b x_i^b x_k^b\varepsilon_{klj}t_l^b. \tag{15}$$

2.4. DISCRETE STRESS TENSOR OF PERIODIC CELL

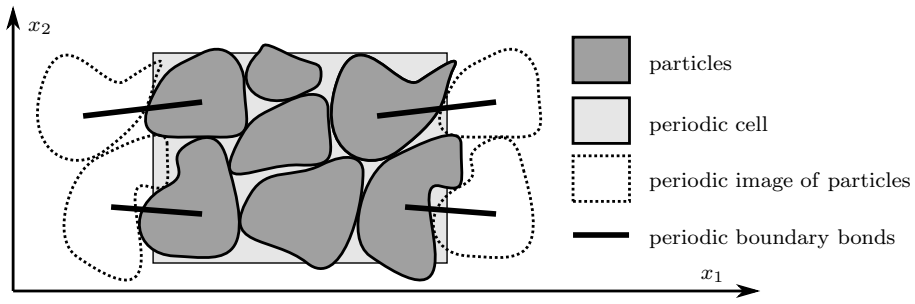

Fig. 4 Two-dimensional representation of periodic cell. Periodicity is shown in x_1 direction

The periodic cell represents a specific part of a virtually infinite region subjected to macroscopically uniform deformation. Such approach is often used for example in multiscale simulations. The principal idea is, as the name suggests, that all quantities are periodic. In our study, we are interested in force and moment quantities, so the situation may look like in Fig. 4.

The equivalent stress and couple stress tensors can be evaluated directly from equations (12) and (13), but the stress tensor can also be evaluated as the volume average of per-particle equivalent stresses over all particles p:

$$V\overline{\sigma}_{ij} = \sum_p V^p \sigma_{ij}^p = \sum_p \sum_b x_i^{pb} f_j^{pb} = \sum_l l_i^l f_j^l, \tag{16}$$

where $l_i = x_i^b - x_i^a$ is the branch vector of a bond connecting centers of particles a and b, and f_i is the internal force of this bond. The last sum is created by summing pairs of bonds divided in two parts.

While the equivalent stress tensor of a periodic cell yields a simple elegant formula, the equivalent couple stress cannot be evaluated as a mere average of the couple stresses of individual particles. For illustration, see Fig. 5, where the couple stress of each particle vanishes, but the equivalent couple stress is nonzero. For couple stress evaluation, we therefore recommend to use formula (13). The simplified formula for the couple stress of a periodic cell will be the subject of further investigation.

3. ILLUSTRATION

For illustration of the derived formulas, we show an academic example of four particles connected in a regular grid, see Fig. 5. On this extremely simple example one can directly see what the resulting stress and couple stress should be, which makes it suitable for method demonstration. All presented formulas, namely (7), (13), (14), (15) and (16), give expected results.

Dimensions of one gray square is 2×2 length units, the applied forces have magnitude 4 force units and the moments have magnitude 8 (larger arrows) or 4 (smaller arrows) force $\times$ length units.

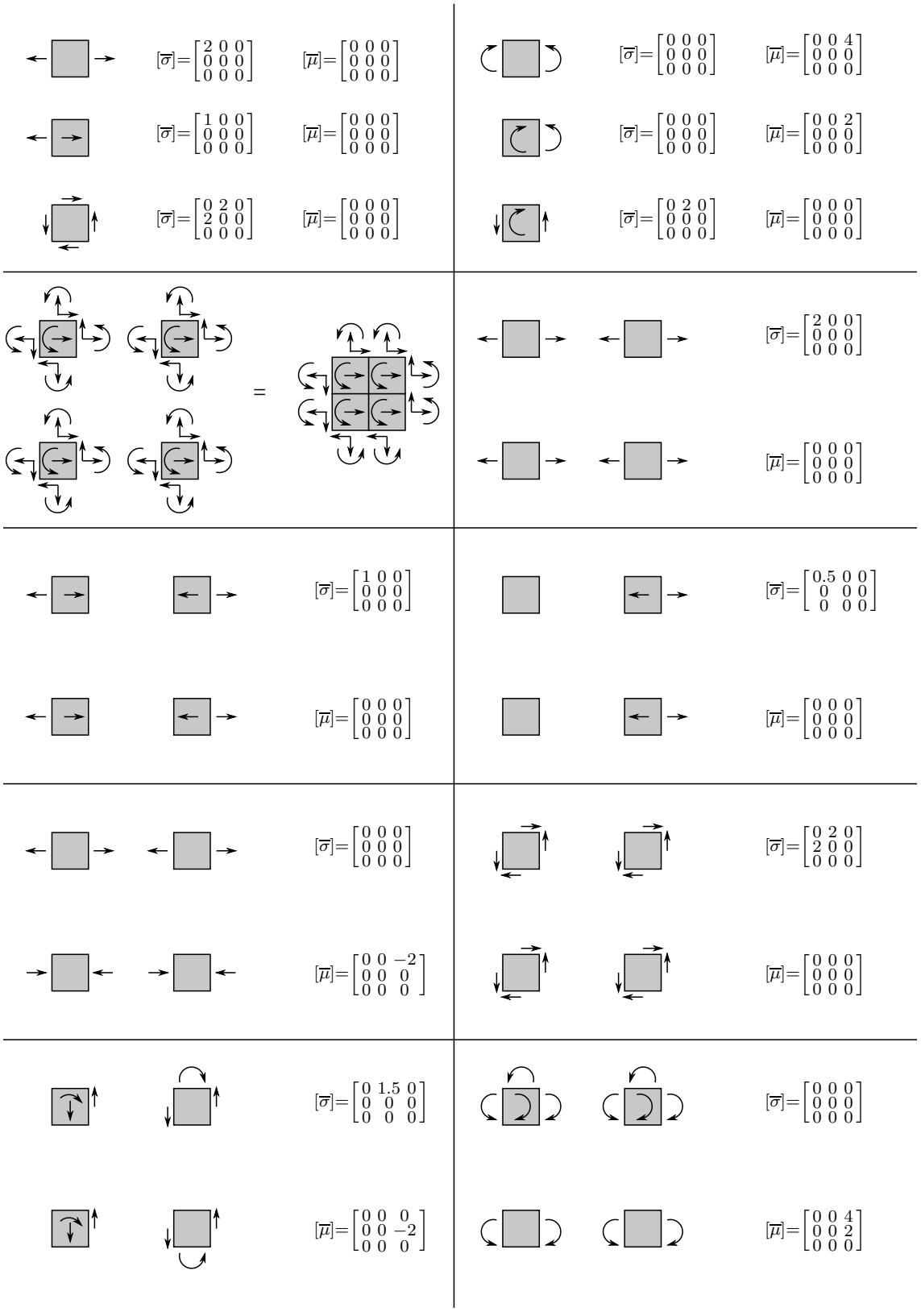

Fig. 5 Illustration of presented method

4. CONCLUSION

The theory of equivalent stress tensor of discrete systems has been reviewed in this contribution. The derivation based on equilibrium equations has been performed for both statics and dynamics and has been verified on simple examples. The static case matches the results derived from the virtual work principle [3].

ACKNOWLEDGEMENT

Financial support of the Czech Technical University in Prague under project SGS12/027/OHK1/1T/11 is gratefully acknowledged.

REFERENCES

[1] Love, A. E. H. *A Treatise on the Mathematical Theory of Elasticity (4th ed.)*. Cambridge, University press, 634 p., 1927.

[2] Alonso-Marroquín, F. Static equations of the Cosserat continuum derived from intra-granular stresses. *Granular matter, 13*, 2011, pp. 189–196.

[3] Ching, S. C. & Kuhn, M. R. On virtual work and stress in granular media. *International Journal of Solids and Structures, 42*, 2005, pp. 3773–3793.

[4] Bagi, K. Stress and strain in granular assemblies. *Mechanics of Materials, 22*, 1995, pp. 165–177.

[5] Bardet, J. & and Vardoulakis I., The asymmetry of stress in granular media. *International Journal of Solids and Structures, 38*, 2001, pp. 353–367.

[6] Bagi, K. Discussion on "The asymmetry of stress in granular media". *International Journal of Solids and Structures, 40*, 2003, pp. 1329–1331.

[7] Kuhn, M. Discussion on "The asymmetry of stress in granular media". *International Journal of Solids and Structures, 40*, 2003, pp. 1805–1807.

[8] Bardet, J. & Vardoulakis, I. Reply to discussion by Dr. Katalin Bagi. *International Journal of Solids and Structures, 40*, 2003, pp. 1035.

[9] Bardet, J. & Vardoulakis, I. Reply to Dr. Kuhn's discussion. *International Journal of Solids and Structures, 40*, 2003, pp. 1809.

[10] Vardoulakis, I. *Lecture notes on Cosserat continuum mechanics with application to the mechanics of granular media*. [online]. [2009] [cit. 2012-08-14]. Available from WWW: <http://geolab.mechan.ntua.gr/teaching/lectnotes/CCM2009.pdf>.

DEVELOPMENT OF MECHANICAL PROPERTIES OF GYPSUM DURING ITS HARDENING

Richard ŤOUPEK[1], Tomáš PLACHÝ[2], Pavel TESÁREK[3]

Abstract: *The article describes the development of mechanical properties of grey gypsum during its hardening. Non-destructive resonance method was used for establishing mechanical properties of gypsum samples (Dynamic Young's Modulus and Dynamic Shear Modulus, Poisson's ratio).*

Keywords: *gypsum, Dynamic Young´s Modulus, Poisson´s ratio, resonant frequency, impulse excitation.*

1. INTRODUCTION

During laboratory measurements the changes of characteristic material properties of samples made of grey gypsum during its hardening were observed in the first sixty hours from the time of sample production. Non-destructive resonant method was used for determination of basic resonant frequencies of longitudinal, transverse and torsional vibration of gypsum samples. Dynamic Young's Modulus and Dynamic Shear Modulus were determined from measured and evaluated values. Then these values were used for determination of Poisson's ratio.

1.1. MATERIAL AND SAMPLES

Grey gypsum produced by Gypstrend co. Ltd. was used for experimental testing. It is made of two components. These two components are natural gypsum and gypsum from chemical industry mixed in one-to-one ratio. Used gypsum was classified as G2 BII, where G2 describes the class of binding agent and gives the minimal compression strength [MPa]. This grey gypsum has minimal compression strength 2 MPa after two hours of hardening. BII marker describes gypsum binding agent as normally hardening, moderately ground. Water coefficient equal to 0.71 was used for this gypsum according to the standard ČSN 72 2301 "Gypsum binders" [1] and corresponds to gypsum paste with normal consistence.

[1] Ing. Richard Ťoupek, Department of Mechanics, Faculty of Civil Engineering, CTU in Prague; richard.toupek@fsv.cvut.cz

[2] Ing. Tomáš Plachý, Ph.D., Department of Mechanics, Faculty of Civil Engineering, CTU in Prague; plachy@fsv.cvut.cz

[3] Ing. Pavel Tesárek, Ph.D., Department of Mechanics, Faculty of Civil Engineering, CTU in Prague; tesarek@fsv.cvut.cz

Three identical gypsum samples of size 40 × 40 × 160 mm were made for determination of basic material characteristics. The samples were marked as Specimen I, Specimen II and Specimen III.

2. MEASUREMENTS

The Dynamic Young's Modulus is determined based on the basic resonant longitudinal or transverse frequency of vibration of the tested sample. Dynamic Shear Modulus is calculated from the measured values of resonant frequency in torsional vibration of the tested samples. Resonant frequencies were determined in laboratory (Fig. 1) by measuring unit Bruel&Kjaer Front-end 3560B-120 [2]. The acceleration transducer Bruel&Kjaer type 4519-003, and the impact hammer Bruel&Kjaer type 8206 [2] were connected to the unit.

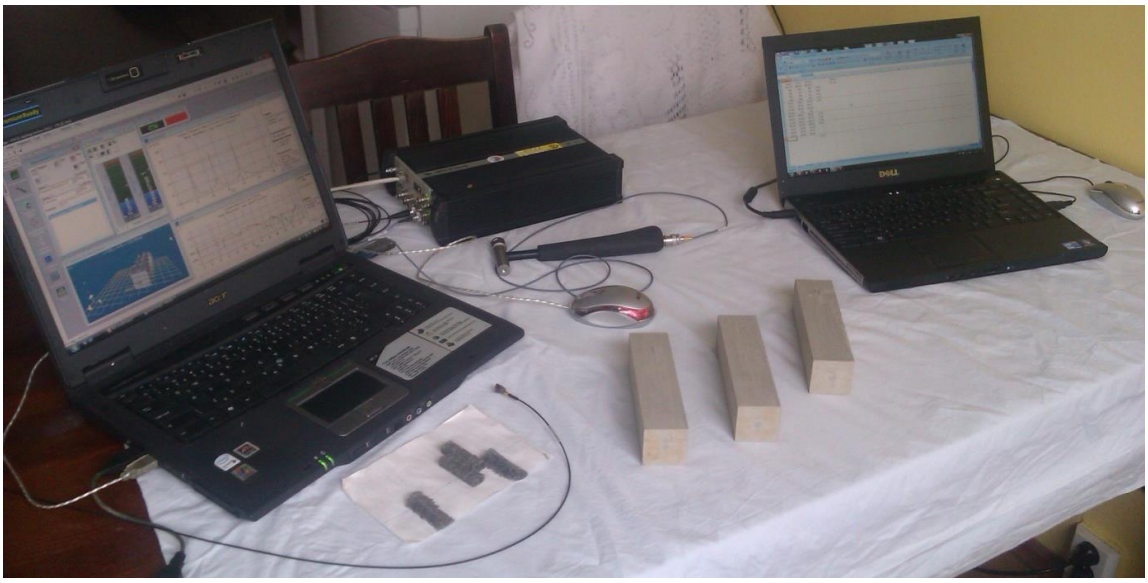

Fig. 1 The measurement line.

The excitation force and the response (acceleration) are transformed from time domain to the frequency domain and the Frequency Response Function (FRF) is evaluated as the ratio of response to excitation force. Then the basic resonant frequencies of longitudinal, transverse and torsional vibration of the sample are determined from FRFs. The operations are executed in PC software PULSE 14.0. Dynamic Young's Modulus Ed and Dynamic Shear Modulus Gd are determined from the calculated values.

The equation for establishing Ed value from longitudinal vibration [3]:

$$E_d = \frac{4\, l\, m\, f_l^2}{b\, h}\ , \qquad (1)$$

where: E_d is the Dynamic Young´s Modulus [Pa], f_l is the fundamental longitudinal frequency [Hz], b is the width of the specimen [m], h is the height of the specimen [m], l is the length of the specimen [m], m is the mass of the specimen [kg].

The equation for establishing Ed value from transverse vibration:

$$E_d = 0{,}9464 \left(\frac{m f_r^2}{b}\right)\left(\frac{l}{h}\right)^3 A_f \,, \qquad (2)$$

where: E_d is the Dynamic Young´s Modulus [Pa], f_r is the fundamental transverse frequency [Hz], b is the width of the specimen [m], h is the height of the specimen [m], l is the length of the specimen [m], m is the mass of the specimen [kg], A_f is the correction factor.

The equation for establishing Gd value from transverse vibration:

$$G_d = \left(\frac{4lmf_t^2}{bh}\right) A_t \qquad (3)$$

where: G_d is the Dynamic Shear Modulus [Pa], f_t is the fundamental torsional frequency [Hz], b is the width of the specimen [m], h is the height of the specimen [m], l is the length of the specimen [m], m is the mass of the specimen [kg], A_t is the empirical correction factor.

Poisson's ratio is calculated from the final values of the Dynamic Young's Modulus and the Dynamic Shear Modulus according to the equation [3,4]:

$$\mu = \frac{E_d}{2\,G_d} - 1 \,. \qquad (4)$$

where: μ is the Poisson´s ratio [-], E_d is the Dynamic Young´s Modulus [Pa], G_d is the Dynamic Shear Modulus [Pa].

Gypsum samples during every laboratory measurement of material characteristics were measured and weighed. Measured sizes and weights were used for establishing values of the Dynamic Young's Modulus and the Dynamic Shear Modulus for every one of approximately 60 measurements during the first sixty hours from the sample production.

All samples were during whole procedure of measuring in laboratory environment. Average laboratory temperature was 23°C and average relative humidity was 42%.

3. RESULTS

The first established value was the Dynamic Young's Modulus determined from the longitudinal vibration (Fig. 2). As can be seen in Fig. 2, value of Dynamic Young's Modulus Ed increased by 4% from average value 3.8 GPa to 3.95 GPa in the first 3 hours after production. During the next two days (48 hours) the value of E_d remains relatively stable between 3.7 GPa and 3.9 GPa.

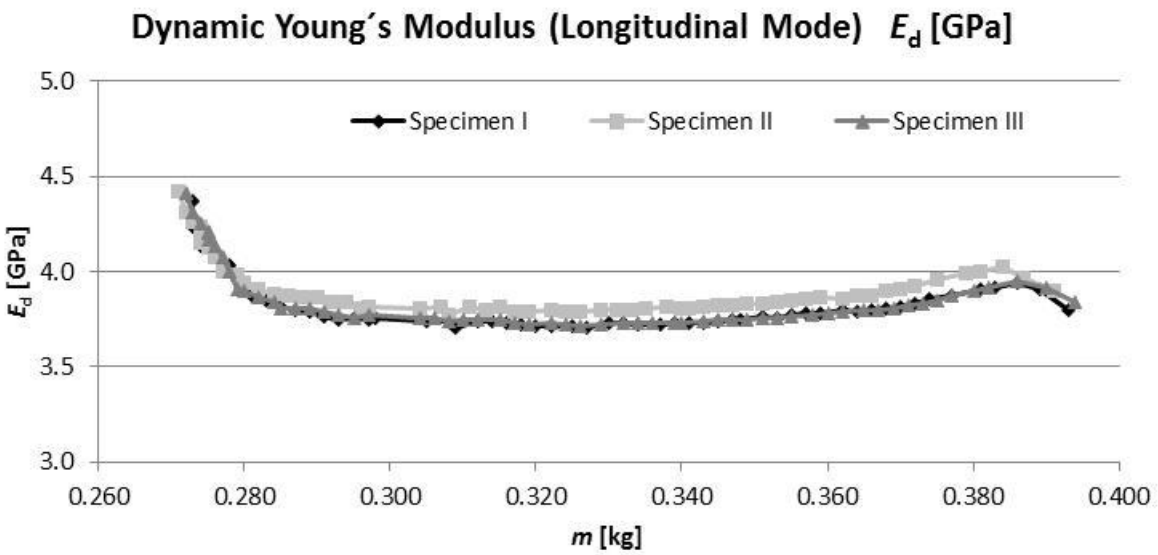

Fig. 2 Dynamic Young´s Modulus (Longitudinal Mode)

During the last ten hours of laboratory measurements maximal release of free humidity which is possible in described laboratory environment occurred. Initial weight of samples was 395 g. Weight during measurements decreased to the values between 280 and 290 g. Increase of E_d values was observed at the end of laboratory measurements (the last 10 hours). The maximal value of E_d established from longitudinal vibration of samples reached 4.4 GPa.

E_d values established from the transverse vibration were determined from measured values of resonant frequencies (Fig. 3). According to formula (2) for E_d values, greater scattering of E_d values comes when E_d is established from transverse vibration of samples. It is possible to say that values developments from both Fig. 2 and 3 are very similar.

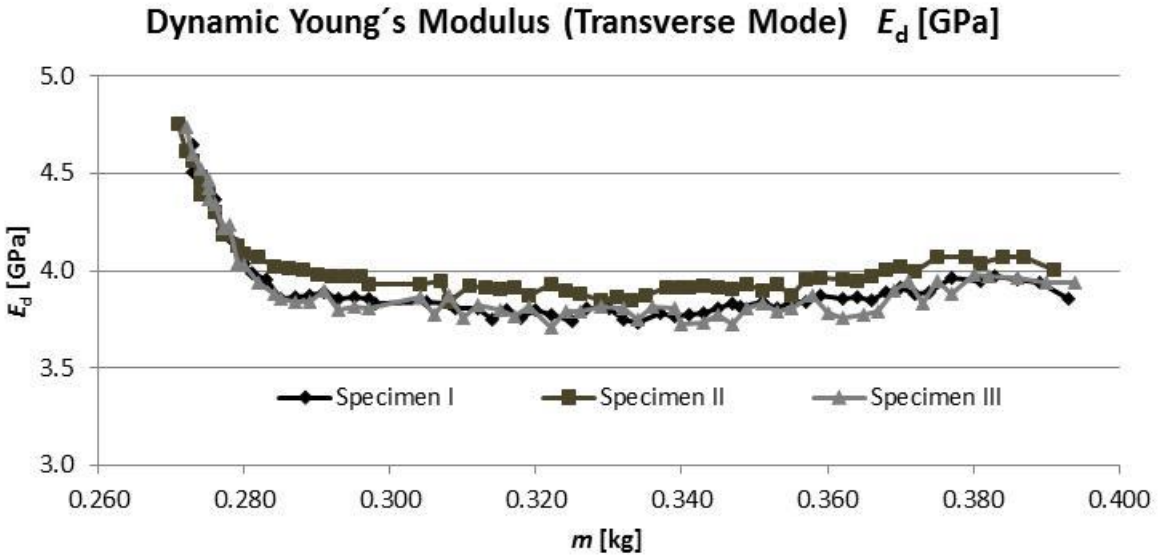

Fig. 3 Dynamic Young´s Modulus (Transverse Mode)

The Dynamic Shear Modulus was established in the next stage of evaluation of measured values. Values were established from formula (3).

G_d values present almost no change during the whole procedure of hardening and loss of free humidity. Values were constantly between 1.35 and 1.5 GPa. In the final stage of measurements, increase of G_d values occurs similar to the case of E_d measurements. G_d values increased by 17 % to 1.75 GPa during the weight loss of the last 10 g of free humidity from the gypsum samples.

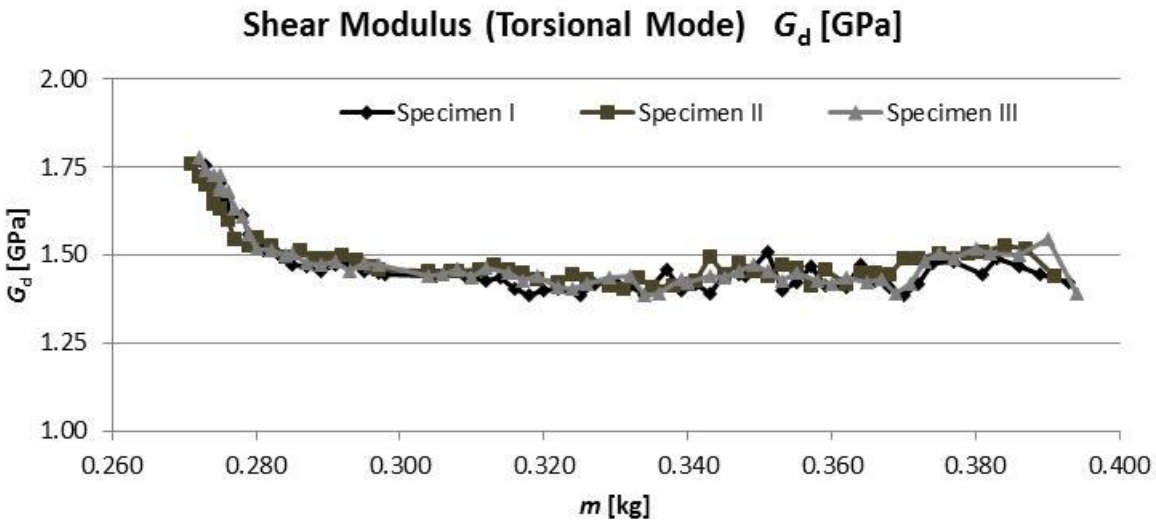

Fig. 4 Shear Modulus (Torsional Mode)

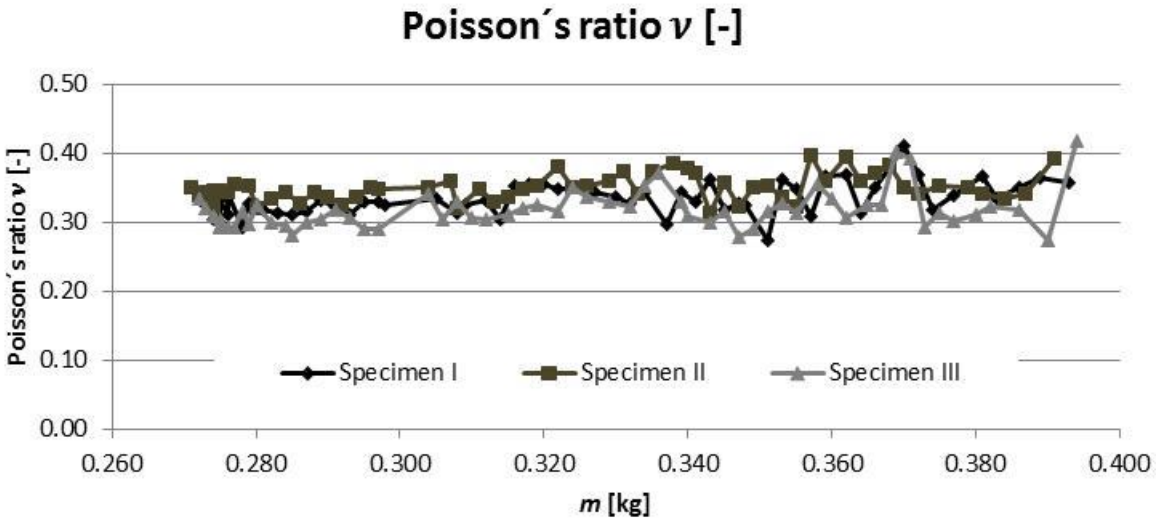

Fig. 5 Poisson´s ratio

Based on established values of E_d and G_d it was possible to determine the Poisson's ratio for each measurement of the samples. The progress of the values of ν is presented in Fig. 5. The majority of the values falls into the range between 0.30 and 0.33 without any regard to when the value was determined.

4. CONCLUSION

The article presents the results of an experiment during which the development of the Dynamic Young's Modulus, the Dynamic Shear Modulus and the Poisson's ratio of three grey gypsum samples were monitored in time. It was observed how the values change during the first 60 hours after the production of the samples in laboratory environment. The characteristic values were observed from the time of production until the release of free moisture that is until the loss of approximately 100 g of the original weight. The experiment gives more accurate knowledge of the behaviour of gypsum samples in laboratory environment and it is one of the further steps of deeper research on the behaviour of gypsum binders, particularly grey gypsum.

ACKNOWLEDGEMENT

The financial support of this experiment by the Faculty of Civil Engineering, Czech Technical University in Prague (SGS project No. 12/117/OHK1/2T/11) is gratefully acknowledged.

REFERENCES

[1] ČSN 72 2301, Gypsum binders, (in Czech), Prague, Czech Standards Institute, 2009

[2] Ťoupek, R., Determination of mechanical properties of materials on the gypsum basis using non-destructive method, (in Czech), Thesis, Prague, Faculty of Civil Engineering, CTU in Prague, 2011, 97 p.

[3] ASTM C215, Standard Test Method for Fundamental Transverse, Longitudinal, and Torsional Resonant Frequencies of Concrete Specimens, Annual Book of ASTM Standards, American Society for Testing and Materials, 1991, 7 p.

[4] ASTM E1876-01, Standard Test Method for Dynamic Young's Modulus, Shear Modulus, and Poisson's Ratio by Impulse Excitation of Vibration, Annual Book of ASTM Standards, American Society for Testing and Materials, 2006, 14 p.

[5] Papán, D., Experimental measurements of paraseismic effects due to traffic. Proceedings of the 20th European Regional Earthquake Engineering Seminar: Seismic assessment and upgrading of existing structures, Institute Universitaire Kurtz Bosch, Sion, Switzerland, pp. 144-145, 2001

[6] Benčát, J., Papán, D., Experimental dynamic analysis of Ružín railway bridges. Proceedings of the 22nd Danubia-Adria Symposium on Experimental Methods in Solid Mechanics, DAS 2005, Parma, Italy, pp. 253-254, 2005

DEVELOPMENT OF STRENGTH OF CONCRETE FROM ORLIK DAM

Ondřej ZOBAL[1], **Zdeněk BITTNAR**[2], **Pavel PADEVĚT**[3]

Abstract: *The Orlík Dam is ranked among the most important construction works on the territory of the Czech Republic. This construction provides a chance to analyze the perfect technological process and used material. In the concrete mixture for construction of the dam, almost 30% of cement was replaced with power plant fly ash. The reason for using fly ash was to prevent construction damage due to high increase of hydration heat. So there is a unique chance for analyzing such material after more than 50 years of operation. This paper deals with the development of compressive strength and tensile strength.*

Keywords: *Orlik Dam, Concrete, Fly Ash, Compressive Strength, Tensile Strength*

1. INTRODUCTION

Construction of the Orlík Dam started in 1956 and it was completed in 1961. The Orlík Dam is the largest waterworks in the Czech Republic and it is a part of the Vltava Cascade. The dam unit of the Orlík Dam is a linear gravity concrete dam of the height of 81.5 m and crest length of 450 m [1]. 923 000 m^3 of concrete were used for construction of the dam. Perfect schedule of works and plotted technological solution, however, allowed concreting of 83 % of the cubic capacity as soon as in 32 months [2].

Cracking in the construction started to appear after the first phase. The cracks were caused by high increase of hydration heat. To solve the problems the variant, when certain part of cement is replaced with power plant fly ash in the concrete mixture, was chosen. For construction of the dam two mixtures were used – cover concrete B170 with 200 kg/m^3 of cement and 50 kg/m3 of fly ash and center concrete B80 with 130 kg/m3 of cement and 50 kg/m^3 of fly ash [3].

[1] Ing. Ondřej Zobal, Department of Mechanics, Faculty of Civil Engineering, CTU; ondrej.zobal@fsv.cvut.cz

[2] prof. Ing. Zdeněk Bittnar, CSc., Department of Mechanics, Faculty of Civil Engineering, CTU, bittnar@fsv.cvut.cz

[3] Ing. Pavel Padevět, Ph.D. , Department of Mechanics, Faculty of Civil Engineering, CTU, pavel.padevet@fsv.cvut.cz

2. EXECUTED TESTS

The analysis of material and mechanical properties was carried out in this specific concrete. This paper presents the test of compressive strength and tensile strength.

2.1. THE TEST OF COMPRESSIVE STRENGTH

Cubes with the edge of 200 mm were cut from cylinders with diameter of 300 mm by a diamond saw and the test of compressive strength was carried out. The test was carried out with four cubes and the value of compressive strength ranged from 42 to 51 MPa. In the Fig. 1, there is a photograph of the body ready for test.

Fig. 1 Test Preparation: specimen for test of the compressive strength

2.2. THE SPLITING TEST

The Splitting test was carried out on the cylinders with the diameter of 300 mm and height of 220 mm and tensile strength was established. The test was carried out on six bodies and the value ranged from 3 to 4.5 MPa, which corresponds with c. 10% of compressive strength, which is stated in Chapter 2.1. In Fig. 2, there is a photograph of the body ready for measurement. We can see steel prisms in the upper and lower parts and one of the extensometers to measure related deformations in the middle.

Fig. 2 Test Preparation: specimen for the Splitting test

3. EVALUATION

In this chapter, there are examples of typical course of individual tests of compressive strength and tensile strength. The course of dependency of the compressive strength on reshaping when maximum value of compressive strength for this testing body is 42 MPa is graphically illustrated in Fig. 3. The course of dependency of the tensile strength on reshaping when the maximum value of tensile strength for this testing body is 3.1 MPa is graphically illustrated in Fig. 4.

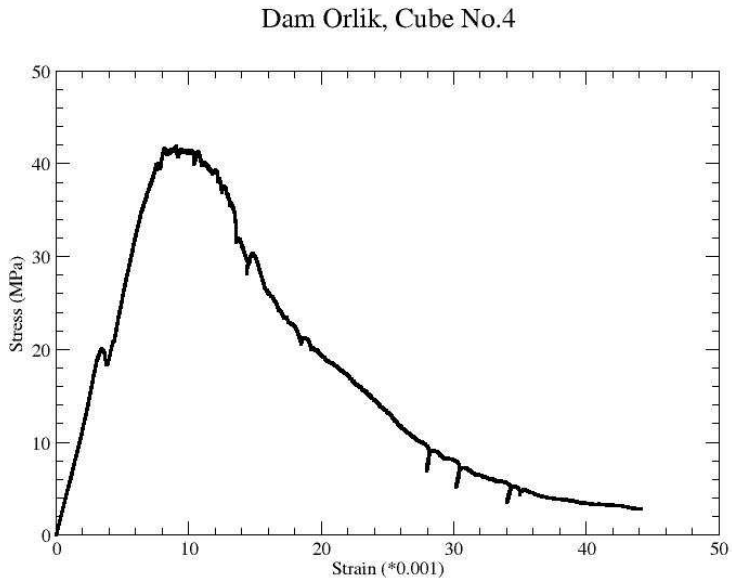

Fig. 3 The Orlík Dam – concrete mixed with fly ash after 50 years – dependence of compressive strength on deformation

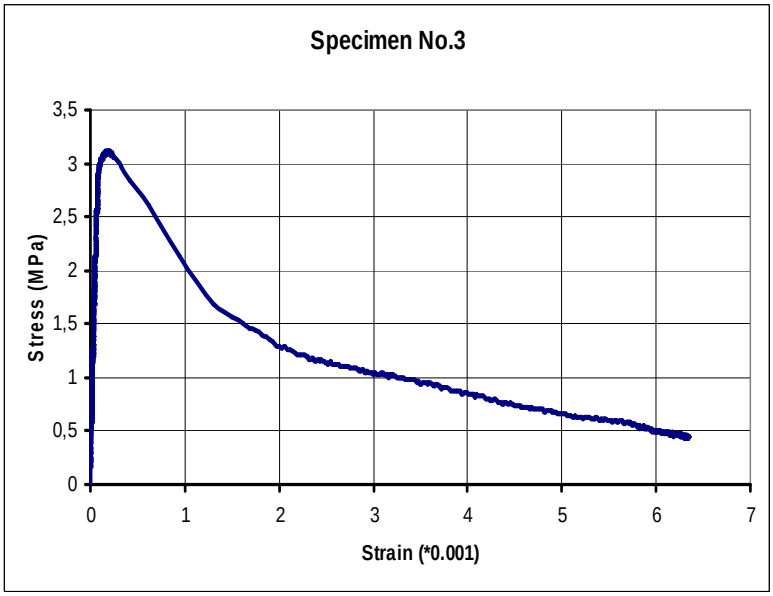

Fig. 4 The Orlík Dam – concrete mixed with fly ash after 50 years – dependence of tensile strength on deformation

4. CONCLUSION

The executed analysis verified excellent properties of the concrete, which was used for production of the dam unit of the Orlík Dam. Huge quantity of the building materials caused difficulties with variability of the used materials quality. For this reason, the construction site control was established and 9000 different tests and 30 000 non-destructive measurements of the concrete properties development were carried out during the construction [2]. The resulting concrete is a very compact material with minimum hollows and pores with high strength, which still grows with time (average compressive strength for B80: 28 days – 10.1 MPa, 90 days – 18 MPa, 360 days 23.4 MPa, 50 years – 47.3 MPa [4]). This is a very positive fact that should convince sceptics of using more power plant fly ash during production of concrete. The analysis proved that substitution of almost 30% of cement for fly ash had no negative effect on long-term qualities of the resulting concrete.

ACKNOWLEDGEMENT

The financial support of this experiment by the Faculty of Civil Engineering, Czech Technical University in Prague (MPO ČR project FR-TI3/757) is gratefully acknowledged.

REFERENCES

[1] Vodní díla a nádrže (in Czech), Povodí Vltavy s. p., pp. 9-10, 2011 (http://www.pvl.cz/vodohospodarske-informace/vodni-dila/vodni-dila-a-nadrze)

[2] Keil, J.: Výstavba vodního díla Orlík – sborník statí (in Czech), Národní podnik vodní stavby, pp. 90-113, 1966

[3] Hydroprojekt Praha: Vodní dílo Orlík souhrnný elaborát – svazek ¼ - textová část (in Czech), Státní ústav pro projektování vodohospodářských staveb Hydroporojekt, pp. 35-41, 1956

[4] Hydroprojekt Praha: Vodní dílo Orlík souhrnný elaborát – svazek 2/4 - výkresová část (in Czech), Státní ústav pro projektování vodohospodářských staveb Hydroporojekt, pp. 2376/1220/27, 1956

COMPLEX MICROSTRUCTURAL ENRICHMENT FUNCTIONS BASED ON EXTENDED WANG TILE SETS

Lukáš ZRŮBEK[1], **Anna KUČEROVÁ**[2],
Jan NOVÁK[3]

Abstract: *This contribution addresses the so called extended Wang tile sets to create aperiodic microstructural enrichment functions by means of stochastic Wang tiling synthesis technique. Acquired constructions are more self-equilibrated and better correspond with spatial statistics of underlying microstructures than the functions synthetized from standard sets and designed by means of a multi-objective optimization. The use of synthetized enrichments is seen in numerical simulations of disordered material systems in Generalized and Hybrid Finite Element environments.*

Keywords: *Wang tilings; random materials; FFT solver; local field synthesis;*

1. INTRODUCTION

Nowadays, sustainable environment tendencies along with the political-socio-economic aspects lead to highly optimized design of majority consumable products. In Civil or Mechanical Engineering industry, this is mirrored by a pressure to a less material consumption, provided final commodities keep improving their original performance from customer appealing perspectives (for example a new season model of rain coat is lighter and cheaper but it exhibits better water resistance). Such, somehow idealized, benefits are often contradictory and barely possible without a detailed understanding of characteristic physical processes taking place on various scales of materials with heterogeneous microstructures.

In the current engineering practice, the detailed study of existing or newly designed materials is inconceivable without computer aided simulations with numerical methods at heart. For instance, let us recall the Finite Element Method (FEM) which shows robustness for structural-scale computations, however it is less decisive for microstructural details. By virtue of this fact, the conventional FEM variants have been modified in order to deal with an a priory knowledge on local scale behaviour without the need for detailed resolution.

[1]Bc. Lukáš Zrůbek , Department of Mechanics, Faculty of Civil Engineering, Czech Technical University in Prague, lukas.zrubek@fsv.cvut.cz

[2]Ing. Anna Kučerová, Ph.D., Department of Mechanics, Faculty of Civil Engineering, Czech Technical University in Prague, anicka@cml.fsv.cvut.cz

[3]Ing. Jan Novák, Ph.D., Institute of Structural Mechanics, Faculty of Civil Engineering, Brno University of Technology; Department of Mechanics, Faculty of Civil Engineering, Czech Technical University in Prague, novakj@cml.fsv.cvut.cz

One of those concepts, the Trefftz Stress Finite Element Method (TSFEM) [1] is outlined in the sequel. It focuses on enhancing the standard approximation basis by means of microstructural enrichment functions. In the context of this method, the enrichments characterize the stress filed at the level of material constituents. The components of sought tensorial function are embedded in a matrix Σ^* which is involved in ansatz (1). For the detailed discussion on the method in the current context or micromechanics-based enrichment constructions, respectively, we refer to [2] and [3].

1.1. HYBRID TREFFTZ STRESS ELEMENT APPROACH

In the hybrid approach that builds on the Trefftz stress element formulation by Teixeira de Freitas [4], we seek for the approximate solution to local stresses within an element open domain Ω_e in the form

$$\sigma^h(\boldsymbol{x}) = [\Sigma(\boldsymbol{x}) + \Sigma^*(\boldsymbol{x})]\,\mathsf{a} \quad \forall \boldsymbol{x} \in \Omega_e, \tag{1}$$

where the matrices $\Sigma(\boldsymbol{x})$, $\Sigma^*(\boldsymbol{x})_{3\times 3}$, respectively, ensemble the macroscopic stress approximation functions and their self-equilibrated microscopic counterparts [3]; a stands for the vector of standard degrees of freedom, noting that no extended degrees of freedom are introduced due to the imposed compatibility between macro and micro (perturbation) basis.

1.2. COMPLEX MICROSTRUCTURAL ENRICHMENT FUNCTIONS

A determination of individual components $\Sigma^*_{ij}(\boldsymbol{x})$ of the matrix $\Sigma^*(\boldsymbol{x})$ is a tremendous task, namely if considering large supports over which they are usually desired to be evaluated. This is why, geometrically simple low-scale phenomena as e.g. stress jumps on material interfaces, smeared reinforcement bond slip, crack propagation, etc. is usually considered. Techniques to evaluate functions that can reflect complex geometrical and topological arrangement of heterogeneities are very limited. To name a few, analytical micromechanics was successfully used for thousands of ellipsoidal inclusions in an isotropic matrix [3]. Fast summation solvers [5], on the other hand, allow for a complex non-analytic geometry, but perform well for small supports only. Recently a new technique blending Wang tilings, single-objective optimization and mentioned Fast Fourier transform based tools has been proposed [2]. However, the incompatibility of local stresses among individual tiles revealed excessively strong. Moreover, the situation deteriorates when further emphasizing spatial features of reconstructed microstructures.

In this contribution we thus present the preliminary outcomes of yet another approach which reduces the number of optimization parameters and is accurate and efficient from computational overhead point of view. Preliminary observations show that the adopted strategy leads to reconstructed fields exhibiting better balance in spatial statistics of underlying and reconstructed microstructures as well as compatible fields on congruent tile edges. The method consists in complete removal of optimization parameters with respect to mechanical field components and their substitution with so called extended tile sets obtained from solutions to specifically arranged small valid tilings being the subject to uniform strain excitation.

2. METHODOLOGY

2.1. A BRIEF INTRODUCTION TO WANG TILINGS

As the subject of Wang tilings is rather rare to computational mechanics community let us briefly remark on this topic at first.

The gaming pieces, dominoes have spread throughout Europe from Italy where it had been brought from China in the early 18th century. In the most likely country of origin China[4], however, it is believed to be known since six centuries backwards. Despite the above historical evidence, the idea of Wang tilings is quite recent, introduced to scientific community in the early sixties of the last century for purposes of mathematical theorem proofs by means of pattern recognition [6]. It uses a concept of four-sided square dominoes – tiles, gathered in sets, capable of covering portions or entire 2D planes called tilings. Contrary to original gaming dominoes which are linked together through the rules related to morphological information within each block half, the fusion of Wang tiles is allowed through a morphology assigned to congruent edges distinguished by colors, near-edge locking patterns and either numerical or alphabetical codes [7]. The tiles are not allowed to rotate when fusion performed, thus two tiles with the same sequence of edge codes mutually rotated by $k\pi/4$ are considered different. The tiling synthesis algorithms, stochastic or deterministic [8, 9], are designed so that no sequence of tiles periodically repeats, which together with carefully designed tile surface textures predisposes the technique to compress morphological information of complex random microstructures [7].

2.2. RECONSTRUCTION OF MICROSTRUCTURAL ENRICHMENTS ON OPEN DOMAINS

Contrary to purely morphological results evidenced so far [7], the current effort is more difficult as it aims at compression and reconstruction of tensorial functions. With respect to non-local character of mechanical quantities, we do not last with standard Wang sets with minimum corner edge combination duplicates but must extend them according to Tab. 1. Moreover, individual enrichment functions $\Sigma^*_{ij}(\boldsymbol{x})$ should still correspond with underlying microstructure quantified by the two-point probability function S_2 in order to avoid parasitic long range orientation orders as discussed in [2]. The reconstruction of required quantities itself is performed by means of stochastic tiling synthesis due to Cohen *et al.* [8].

2.3. EXTENDED TILE SETS AND THEIR MORPHOLOGY DESIGN

As reported in [7], the creation of tiles and sets that store strictly scalar information as material microstructure or a surface texture is fairly straightforward. Certain difficulty reveals when one attempt to deal with patterns of non-scalar quantities as stresses, strains or displacements. In this case, a morphological appearance of each tile in tiling depends on other tiles, at least on those placed in a near neighbourhood. The extent of this dependence is given by a physics and particular governing equa-

[4]Egyptian or Arabian origins are also theorized.

tions of sought quantity and also the ratio between tile edge dimension and characteristic microstructural length(s). Contrary to the strategy adopted in [2] the design of tiles with microstructural patterns and those carrying local fields has been decoupled. Thus originally multi-objective optimization reduces to a single-objective optimization of the microstructure. Other quantities are calculated separately. This goes, however, at the expense of drastic increase of number of tiles in the set, Tab. 1, here called extended set. For example, instead of eight tiles necessary to reconstruct either microstructural or stress patterns according to the methodology reported in [2], this number increases to $32,768$ by making use current strategy, first row of Tab. 1. Nonetheless, local stresses in these tiles are calculated in consid-

Tab. 1 Number of tiles in extended tile sets. Last column addresses the time complexity of extended set morphology design, provided that the evaluation of a single combination is in order of $O(10^0)$ seconds.

Tile set	No. tile combinations in cardinal i-th and ordinal ij-th directions									Time complexity‡
	1	*2*	*3*	*4*	*13*	*23*	*24*	*14*	$n_{3\times3}^{\text{comb}}$	
W8/2-2	4	4	4	4	2	2	2	2	$32,768$	$O(10^1)$ hours
W16/2-2	8	8	8	8	4	4	4	4	$16,777,216$	$O(10^2)$ days
W18/3-3	18	18	18	18	9	9	9	9	$12,397,455,648$	$O(10^5)$ days

erably simpler and smaller subdomains and only once comparing to thousands of evaluations during multi-objective optimization process. The domains are synthesized of a single Wang tile t_i and eight adjacent neighbours situated along cardinal and ordinal directions, Fig. 1b. These are then the subject to periodic boundary conditions and strain field excitation, successively set to one for normal and shear components. The resulting local mechanical fields within t_i as the functions of particular load case and unique combination of boundary tiles are thus delivered. The extended set of tiles with stress patterns is then gathered from all admissible combinations of tiles t_i from a standard Wang set as shown e.g in Fig. 1a, and those around its boundary, Fig. 1b. A total number of combinations renders the total extent of extended sets as listed in the penultimate column of Tab. 1.

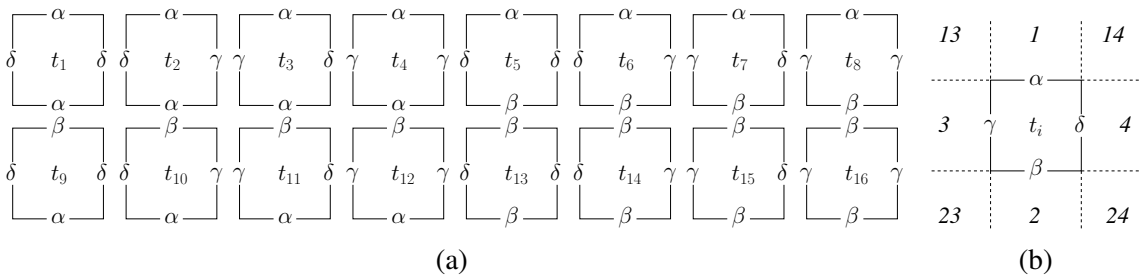

(a) (b)

Fig. 1 a) Wang tile set $W16/2-2$ made of 16 tiles with two distinct edge codes in vertical (α,β) and horizontal γ,δ directions, b) tile t_i within its neighborhood given by cardinal-i and ordinal-ij directions.

3. NUMERICAL EXPERIMENTS

The proposed methodology has been tested on the same benchmarks as numerical experiments reported in [2]. Summarized, a two phase random composite made up of homogeneous isotropic matrix with uniformly distributed equi-sized circular disks of radius ρ is considered. Young modulus and Poissons ratio of the matrix and the disk phase, respectively, is set to $E_m = 1,\ \nu_m = 0.1$ and $E_d = 10,\ \nu_m = 0.4$. Moreover, a converse example with swapped stiffnesses is also explored. The synthesized stress enrichment functions are plotted over the reconstructed domain $\widetilde{\Omega}$ consisting of 9×9 tiles whose appearance is shown in Fig. 4b.

First, in Fig. 2, it is shown the distribution of the first component Σ^*_{11} of the matrix of perturbation stress approximation functions calculated directly in the reconstructed domain $\widetilde{\Omega}$, Fig. 2a, its synthesized counterpart $\widetilde{\Sigma}^*_{11}$, Fig. 2b, and relative error, Fig. 2c, calculated according to Eq. (2).

$$f_{\tilde{\sigma},ij}(\boldsymbol{x}) = \frac{\|\Sigma_{ij}(\boldsymbol{x}) - \widetilde{\Sigma}^*_{ij}(\boldsymbol{x})\|_1}{\|\Sigma_{ij}(\boldsymbol{x})\|_1} \quad \forall \boldsymbol{x} \in \widetilde{\Omega},\ i,j = 1,2,3. \tag{2}$$

The results for the swapped contrast of Young's moduli are displayed in Fig. 3. It is evident from both

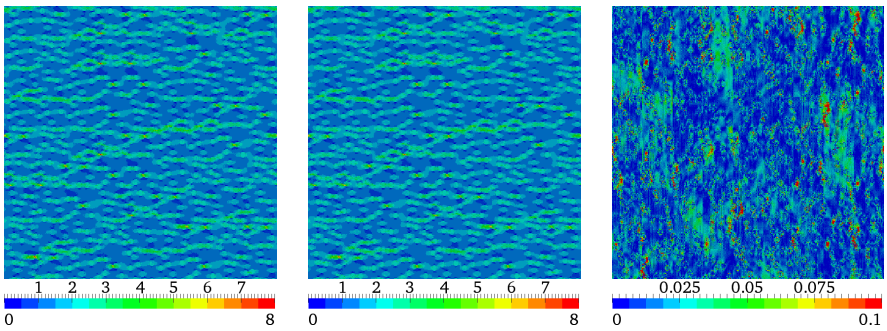

(a) (b) (c)

Fig. 2 Comparison of reference and synthesized stress field approximation function for contrast $E_d/E_m = 10^1$, a) Σ^*_{11} evaluated directly in reconstructed domain $\widetilde{\Omega}$, b) $\widetilde{\Sigma}^*_{11}$ synthesized from extended tile set, c) relative error according to Eq. (2).

figures that the relative error is less than 2.5% or 5% in most points of $\widetilde{\Omega}$ for respective contrasts except tiny local regions (in red) where the acquired error may go from 10% to approximately 60%, noting that the color patterns ware rescaled between zero and 10% for clear visualization of low error regions. As for the quality of reconstructed microstructure, Fig. 4b, it evidently exceeds those obtained with the help of multi-objective optimization, Fig. 4c,d. Moreover, its proximity to reference morphology, Fig. 4a, is well captured for long range orientation orders since parasitic artifacts are difficult to observe. However, it is less conclusive for short range orientation orders, namely due to the choice of S_2 as the only descriptor. To improve the situation, an additive descriptor, e.g. the Lineal path function, would be necessary. Rather weak long range spatial artifacts are also underpinned by the curves in Fig. 5a, obtained as the

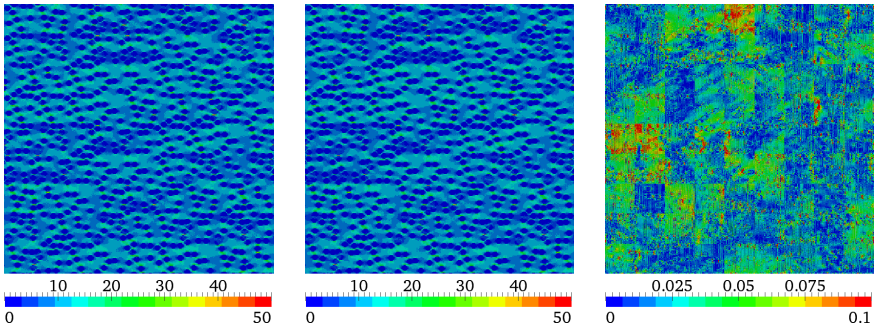

Fig. 3 Comparison of reference and synthesized stress field approximation function for contrast $E_d/E_m = 10^{-1}$, a) Σ^*_{11} evaluated directly in reconstructed domain $\widetilde{\Omega}$, b) $\widetilde{\Sigma}^*_{11}$ synthesized from extended tile set, c) relative error according to Eq. (2).

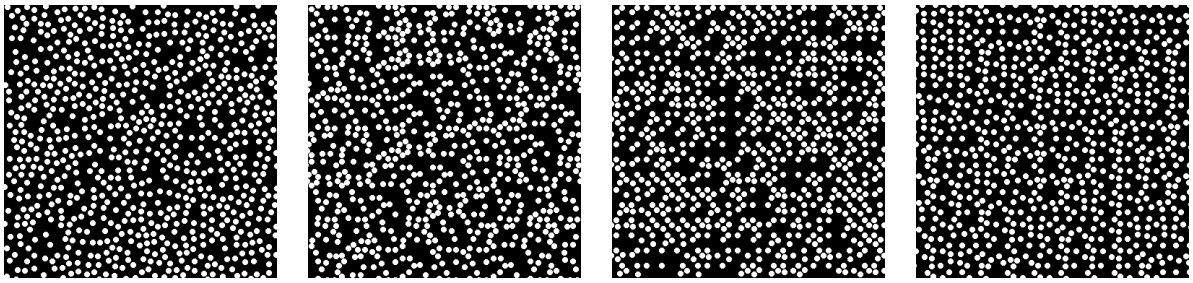

Fig. 4 Microstructural patterns for a) reference medium, b) synthesized medium by single-objective optimization ($\alpha = \infty$), c) synthesized medium by multi-objective optimization ($\alpha = 10^4$), d) synthesized medium by multi-objective optimization ($\alpha = 10^5$).

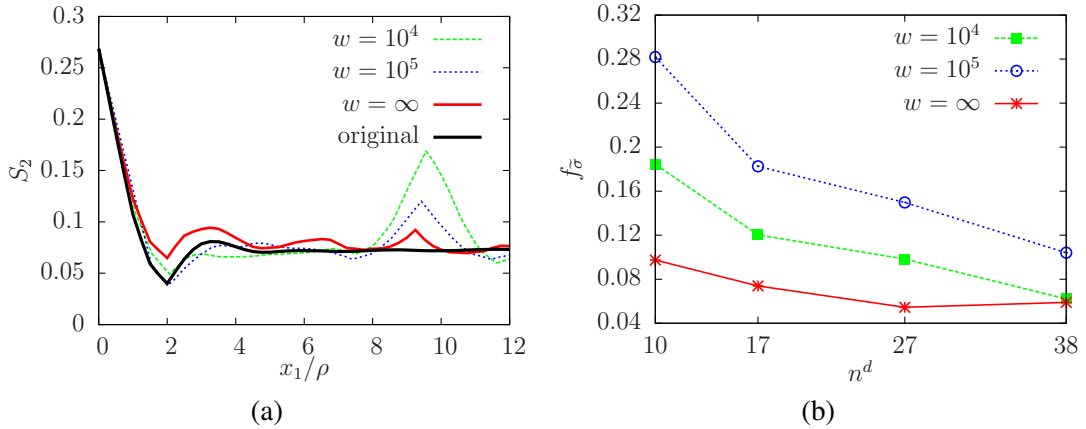

Fig. 5 a) Two-point probability functions of reference and reconstructed media obtained by single and multi-objective optimization, b) relative stress error with respect to number of disks within tile set.

cross-sections through S_2 functions for each microstructure representation displayed in Fig. 4.

The optimal configuration of perturbation stress patterns in extended set can be further supported by the evolution of the relative cumulative error, Fig. 5b, defined as [2]

$$f_{\widetilde{\sigma}} = \frac{1}{|\widetilde{\Omega}|} \int_{\widetilde{\Omega}} \delta_{ij} f_{\widetilde{\sigma},ij}(\boldsymbol{x}) \, \mathrm{d}\boldsymbol{x}, \tag{3}$$

where δ_{ij} denotes the Kronecker delta and for a single component $f_{\widetilde{\sigma},ij}(\boldsymbol{x})$ holds [2]

$$f_{\widetilde{\sigma},ij}(\boldsymbol{x}) = \frac{\|\Sigma_{ij}(\boldsymbol{x}) - \widetilde{\Sigma}^*_{ij}(\boldsymbol{x})\|_1}{\|\max_{\boldsymbol{x}} \Sigma_{ij}(\boldsymbol{x}) - \min_{\boldsymbol{x}} \Sigma_{ij}(\boldsymbol{x})\|_1} \quad \forall \boldsymbol{x} \in \widetilde{\Omega}, \; i,j = 1,2,3. \tag{4}$$

The results clearly demonstrate that in the original multi-objective algorithm $f_{\widetilde{\sigma}}$ increases with increasing w, see [2] for more details. Contrary, in the proposed method, which corresponds with $w = \infty$ in original algorithm, the error remains independent of S_2 and keeps its values underneath those for $w = 10^4$. Moreover, it exhibits positively descending trend for tiles involving more morphological information, which is mirrored by increasing number of disks n^d in the set or dimension of tile edges. However, this conjecture seems somehow violated for tiles larger than a threshold value $n^d = 27$ and must be carefully explored in years to come.

4. CONCLUSIONS

In this contribution we have outlined a new way of synthesizing complex microstructural stress enrichment functions by means of extended Wang tile sets, single-objective optimization and stochastic tiling synthesis. On the basis of acquired results we have conjectured that

- the proposed technique is better posed regarding the quality of calculated mechanical fields and microstructural patterns than the original multi-objective optimization based method reported in [2].
- extended sets can be used similarly to standard Wang sets to synthesize micromechanical fields on open domains.
- less than 15% of the synthesized function support is burdened with relative cumulative error larger than 10%, Fig. 6.

ACKNOWLEDGEMENT

The authors acknowledge the European Social Fund endowment under Grant No. CZ.1.07/2.3.00/30.0005 of Brno University of Technology (Support for the creation of excellent interdisciplinary research teams at Brno University of Technology). Furthermore, this work was supported in part by the Czech Science Foundation, Grant No. 105/12/0331.

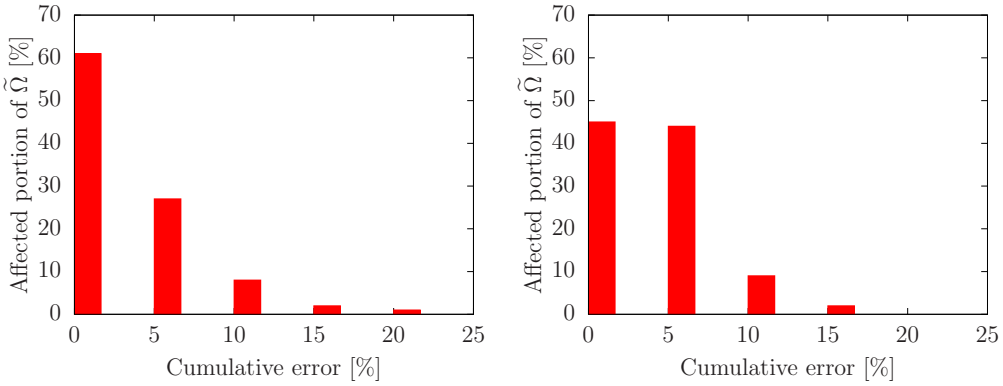

Fig. 6 Histograms of relative cumulative error, Eq. (2), for a) $E_d/E_m = 10^1$, b) $E_d/E_m = 10^{-1}$.

REFERENCES

[1] Herrera I. *Trefftz method: a general theory*. Numerical Methods for Partial Differential Equations, 16(6):561–580, 2000. ISSN 1098-2426.

[2] Novák J. - Kučerová A. - Zeman J. *Microstructural enrichment functions based on stochastic Wang tilings*. 2011. Available at: http://arxiv.org/abs/1110.4183.

[3] Novák J. - Kaczmarczyk Ł. - Grassl P. - Zeman J. - Pearce C. J. *A micromechanics-enhanced finite element formulation for modelling heterogeneous materials*. Computer Methods in Applied Mechanics and Engineering, 201–204(0):53 – 64, 2012. ISSN 0045-7825.

[4] Teixeira de Freitas J. A. *Formulation of elastostatic hybrid-Trefftz stress elements*. Computer Methods in Applied Mechanics and Engineering, 153:127–151, 1998. ISSN 0045-7825.

[5] Zeman J. - Vondřejc J. - Novák J. - Marek I. *Accelerating a FFT-based solver for numerical homogenization of periodic media by conjugate gradients*. Journal of Computational Physics, 229(21):8065–8071, 2010. ISSN 0021-9991.

[6] Wang H. *Proving theorems by pattern recognition–II*. Bell Systems Technical Journal, 40(2):1–41, 1961. ISSN 0005-8580.

[7] Novák J. - Kučerová A. - Zeman J. *Compressing Random Microstructures via Stochastic Wang Tilings*. 2011. Available at: http://arxiv.org/abs/1206.0933.

[8] Cohen M.F. - Shade J. - Hiller S. - Deussen O. *Wang tiles for image and texture generation*. ACM Transactions on Graphics, 22(3):287–294, 2003. ISSN 0730-0301.

[9] Culik K. *An aperiodic set of 13 Wang tiles*. Discrete Mathematics, 160:245–251, 1996. ISSN 0012-365X.